

**Computer Simulations of Amyloid
Aggregation Considering *in vivo*
Conditions**

Inaugural dissertation

for the attainment of the title of doctor
in the Faculty of Mathematics and Natural Sciences
at the Heinrich-Heine-Universität Düsseldorf

presented by

Hebah Fatafta

from Amman, Jordan

Jülich, June 2022

From the institute for Biological Information Processing (IBI-7): structural Biochemistry
at the Forschungszentrum Jülich

Published by permission of the
Faculty of Mathematics and Natural Sciences at
Heinrich Heine University Düsseldorf

Supervisor: Prof. Dr. Birgit Strodel

Co-supervisor: Prof. Dr. Henrike Heise

Date of the oral examination: 05. May 2022

Declaration of Authorship

I, Hebah Fatafta, hereby certify that the work presented here is, to the best of my knowledge and belief, original and the result of my own investigations. I have fully acknowledged and referenced the ideas and work of others, whether published or unpublished, in my thesis. My thesis contains no material published elsewhere or extracted in whole or in part from a thesis submitted for a degree at this or any other university. Where the results are produced in collaboration with others, I have clearly mentioned my contributions.

Signed:

Date:

Abstract

Amyloid associated diseases, such as Alzheimer’s disease and type 2 diabetes are markedly characterized by the abnormal aggregation of amyloid peptides into fibrillar aggregates. A large body of evidence supports the view that amyloid oligomers are more toxic than mature fibrils. Therefore, many studies focus on the linkage of these oligomers and the disease, but most of them are performed in the test tube without taking into account the *in vivo* environment. However, amyloid aggregation is a complex process that is sensitive to external conditions. Thus, it is of great relevance to extend these investigations to mimic the real environment conditions, where the amyloid formation is affected by other biomolecular interactions. The aim of this thesis work is to investigate the behavior of the amyloid-beta ($A\beta$) peptide and human islet amyloid polypeptide (hIAPP), that are linked to the development of Alzheimer’s disease and type 2 diabetes, respectively, in an environment that mimic some aspects of the brain or the pancreatic β -cell conditions. To this end, I employed all-atom molecular dynamics (MD) simulations to perform multiple studies that focused on (i) the interplay between $A\beta_{42}$ dimers and the neuronal membrane, (ii) the effect of free lipids in the aqueous phase as a possible interaction partner of $A\beta_{42}$ on the peptide structure and its interaction with a lipid membrane, (iii) the effect of oxidized glycine residues, Gly25, Gly29, and Gly33, of $A\beta_{42}$ on its conformation and interaction with a lipid membrane, (iv) the effect of macromolecular crowding on $A\beta_{16-22}$ aggregation, (v) the effect of mutating histidine at position 18 in hIAPP to arginine, lysine, glutamic acid, and alanine on its conformation and interaction with a model membrane. All these studies were realized at atomic resolution to appropriately address the conformational transitions of $A\beta$ and hIAPP. All-atom MD simulation have emerged as a powerful tool to address biological questions from different disciplines, and are widely known as “computational microscope” that provides atomistic detail into the studied systems.

The results from these simulation studies lead to the following conclusions; (i) The dimerization in solution is characterized by a random coil to β -sheet transition that seems on pathway to amyloid aggregation, while the interactions with the neuronal membrane attenuate the peptide’s propensity to form a β -sheet structure. (ii) The $A\beta_{42}$ peptide underwent a disorder-to-order transition in 1:3 complex, but remains largely disordered in 1:1 complexes, yet despite complex formation with lipids the peptide did not insert into the membrane. (iii) The $A\beta_{42}$ peptide oxidized at Gly25 is potentially as toxic as the wild-type peptide assuming that β -sheet formation in $A\beta$ is connected to its toxicity. (iv) Macromolecular crowding enhances the dimer and hexamer formation with β -sheets of $A\beta_{16-22}$. (v) For all IAPP variants but H18E-IAPP, the membrane-bound IAPP adopted an amphipathic-helical structure, which turned on to be on the way to IAPP

amyloid aggregation apart for IAPP with glutamic acid at position 18 that remained in a stable helical conformation.

In summary, the simulation studies in this thesis were useful toward uncovering the combined effect of several *in vivo* conditions on A β and hIAPP, which is expected to be of relevance for other amyloid proteins too.

Acknowledgements

I would like to express my deep and sincere gratitude to my supervisor Prof. Birgit Strodel, who encouraged me for the scientific study of my PhD research at the Forschungszentrum Jülich. Her expertise and depth knowledge always inspire me to do my best. I acknowledge her for giving me the chance to realize my potential and to pursue research as a career later in my life. I hope one day I will be able to help students achieve their goals just as you have helped me. It was a great honor and privilege to work under your guidance!

I am appreciative to Prof. Henrike Heise for her commitment in offering thorough feedback on this thesis. I am grateful to my collaborators for the different research projects, I acknowledge their help and support that guide me finding my way through the field. Sincere thanks go to Prof. Abdallah Sayyed-Ahmad, Dr. Michael Owen, Dr. Chetan Poojari, and to my colleagues at Strodel's lab Dr. Batuhan Kav, Jennifer Loschwitz, Mohammed Khaled and Bastian Bundschuh. Your effort is really appreciated!

I acknowledge the Forschungszentrum Jülich for the wonderful research environment that is always inspiring me, as well as Jülich Supercomputing Center (JSC) for the computing resource on Jureca. I acknowledge the financial support from BMFB, the Palestinian-German Science Bridge (PGSB) that initiated fruitful scientific cooperation which enable me and other Palestinian students to gain the study and research experience at German institutions. Three years ago, I was very happy and appreciative to learn that I was selected as the recipient of the scholarship. My heartfelt thanks for the generosity and support that allow me to pursue my goals. I will work very hard to give back to the community and hopefully to support future students.

I thank my previous and current colleagues for their stimulating discussions as well as happy distractions to rest my mind outside of my research. I enjoyed the time with you!

I take the opportunity and extend my thanks to my institution, the institute of Biological Information processing (IBI-7) for the inspiring and lovely working environment, and express gratitude to the institutional head Prof. Dieter Willbold for supporting us in keeping up the good work.

I am forever indebted to my husband for his continuous support. It's hard to imagine the PhD journey without you. I am extending my warmest thanks to my parents for their love, and prayers. My heartfelt thanks goes to my kids too. I am extremely thankful for your love. It is the engine for my improvement!

Finally, thanks God for letting me through all difficulties and blessing me with continuing my research.

Contents

Declaration of Authorship	i
Abstract	ii
Acknowledgements	iv
Abbreviations	vii
1 Introduction	1
1.1 Amyloid aggregation and disease	2
1.1.1 Amyloid- β peptide	5
1.1.2 Human islet amyloid polypeptide	6
1.2 Impact of the physiological conditions	8
1.2.1 Biological membranes	9
1.2.2 Interaction partners	12
1.2.3 Oxidative stress	13
1.2.4 Macromolecular crowding inside the cell	15
2 Methods	17
2.1 Historical background	18
2.2 Molecular dynamics theory	19
2.3 Potential function and energy landscape	20
2.3.1 Integration algorithms: The velocity Verlet algorithm	24
2.4 Simulation environment	26
2.4.1 Thermostat	27
2.4.2 Barostat	28
2.5 Periodic Boundary conditions (PBCs)	29
2.6 MD recipe	31
2.6.1 Energy minimization	31
2.6.2 Equilibration	32
2.6.3 Production run	33
2.7 MD limitations	33
2.7.1 Metadynamics (MetaD)	34
2.7.2 Replica Exchange Molecular Dynamics (REMD)	36
2.8 Aims	38

3	Results	39
3.1	Publication I: A β 42 and the neuronal membrane	39
3.1.1	Background	40
3.1.2	Results	41
3.1.3	Conclusion	43
3.2	Publication II: A β 42-lipid complex	43
3.2.1	Background	43
3.2.2	Results	45
3.2.3	Conclusion	48
3.3	Publication III: A β 42 and oxidative stress	48
3.3.1	Background	49
3.3.2	Results	49
3.3.3	Conclusion	51
3.4	Manuscript IV: A β 42 and macromolecular crowding	52
3.4.1	Background	53
3.4.2	Results	53
3.4.3	Conclusion	56
3.5	Publication V: hIAPP and membrane binding	57
3.5.1	Background	57
3.5.2	Results	58
3.5.3	Conclusion	60
4	Conclusions	62
A	Published Articles	67
A.1	Publication I	68
A.2	Publication II	91
A.3	Publication III	106
A.4	Manuscript IV	135
A.5	Publication V	153
	Bibliography	176

Abbreviations

DNA	Deoxyribonucleic Acid
RNA	Ribonucleic Acid
AD	Alzheimer's Disease
T2DM	Type 2 Diabetes Mellitus
IDPs	Intrinsically Disordered Proteins
$A\beta$	Amyloid-beta
APP	Amyloid Precursor Protein
hIAPP	Human Islet Amyloid Polypeptide
MD	Molecular Dynamics
ROS	Reactive Oxygen Species
GM1	Ganglioside
PC	Phosphatidylcholine
PS	Phosphatidylserine
PE	Phosphatidylethanolamine
MM	Molecular Mechanics
FFs	Force Fields
PBCs	Periodic Boundary Conditions
MetaD	Metadynamics
CV	Collective Variable
REMD	Replica Exchange Molecular Dynamics
HREMD	Hamiltonian Replica Exchange Molecular Dynamics
POPC	1-palmitoyl-2-oleoyl-sn-glycero-3-phosphocholine
POPE	1-palmitoyl-2-oleoyl-sn-glycero-3-phosphoethanolamine
POPS	1-palmitoyl-2-oleoyl-sn-glycero-3-phospho-L-serine
CHOL	Cholesterol

SM	Sphingomyelin
DPPC	1,2-dipalmitoyl-sn-glycero-3-phosphocholine
wt	wild-type
CG	Coarse-Grained
DMD	Discontinuous Molecular Dynamics
FES	Free Energy Surface
FTIR	Fourier-Transform Infrared
TEM	Transmission Electron Microscopy
DOPC	1,2-dioleoyl-sn-glycero-3-phosphocholine
DOPS	1,2-dioleoyl-sn-glycero-3-phospho-L-serine

Chapter 1

Introduction

Biomolecules or biological molecules are the molecules produced by cells and living organisms, and are important for their functioning. They are all organic matter of different sizes and structures, mainly classified into four major types including carbohydrates, lipids, nucleic acids and proteins (Fig. 1.1). Typical cells contain 10,000 to 100,000 kinds of biomolecules, which can exist in simple (e.g. monomeric) or complex (e.g. polymeric, oligomeric) forms.

Among the existing biomolecules, proteins are the predominant biomolecules, which are found in each cell and constitute 50% of its dry weight. Proteins form the structural and physiological basis of all life processes. According to the central dogma of molecular biology, the deoxyribonucleic acid (DNA) encodes the genetic information that is transcribed into messenger ribonucleic acid (RNA) and then translated into an amino acid sequence (polypeptide chain) that folds into a protein. Following its synthesis, the polypeptide chain usually folds into its three-dimensional native (globular) structure in order to properly perform its biological function [1]. Protein folding within the cell is a complex process in which the protein should withstand different environmental conditions including temperature, pressure, molecular crowding etc. The cell has its own preventative or corrective mechanisms to rescue proteins and avoid their misfolding. Nonetheless, protein misfolding can still occur and lead to the formation of reversible or irreversible aggregates [2–5].

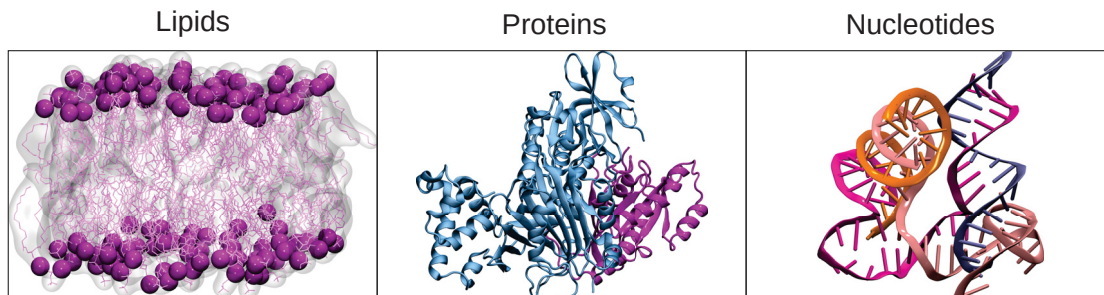


FIGURE 1.1: Biomolecules of life. Lipids form cell membranes, proteins do the work of the cell, and nucleotides are the protein blueprints and fabrication.

1.1 Amyloid aggregation and disease

Protein self-aggregation (self-assembly) is a wide-ranging phenomenon and is of great importance for a wide area of sciences including protein biochemistry, biotechnology, and medicine [6]. Such phenomenon occurs naturally *in vivo* for several globular proteins such as tubulin and actin, in which the protein form reversible fibrils [7, 8]. However, some other proteins form irreversible (locked) amyloid fibrils [7, 8] that are implicated in the pathogenesis of several degenerative human diseases, including Alzheimer’s disease (AD), Parkinson’s or type 2 diabetes mellitus (T2DM) [9–12]. These proteins are commonly known as amyloid forming proteins, they are often intrinsically disordered proteins (IDPs) or are proteins that contain one or more intrinsically disordered regions [13, 14].

The currently accepted meaning of disorder embraces protein regions or proteins that are biologically active, but are dynamically flexible either at the secondary and/or tertiary structure level [15]. This disordered nature renders IDPs not only with functional versatility, but also with a tendency to trigger protein misfolding. The former allows IDPs to perform different biological activities, including transcription and translation regulation, cellular signal transduction, the storage of small molecules, protein phosphorylation, and self-assembly regulation [16, 17](Fig. 1.2). However, the latter may result in the formation of protein aggregates such as amyloid fibrils that is associated with the development of various amyloid diseases [18, 19].

Amyloid associated diseases share a common pathology in which the misfolded or disordered proteins tend to aggregate, intra- or extra-cellularly, into proteinaceous deposits or plaques in various tissues and organs [20–22]. It is believed that the accumulation of plaques plays a crucial role in the progression of the resultant diseases, either via ‘the

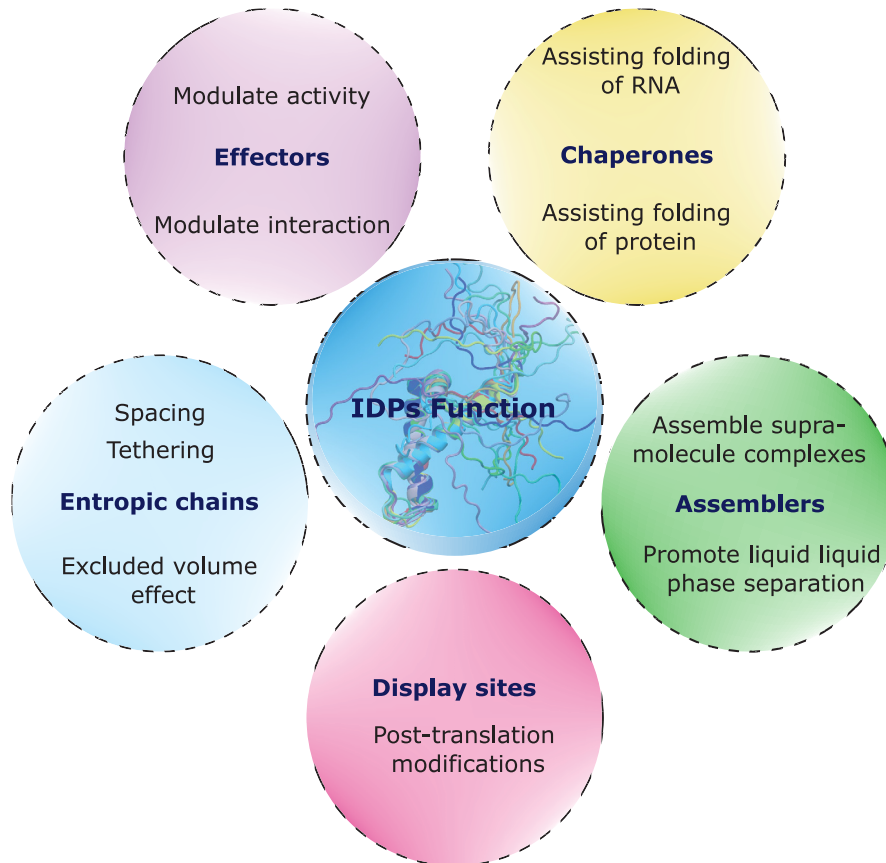


FIGURE 1.2: Overview of different functions of intrinsically disordered proteins.

gain of toxicity’, i.e. destroying the surrounding cells, tissues and organs, or via the ‘loss of normal function mechanism’, i.e. the failure of cellular process as a result of sequestering important proteins in the plaques and hence disease formation [22, 23].

The major constituent of amyloid plaques is the amyloid fibrils, the end product of protein aggregation. Amyloid fibrils are usually polymorphic, but their structures are all composed of arrays of cross β -sheets formed by β -strands of individual peptide or protein units [24, 25]. The assembly of the soluble protein into such fibrillar structures can occur via nucleated or non-nucleated pathways [26, 27]. The widely accepted model for fibril assembly (supported by several *in vitro* experimental observation) is the nucleated-polymerisation model, which proposed the nucleus formation as the rate-limiting step in the assembly pathway (Fig. 1.3). According to the nucleated-polymerisation model, the evolution from soluble monomers to mature fibril is a stepwise process in which the nucleation phase and elongation phase precede the fibril formation. Monomers associate to form the thermodynamically unfavourable nucleus (oligomer) in the so-called nucleation phase, then the preformed nucleus can polymerize quickly upon the addition of

further monomers in the so-called elongation phase to form the mature fibrils.

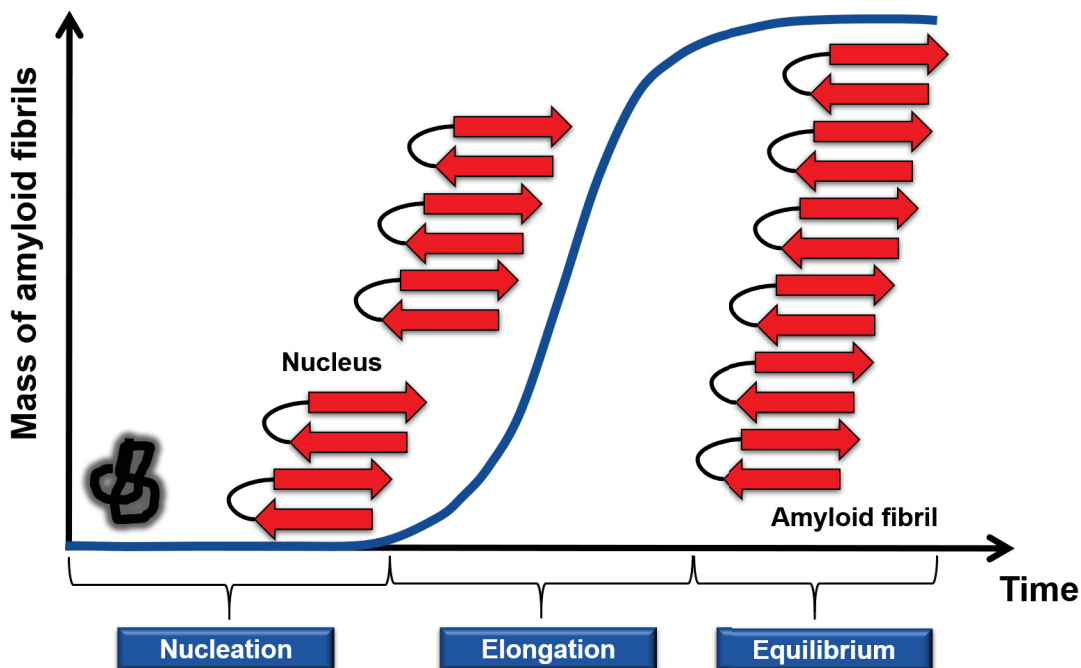


FIGURE 1.3: Representative illustration of the nucleated-polymerization model, with its three phases labeled, i.e. nucleation, elongation, and equilibrium.

To date, a wealth of research studies has been published about amyloid fibrils; it is particularly difficult to capture and characterize the early formed oligomers due to their transient nature resulting from their high aggregation rate. Thus, most studies target the amyloid fibrils to gain more insight into the aggregation mechanism and its early stages. Nonetheless, the oligomers remain elusive. Moreover, most of the available studies on the amyloid aggregation have been performed in the test tube, i.e. under conditions far from physiological conditions. However, it is important to extend these investigations to *in vivo* conditions, in which the aggregation process is affected by the environmental conditions in the cell including oxidative stress, cell membrane and molecular crowding. Advancing our understanding of the effect of physiological conditions on amyloid proteins is a step forward toward better understanding of the aggregation mechanisms that underlies several of the devastating amyloid diseases, especially with the existing demand for a therapy to cure or prevent the occurrence of such diseases.

The focus of this thesis work will be on two amyloid peptides; the amyloid- β peptide and the human islet amyloid polypeptide (hIAPP) which are related to Alzheimer's disease and diabetes disease respectively. In my research on these amyloid proteins, I

have used molecular dynamics simulations to model various *in vivo* conditions found in their real environment, in particular the presence of lipids and lipid membranes as well as molecular crowding.

1.1.1 Amyloid- β peptide

The amyloid- β peptide ($A\beta$) is a soluble disordered peptide generated normally in the brain by the proteolytic cleavage of a transmembrane protein called amyloid precursor protein (APP), catalyzed by the enzymatic activities of β - and γ -secretases (Fig. 1.4) [28]. Following its production, the peptide level in the brain is maintained via a clearance mechanism, however faulty in the clearance mechanism leads to abnormally elevated levels of $A\beta$ and results in its accumulation and the formation of the extracellular plaques deposits in the brain; a hallmark of Alzheimer's disease (AD).

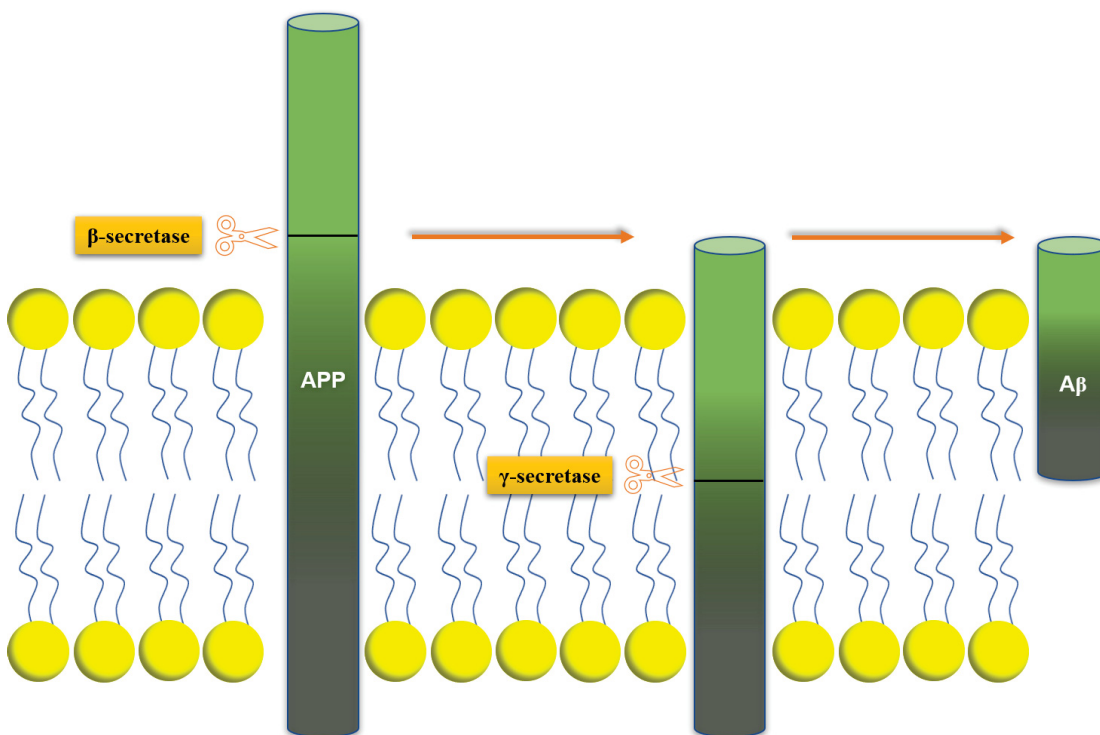


FIGURE 1.4: The sequential cleavage of the amyloid precursor protein (APP) by β - and γ -secretases to produce $A\beta$.

AD is a neurodegenerative disease affecting people with an age of 65 years and older, and known to be the most common form of dementia among the elderly [29, 30]. It is characterized clinically by a progressive decline in cognitive function and pathologically by neuronal dysfunction and neuronal loss, in addition to the accumulation of amyloid

plaques as the main hallmark [31–33]. The disease is named after Dr. Alois Alzheimer, who noticed changes in the brain of a woman that died out of unusual mental illness in 1906 [34]. After her death, the doctor examined the brain and found many abnormal clumps, the nowadays called amyloid plaques, and tangled bundles of fibers, nowadays known as neurofibrillary, or tau, tangles. Since then, several hypotheses emerged to explain the pathogenesis of AD [35], with the amyloid-cascade hypothesis being the most widely accepted one [36]. It dates back to 1992 when Hardy and Higgins postulated for the first time the accumulation of $A\beta$ peptides in the brain as the central event in the pathogenesis of Alzheimer’s disease. According to this hypothesis, $A\beta$ is strongly linked to the disease progression and severity.

In the brain, the APP cleavage yields $A\beta$ peptides of different length, with $A\beta_{40}$ and $A\beta_{42}$ being the most common alloforms, that contain 40 or 42 amino acids, respectively [37–39]. While $A\beta_{40}$ is the most prevalent alloform, $A\beta_{42}$ is reported to be predominant in senile plaques and is known to be more toxic than $A\beta_{40}$ [40–42]. In term of their amino acid constituents, the only difference between $A\beta_{42}$ and $A\beta_{40}$ are the additional hydrophobic residues at the C-terminus of $A\beta_{42}$ (see Fig. 1.5), an isoleucine and an alanine residue. These two residues were reported to affect the peptide flexibility via forming a β -hairpin at residues 31–34 and 38–41. This in turn might explain the greater tendency of $A\beta_{42}$ to aggregate. According to these observations the necessity to study the involvement of $A\beta_{42}$ in AD in detail emerges [43].

Over the last years a huge body of evidence has accumulated and shed light on the smaller soluble $A\beta$ oligomers, formed in the earlier stages of the aggregation process, as the main cytotoxic species (rather than the mature fibrils) [44–48]. Therefore, a detailed characterization of $A\beta_{42}$ oligomerization and its implication in AD at the molecular level is an essential step toward developing a better understanding of the aggregation process.

1.1.2 Human islet amyloid polypeptide

Human islet amyloid polypeptide hIAPP (also known as amylin), is a 37 residue peptide hormone synthesized and co-secreted with insulin from pancreatic β -cells (Fig. 1.6) [49–51]. hIAPP plays many biological roles in islet functions, including carbohydrate metabolism, insulin secretion, bone resorption, gastric clearance, and blood glucose regulation. However, under some unphysiological conditions, the peptide can misfold and assemble into

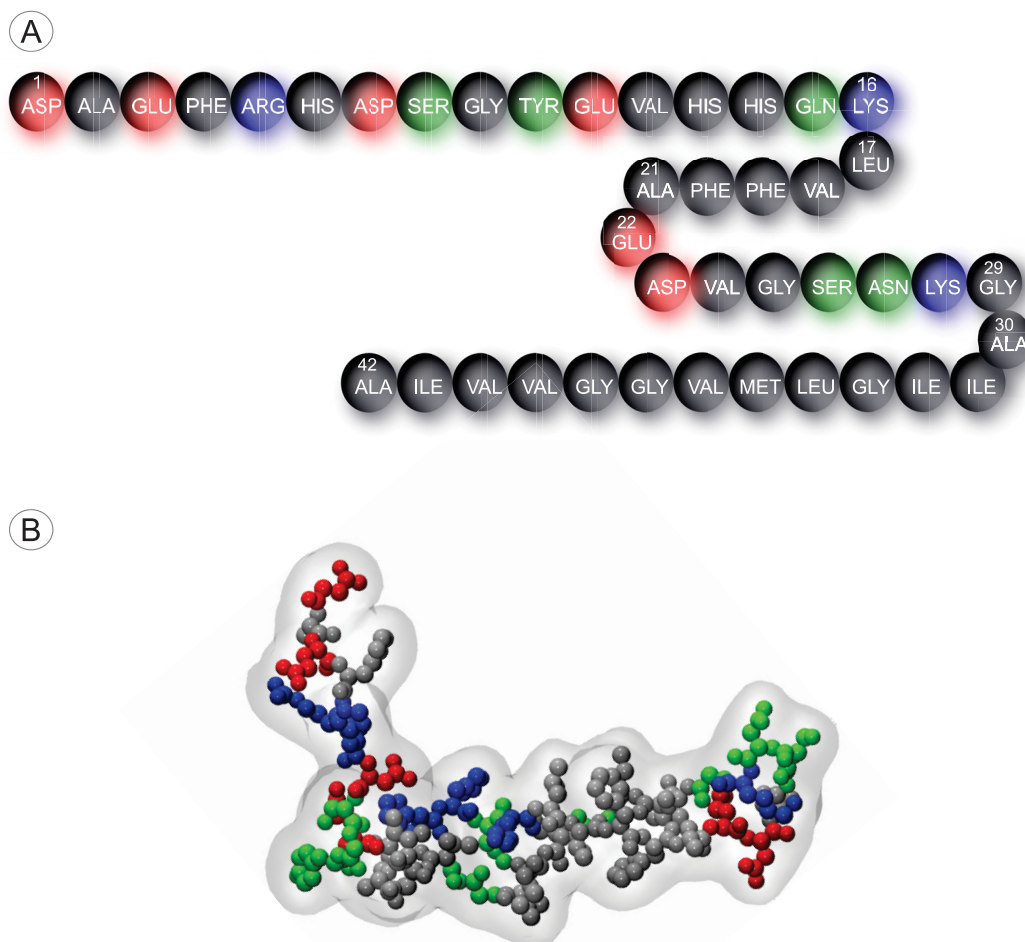


FIGURE 1.5: (A) The sequence of A β 42 with its amino acids colored such that acidic residues are shown in red, basic residues in blue, hydrophobic residues in black, and polar residues in green. The residues ASP1-LYS16 form the metal-binding region, residues LEU17-ALA21 form the central hydrophobic core, residues GLU22-GLY29 represent the central polar region, and the C-terminal hydrophobic region extends from ALA30-ALA42 residues. (B) van der Waals representation of the full-length A β 42 peptide with its amino acids being colored as explained in (A).

aggregates of different sizes and structures. It is thought that these aggregates, especially the small oligomers contribute to the death of β -cells responsible for the pathology of type 2 diabetes (T2DM) [52, 53]. The mechanism by which hIAPP induces β -cell death is a complex process that involves different pathways, including the formation of reactive oxygen species, the increase in endoplasmic reticulum stress, the initiation of inflammatory response, and membrane disruption. It has been found by several studies that membrane disruption plays an important role in cell toxicity [54, 55]. It has been demonstrated that hIAPP oligomers can interact directly with the cell membrane disrupting its integrity, function and permeability leading to ionic homeostasis perturbation, changes in signalling pathways, oxidative injury and consequently cell death [55–57]. Therefore,

understanding the interactions of hIAPP monomers and oligomers with the cell membrane is of great importance toward a better understanding of hIAPP aggregation and toxicity.

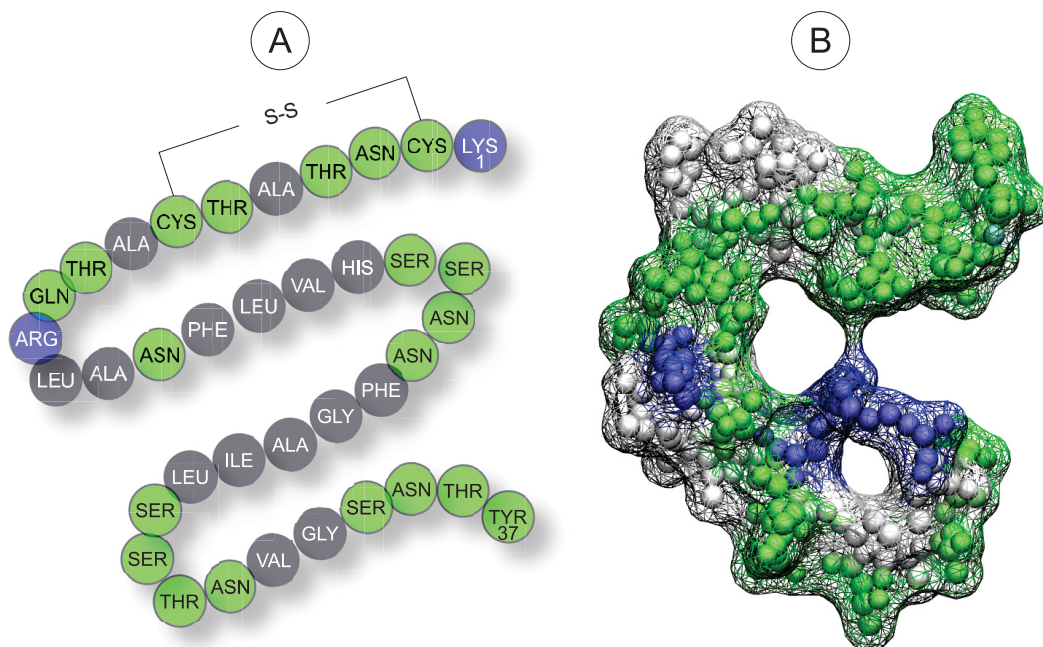


FIGURE 1.6: (A) The sequence of the hIAPP peptide with its amino acids colored such that basic residues are shown in blue, hydrophobic residues in black, and polar residues in green. The disulfide bridge (S-S) between cysteine residues 1 and 7 is shown. (B) Surface representation of hIAPP with its amino acids shown as spheres and colored as explained in (A).

1.2 Impact of the physiological conditions

Given the importance of amyloid forming proteins and their connection to devastating human diseases, it is important to characterize these proteins behavior in a more realistic environment, the so called *in vivo* environment. Amyloid aggregation in the *in vivo* environment is a more complex process than under controlled *in vitro* conditions. First of all, the *in vivo* concentration is much lower compared to *in vitro*. Second and importantly, is the effect of different physiological conditions in the *in vivo* environment such as biological membranes, molecular crowding, interaction partners and oxidative stress that may enhance or retard oligomer/fibril formation (see Fig. 1.7). Elucidating the effects of these conditions on the behavior of the amyloid proteins A β and hIAPP at the atomistic level using molecular dynamics (MD) simulations to this end, is the topic of this thesis work. MD simulations provide the scientific community with a powerful

platform that enable probing high resolution in space (single atom), time (femtosecond), and energy. Hence, there is hope that the computational approach will be able to capture the subtle and complex effects of different *in vivo* conditions on amyloid proteins, accordingly enhance our understanding on the nature of the cellular environments and our ability to make inferences based on that. The knowledge gained will bring us toward a quantitative understanding of the influences of the *in vivo* conditions on amyloid aggregation.

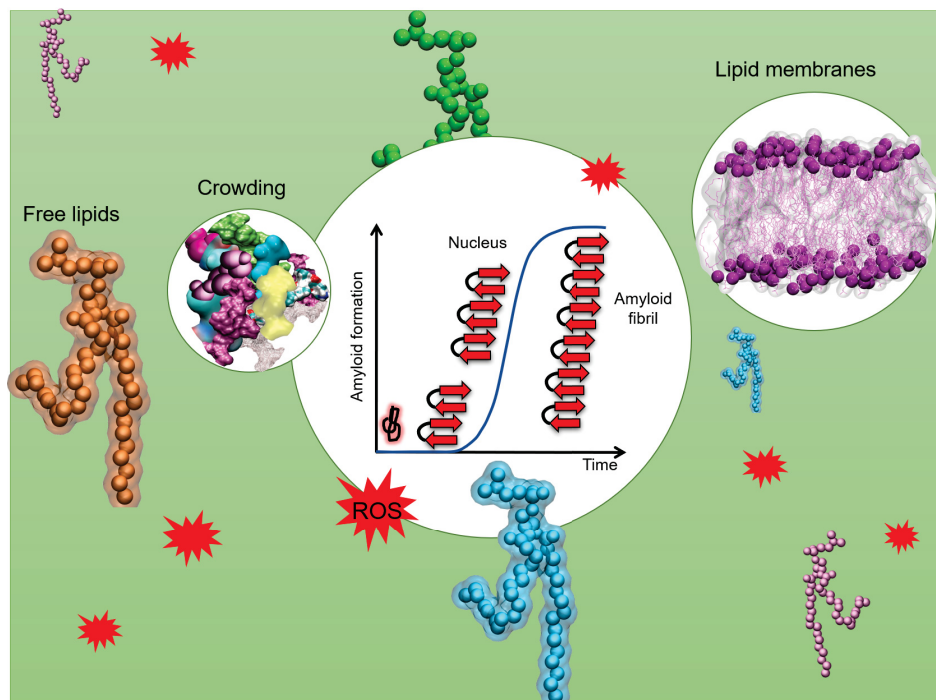


FIGURE 1.7: The figure shows the different *in vivo* conditions affecting amyloid aggregation that were studied in this thesis work. Lipid membranes, crowding effect, free lipids and reactive oxygen species (ROS) are all shown and labeled.

1.2.1 Biological membranes

Biological membranes are lipid bilayers that define the boundary of a living cell or intracellular compartments and range from 5 to 10 nm in thickness. They consist of lipids and proteins that give the membrane a fluid character [58]. Membrane lipids include three main classes; phospholipids, glycolipids, and sterols which are composed of fatty acid chains that determine whether a membrane is formed in a long sheet or round vesicle [59]. In 1925, Evert Gorter and François Grendel were the first to demonstrate that biological membranes are bilayers of lipid solely, and further deduced

that the plasma membrane must be composed of two layers of lipids [60]. This simple model served as the basic assumption for further refinements that evolved somewhat over time [61]. Later, in 1972 the fluid mosaic model, proposed by S. Jonathan Singer and Garth Nicolson, shed light on the complex mosaic nature of membranes in which proteins form globular entities and are embedded in the lipid bilayer [62]. The model has further evolved over time, but it remains the best one to account for the structure and functions of biological membranes.

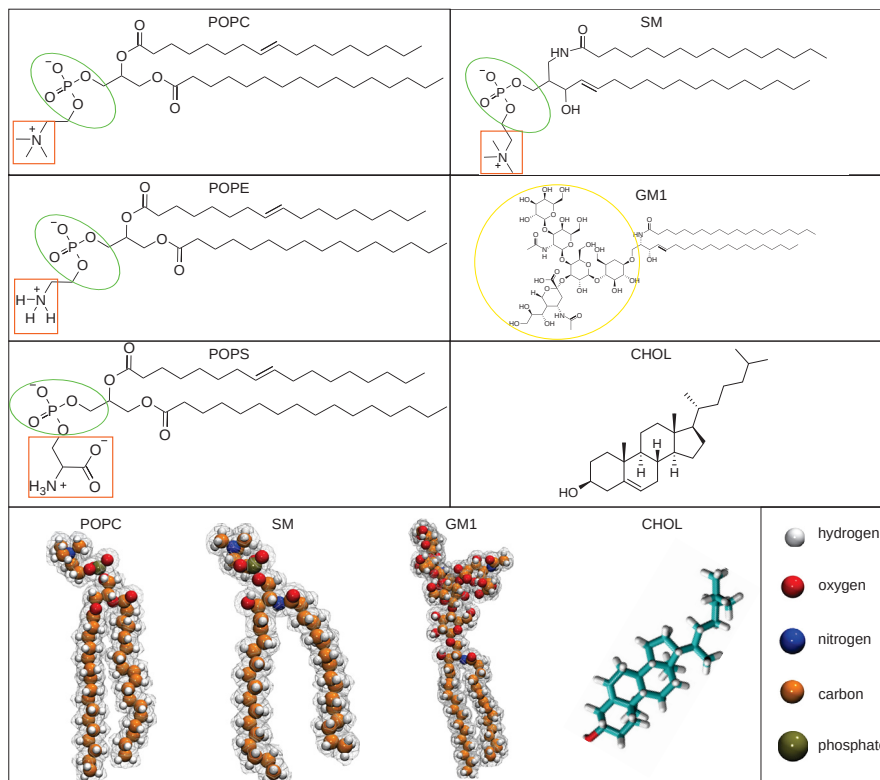


FIGURE 1.8: The chemical structures of different lipid types are shown. The corresponding lipid name is given, the choline group of POPC, serine of POPS, and ethanolamine of POPE lipids are marked in orange, the phosphate group is marked in green, and the sugar moiety of ganglioside (GM1) is marked in yellow. In the bottom row of the figure, snapshots of the lipid molecules in which the atoms are represented as spheres and colored according to the code as indicated in the legend are shown.

Each lipid class from the membrane lipids is composed of numerous variants [63, 64]. Phospholipids are the most abundant lipids in biological membranes and can be glycerol-based known as glycerophospholipids or sphingosine-based known as sphingophospholipids (see Fig. 1.8). The former consists of two fatty acid chains linked to glycerol and a phosphate group that can be linked to various alcohol headgroups which leads to their classification accordingly. The choline head group involves phosphatidylcholine

(PC), whereas serine or ethanolamine define the phosphatidylserine (PS) and phosphatidylethanolamine (PE) lipids, respectively. The sphingophospholipids such as sphingomyelin consist of a phosphocholine head group linked to one fatty acid and a sphingosine. Glycolipids are characterized by having a monosaccharide (simple sugar) or oligosaccharide that extend on the cell membrane surface and are bound to a lipid moiety containing glycerol or sphingosine. Cholesterol has a quite different structure; it consists of a hydroxyl group (which is the hydrophilic ‘head’ region) linked to a four-ring steroid structure and a short hydrocarbon side chain. All membrane lipids are amphipathic in nature, i.e. are composed of a hydrophilic head group and hydrophobic tails [65] (Fig. 1.9). Indeed, this is the basis for forming bilayers in which the hydrophilic head

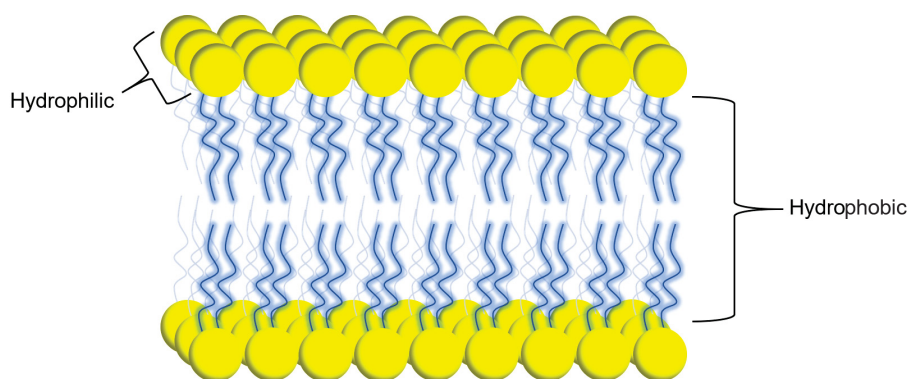


FIGURE 1.9: Schematic representation of a lipid membrane, with its hydrophilic head groups and hydrophobic tails being labeled.

points toward the aqueous environment and the hydrophobic tails point inward facing each others. Thereby, a lipid bilayer cell membrane is formed that separates the fluid within the cell from fluid outside the cell.

In addition to their role in enclosing cells and defining their outer limits, biological membranes carry out a multitude array of cellular functions that are important for life [66, 67], including (i) giving shape to the cell and providing structural support, (ii) storing and transmitting energy, (iii) controlling cell homeostasis via selective permeability of small molecules and ions, (iv) acting as a barrier to the extracellular environment and hence providing cell with protection, (v) permitting cell-cell interactions, adhesion and recognition via membrane proteins. Due to their importance, biological membranes gained much attention and became an active area of research in biomolecular simulations [68]. Lots of computational studies shed light on the interactions of membranes with membrane proteins, lipids, and drugs [69]. But the simulations always use simplified models for several reasons, including computational feasibility. More recently, computational

studies started to incorporate the complexity of real biological membranes in terms of their *in vivo* environment and lipid heterogeneity [70, 71].

In the case of Alzheimer’s disease and diabetes, mounting evidence suggests that the peptide-mediated toxicity is related to its abnormal interactions with the cell membrane, with amyloid formation being linked to membrane disruption [72–74]. Unfortunately, the detailed molecular mechanism of the peptide-membrane interaction is still not fully resolved. Therefore, further studies to understand these interactions and the resulting membrane-damaging mechanisms are warranted and needed.

1.2.2 Interaction partners

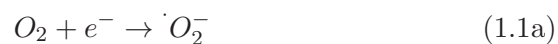
It is generally accepted that critical conformational changes in the intrinsically disordered proteins may trigger a cascade of misfolding events that leads to the formation of cell-toxic protein aggregates implicated in the development of a multitude of diseases [18]. Several, if not most, IDPs undergo a function-related disorder-to-order transition upon binding to a specific interaction partner such as other proteins or small molecules, allowing them to mediate multiple interactions with different partners in the cell [75–80]. The process in which biological macromolecules interact with each other or various small molecules with a high specificity and affinity to form a specific complex, constitutes the basis of all processes in living organisms. For example, proteins, as an important class of biological macromolecules, realize their functions through binding to themselves or other molecules, including peptides, nucleic acids, membrane, substrates, and small molecule ligands such as oxygen, solvent, and metal. Thus, a detailed understanding of the various protein interactions is central to understanding their biology at the molecular level.

In the case of IDPs, most of the theoretical, computational and experimental lines of investigation that explored peptide-membrane interactions focus on studying the peptide behavior in a water/membrane environment [81–83]. Thus, in a search for a scenario that best explains the cause and the mechanism of membrane damage, researchers mainly investigate the behavior of the peptide in a lipid-rich phase, i.e., in the presence of a lipid membrane, paying little attention to the possibility that free lipids can also be a binding partner of IDPs, such as $A\beta$. In this regard, recent studies demonstrated the crucial role of free lipids, which exist at nM to μ M concentration in equilibrium with the membrane, in the formation of peptide-lipid complexes, which enabled an easy

membrane insertion for amyloid proteins such as A β [84, 85]. Based on these results, La Rosa and coworkers proposed a “lipid–chaperone” hypothesis as a unifying framework for amyloid-membrane poration. Some experimental and MD studies reported on the stability of peptide-lipid complexes in solution their role in assisting protein transport into membranes [84, 86, 87]. In general, lipid-assisted protein transport and the effect that lipid binding has on the peptide conformations are overlooked compared to the well documented lipid-carriage by proteins [88–90].

1.2.3 Oxidative stress

Oxidative stress can be defined as the generation of excess reactive oxygen species (ROS) or the dysfunction of the anti-oxidant system that subsequently leads to an increase in the amount of ROS present in normal cells [91, 92]. The reactive oxygen species are molecules derived from molecular oxygen enzymatically (for example to kill invaders in macrophages) or as a side reaction (like respiratory chain) [93, 94]. ROS are commonly known as free radicals (chemical species with unpaired or an odd number of electrons) that are reactive oxidants and capable of causing damage to biomolecules. Nonetheless, they are kept at low level but not totally eliminated due to their function [95, 96]. They are necessary to maintain homeostasis in cells and play important roles in signaling. Most of the reactive oxygen species are generated as a byproduct of the cellular oxygen metabolism during mitochondrial electron transport, where 85% of O₂ is metabolized and partially reduced O₂ intermediates are produced in low quantity [97–99]. As the equation shows, the successive four steps of oxygen reduction via electron addition leads to the formation of different radicals including: superoxide ($\cdot O$) (equation (1.1a)); hydrogen peroxide (H₂O₂) (equation (1.1b)); hydroxyl radical ($\cdot HO$) and hydroxyl ion (HO[−]) (equation (1.1c)).



In cells, a variety of defense mechanisms (enzymes or small antioxidant compounds) have evolved to control the level of ROS and prevent their harmful effects [100–102]. However,

in diseases an imbalance occur between ROS production and clearance, toward overproduction of ROS. Hence, this leads to the accumulation of oxidatively modified molecules such as lipids and proteins that cause dysfunction and eventually lead to cell death. Considering the central role of oxygen in the human body, it is not surprising that oxidative stress is implicated in several diseases including neurodegenerative diseases [103]. In particular, the high oxygen consumption and high amount of polyunsaturated fatty acids (which are sensitive to peroxidation) make the brain, compared to other organs, more susceptible to oxidative stress [104]. The abnormal aggregates of A β in senile plaques (clumps of A β fibrils along with metal ions) in Alzheimer's disease were found to be able to induce oxidative stress. Indeed, the redox-active metal ions, such as copper, can catalyze the production of reactive oxygen species when bound to A β . The resulting ROS may contribute in causing damage to the A β peptide itself and the surrounding biomolecules including lipids, proteins etc.

In the case of Alzheimer's disease, a growing body of evidence suggests that oxidative stress plays a key role in the disease pathogenesis, along with the presence of A β [105, 106]. This is strongly supported by (i) the observation that oxidative stress occurs in the early stages of AD [107], (ii) the elevated levels of A β ₁₋₄₀ and A β ₁₋₄₂ have been reported to be associated with the increased levels of oxidation products from proteins, lipids and nucleic acids in AD hippocampus and cortex [108, 109], and (iii) the inherent tendency of A β for generating free radicals [110, 111] and its high affinity to bind metals such as Cu²⁺, Zn²⁺ [112, 113]. In this context, lots of *in vitro* studies have been devoted to study oxidative stress in the context of AD. Part of the recent research is interested in the characterization of the oxidative damages suffered by the A β peptide itself, and the other part focuses on exploring the possibility that oxidation may favor the formation of small oligomeric species, which are known to be more toxic than the final fibrils. The link between oxidative stress and the amyloid- β peptide is now well established [108, 114]. However, it remains under debate whether the accumulation of A β increases the level of oxidative stress or whether the high level of oxidative stress drives A β accumulation [115].

It is essential to characterize A β peptides from *in vivo* samples in order to ascertain the biological relevance of the wealth of *in vitro* studies. Although the occurrence of oxidative stress in several neurodegenerative diseases is well-established, there are few experimental evidences on the effect of radicalization on peptide-membrane interactions.

The inherent difficulty in characterizing $A\beta$ *in vivo* makes it more difficult when it comes to the identification of the oxidative damages potentially undergone by $A\beta$ peptides. In this context, and because the role of $A\beta$ in oxidative stress related mechanisms of AD progression is still unclear, efforts toward exploring the $A\beta$ -membrane interactions under oxidation conditions, especially when considering the reported finding that the peptide affinity for membrane interaction increases in the case of oxidative stress, is of great importance for better understanding the disease causes and development.

1.2.4 Macromolecular crowding inside the cell

The living cell environment is crowded by many molecules, including water, ions, metabolites, lipids and macromolecules. The concentration of these macromolecules reaches up to 400 g/L [116, 117]. In terms of volume, up to 40% of the cell volume is occupied by macromolecules. Such a complex environment can affect biomolecular function *in vivo* through macromolecular crowding and confinement. The former refers to the volume excluded by soluble macromolecules, whereas the latter refers to the volume excluded by a fixed (confining) boundary.

Recently, the crowded cellular environment gained much attention as more and more researchers started to study the effects of crowded conditions found in the cell. Lots of *in vitro* and *in vivo* studies on macromolecular crowding point to its effect on the kinetics and equilibria of biochemical processes. These studies highlight the consequences of crowding on (i) protein and aggregate stability via steric repulsion, specific and non-specific macromolecular interactions such as van der Waals, hydrogen bonding or electrostatic interactions [118–120], (ii) the aggregation kinetics (rate of folding, association with other molecules and intracellular transport) via inducing changes to viscosity and diffusive behaviour [121–124]. It is now well recognized that the crowded conditions found in the cellular environment strongly affect key processes in living cells ranging from life emergence up to regulation of cell sizes. The crowding impact varies from modest (e.g. effect on stability of protein folding) to drastic (e.g. effect on the rates of protein aggregation linked to disease).

One of the most pronounced effect of crowding occurs in proteins with intrinsically disordered fragments or proteins that undergo significant conformational transitions as a part of their function, for example during ligand binding. Several experimental and

computational studies have been conducted mimicking the *in vivo* conditions to explore the protein behavior in a crowded cellular environment. They further shed light on the key role played by crowding in human diseases that are related to protein aggregation and fibril formation [125–133]. In this context, previous studies on A β were traditionally performed in a solely homogeneous, ideal solution without considering the actual complexity of the cellular environment. Recently, few number of experimental studies [134] have explored the crowding effect on amyloid- β peptide along with theoretical models [135–137] that used simple hard particles to mimic reactant and crowder molecules. The computational approach, with its ability to represent proteins and crowders at the atomistic level potentially holds predictive power that enables simulating the protein in the presence and absence of crowders. In addition to providing more detailed information about the protein-crowder interactions and the excluded volume effect, it enables quantitative understanding and better interpretation of the *in vivo* behavior of proteins, that can further complement/link to experimental findings.

Chapter 2

Methods

The main method used in the studies of this thesis work is molecular dynamics (MD) simulations [138, 139], which is based on classical molecular mechanics (MM) to model molecular systems [140, 141], an approach that is widely applied in Monte Carlo simulations [142], ligand-docking [143] simulations, and molecular dynamics simulations [138, 139].

Typically, molecular mechanics models a system of classical particles as spherical atoms connected by springs which represent bonds, whose dynamics is described by Newtonian mechanics [138, 144]. The internal forces experienced in the modeled system include the bonded and the nonbonded interactions [145], which are described using simple mathematical functions such as Hooke's law, the Coulomb and the Lennard-Jones potential. MD simulations allow to numerically solve Newton's equations of motion, and follow the time evolution of the structural fluctuations. MD simulations are the most widely used computer simulation technique to address many biological questions and enable better understanding of various dynamic aspects of biomolecular structures, recognition, and function. Moreover, these simulations are considered as a powerful complement to experimental techniques due to their ability to probe high resolution in space (single atoms), time (femtoseconds), and energy, hence, allow for obtaining molecular information that is difficult or impossible to obtain experimentally. Consequently, MD simulation can be considered as a virtual experiment that best mimics the modeled system's natural environment at the interface between theory and real experiments.

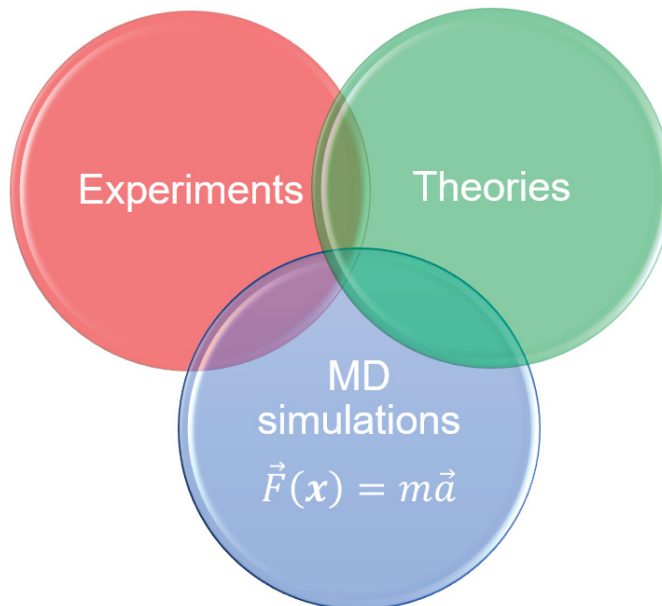


FIGURE 2.1: MD simulations at the interface between theory and real experiments.

In the following sections, I will briefly describe the theoretical foundations of MD simulations, describe the MD method, force field (potential function and energy landscape), with a special emphasis on the simulation environment, periodic boundary conditions, and the MD recipe applied in the context of this thesis.

Parts of this chapter were excerpted from a publication submitted by the author to the Progress in Molecular Biology and Translational Science as Fatafta, H., Samantray, S., Sayyed-Ahmad, A., Coskuner-Weber, O., Strodel, B. (2021). Molecular simulations of IDPs: from ensemble generation to IDP interactions leading to disorder-to-order transitions.

2.1 Historical background

The concept of MD simulations is not new, it was originally developed in the 1950s. Particularly, in 1957 this technique witnessed its first usage by the theoretical physics community, introduced by Alder and Wainwright [146]. They used computers to perform an MD simulation using the hard sphere model in which atoms interact through perfectly elastic collision. In 1964, Rahman published a simulation that compared well with experimental data, in which he applied a continuous potential to mimic real atomic interactions [147]. Following the development of new computers in 1970s, making them

more generally accessible, interests in MD simulations expanded and extended to simulate more complex systems in biochemistry and biophysics. The first MD simulation of a protein dates back to the late 1970s [148, 149], though the simulation was for a small sized protein, performed in vacuum and lasted for only 9.2 ps, it nonetheless enhanced our view of proteins as a dynamic systems, whose internal motions play functional roles, rather than being rigid structures. The groundwork that enabled these simulations was among the achievements recognized by the 2013 Nobel Prize in Chemistry [150]. Since then, MD simulations have advanced from simulations of hundreds of atoms to simulations of systems with biological relevance including entire proteins in explicit solution (i.e., a physical, spatially resolved description of the solvent) [151, 152], multi-protein complexes [153], membrane-embedded proteins [154] or large macromolecular complexes such as ribosomes [155, 156]. This rapid development in MD simulations has been fuelled by the development of high-performance computers and the implementation of computationally efficient MD codes. In the course of this development, the simulations of systems having 50,000 – 100,000 atoms are now routine, and the simulations of 500,000 atoms are possible within the available facilities. Today, simulations are applied to a wide range of problems in different disciplines, including computational drug discovery [157–159], molecular biology [160, 161], structural bioinformatics [162], etc.

2.2 Molecular dynamics theory

The fundamental idea behind MD simulations is to simulate the molecular motions of classical interacting particles as a function of time [163], which is realized by the numerical solution of the classical Newtonian dynamic equations (2.1). This implies iterative numerical calculation of the instantaneous forces present in the system and the consequent movement. For a system consisting of N atoms, the atoms move in response to their interactions according to Newtonian mechanics:

$$\mathbf{F}_{i,a}(\mathbf{q}) = m_i \frac{\partial^2 \mathbf{q}_{i,a}}{\partial t^2} \quad (2.1)$$

where m_i is the particle’s mass, and $\mathbf{q}_{i,a}$ is its coordinate in direction a with $a = x, y$ or z , and $\mathbf{F}_{i,a}$ is the force acting on particle i in direction a . On the other hand, $\mathbf{F}_{i,a}$ can be represented by the gradient of the potential energy of the whole system as follows:

$$\mathbf{F}_{i,a}(\mathbf{q}) = -\frac{\partial U(\mathbf{q})}{\partial \mathbf{q}_{i,a}} \quad (2.2)$$

where $U(\mathbf{q})$ is the potential energy of the system that depends on the positions of its N atoms. By combining equation (2.1) and (2.2), Newton’s equation of motion can then relate the derivative of the potential energy to the changes in position as a function of time:

$$-\frac{\partial U(\mathbf{q})}{\partial \mathbf{q}_{i,a}} = m_i \frac{\partial^2 \mathbf{q}_{i,a}}{\partial t^2} \quad (2.3)$$

Equation (2.3) summarizes the core of MD simulations, which is to start with an initial configuration, i.e. initial positions and velocities of all system particles, then repeatedly apply a “recipe” (see section 2.6) to update each particle’s position and velocity from time t to time $t + \Delta t$ (Fig. 2.2A). In other words, once the structure of the biomolecular system is given, then the computational method can be applied to investigate its dynamics. This process generates a time trajectory of the particles in the studied system, i.e., a three-dimensional movie that describes the atomic-level configuration of the system at every point during the simulated time interval (Fig. 2.2B). However, the dynamics is strongly dependent on the availability of a suitable potential energy function that best mimics the real energy landscape of the studied system in terms of its atomic coordinates. This aspect will be introduced in the next section.

2.3 Potential function and energy landscape

It is critical for a valid and traceable MD simulation to choose the appropriate energy function that best describes the inter-atomic and intra-atomic interactions. In conventional MD simulations, the potential energy is represented as the sum of the bonded and the nonbonded interactions within the simulated system. The bonded interactions involve covalent bonds, bond angles, and dihedral angles and are described by two-body, three-body, and four-body terms, whereas the nonbonded interactions are described by the pairwise additive functions as can be seen in equation (2.4). This set of functions with its associated set of parameters are commonly known as the force field [164]. The

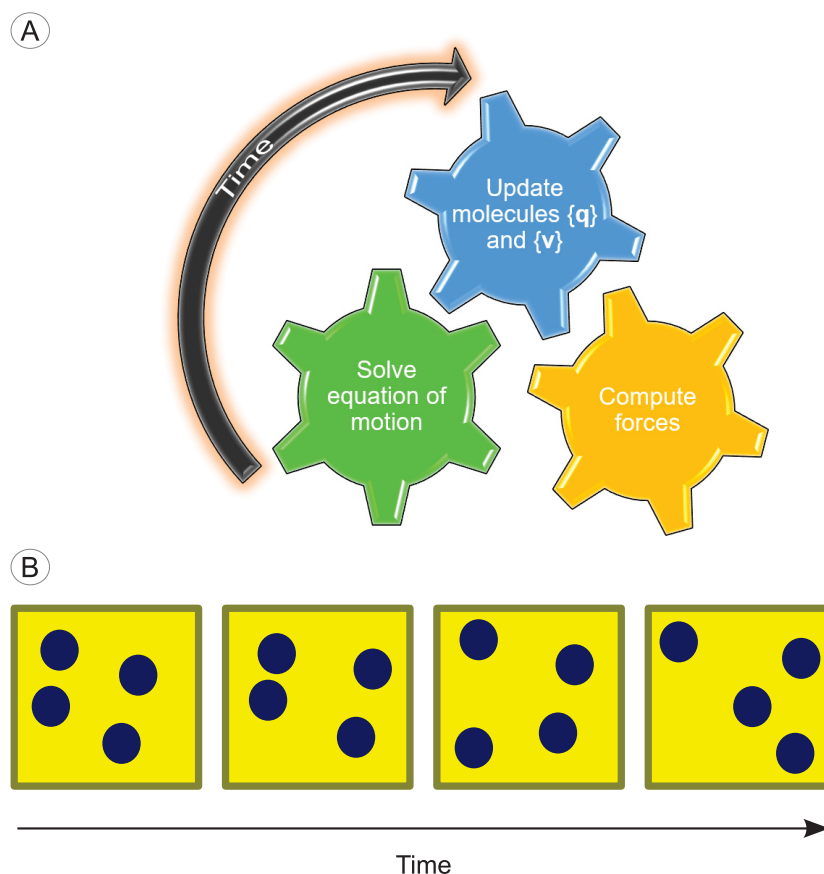


FIGURE 2.2: (A) Basic idea of a molecular dynamics simulation. (B) Example of a molecular dynamics simulation in a simple system, each circle represents the position of one atom that is changing with time as the figure shows.

parameters are usually obtained from experimental and/or quantum mechanical studies of small molecules or molecular fragments and assumed to be transferable to large molecules.

In molecular modeling, a wide range of force fields with different parametrization schemes have been developed specifically for the simulation of biomolecules [165]. Such parametrization is generally considered to give a reasonable approximation of the potential-energy landscape. Among the existing force fields, CHARMM force fields (FFs) [166, 167] are widely used in the simulation of proteins [168], IDPs [169], and lipids [170, 171]. They have been separately parametrized for proteins, nucleic acids, lipids, and carbohydrates with the goal of consistency between these sets, allowing for simulation of heterogeneous systems. Several discrete terms constitute the force field, each has a simple functional form and describes the inter- or intra-molecular forces within a system given the set

of atomic coordinates. The potential energy function which is used by the various CHARMM FFs is given by:

$$\begin{aligned}
U(\mathbf{q}) = & \sum_{bonds} k_b(b - b_0)^2 + \sum_{angles} K_\theta(\theta - \theta_0)^2 \\
& + \sum_{dihedrals} V_\varphi(1 + \cos(n\varphi - \delta)) + \sum_{impropers} k_\omega(\omega - \omega_0)^2 \\
& + \sum_{i,j(LJ)} \epsilon_{ij}^{\min} \left[\left(\frac{R_{\min,ij}}{r_{ij}} \right)^{12} - 2 \left(\frac{R_{\min,ij}}{r_{ij}} \right)^6 \right] + \sum_{i,j(Coul.)} \frac{q_i q_j}{4\pi\epsilon_0 r_{ij}} \\
& + \sum_{Urey-Bradley} k_{UB}(s - s_0)^2 + \sum_{CMAP} U_{CMAP}(\phi, \psi)
\end{aligned} \tag{2.4}$$

Here, \mathbf{q} denotes the conformation of the system consisting of N atoms with coordinates $\mathbf{q} = (q_{1,x}, q_{1,y}, q_{1,z}, q_{2,x}, q_{2,y}, q_{2,z}, \dots, q_{N,x}, q_{N,y}, q_{N,z})$. The bonded energy terms describe bond stretching around the equilibrium values b_0 with force constants k_b , angle bending around equilibrium angles θ_0 and with force constants k_θ , torsions around bonds as characterized by the dihedral angles φ , periodicity n , shift δ and energy barrier V_φ , and out-of-plane bending, also called improper torsion, with the minimum at ω_0 and force constant k_ω . The non-bonded interactions contain Lennard-Jones and Coulomb potentials for interacting particles i and j . The Lennard-Jones (LJ) potential is a 12-6 potential, where the repulsive $1/r^{12}$ term describes the Pauli repulsion at short distances of the interacting particles due to overlapping electron orbitals, and the attractive $1/r^6$ term describes attractions arising from dispersion forces, which are also called van der Waals (vdW) interactions. The distance between the two interacting particles is given by r_{ij} , ϵ_{ij}^{\min} is the depth of the potential well, $R_{\min,ij}$ is the distance at which the particle-particle LJ potential energy is minimal and can be calculated from the van der Waals radii of the particles i and j . The Coulomb potential models the electrostatic interactions between the partial charges q_i and q_j of atoms i and j with distance r_{ij} between them, where ϵ_0 is the vacuum permittivity. The terms described thus far, which are summarized by schematic representation in Fig. 2.3, are common to all all-atom biomolecular force fields as found in the AMBER [172], CHARMM [173], OPLS-AA [174], and GROMOS [175] families of force fields. Though, depending on the force field, small differences to equation (2.4) can occur, such as that $\cos(\theta)$ is used for defining the harmonic potential describing angle bending. In the CHARMM FFs, two correction terms are added to the potential energy. The Urey-Bradley (UB) term is used to improve

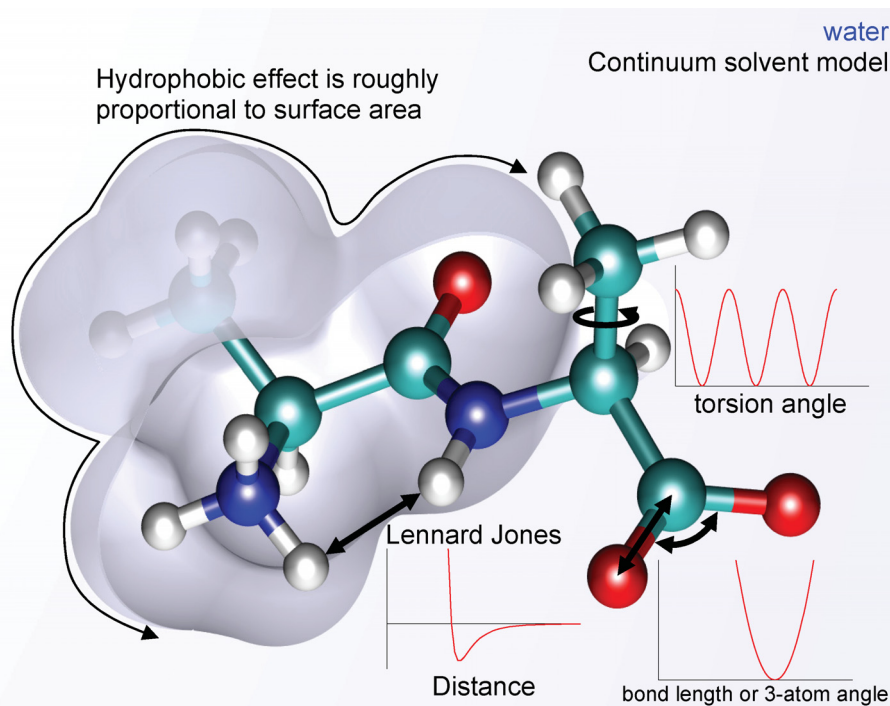


FIGURE 2.3: Contributions in all-atom force fields. The interactions between the atoms are divided in bonded and non-bonded interactions. Harmonic potentials are used to describe the vibrations of bonds and bond-angle bending, while periodic functions are needed for modeling the torsion around bonds. The non-bonded interactions are between atoms that are separated by at least three bonds or between atoms of different molecules. They arise from charge-charge interactions as described by the Coulomb potential, and from hydrophobic interactions as well as repulsive interactions if two atoms get too close to each other, which are collectively modeled by the Lennard-Jones potential. The water around a protein or other biomolecules can be modeled explicitly (not shown) using typical water models, such as TIP3P or TIP4P, or using an implicit solvent model. Explicit modeling of the water molecules gives usually better results, especially in the case of IDPs. Reproduced with permission ([https://en.wikipedia.org/wiki/Force_field_\(chemistry\)](https://en.wikipedia.org/wiki/Force_field_(chemistry))).

the description of angle bending, where s is the distance between the first and third atom that define a bond angle. However, most force fields do not include Urey-Bradley terms, and also in CHARMM FFs no new UB terms were added in the past, since the only advantage of these terms is the better reproduction of subtleties in vibrational spectra. However, the goal of classical MD simulations seldomly is the calculation of infrared spectra. In fact, in most of the MD simulations of proteins the bond lengths are anyhow restrained to their equilibrium values in order to allow an increase in the time step used for the integration of the equations of motions. Moreover, many of the vibrations, especially those involving hydrogen bonds, would require a quantum mechanical description for proper modeling as classical simulations reach their limit of validity here. The second correction term is called CMAP, which is a grid-based

correction and accounts for the correlation between the backbone dihedral angles ϕ and ψ . Unlike the UB term, the CMAP correction has gained in popularity and was included in other FFs too.

As can be seen from equation (2.4), the potential energy is a function of the atomic positions ($3N$) of all the atoms in the system, which leads to certain complexity for a system with a large number of particles N . Due to such complexity, the analytical solution to the equations of motion is not feasible; they must be solved numerically. Consequently, numerous numerical algorithms have been developed for integrating the equations of motion, such as the Verlet algorithm [176, 177], leapfrog algorithm [178–180], velocity Verlet [181, 182], and Beeman’s algorithm [183, 184]. In choosing which algorithm to use, one should make sure that the algorithm (i) conserves energy and momentum, (ii) is computationally efficient, and permits a long-time step for integration. In the next subsection, I will introduce one of the most widely used integration algorithms. For other numerical integration techniques, the readers are referred to the following references [176–180, 183, 184].

2.3.1 Integration algorithms: The velocity Verlet algorithm

All the integration algorithms used to integrate the equations of motion in MD simulations assume that the positions, velocities (the first derivative of the positions with respect to time) and accelerations (the second derivative of the positions with respect to time) can be approximated by a Taylor series expansion [185–187], where the simulation time is discretized into time steps of equal length Δt . The accuracy of the integrator depends on the degree to which the Taylor expansion is truncated, such that the largest term still considered in the truncation scheme determines the order of the method. Moreover, all valid integrators are time-reversible numerical methods [188]; hence, the method can take k steps forward in time, followed by k steps backwards in time, and arrive at the same initial conditions used to start the simulation. The velocity Verlet algorithm is a frequently used algorithm to calculate trajectories of particles in molecular dynamics simulations, especially when extremely accurate integration with temperature and/or pressure coupling is required [181, 182].

The velocity Verlet method synchronizes the calculation of positions, velocities, and accelerations without sacrificing precision. It truncates the Taylor expansion to the

second order in position (equation 2.5) and first order in velocity (equation 2.6), and updates both positions and velocities according to:

$$\mathbf{q}_i(t + \Delta t) = \mathbf{q}_i(t) + \mathbf{v}_i(t)\Delta t + \frac{1}{2}\mathbf{a}_i(t)(\Delta t)^2 \quad (2.5)$$

$$\mathbf{v}_i(t + \Delta t) = \mathbf{v}_i(t) + \frac{1}{2}[\mathbf{a}_i(t) + \mathbf{a}_i(t + \Delta t)](\Delta t) \quad (2.6)$$

This implementation assumes that the position is first updated, the force and thus acceleration are calculated at the new position, and then the velocity is updated. As can be seen, the velocity update in equation (2.6) is directly applicable only if $a_i(t + \Delta t)$ does not depend on $v_i(t + \Delta t)$; that is, $a_i(t)$ depends only on the positions of the particles.

By using equations (2.5) and (2.6), we obtain the flow chart shown in Fig. 2.4. Most of the computational time is used to determine the accelerations, which require the explicit

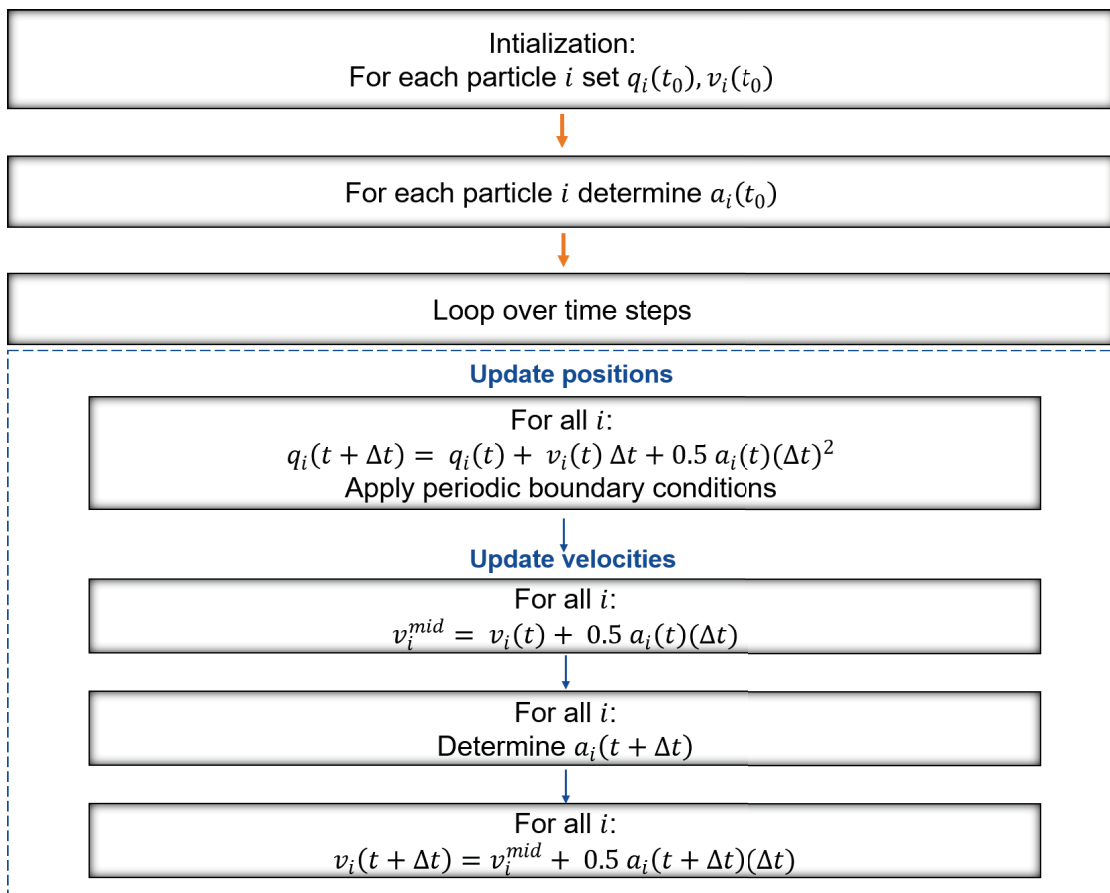


FIGURE 2.4: Flow chart for a molecular dynamics simulation involving the velocity Verlet algorithm.

calculation of the force field according to equation (2.4). In MD simulations involving many time steps (millions to trillions), a substantial amount of the computation is spent at every time step for the calculation of the non-bonded interactions, as these act between every pair of atoms and thus scale with N^2 for a system of N atoms.

2.4 Simulation environment

A reasonable representation of the biomolecule’s environment is important for characterizing its properties through simulations. However, it is not possible to fully characterize the physiological environment for any biomolecule, as the system would be too complicated and computationally demanding. Thus, aqueous solvent is selected as the environment for the vast majority of simulations [149, 189] (Fig. 2.5). At today’s level of understanding and availability of computer resources, great strides have been made toward achieving simulations in more specific environments that mimics more realistic environments, such as those for transmembrane proteins [190, 191], or accurately simulate the experimental conditions to be replicated such as pressure and temperature [192–194]. Most early simulations were conceived for isolated systems that corresponded to the microcanonical ensemble, in which a thermodynamic state is characterized by a fixed number of atoms, N , fixed volume, V , and fixed energy, E . However, since it is more desirable to mimic the real environment conditions, simulations are now usually performed to sample configurations from the canonical ensemble i.e. at constant temperature and volume (NVT) [194–196], or from the isobaric-isothermal ensemble, i.e., at constant pressure and temperature (NPT) [197, 198].

In a simulation at constant energy, the temperature will be fluctuating due to the spontaneous inter-conversion of the kinetic and potential components of the total energy. The instantaneous temperature can be then evaluated from the atomic velocities using the equipartition theorem:

$$\frac{1}{2}k_B T = \frac{1}{2}m_i v_{i,a}^2 \quad (2.7)$$

where k_B is Boltzmann’s constant, m_i and v_i are the mass and velocity of atom i , respectively. If a constant temperature is desired during the course of a simulation, then the atomic velocities need to be rescaled or modified. This can be achieved using a so-called thermostat. Similarly, if a constant pressure is desired, then the volume

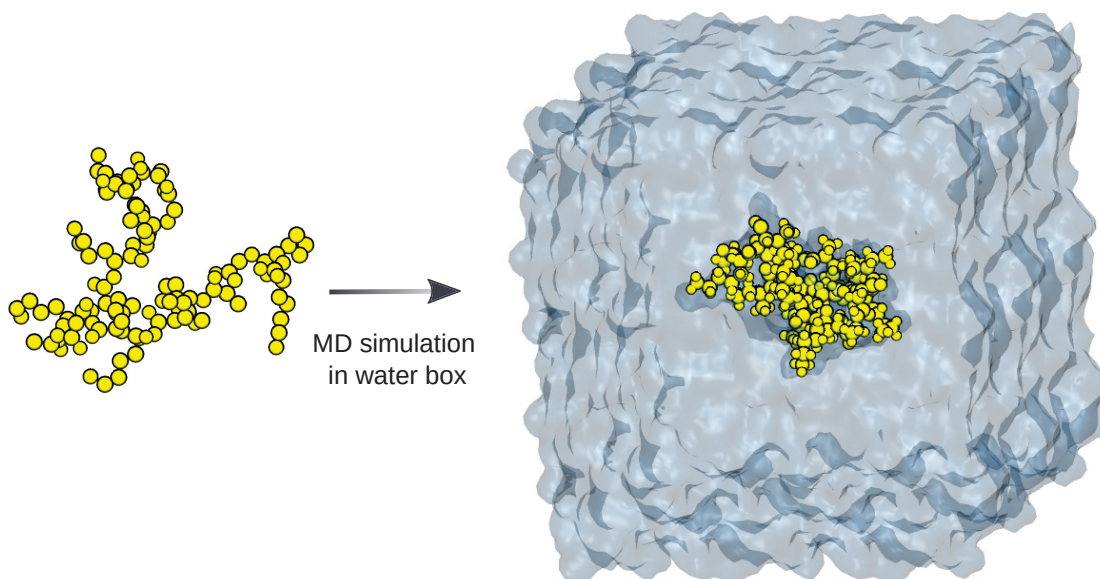


FIGURE 2.5: A snapshot of a peptide simulated in a cubic box solvated with water molecules.

of the simulation box needs to be allowed to fluctuate by adjusting the dimensions of the box and rescaling the atomic positions accordingly. This can be achieved using a barostat. Numerous methods with different algorithms exist to run MD simulation at constant temperature and pressure. In the following subsections I'll be highlighting some of them.

2.4.1 Thermostat

Simulations at constant temperature are needed to understand features of the molecular systems that are related to temperature such as folding and unfolding of proteins, or phase transitions of lipids. It is also important for comparing simulations to experiments, since experiments are commonly performed at constant temperature. Many algorithms have been developed for NVT simulations [199] including the weak coupling scheme of the Berendsen thermostat [200–202], the velocity rescaling thermostat [203, 204], and the extended-ensemble Nosé-Hoover thermostat [201, 205, 206]. The first two algorithms are extremely efficient for relaxing the system to the target temperature, but unfortunately,

they suppress the fluctuations of the kinetic energy, hence do not generate a proper canonical ensemble (i.e., incorrect sampling) [207]. For an overview of these algorithms, we recommend [199]. In this subsection, I'll describe a thermostat that is commonly known to enable canonical ensemble simulations; the Nosé-Hoover thermostat.

The Nosé-Hoover thermostat supports the extended ensemble approach proposed by Nosé first [208] and later modified by Hoover [209]. In their approach, they modified the equation of motion by adding a thermal reservoir and a friction term as shown in equation (2.8), and demonstrated that such modification to the equations of motion would better sample the phase space of a canonical ensemble. The friction force is proportional to the product of the particle's velocity ($\frac{d\mathbf{q}_i}{dt}$) and a friction parameter ζ (heat bath variable), the latter is a dynamic quantity and has its own momentum p_ζ and equation of motion, the time derivative is calculated from the difference between the current kinetic energy and the reference temperature:

$$\frac{d^2\mathbf{r}_i}{dt^2} = \frac{\mathbf{F}_i}{m_i} - \frac{p_\zeta}{Q} \frac{d\mathbf{q}_i}{dt} \quad (2.8)$$

where Q determines the coupling strength and is called the 'mass parameter' of the reservoir, and the equation of motion for the heat bath parameter ζ is

$$\frac{dp_\zeta}{dt} = (T - T_{bath}) \quad (2.9)$$

with T_{bath} being the reference temperature and T is the system temperature.

2.4.2 Barostat

Simulations at constant pressure are needed to understand the behavior of the system at a certain pressure. Many experimental measurements are done under constant pressure and temperature. Thus, NPT simulation are most relevant to experiment comparison.

To maintain constant pressure during a simulation, the system can be coupled to a pressure bath using a so-called barostat [204, 210]. Many algorithms have been developed for NPT simulations including the Berendsen algorithm that scales coordinates and box vectors of every step [211], the or extended-ensemble Parrinello-Rahman approach [212]. Both the Berendsen and the Parrinello-Rahman barostat can be combined with any of the temperature coupling methods. However, in simulations where the fluctuations in

pressure or volume are important such as the simulation of a lipid bilayer, the Berendsen barostat with its weak coupling does not simulate the true NPT ensemble [213]. In such cases, the Parrinello-Rahman approach supports constant-pressure simulations and gives the true NPT ensemble. This approach is similar to the Nosé-Hoover temperature coupling and, in most cases, is combined with it.

With the Parrinello-Rahman barostat, the box vectors are described as:

$$\frac{d^2\mathbf{b}}{dt^2} = \frac{V}{\mathbf{W}\mathbf{b}'}(P - P_{bath}) \quad (2.10)$$

Here, \mathbf{b} represents the box vector, V is the volume of the box, and \mathbf{W} is a matrix parameter that determines the coupling strength. P and P_{bath} refer to the current and reference pressure respectively. The equations of motion for the particles are also changed, just as for the Nosé-Hoover coupling.

2.5 Periodic Boundary conditions (PBCs)

Periodic boundary conditions (PBCs) are used to approximate a system of large (infinite) size [214–216, 216]. The use of PBCs in MD simulations is realized by duplicating the system periodically in all directions to represent an essentially infinite system, and further to ensure that all simulated atoms are surrounded by neighboring atoms, whether those neighbors are images or not [217]. The minimum image convention [218] guarantees that for atoms i and j , only one j atom, the closest original or image, is considered in the pair interaction calculations with atom i as part of the short-range non-bonded interaction terms. This implies the use of a cut-off radius, to truncate non-bonded interactions, that may not exceed half the shortest box vector. But for systems with charged particles this might be problematic due to the charge accumulation at the cut-off boundary, which would lead to wrong energies. To this end, one considers different algorithms for long-range electrostatic calculations, such as the particle mesh Ewald method.

An illustration of PBCs applied for a two-dimensional system of linear dimension L is shown in Fig. 2.6. The system (framed by black frame) is assumed to be surrounded by periodic images (shaded squares). For particle i , the neighboring particles within

a distance $r_{cut}^{\alpha\beta}$ are the particles inside the large circle. To determine the distance r_{ij} between particles i and j , we use the “minimum image convention”. For example, the distance between i and particle $j = 18$ would be $r_{ij} > r_{cut}^{\alpha\beta}$ without using periodic images because particle 18 in the left bottom corner of the system is outside the large circle. But with periodic images $r_{ij} < r_{cut}^{\alpha\beta}$ because the nearest periodic image of particle 18 is above particle i within the circle. For particles i and $j = 20$, we use the direct distance between the two particles within the system (black frame), because this distance is less than the distance to any of the periodic images of $j = 20$.

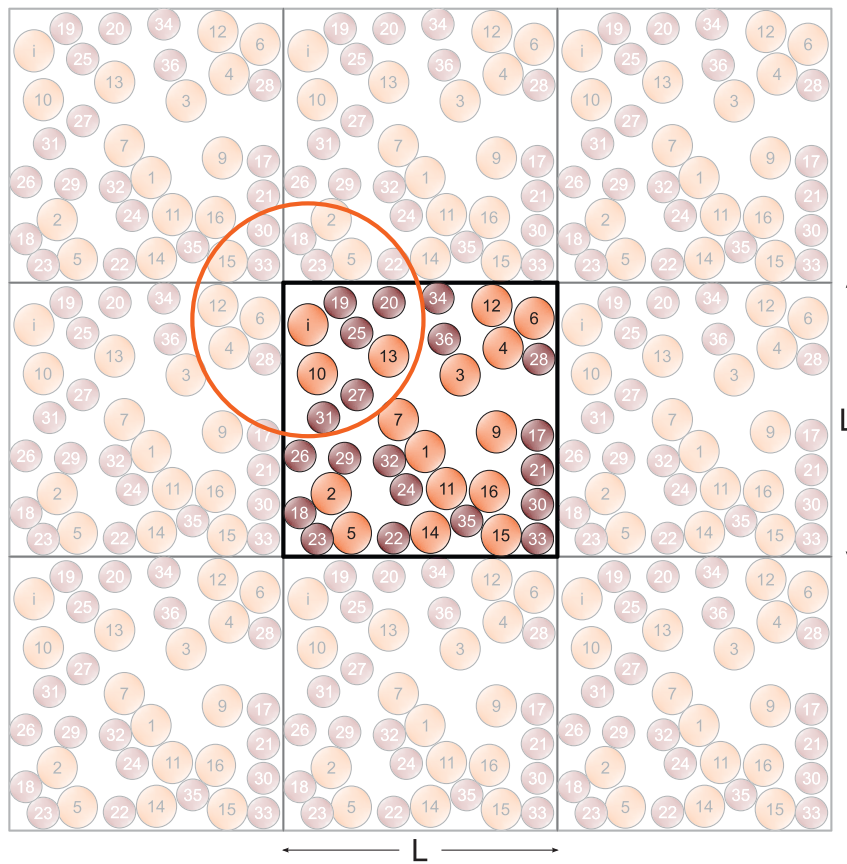


FIGURE 2.6: A schematic periodic square lattice illustrating periodic boundary conditions and the minimum image convention. The square in the middle highlighted with a black frame corresponds to the simulated system. To identify the neighbors j of particle i , the position r_j of particle j is either chosen from within the system (i.e., within the black frame) or as the positions of j 's periodic images (i.e., within the shaded boxes), such that r_{ij} is minimal. Short-range interactions are only calculated for neighbors of i satisfying $r_{ij} < r_{cut}^{\alpha\beta}$, as indicated by the orange circle.

Different geometries can be used for the PBCs such as cubic systems, a rhombic dodecahedron or a truncated octahedron [219]. The latter two are special cases of triclinic unit cells that are closer to a sphere than a cube, thus can significantly reduce the number

of solvent atoms required in the system, leading to a corresponding reduction in the computational requirements.

2.6 MD recipe

All-atom MD simulations discussed in this thesis were performed using the GROMACS (**GRO**oningen **MA**chine for **C**hemical **S**imulations) software [220, 221]. Performing an MD simulation is relatively straightforward. It starts with preparing the molecular system, which in this thesis consists of protein localized at a certain distance from a membrane containing few types of lipids. This step involves to add missing atoms to the protein structures determined by experimental techniques (such as hydrogen atoms, which are generally not resolved in crystal structures), adding solvent molecules such as water, salt ions, and assigning the force field parameters. The web utility CHARMM-GUI was used to build the lipid bilayers [222–224]. Then, the simulations were performed following the MD recipe as explained in the following subsections.



FIGURE 2.7: Summary of the steps involved to prepare and perform an MD simulation.

2.6.1 Energy minimization

The first step of an MD simulation is normally to relax the solvated system to a low-energy state before heading to perform the MD. The potential energy function of the system is determined by the force field calculations, as already explained in section 2.3.

It is a very complex energy landscape involving a large number of dimensions, with one deepest point, the global minimum, and a very large number of local minima. A complete description of the system dynamics, relevant to the protein conformations and their free energy, requires knowledge of all the local minima and the global minimum. Unfortunately, sampling the configurational space at a sufficient number of points to obtain a complete survey is impossible for large systems with high dimensionality and large number of local minima. On the other hand, it could be that the starting configuration is very far away from equilibrium and does not correspond to any of the minima of the underlying energy landscape. It may even involve overlaps between atoms, such that the forces may be excessively large and the MD simulation may fail. To resolve such problems, it is recommended to run short energy minimizations to remove any bad contacts that would lead to unstable molecular dynamics [225].

In energy minimization, the conformation of the system can be changed to locate lower energy conformations through the process. The existing minimization methods can help in finding the nearest local minimum i.e. the minimum that can be reached by systematically moving down the steepest local gradient, but can not guarantee the determination of the global minimum in any practical amount of time. Nonetheless, this would be good enough for beginning an MD simulation. There are different minimization algorithms available such as the steepest descent and conjugate gradient methods [226]. The steepest descents algorithm brings the system close to the nearest local minimum very quickly, while the conjugate gradient method is good at bringing the system to the local minimum, but performs worse when the system is far away from a minimum.

2.6.2 Equilibration

Equilibration is the step that always follows the energy minimization, to bring the system to a representative dynamical state suitable for the initiation of a simulation at the given thermodynamic parameters (T, p) [227–229]. The equilibration protocol is still a matter of personal preference. It is recommended to first perform thermal equilibration to fix the temperature to the desired range, followed by fixing the pressure. The first stage entails coupling all the system atoms to a thermal path at a given temperature as described in the thermostat subsection. This is followed by coupling the system to a barostat to reach a pressure of 1 bar. Important, at this stage is to maintain the

structural integrity of the membrane and protein in the studied system. Therefore, soft positional restraints are implied in the equilibration phase to prevent drastic changes of the initial structure before simulating the desired simulation. In this thesis, heavy atoms are initially restrained with $1000 \text{ kJ}\cdot\text{mol}^{-1}\cdot\text{nm}^{-2}$. The V-rescale thermostat and Berendsen barostat were used to converge temperature and pressure to the ideal values.

2.6.3 Production run

This step refers to the main simulation after the system is equilibrated. In the thesis, the simulation lengths were on the microsecond time scale. The Nose-Hoover thermostat and the Parrinello-Rahman barostat were used to maintain the temperature and pressure respectively. More details on the various MD simulations performed in this work can be found in publications that are part of this thesis. Therein, all force field choices and settings as well as the parameter settings used for the various algorithms can be found.

2.7 MD limitations

It is important to be aware of the limitations of MD simulations in order to make reasonable use of it [230]. Some of these limitations include (i) the design of an accurate simulation studies that is strongly influenced by the availability of experimental structures, particularly if the simulation study meant to be compared with experimental results, but this is not the case when simulation is designed to guide experimental study or to complement it, (ii) the force field issue, as it is parametrized to give a reasonable approximation of the potential-energy landscape, but they are improved substantially, (iii) the covalent bonds do not break or form during typical MD simulations, meaning that the protonation states of titratable amino acid residues are fixed and must be set carefully at the beginning of a simulation, unless constant pH simulation approaches are employed (Goh et al., 2014), the same is true for disulfide bonds, (iv) Finally, important biomolecular processes, including ligand binding and conformational change, often take place on longer timescales than those accessible by classical all-atom MD simulation. At the time scales that are accessible by conventional MD simulations, a peptide or protein often remains trapped in an energy basin and seldomly overcomes relevant energy barriers. This restricts the study of slow dynamic processes that occurs on the

(sub-)millisecond or longer time scale. Since typical simulation time steps in all-atom MD simulations are on the order of femtoseconds, $> \sim 10^{12}$ time steps are needed to observe such slow dynamics.

For the latter, different approaches based on MD simulations were developed to enhance the conformational-space sampling and allow simulations to capture longer-timescale events. These approaches employ a wide variety of strategies, such as pulling a biomolecule from a desired initial conformation to a desired final conformation (e.g., targeted MD [231]), altering the force field to reduce the height of energetic barriers (e.g., accelerated MD [232]), pushing a simulation away from regions of conformational space it has already visited (e.g., metadynamics [233]), raising the effective temperature associated with certain degrees of freedom (e.g., replica exchange and temperature accelerated MD [234, 235]). With the scope of the thesis work, I will explore the last two approaches in the next subsection. We recommended the reader with the following references [236–238] for further information on other techniques.

2.7.1 Metadynamics (MetaD)

Metadynamics is an enhanced sampling method originally developed by Parrinello and coworkers [239]. It is widely applied for the calculation of free energies and accelerating rare-event sampling in complex biomolecular systems. The idea of MetaD [240] is to fill the free energy minima of a metastable state with bias potentials ($V(\mathbf{s}(\mathbf{q}))$) in a controlled manner to enhance the exploration of other states in the energy landscape (Fig. 2.8A). This scheme can be achieved by running the MD simulation with a modified Hamiltonian for which a history dependent bias potential $V(\mathbf{s}(\mathbf{q}), t)$ is added. This bias potential is a function of $\mathbf{s}(\mathbf{q})$, and can be built as a sum of Gaussian potentials deposited within the collective variable (CV) space to push the system toward sampling unexplored configurations:

$$V(\mathbf{s}, t) = \sum_{k\tau < t} W(k\tau) \exp\left(-\sum_{i=1}^{N_{\text{CV}}} \frac{(\mathbf{s}_i - \mathbf{s}_i(\mathbf{q}(k\tau)))^2}{2\sigma_i^2}\right) \quad (2.11)$$

where σ_i is the width of the Gaussian function for the i^{th} collective variable, $W(k\tau)$ is the height of the Gaussian at the simulation time $t = k\tau$, which is constant in the case of standard metadynamics, and τ is the deposition rate of the Gaussian functions.

Ultimately, the bias potential converges in the long-time limit to the negative of the free energy as a function of the collective variables,

$$V(\mathbf{s}, t \rightarrow \infty) = -F(\mathbf{s}) + C \quad (2.12)$$

where C is a constant. The latter equation implies that the deposited bias potential is optimal to enable transition events as it flattens the biased energy landscape. In standard MetaD, the height of the added Gaussian potentials is constant during the simulation. Therefore the estimated free energy landscape oscillates when converging toward the real free energy profile. This limitation can be overcome by utilizing well-tempered MetaD [241, 242] that rescales the height of the added Gaussian potentials such that it is decreasing with time. In addition to well-tempered MetaD, different variants of standard MetaD have been implemented to enhance its sampling efficiency, such as parallel-tempering MetaD [243, 244], multiple-walkers MetaD [245], and bias-exchange MetaD [246]. However, an outstanding drawback of MetaD is the possibility of driving the system into a physically irrelevant region of the space. Its accuracy is strongly dependent on the proper choice of CVs and the proper selection of the Gaussian parameters $W(k\tau)$ and σ [240, 247].

MetaD has been applied to study the binding of IDPs [248] and also the free energy landscape of IDPs [249].

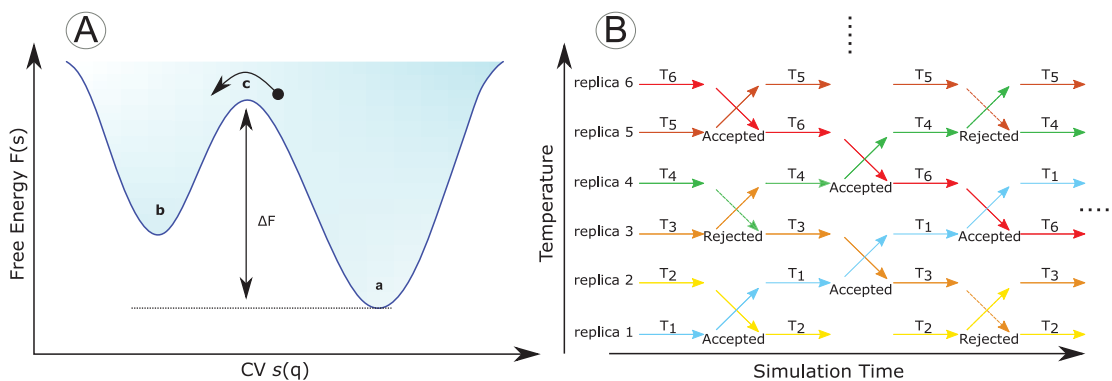


FIGURE 2.8: Schematic representation of (A) metadynamics (MetaD) with a free energy profile of two energy basins (a and b) separated by an energy barrier ΔF at c. Filling the wells with a bias potential (light blue) allows the system to transition between a and b by crossing c. (B) Presentation of the REMD method for a system with 6 replicas simulated at different temperatures from T_1 (lowest T) to T_6 (highest T). Exchange attempts between neighbored replicas are marked by arrows. Reproduced with Copyright ©2021 Elsevier

2.7.2 Replica Exchange Molecular Dynamics (REMD)

REMD is one of the non-CV based methods that alleviates the problem of prior knowledge of the system under study as required by CV-based methods. The idea of REMD is to run several replicas of the same system, yet at different temperatures. Exchanges between the temperatures or the configurations of neighbouring replicas are attempted every few time steps (Fig. 2.8B) [250]. This way, configurations that are accessible at high temperatures are exchanged with those sampled at a lower temperature. This process enhances the conformational sampling of the system and allows to accurately compute its thermodynamic properties. REMD has been widely applied in the study of conformational ensemble of IDPs. Its first application was by Sgourakis et. al to explore the differences in the conformation accessible to the hydrated A β monomers (A β 40 and A β 42) [251]. Similarly, it was then employed to understand the conformational preferences of the histone tails (highly flexible N- or C-terminal) and its effect on the binding affinity to linker DNA [252]. It has been further utilized to understand the interplay of residual structure and conformational fluctuations in coupled binding and folding of IDPs applied to transcription coactivator CREB [253, 254]. Miller et al. studied the conformational ensemble of several IAPP variants [255]. REMD simulations have been also used to investigate how post-translational modifications affect the conformational ensemble of different IDPs such as tau , hIAPP [256], and KIDS [257]

However, this approach is computationally demanding as the number of replicas grows with the square root of system size. A more efficient version of REMD, called Hamiltonian replica exchange MD (HREMD), was developed by Bussi et al [258]. In this approach, the different replicas of the system evolve according to different Hamiltonians. It is rendered to be more efficient than REMD due to the lower number of replicas needed. Different types of HREMD approaches have been developed, which mainly differ by the modifications made to the Hamiltonian in the different replicas. In the approach of Bussi et al. [258] the system is divided into a hot (H) and a cold (C) region, and Hamiltonian of the H-region is modified in order to accelerate the sampling. For a system of N_{rep} replicas with \mathbf{q}_i being the coordinates of the i^{th} replica, the ensemble probability is defined as

$$p(\mathbf{q}_1) \times \dots \times p(\mathbf{q}_{N_{\text{rep}}}) \propto \exp\left(\frac{-U_1(\mathbf{q}_1)}{k_B} \dots \frac{-U_{N_{\text{rep}}}(\mathbf{q}_{N_{\text{rep}}})}{k_B T}\right) \quad (2.13)$$

Thus, in HREMD the energy and not the temperature is modified; instead all replicas are usually simulated at the same temperature. The Hamiltonian of the system in the H-region will be changed depending on a scale factor λ such that only the force field terms contributing to noteworthy energy barriers are scaled, whereas the Hamiltonian of the C-region is kept unperturbed. In particular, the charges of the atoms in the H-region are scaled by a factor of $\sqrt{\lambda}$, while the Lennard-Jones parameters ϵ are scaled by a factor of λ . The proper dihedral potential is scaled by a factor of λ or $\sqrt{\lambda}$ depending on if both the first and fourth atoms or only one of them is in the H-region.

Considering that the temperature and energy are related as shown in equation (2.13) (for example, scaling the energy to its half is equivalent to doubling the temperature), it is plausible to think of the HREMD scheme as simulating each region at an "effective temperature" of $\frac{T}{\lambda}$, $\frac{T}{\sqrt{\lambda}}$ and T for interactions inside the H-region, between the H- and the C- regions, and inside the C-region, respectively. The scaling factor λ ranges from 1 (for the unmodified system) to minimal 0 (infinite temperature or zero interaction in the hot region). In praxis, the lowest λ value is usually chosen as 0.6 or 0.5. The probability for exchanges between replicas should satisfy the Metropolis criterion to ensure detailed balance as a condition to obtain the correct ensemble for the Hamiltonian of interest:

$$p(\mathbf{q}_i \leftrightarrow \mathbf{q}_j) = \min \left[1, \exp \left(\frac{U_i(\mathbf{q}_i) - U_i(\mathbf{q}_j)}{k_B T} + \frac{U_j(\mathbf{q}_j) - U_j(\mathbf{q}_i)}{k_B T} \right) \right] \quad (2.14)$$

Though enhanced sampling techniques yield the relevant thermodynamic state of the studied system and allow the calculation of the corresponding thermodynamic properties accurately, estimating the transition rate among different states in the configuration space remains a limiting step.

HREMD has been successfully applied in the study of different IDPs, including A β [259, 260], A β fragments [261], the disordered N-terminal of c-Src kinase [262], histatin 5 (24 residues), and Sic 1 (92 residues). Furthermore, HREMD has also been coupled with a CG force field to further enhance the sampling efficiency [263].

Enhanced sampling methods are implemented in different MD programs, such as the Colvars module in NAMD [264] that enables MetaD simulations and is flexible in defining CV using Tcl scripts. Similarly, the Plumed plugin [265] together with GROMACS [221] enables running HREMD and MetaD simulation.

2.8 Aims

Scientific research on amyloid proteins associated with amyloid diseases is being carried out globally by a large number of theoretical and experimental research groups. Each incremental step in this field of research is needed toward filling the gap in understanding the mechanism of the disease development and for finding a potentially effective treatment, which is still lacking. Among these amyloid proteins are the amyloid- β and hIAPP that are associated with the development of Alzheimer's and diabetes diseases, respectively. In this thesis work, we focus on providing insight into the behavior of A β and hIAPP in an environment that mimics the *in vivo* environment. This is accompanied by designing and running multiple all-atom MD simulations, where in each MD study a certain aspect from the real amyloid-peptide environment is taken into account, such as the cell membrane composition, the free lipids in the aqueous phase, the oxidative stress, and the macromolecular crowding in the cellular environment. The aim of these simulations is to unravel how these different conditions affect the conformational preferences of the two peptides, their aggregation and interactions with lipid membranes. This atomic level knowledge will give insight into the influences of different *in vivo* conditions in disease development, assuming the aggregation into β -sheet structure is the disease-defining step. The power of the MD simulation technique in addressing biological questions has considerably increased since its first introduction in 1950, such that it is widely used nowadays as a complement to experiment or in furthering our understanding of the studied systems at higher resolution. This is the motivation beyond using it as tool toward achieving the intended goals in this thesis work.

Chapter 3

Results

The main aim of this thesis work was to investigate the behavior of the amyloid peptides $A\beta_{42}$ and hIAPP in an environment that consider certain aspects of the *in vivo* environment. To this end, we performed all-atom MD simulations to study (i) $A\beta_{42}$ in the presence of a neuronal membrane (Publication I), (ii) $A\beta_{42}$ interactions with free lipids in the aqueous phase (Publication II), (iii) $A\beta_{42}$ under oxidative stress (Publication III), (iv) $A\beta_{16-22}$ in the presence of macromolecular crowding (Manuscript IV), (v) hIAPP and membrane binding (Publication V). In the following sections, brief summaries of these studies are provided, while the full publications or manuscripts are reproduced in sections (A.1-A.5).

3.1 Publication I: $A\beta_{42}$ and the neuronal membrane

Amyloid- β peptide dimers undergo a random coil to β -sheet transition in the aqueous phase but not at the neuronal membrane

Fatafta H., Khaled M., Owen MC., Sayyed-Ahmad A., Strodel B. PNAS., 2021 Sep 28; 118(39):e2106210118. doi: 10.1073/pnas.2106210118.

Original publication, see Publication I in section A.1, contribution: execution and analysis of molecular dynamics simulations involving the neuronal membrane, producing the figures, and writing the first draft of the paper.

3.1.1 Background

Recently, a large body of evidence supports the view that $A\beta$ oligomers are the most toxic species that play a key role in Alzheimer's disease development [44–46]. This is contrary to what earlier researchers used to believe since the proposal of the amyloid cascade hypothesis in 1991 [81] is that the mature amyloid fibrils are the cause for the neuronal loss and damage. Thus, the focus is now towards better understanding of the role of these toxic species in Alzheimer's disease progression and further probing the source of toxicity. Over the years, the neuronal membrane has been suggested to be the main site for the $A\beta$ oligomer mediated toxicity via damaging protein-membrane interactions or via changes in the lipid bilayer properties. Several studies aimed to shine light on the details of $A\beta$ -membrane interactions; however, it is extremely difficult to capture these transient interactions with experimental methods. This becomes possible with MD simulations and this problem was addressed in the current research study.

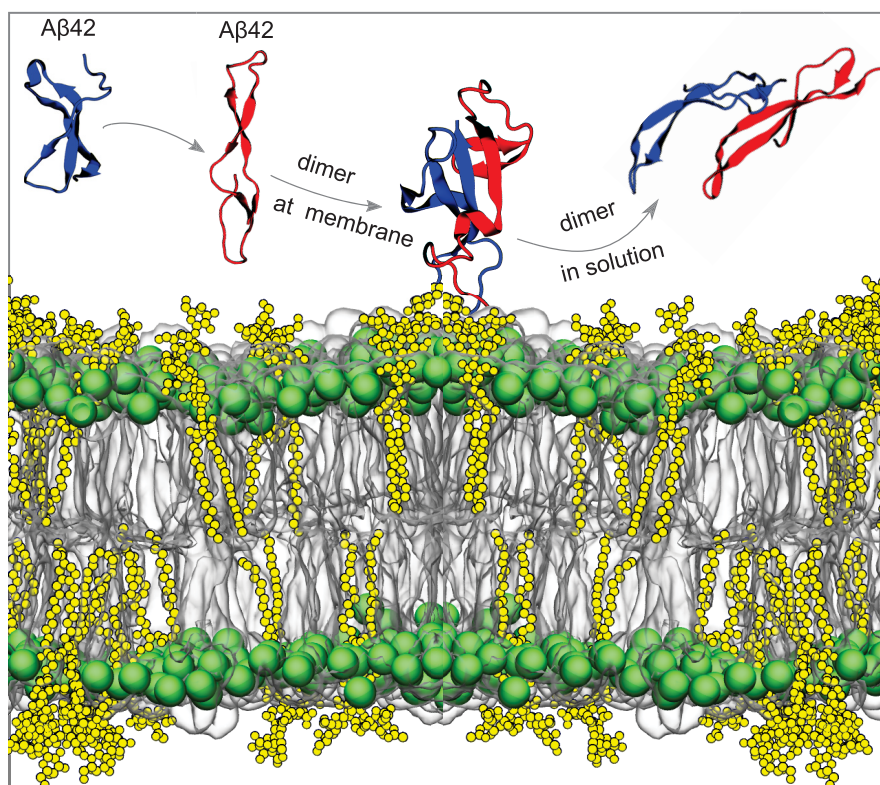


FIGURE 3.1: A schematic representation that illustrates the focus of the study involving $A\beta$ dimers in the presence of a neuronal membrane.

3.1.2 Results

In this study, we contrast the dimerization of the full-length $A\beta_{42}$ in solution and at the neuronal membrane using an aggregate of 24 μs of all-atom MD simulations (see Fig. 3.1). We built two systems for the $A\beta_{42}$ dimer; one in solution, and the other one is in the presence of a neuronal membrane. For the second system, we built a model lipid bilayer of $9.6 \times 9.6 \text{ nm}^2$ consisting of six lipid types (38% 1-palmitoyl-2-oleoyl-sn-glycero-3-phosphocholine (POPC), 24% 1-palmitoyl-2-oleoyl-sn-glycero-3-phosphoethanolamine (POPE), 5% 1-palmitoyl-2-oleoyl-sn-glycero-3-phospho-L-serine (POPS), 20% cholesterol (CHOL), 9% sphingomyelin (SM), and 4% monosialotetrahexosylganglioside (GM1)) to mimic the composition of a neuronal cell membrane. For both systems we employed Charmm36m to model $A\beta$, a force field adjusted for intrinsically disordered proteins (IDPs), as reported in section 2.3.

There are key difference compared to previous simulations in the field; the first one concerns the time scale of this study which is exceeding previous studies on $A\beta$ -membrane interactions by an order of magnitude, and the second one is the simulation of a complex lipid membrane of more than three lipid components at the atomistic detail, which to the best of our knowledge has not been done yet. In addition, we were also able to follow the details of the dimerization pathway using transition networks. Our results highlighted that the dimerization occurs in both systems but the dimer in solution reveals a random coil to β -sheet transition, leading to structures similar to those found in $A\beta$ fibrils (Fig. 3.2A and B). The conclusion thus is that the $A\beta$ dimers sampled in solution are on-pathway to amyloid aggregation. In contrast, the neuronal membrane attenuates the peptide's tendency to form β -sheets.

On the neuronal membrane, our observations revealed an adsorption of the $A\beta_{42}$ dimer on the membrane but no peptide insertion into its hydrophobic region (Fig. 3.2D). Furthermore, the membrane adsorption of the $A\beta_{42}$ dimer is mainly driven by electrostatic interactions between the charged N-terminal residues of $A\beta$ and the headgroups of PC, PE, and PS, in addition to hydrogen bonding with GM1 lipids (Fig. 3.2C). Our simulations shed light on the role of gangliosides (GM1) as the main lipid interaction partner of the peptide. Here, the sugar groups of GM1 form hydrogen bonds with the peptide, thereby reducing the possibilities for other hydrogen bonds to form within $A\beta$ or between the two $A\beta$ peptides. This is the reason beyond the divergence of the dimer

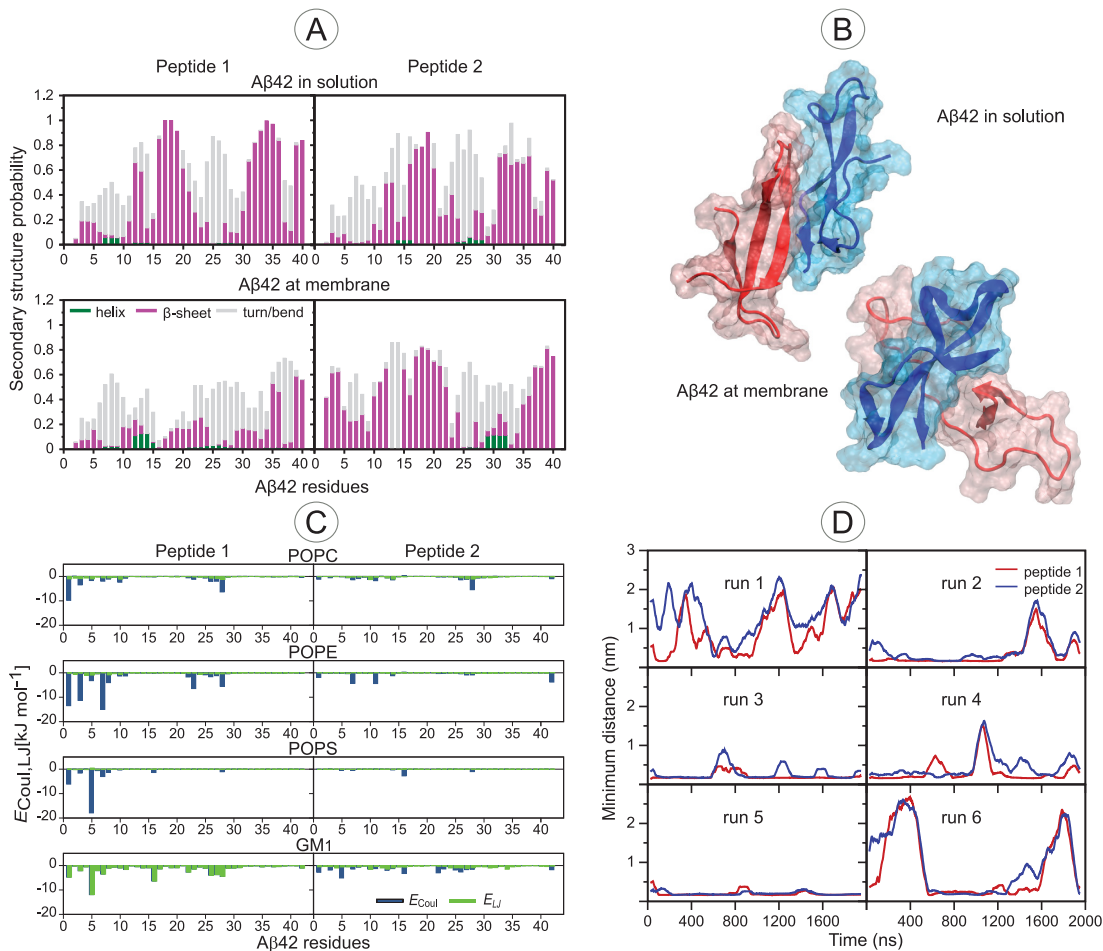


FIGURE 3.2: (A) Probability of secondary structures to form in each residue of the peptides in the aqueous phase (top) and in the presence of the neuronal membrane (bottom). The bars represent the cumulative secondary structure probabilities consisting of helix (green), β -strand/bridge (magenta), and turn or bend (gray). The difference from 1.0 presents the probability of the random coil state. (B) Snapshots of A β 42 dimer in the aqueous phase (top) and in the presence of the neuronal membrane (bottom). Peptide 1 and peptide 2 are shown as cartoons in red and blue, respectively. (C) The average interaction energies of peptide 1 (left) and peptide 2 (right) with each lipid of the neuronal membrane. Electrostatic and Lennard-Jones energies are shown in blue and green, respectively. The more negative an energy is, the more attractive is the corresponding interaction. (D) The minimal distance between the A β 42 peptides and the neuronal membrane surface for each of the six simulations (run1–run6). Results for peptide 1 and peptide 2 are shown in red and blue, respectively.

configurations in solution and at the neuronal membrane. Assuming that the β -sheet structure is the membrane-damaging species, this suggests a neuroprotective effect of GM1. This is further supported by our observation that the membrane adsorption of the dimer was found to have profound effects on the A β 42 dimer, while the membrane was only marginally affected.

3.1.3 Conclusion

In this study we were able to shine light on the dimerization of A β 42 both in solution and in the presence of a neuronal membrane. In term of dimer formation, the dimer formed in both cases but with significant differences. In solution, the resulting dimer is characterized by its high β -sheet content, that convey the structural transition from random coil to β -sheet. This, to the best of our knowledge, was not seen yet by other unbiased MD simulations, and the obtained structures bear certain similarities to the U-shaped A β 42 fibril. Thus, we concluded that with our microsecond time scale simulations in solution we were able to observe this structural transition that counts as on pathway for amyloid aggregation. In the presence of a neuronal membrane, the dimer is less ordered with reduced β -sheet content. GM1 is the preferable site for membrane interaction of A β 42 a finding that is in line with our previous study (see Publication III). Thus, we concluded that GM1 is neuroprotective against A β -mediated toxicity. Furthermore, the consideration of the neuronal membrane in this study is a step forward in studying A β -membrane interactions compared to previous studies with three lipid types or fewer.

3.2 Publication II: A β 42-lipid complex

Disorder-to-order transition of the amyloid- β peptide upon lipid binding

Fatafta H., Kav B., Bundschuh B., Loschwitz J., Strodel B. *Biophys Chem.*, 2022 Jan; 280:106700. doi: 10.1016/j.bpc.2021.106700

Original publication, see Publication II in section A.2. Contribution: execution of some of the molecular dynamics simulations, participating in the analysis, producing the structure figures, and writing the first draft of the paper.

3.2.1 Background

On the same line with the previous study, it is now well established that A β exert its toxicity via abnormal interaction with the neuronal membrane. Presently, there is intense interest in elucidating the peptide-membrane interactions to gain a good understanding

of the underlying toxicity mechanism. Hence, the interaction of $A\beta$ with the membrane environment has been extensively studied [36, 82, 83], with the focus on investigating $A\beta$ in a lipid-rich phase. However, there are emerging evidences pointing to the importance of the free lipids in the aqueous environment that exist at equilibrium with the membrane at nM to μ M concentration [84, 85, 87]. Indeed, these free lipids found to bind $A\beta$ forming $A\beta$ -lipid complexes which enabled an easy membrane insertion for $A\beta$ and other amyloid proteins. This finding encourage La Rosa and coworkers to propose a "lipid-chaperone" hypothesis [86] where lipid-assisted protein transport enables the membrane insertion of proteins. They further remarked that lipid-assisted protein transport and the effect of lipid binding on protein conformation are overlooked. Few experimental and molecular dynamics studies reported on the stability of the peptide-lipid complexes in solution and their role in assisting protein-transport into membranes [84, 86, 87]. Thus, improved understanding of these complexes and their role in affecting peptide-membrane interactions are warranted and needed. This can be achieved from the viewpoint of molecular dynamic simulations and was addressed in this study.

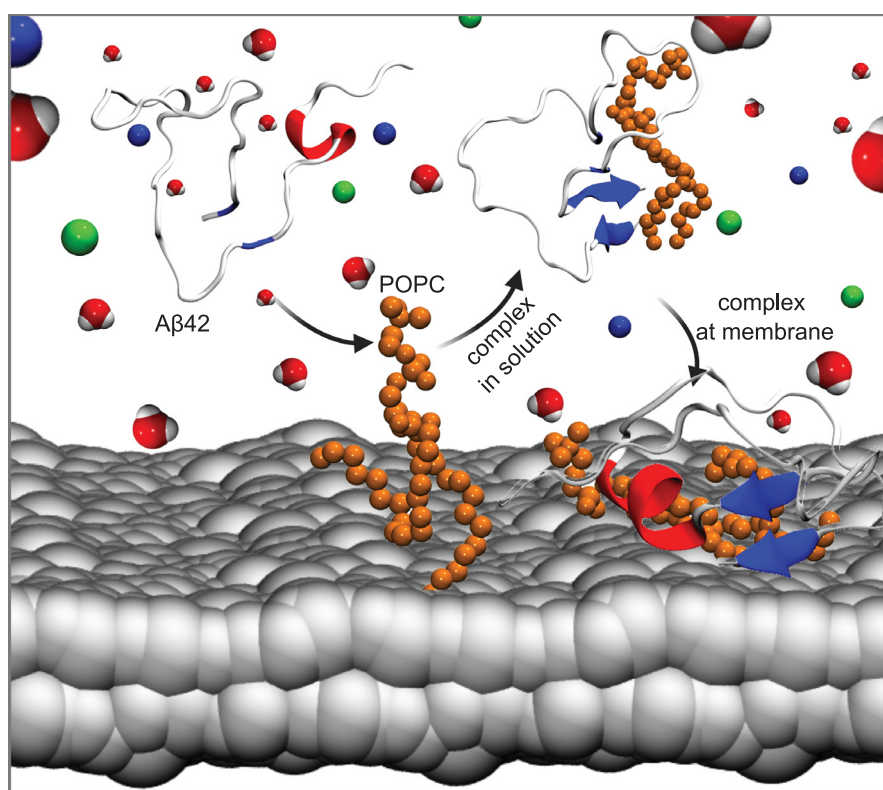


FIGURE 3.3: A schematic representation that illustrates the focus of the study involving $A\beta$ -POPC complex in solution and in the presence of POPC membrane.

3.2.2 Results

We performed all-atom MD simulation on the microsecond time scale to study the complex formation between A β 42 and lipid molecules in solution (see Fig. 3.3). We considered the most abundant lipids in mammalian cells; POPC and 1,2-dipalmitoyl-sn-glycero-3-phosphocholine (DPPC), and to further investigate the interactions of these complexes with membranes, we also included pre-assembled lipid membranes. We built three different systems including two systems in solution composed of a single A β 42 peptide with either a single POPC or DPPC lipid molecule in (1:1 ratio) or with three POPC lipid molecules (1:3 ratio), and one system in the presence of a lipid membrane composed of a A β 42-POPC complex in 1:1 ratio with a model lipid membrane of $10.0 \times 10.0 \text{ nm}^2$ consisting of 154 POPC lipids. In all cases we considered reference systems containing either the single A β 42 peptide in solution or the single A β 42 or the single POPC molecule in the presence of the POPC lipid membrane.

The first set of MD simulations aimed at assessing the complex formation and complex stability in solution. Our observations revealed the formation of stable A β 42-lipid complexes in solution both in 1:1 and 1:3 ratios, but the resulting complexes showed significant differences. We found that A β 42 remains largely disordered when bound to a single lipid molecule (Fig. 3.4A and B), but folds into either helical or β -sheet structures once it bound to three lipid molecules (Fig. 3.4C). This indicates that A β 42 underwent a disorder-to-order transition upon binding to a sufficient numbers of lipid molecules, which are three lipid molecules in our case. An interesting observation in the 1:3 complex is the helix-kink-helix conformation which was stable for the last 200 ns in one of our simulations (Fig. 3.4C run 1), and transiently formed in the other two repeat simulations (Fig. 3.4C run 2 and 3). The lipid tails dominate the interaction with A β 42 in the complexes, which in turn drive the structural transitions. The formation of this particular helix-kink-helix found to be dependent on specific residue-POPC contacts. It is stabilized by hydrophobic interactions between the lipid tails and the hydrophobic residues Leu17, Ala21, Ile32, and Val36.

To follow the interplay between the complex and a model lipid membrane, particularly to examine if the complex can indeed drive easier peptide insertion, we simulated one of the resulting complexes with a POPC membrane. For the purpose of simplicity we only simulated the complex in 1:1 ratio, and further compared the results to simulations

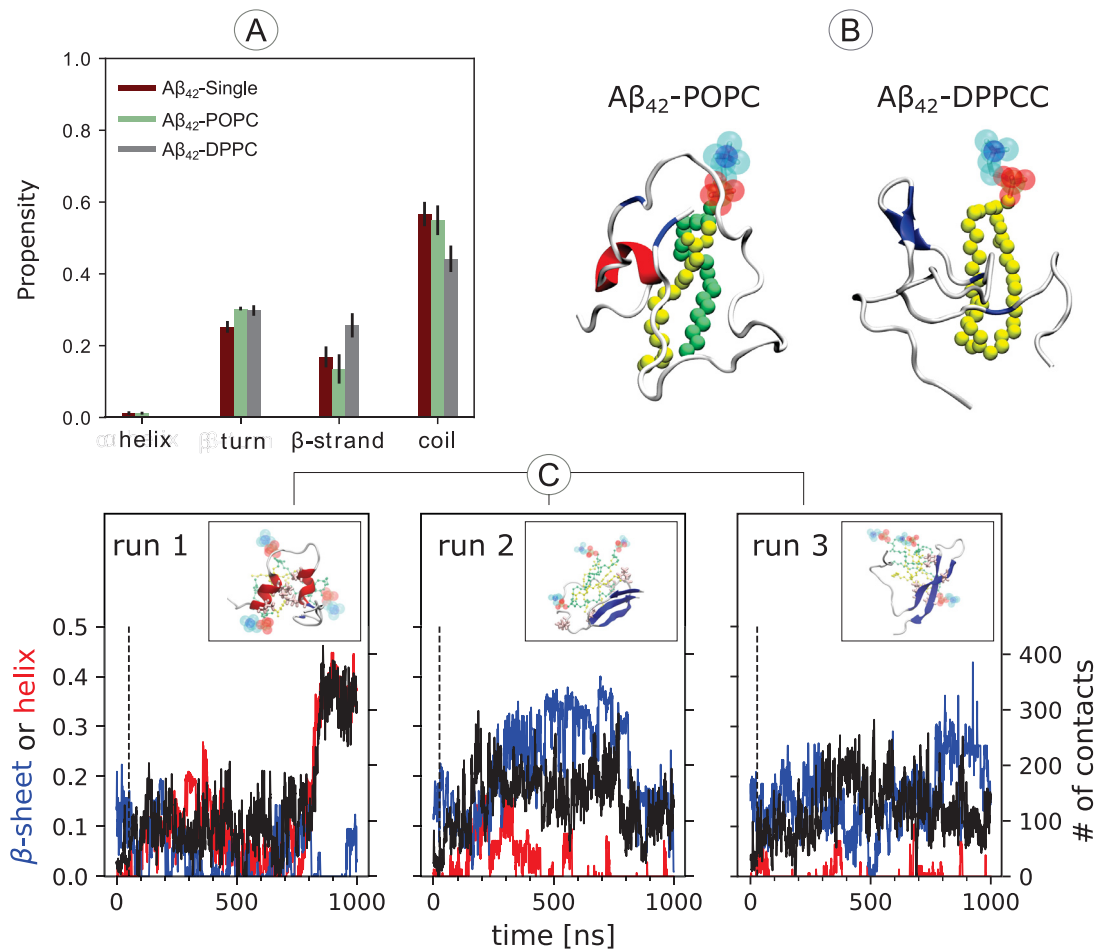


FIGURE 3.4: (A) The secondary structure propensities of $A\beta_{42}$ when being an individual peptide (red) or in complex with a POPC lipid (light green) and DPPC (gray). The values are averaged over three independent runs and error bars represent the standard error of the mean. (B) Snapshot of an $A\beta_{42}$ -POPC and $A\beta_{42}$ -DPPC 1:1 complex, respectively. POPC and DPPC are shown as spheres, with the lipid head group, oleoyl chain, and palmitoyl chain colored in light red and light blue, green, and yellow, respectively. (C) Evolution of the β -sheet (blue) and helix content (red) as well as the number of atom-atom contacts formed between the POPC lipids and $A\beta_{42}$ residues Leu17, Ala21, Ile32, and Val36 obtained from the three simulations of 1:3 $A\beta_{42}$ -POPC complexes. The dashed vertical lines mark time when all three POPC lipids had bound to $A\beta_{42}$. The top corner shows representative snapshots showing the helix-kink-helix structure that formed at the end of run 1 and β -sheet structures sampled in runs 2 and 3. The peptide is shown as cartoon and the sidechains of Leu17, Ala21, Ile32, and Val36 are explicitly shown. The lipid headgroups are indicated by blue and red spheres, and the oleoyl, and palmitoyl chains are represented with green and yellow lines, respectively.

with a single peptide or a single POPC lipid with the membrane. The simulation with a single POPC molecule revealed its insertion into the lipid membrane (Fig. 3.5A and C), whereas the simulation with a single $A\beta_{42}$ molecule revealed its adsorption to the membrane surface but no insertion (Fig. 3.5A). Similar to the single $A\beta_{42}$ peptide, the $A\beta_{42}$ in complex with a POPC molecule did not insert into the membrane. However, the

bound POPC molecule in the complex affects $A\beta_{42}$'s interactions with the membrane in terms of (i) its conformation such that the peptide bears helical content when bound to membrane, while the dominant structure in the single $A\beta_{42}$ is random coil and β -sheet (Fig. 3.5B), (ii) insertion depth such that the observed helix in the $A\beta_{42}$ -POPC complex tends to insert more deeply into the membrane. While, this observed helix is different from the helix-kink-helix structure formed in the 1:3 complex, it is noteworthy and sheds light on a possible insertion mechanism for the peptide.

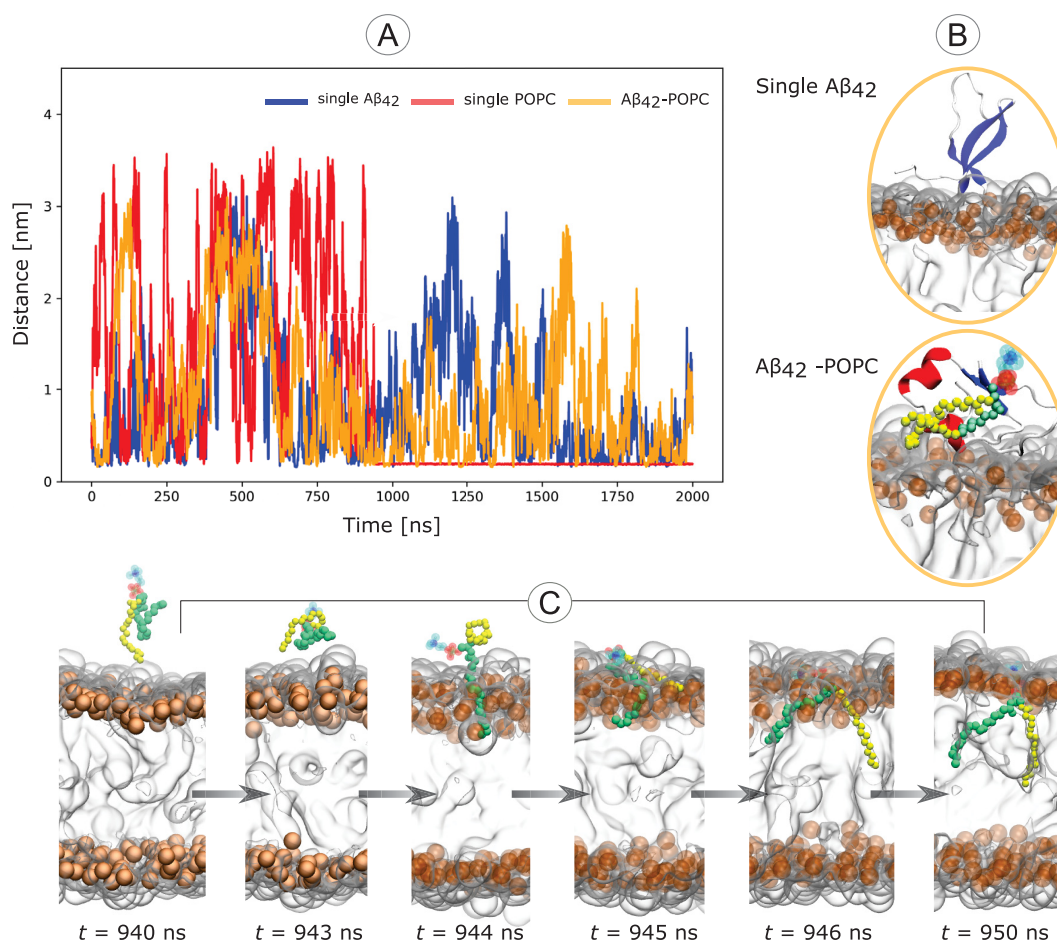


FIGURE 3.5: (A) The minimal distance between the single $A\beta_{42}$ peptide, single lipid molecules and the complexes from the POPC lipid bilayer. Colors as indicated. (B) Snapshots of $A\beta_{42}$ interacting with the POPC membrane, either for the individual peptide or as part of the $A\beta_{42}$ -POPC lipid complex. The same representations for the peptide, and lipid in complex as in the Fig 3.4. (C) Snapshots of a POPC molecule inserting into a POPC membrane. At $t = 940$ ns the first contact between the POPC lipid and membrane was established and at $t = 950$ ns the insertion was completed. The oleoyl and palmitoyl chains of the inserting lipid are shown in green and yellow, respectively. The POPC membrane is shown as translucent surface, with the lipid headgroups being indicated by orange spheres.

3.2.3 Conclusion

Our findings on the complex formation agrees well with the findings of La Rosa and coworkers in terms of the complex stability, but they are in partial agreement in terms of the structural conformation anticipated by the peptide. La Rosa and coworkers reported an increment in the helical content upon complex formation which is not revealed from all of our MD simulations. Our simulations highlighted a disorder-to-order transition once A β 42 is in complex with three POPC molecule, whereas the peptide remains largely disordered when complexed with a single lipid. Thus we concluded that A β 42 undergoes a coupled binding and folding process in the vicinity of a sufficient number of lipids.

The membrane simulation revealed that in the case of complex interaction with the lipid membrane the presence of POPC bound to A β 42 encouraged the formation of a helical structure that dips deeper into the membrane. This implies that the complex decreases the energy barrier for membrane insertion, and further suggests a possible mechanism for peptide insertion. Of note is the observation of a β -sheet conformation in the single A β 42 interacting with the membrane. This finding is in contrast with Publication I on the dimerization of A β 42 in the presence of the neuronal membrane, where GM1 was found to decrease the order of A β 42 via attenuating its propensity to form β -sheet. This shows that in our future studies testing the lipid-chaperone hypothesis, we should and will include more realistic cell models.

3.3 Publication III: A β 42 and oxidative stress

Role of Oxidized Gly25, Gly29, and Gly33 Residues on the Interactions of A β ₁₋₄₂ with Lipid Membranes

Fatafta H., Poojari C., Sayyed-Ahmad A., Strodel B., Owen MC. ACS Chem Neurosci., 2020 Feb 19; 11(4):535-548. doi: 10.1021/acchemneuro.9b00558.

Original publication, see Publication III in section A.3. Contribution: execution of some of the molecular dynamics simulations, analyzing all simulations, producing the figures, and writing the first draft of the paper.

3.3.1 Background

The human brain is more vulnerable to oxidative stress than any other organ in the body, especially when considering that it constitutes 2% of the body weight but consumes approximately 20% of the oxygen provided by the respiratory system [266, 267]. Neurons, as the basic units in the brain together with astrocytes, are preferable site for oxidative damage [268–270]. Neurons contain high amounts of polyunsaturated fatty acids in addition to proteins and nucleic acids that can interact with reactive oxygen species, which in turn lead to their oxidation. Thus, oxidative stress is an important participant in the pathogenesis and development of AD, and it is closely correlated with the emergence of amyloid- β aggregates [105, 107]. The amyloid aggregates and the excessive reactive oxygen species are known as the principal features observed in AD brains. However, it is not well resolved yet, whether A β elicits further oxidative stress on the neuron or the oxidative stress initiates further A β accumulation. On the other hand, it is well established that the plasma membrane of neurons plays an important role in modulating the peptide's toxicity, which we investigated in publications I and II. In this study, we sought to analyze the impact of the A β peptide oxidized at selected glycine residues on its conformation and interaction with a model membrane.

The relationship between glycine residues in the C-terminal region of A β and oxidative stress can be explained by the amyloid radical hypothesis. This hypothesis describes how the C atom of glycine residues is susceptible to the loss of an H atom upon oxidation of Met35, which in turn causes the formation of a protein backbone radical, stabilized by the capto-dative effect [271, 272] and prone to adopt an extended structure perfect for β -sheet formation [273]. In this hypothesis, Gly33 is predicted to be more susceptible to oxidation by the methionine-based sulfuranyl free radical due to the close proximity of these residues in the A β 42 primary structure. Several experimental studies have been attempted to explore the effect of radicals on proteins but challenges in locating the center of a radical in protein hinders systematic experimental investigations [274, 275].

3.3.2 Results

In this study, we focused on exploring the effect of oxidizing selected glycine residues of the A β 42 peptide (Gly25, Gly29 or Gly33) on its conformation and interaction with

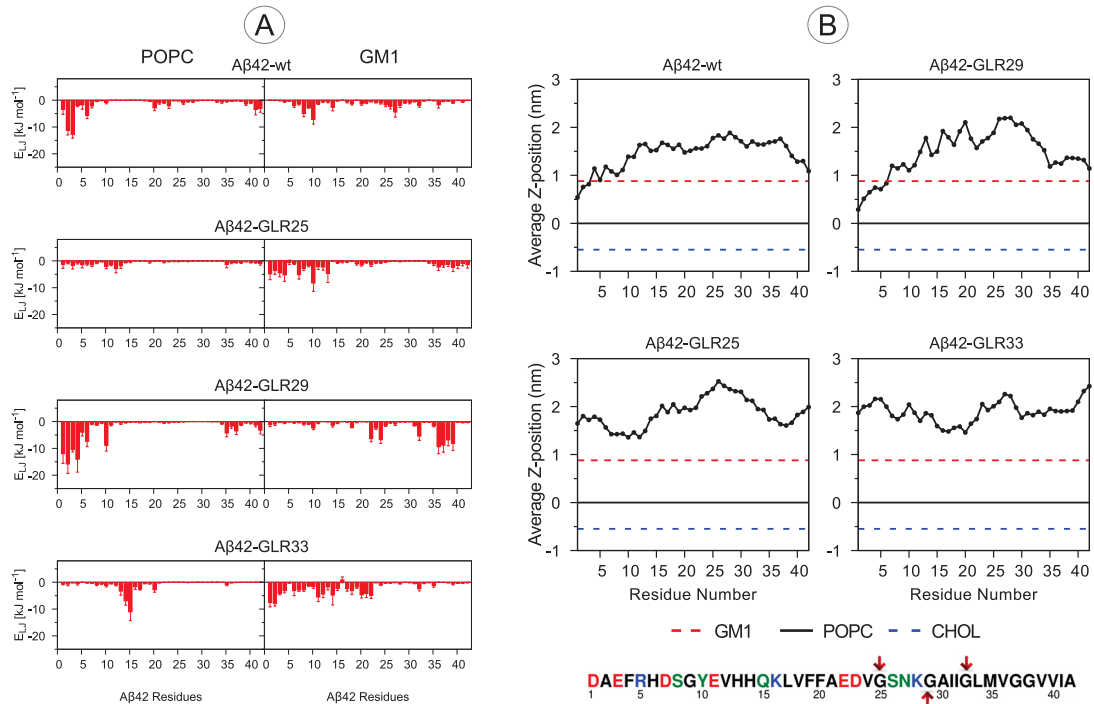


FIGURE 3.7: (A) The Lennard-Jones interaction energy of each A β 42 residue (and standard deviation of the mean) between A β 42 and POPC (left) and GM1 (right) head groups. (B) The average insertion distance of each A β 42 residue with respect to the POPC and GM1 head groups and CHOL hydroxyl group. The head group of GM1, POPC, and CHOL are shown in red, black, and blue respectively.

and A β 42-GLR33, which interacted the most with GM1, have a lower tendency to form β -sheet (Fig. 3.8A and B). The peptide interaction with GM1 involves the formation of hydrogen bonds between A β 42 with the GM1 sugar head groups. This also reduced the number of contacts and hydrogen bonds that the peptide makes with POPC.

3.3.3 Conclusion

We have demonstrated that the oxidation of A β 42 at selected glycine residues has different impacts owing to their distinct positions in the hydrophobic sequence of A β 42 involving the Gly29-XXX-Gly33-XXX-Gly37 motif (zipper motif) and to their interaction with the sugar group of GM1. The significant difference on the membrane interaction was manifested by the high preference of A β 42-GLR29 and A β 42-GLR33 to bind the bulky GM1 lipid, and the high preference of A β 42-GLR29 and A β 42-wt to bind to POPC lipids. GM1 binding affects the peptide conformation via reducing the β -sheet formation in A β 42-GLR29 and A β 42-GLR33 variants compared to the A β 42-GLR25 variant and the A β 42-wt, whereas POPC binding enhances membrane insertion. Thus,

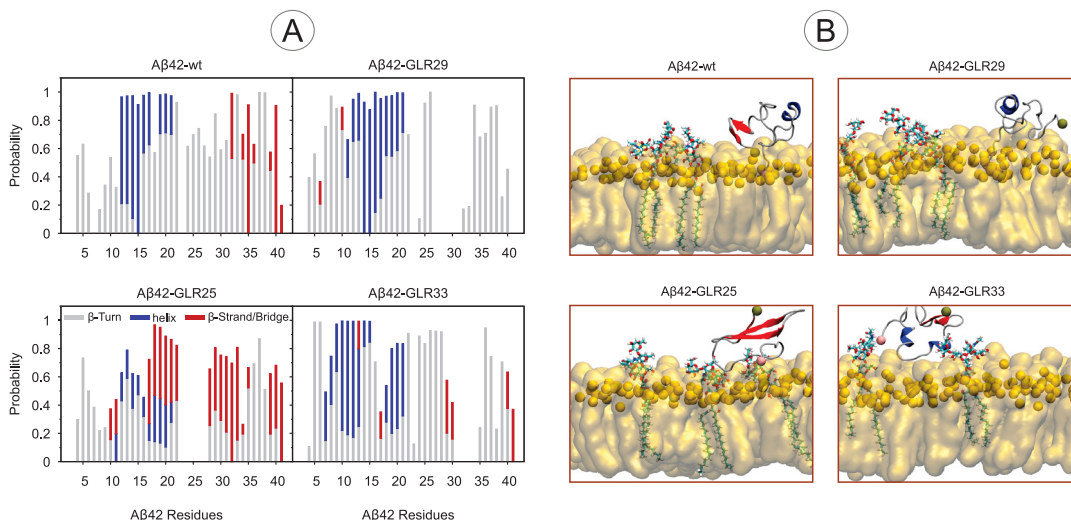


FIGURE 3.8: (A) The secondary structure assignment of each $A\beta_{42}$ residue in the case of $A\beta_{42}$ -wt, $A\beta_{42}$ -GLR25, $A\beta_{42}$ -GLR29, and $A\beta_{42}$ -GLR33 in a bilayer comprised of 70% POPC, 25% CHOL, 5% GM1. The β -turn/bend is shown in silver, the helix in blue and the β -strand/bridge is shown in red. The figure shows the additive probability of all secondary structure such that the maximum is 1, those residues showing probability lower than 1 form random coil. (B) The central structure of the the largest cluster of $A\beta_{42}$ -wt (46.7%), $A\beta_{42}$ -GLR25 (33.8%), $A\beta_{42}$ -GLR29 (56.5%), $A\beta_{42}$ -GLR33 (65.6%). In each rendered image the lipids are colored by orange. The phosphate atom of POPC is in orange, the N and C terminals of $A\beta_{42}$ are shown in pink and tan spheres respectively. The protein β sheet is in red, the helix is in blue, coil and turn are shown in silver.

we concluded that $A\beta_{42}$ -GLR25 is potentially as toxic as $A\beta_{42}$ -wt, assuming that β -sheet formation in $A\beta$ is connected to its toxicity. Furthermore, we suggest that the stability of the C-terminal β -sheet in $A\beta_{42}$ -GLR25 might be attributed to the fact that Gly25 does not disrupt the zipper motif. Further studies should test these observations and further determine the role of oxidation in $A\beta$ -mediated AD toxicity.

3.4 Manuscript IV: $A\beta_{42}$ and macromolecular crowding

Atomistic simulations of macromolecular crowding effect on $A\beta_{16-22}$ aggregation

Fatafta H., Strodel B., Sayyed-Ahmad A. Manuscript in preparation

Manuscript in section A.4, contribution: execution and analysis of molecular dynamics simulations, doing the analysis, producing the figures, and writing the first draft of the manuscript.

3.4.1 Background

It has already stated above that amyloid oligomers rather than the matured fibrils are the most toxic agent responsible for AD progression and severity. To unravel how these oligomeric complexes assemble, several studies have investigated the kinetics and thermodynamics of $A\beta$ oligomerization, but most of them have been performed in a diluted aqueous solution, which does not correspond to the actual complexity of the real cellular environment [276, 277]. In the human brain, the intracellular and extracellular environments are quite crowded with a variety of macromolecules that occupy 7 - 40% of the total volume [278]. It has been further reported that the extent to which $A\beta$ forms oligomers/fibrils in such crowded environments differs by orders of magnitude from that *in vitro* [279]. Accordingly, the current knowledge of $A\beta$ oligomerization in a cell-like environment is still limited. The macromolecular crowding effect is difficult to capture experimentally as it is hindered by the dynamic and transient nature of $A\beta$. In this regard, theoretical calculations, particularly MD simulations can complement the experiments [192, 280]. Nonetheless, application of this approach to study the effect of macromolecular crowding on $A\beta$ aggregation is rare. The existing simulation studies used a coarse-grained model and performed discontinuous molecular dynamics (DMD) [135] or Langevin dynamics simulations [133]. Atomistic insight into the molecular crowding effect on $A\beta$, to the best of our knowledge has not been provided yet. Thus, a better understanding of the crowding effect on $A\beta$ at the atomistic level is warranted and needed. This was addressed in this study.

3.4.2 Results

To unravel the effect of macromolecular crowding on amyloid aggregation (see Fig. 3.9), we focus on the dimer and hexamer of the $A\beta_{16-22}$ fragment (with sequence KLVFFAE) of $A\beta$, which has been shown to be a key sequence in the formation of $A\beta$ oligomers and fibrils [27, 28, 29]. To this end, we performed two sets of all-atom MD simulations including (i) unbiased standard MD simulations of six $A\beta_{16-22}$ peptides in solution with and without crowders ($3 \times 1.5 \mu\text{s}$ for each system), and (ii) metadynamics simulations of two $A\beta_{16-22}$ peptides in solution with and without crowders ($1 \times 3 \mu\text{s}$ for each system).

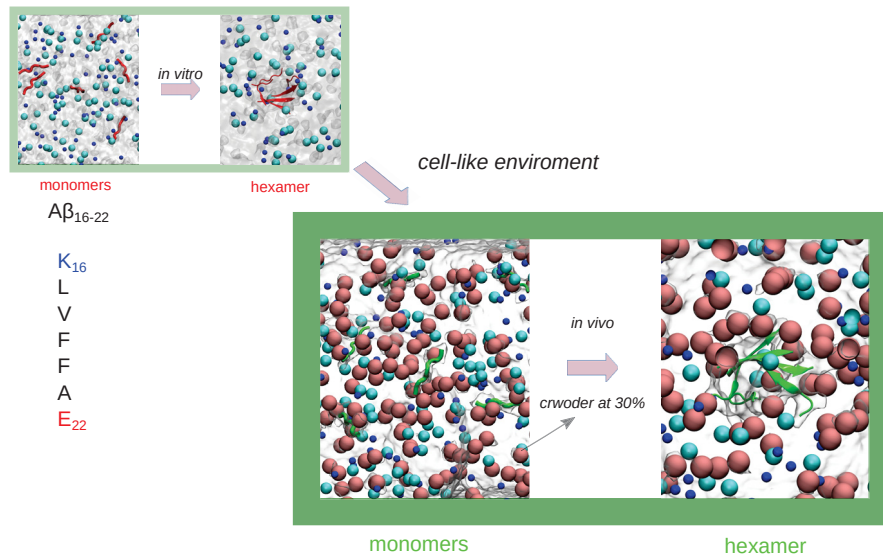


FIGURE 3.9: A schematic representation that illustrates the focus of the study involving $A\beta$ in the presence of macromolecular crowders.

In the simulations with crowders, the crowder was modeled as repulsive sphere of diameter 1.3 nm and added at 30% volume concentration together with the short fragment $A\beta_{16-22}$.

The first set of MD simulations enabled insight into the hexamer formation process in the crowded solution versus diluted solution. Our results revealed that the presence of crowders enhances the formation of the hexamer compared to its formation in diluted solution (Fig. 3.10A and B). Not only this, but also the peptide secondary structure is altered such that the β -sheet formation is enhanced (Fig. 3.10C). Snapshots of the last MD frame show that the resulting hexamers in diluted solution contain β -sheets with small numbers of residues per sheet and/or peptides with random coil conformation (Fig. 3.10D, top row) compared to the hexamers formed in the presence of crowder (Fig. 3.10D, bottom row).

The second set of our MD simulations, the metadynamics simulations, enables us to interpret the free energy surface associated with the transition from monomer to dimer both in the presence and absence of crowders. The two-dimensional free energy surface (2D-FES) as deduced from metadynamics simulations revealed that the presence of crowders drive the peptides to form dimers within a broad energy basin allowing for a structural ensemble of dimers compared to its more structurally restricted formation without crowders (Fig. 3.11A and B). This observation is further augmented considering the one-dimensional FES (1D-FES) (Fig. 3.11C and D) which reflects that the resulting

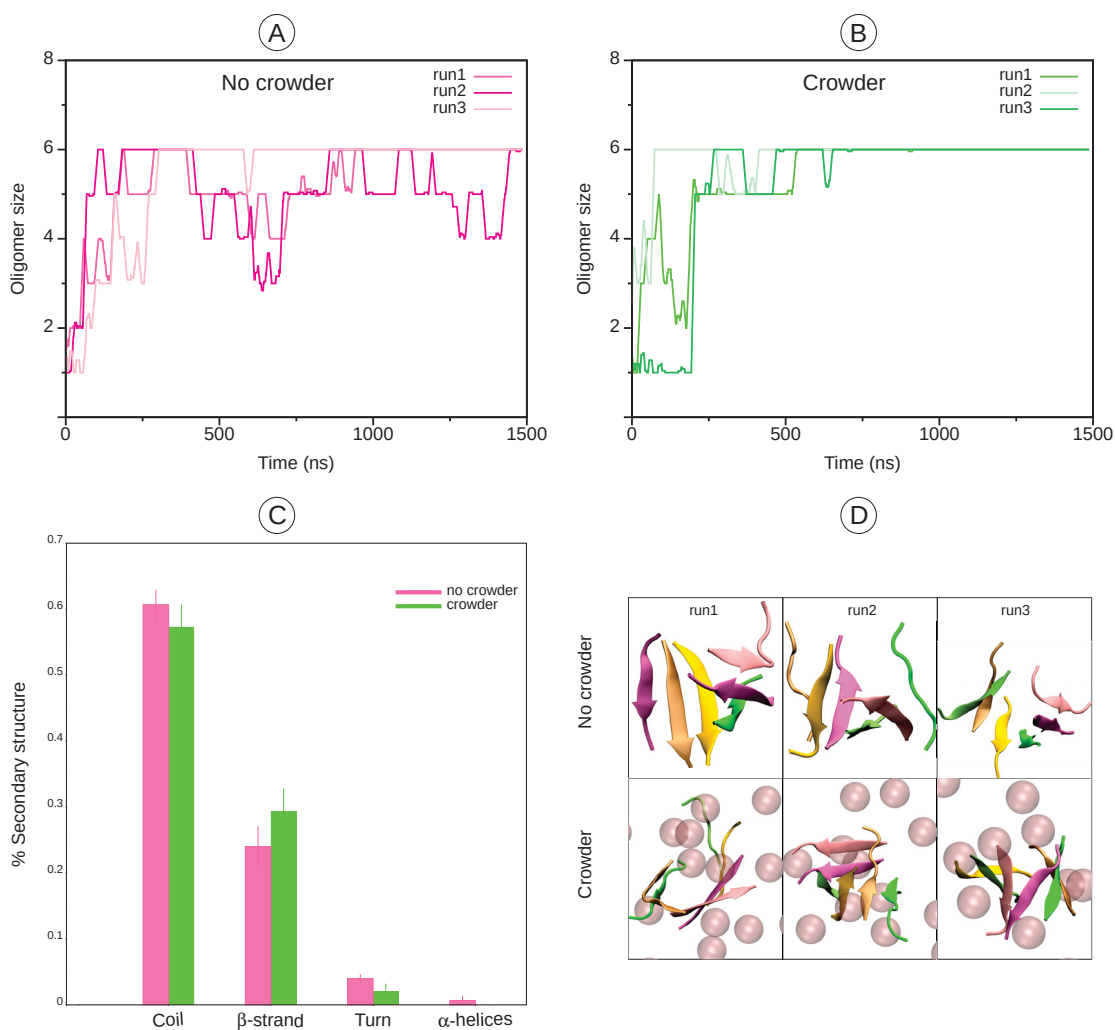


FIGURE 3.10: (A and B) The time evolution of the oligomerization state from each of the triplicate simulations of six $A\beta_{16-22}$ without crowders (left) and with crowders (right). The color of each run is indicated by the color code. (C) The average secondary structure content in the case of simulation without crowders (pink) and simulation with crowders (green). From left to right, the coil, the β -sheet, the bend-turn and the α -helical contents are shown. (D) Representative snapshots of the last frame from the simulation of six $A\beta_{16-22}$ with no crowders (top row) and the system with crowders (bottom row). $A\beta$ peptides are shown as cartoon and the crowders are indicated by light pink spheres.

dimer in the presence of crowders encounter deeper energy basins compared to a less well defined energy minimum for the dimer without crowders. Snapshots of the dimers from the energetically favorable regions are shown together with the 2D-FES at the top right corner.

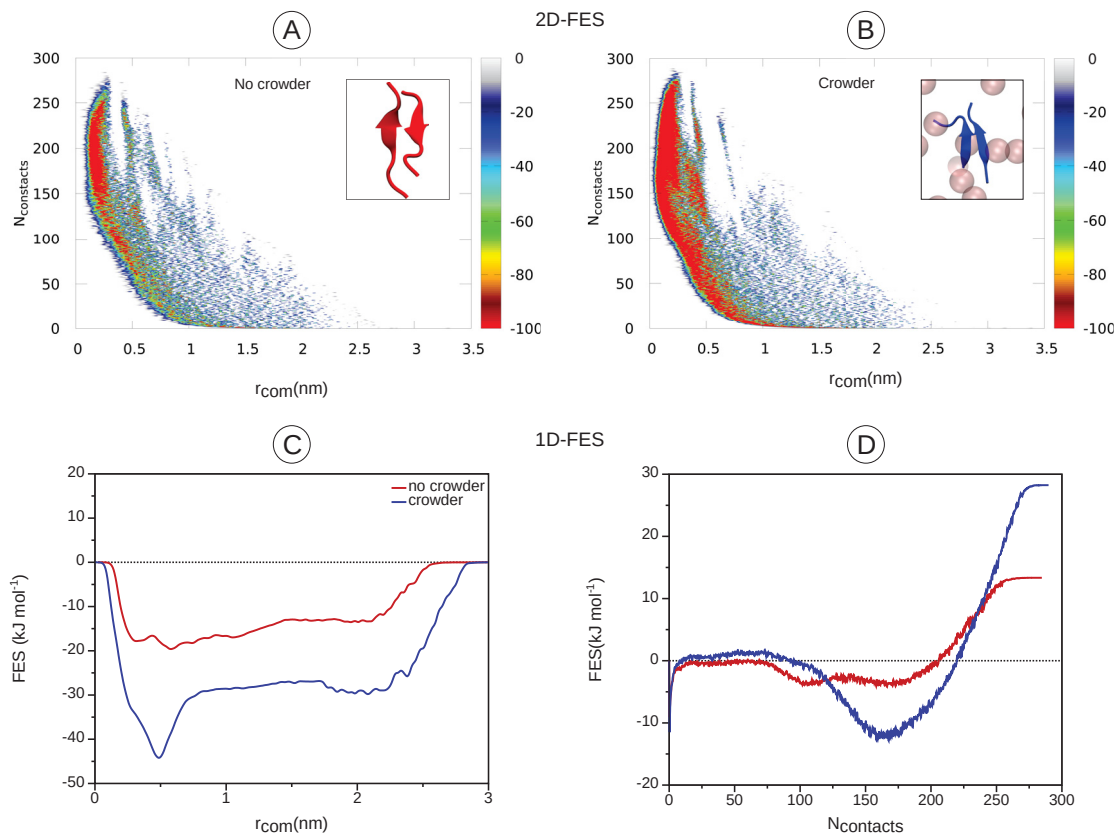


FIGURE 3.11: The 2D-FES (top row) calculated from metadynamics simulations of $A\beta_{16-22}$ simulated without crowders (A) and with crowders (B). The 1D-FES (bottom) is shown as a function of collective variables; the center-of-mass distance between peptide units (r_{com}) (C), and the number of contacts between the peptides (N_{contact}) (D).

3.4.3 Conclusion

It should be noted that this manuscript is under preparation, and the results shown here are preliminary, that more analysis is still to come to view the clear picture. Nonetheless, we believe that the unique contribution of this simulation study is that it provides atomistic insight into the molecular crowding effect on $A\beta$, which to the best of our knowledge has not been done yet. According to the current results, we conclude that the presence of crowders tends to enhance hexamer formation through forcing the peptides to collapse into oligomeric conformations quickly, which then evolve to hexameric β -sheet conformations toward the end of the simulation. The metadynamics simulation of the dimer further revealed that the presence of crowders enhances the formation of energetically favorable dimer structures. Combining both findings, we speculate that a possible scenario that may explain the crowding effect is that the presence of the crowders affects the interstitial space available for the peptides in a way that forces them to come

together quickly and form oligomeric species that is energetically favorable. In other words, the peptide adopts a state that minimizes the volume occupied by the peptides to commensurate to the excluded volume effect due to the presence of crowders.

3.5 Publication V: hIAPP and membrane binding

Structural dissection of the first events following membrane binding of the islet amyloid polypeptide

Khemtemourian L., **Fatafta H.**, Davion B., Lecomte S., Castano S., Strodel B. *Front. Mol. Biosci.*, 2022 Mar 15; 9:849979. doi: 10.3389/fmolb.2022.849979.

Original publication, see Publication V in section A.5. Contribution: execution and analysis of molecular dynamics simulations, producing the simulation-related figures, and writing part of the first draft of the paper.

3.5.1 Background

Increasing evidence suggests that the interaction of the human islet amyloid polypeptide (hIAPP) with lipids may facilitate hIAPP aggregation and cause the death of pancreatic islet β -cells in patients with type 2 diabetes [24, 281]. While the toxic activity of hIAPP is still not completely understood, a link between hIAPP fibril formation at the membrane interface and hIAPP-induced cell death was observed, highlighting the importance of the membrane in hIAPP-induced cell death. Along with these results, it has been recognized that the various amino acids of hIAPP are crucial in hIAPP fibril formation and in hIAPP-membrane interaction. The N-terminal part residues are mainly responsible for membrane binding, the middle core drives amyloid fibril formation, while the C-terminal residues are also involved in amyloid fibril formation yet to a lesser extent [282]. For that reason, it is essential to explore the sequence-amyloid and sequence-membrane binding relationships. The region 20-29, known as the amyloid-prone region that bears key differences of hIAPP from the non-amyloidogenic and non-toxic rat IAPP, is of relevance, but it is not the sole region governing IAPP fibril formation. Recent studies on residue 18, that is highly variable among species [283], indicate that this residue is important in modulating i) IAPP fibril formation in solution and in the presence of membranes [284,

285], ii) membrane interaction and damage [285], iii) cell toxicity [284], and iv) hIAPP-zinc and hIAPP-insulin affinity [286]. Thus, understanding the role of this residue in specific interactions of hIAPP with cell membranes is critical for elucidating the underlying pathogenesis of type 2 diabetes and this is the focus of this study.

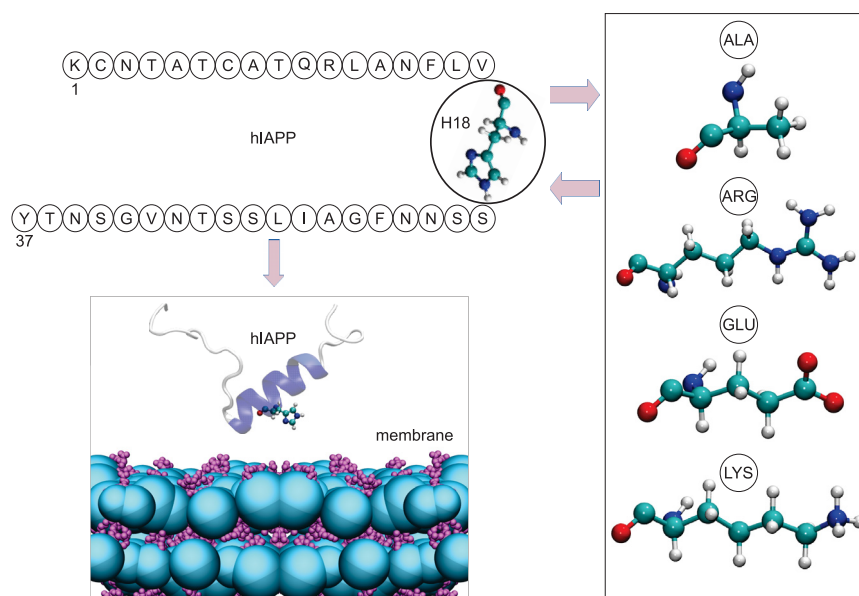


FIGURE 3.12: A schematic representation that illustrates the focus of the study involving the wild-type hIAPP and its variants, mutated at residue 18, in the presence of a DOPC:DOPS lipid membrane.

3.5.2 Results

The purpose of this study is to obtain structural information on IAPP at the membrane interface and to determine the role of histidine 18 in hIAPP-membrane interactions. We performed all-atom MD simulations on the microsecond time scale, in addition to Fourier-transform infrared (FTIR) spectroscopy and transmission electron microscopy (TEM) experiments performed by our collaborators, to assess the influence of residue 18. To this end, a wild-type hIAPP and variants of it with mutations H18A, H18E, H18K, and H18R, in the presence of a 1,2-dioleoyl-sn-glycero-3-phosphocholine/1,2-dioleoyl-sn-glycero-3-phospho-L-serine (DOPC:DOPS) lipid mixture (ratio 7:3), mimicking the eukaryotic β -cell membranes, were studied (see Fig. 3.12).

The FTIR spectra at different incubation times revealed an increment in the β -sheet content in all peptides but H18E, that was accompanied by a reduction in the random coil and α -helix content (Fig. 3.13A). This was further confirmed by TEM images that

revealed long and twisted fibrils in hIAPP and H18K-IAPP, short fibrils and small amorphous aggregates in H18R- and H18A-IAPP, while unstructured aggregates in the case of H18E were observed (Fig. 3.13B). Considering Fig. 3.13B, the fibrils and aggregates morphologies harbor the presence of antiparallel and parallel β -sheets, respectively. Furthermore, the FTIR results showed membrane disturbance upon hIAPP interactions but not in the presence of the mutants. Thus, we concluded that the β -sheet is needed for membrane disturbance, considering that hIAPP is the peptide with the largest amount of β -sheets.

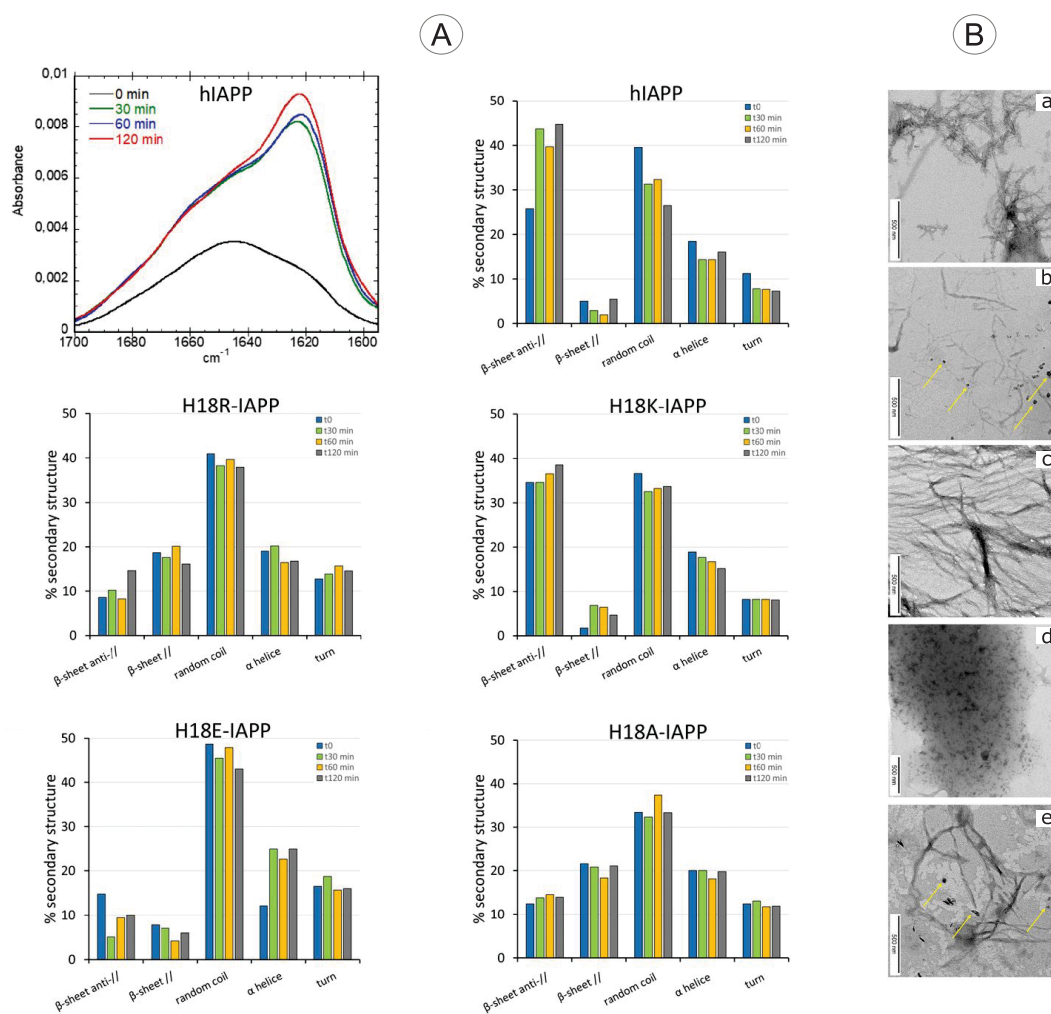


FIGURE 3.13: (A) Time-evolution (from 0 min, black, to 120 min, red) of the ATR-FTIR spectra of hIAPP. Secondary structure analysis for hIAPP and the mutated peptides as the figure label shows. The bars show the averaged content of secondary structures including antiparallel and parallel β -sheets, random coil, α -helices, and turns. (B) TEM image of (a) native hIAPP and the mutated peptides: (b) H18R-IAPP, (c) H18K-IAPP, (d) H18E-IAPP, and (e) H18A-IAPP incubated with DOPC/DOPS liposomes. The yellow arrows indicate the amorphous aggregates found for H18R-IAPP and H18A-IAPP. Scale bars represent 500 nm.

To gain more insights into the impact of residue 18, I performed all-atom MD simulations of the monomeric hIAPP and its mutants in the presence of a same lipid bilayer with the same composition as in the experiments. Our simulations revealed that all peptides approach the membrane via electrostatic interactions between the positively charged residues K1 and R11 and the negatively charged lipids DOPS, which is strengthened when there is a third positive charge at position 18, as seen for H18K- and H18R-IAPP but not hIAPP(H18+) (Fig. 3.14A). We thus concluded that also the size and/or flexibility of the side chain at residue 18 plays a role in affecting peptide-membrane interactions. In addition, the membrane-bound IAPP adopted a helical conformation, which is higher in hIAPP mutants than in hIAPP (Fig. 3.14B). The helical region in the case of H18K- and H18R-IAPP was able to insert just below the headgroups with the hydrophobic residues, whereas the hydrophilic residues directed toward the aqueous phase ((Fig. 3.14C)). This orientation was stabilized by the long and the flexible side chains of K1, R11, and K18 or R18. Nonetheless, our results showed that this insertion slightly affects the membrane thickness around the peptide but does not change the lipid tail order.

3.5.3 Conclusion

The results of this study provide valuable molecular-level insight of the initial IAPP-membrane interactions. Our results revealed that the initial membrane-anchoring occurs via a helix in the N-terminal half of the peptide, as revealed from our MD simulations. This helix turned out to be very stable and resists the transformation into β -sheets, as the FTIR results at different incubation time showed that some residues remained in a helical conformation with a contribution of 15-20%. The membrane disturbance by hIAPP as revealed by FTIR spectroscopy correlates with the toxicity of this peptide. Thus, we concluded that cytotoxicity and the presence of antiparallel β -sheet structures are connected to each other in IAPP. This also led us to conclude that H18E-IAPP, characterized by a reduced β -sheet formation and a high helical content, is the least toxic H18 mutated peptide that we studied.

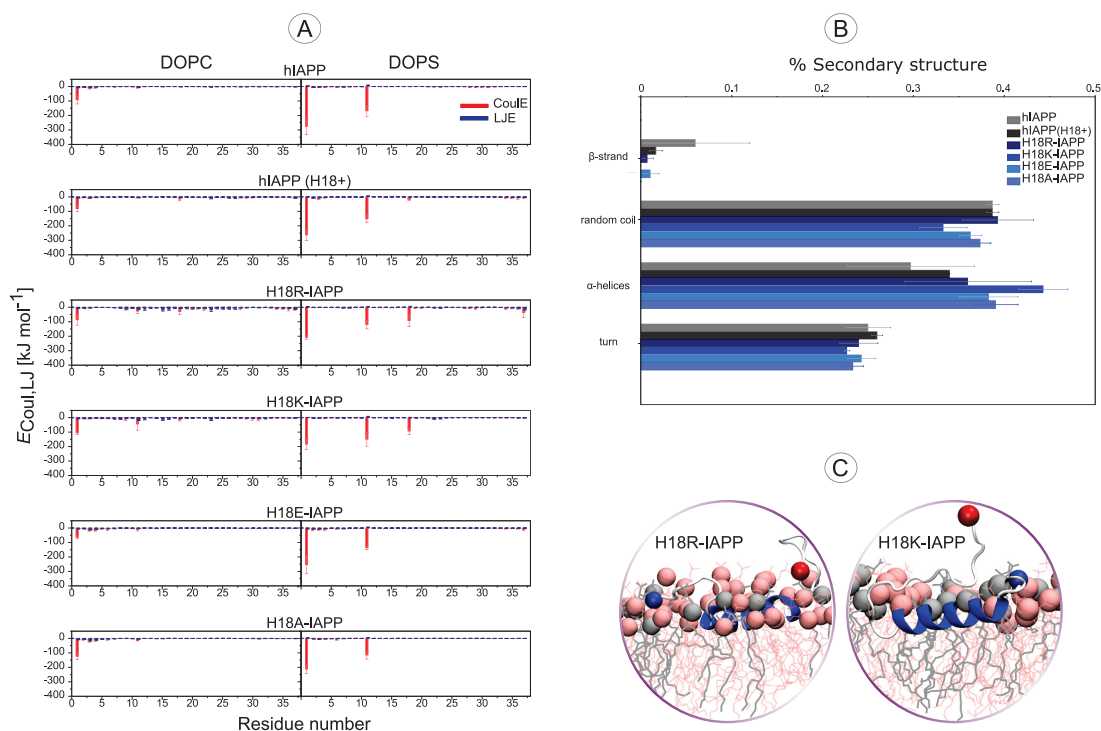


FIGURE 3.14: (A) The average interaction energies (and standard error) of IAPP interacting with DOPC (left) and DOPS (right) lipids. Electrostatic and Lennard-Jones energies are shown in red and blue, respectively. Negative energies indicate attractive forces, positive energies correspond to repulsion. (B) The average secondary structure content (and standard error) in IAPP in the presence of a DOPC/DOPS membrane as obtained from MD simulations. (C) Representative structures of H18R- and H18K-IAPP interacting with the DOPC/DOPS membrane. The peptide is shown as cartoon (with helix, β -sheet and coil being shown in blue, red and white, respectively), with their N- and C-termini being indicated as blue and red spheres, respectively. DOPC and DOPS lipids are shown as pink and gray sticks, respectively, with their P atoms indicated by spheres of the corresponding color.

Chapter 4

Conclusions

In this thesis, we have successfully used MD simulations to model the real environment conditions in studying amyloid proteins. Herein, the computational investigations aimed at modeling two IDPs; the $A\beta$ peptide which is associated with the development and progression of AD, and the hIAPP peptide that it is associated with type 2 diabetes. A common characteristic of these diseases is the aggregation of the respective peptides into structured amyloid fibrils. Though the linkage between these protein aggregates and the devastating disease has been well established over the years, the aggregation mechanism remains elusive. Thus, understanding the aggregation mechanism has become a subject under intense investigation, with the focus being on the emergence of the most toxic species; the amyloid oligomers. To date, most of studies published on amyloid aggregation did not consider the full complexity of the biological environment that plays a crucial role in tuning the aggregation process. Investigating the effects of *in vivo* conditions on $A\beta$ and hIAPP is the main focus in the MD studies of this thesis, toward enhancing the knowledge about these peptides and their role in the development of the associated diseases.

In the simulation studies mentioned in chapter 3, I focused on mimicking four major aspects from the brain or the pancreatic β -cell environment while performing the computer simulations, such as resembling the lipid composition of the neuronal cell membrane or the pancreatic β -cell, examining the oxidative-stress effect commonly associated with neurodegenerative disease, the effect of free lipids in the aqueous phase as a protein

interaction partner, and also the macromolecular-crowding effect. For $A\beta$, we successfully simulated at atomistic level a complex model lipid bilayer consisting of six lipid components (38% POPC, 24% POPE, 5% POPS, 20% CHOL, 9% SM, and 4% GM1) to mimic the neuronal membrane composition, which to the best of our knowledge had not been simulated yet. Furthermore, we employed this lipid bilayer model to study the smallest $A\beta_{42}$ oligomer, i.e. the $A\beta_{42}$ dimers, which is difficult to follow experimentally. In this study, we revealed GM1 from the neuronal membrane to be the main lipid interaction partner of $A\beta_{42}$, and further showed the self-clustering of GM1 in the neuronal membrane. These findings support previous reports on the neuroprotective role played by GM1, especially when considering that the close interaction of the dimer with GM1 hindered to some extent the β -sheet formation and reduces $A\beta_{42}$ order in comparison to dimerization in solution. Additionally, with all-atom MD simulations of the dimer in solution at the microsecond time scale, we were able to capture the structural transitions underwent by $A\beta_{42}$ upon dimer formation –from random coil to β -sheet confirmation– that we believe it is on pathway toward forming amyloid fibrils.

The findings regarding GM1 was also reported in the study of oxidative stress where different variants of $A\beta_{42}$ monomer oxidized at Gly25, Gly29 or Gly33 and the wild-type peptide, was simulated in the presence of a simple lipid bilayer comprised of three lipid components, 70% POPC, 25% cholesterol, and 5% of the ganglioside GM1. Similarly, this study showed the preference of the $A\beta_{42}$ monomer to bind the sugar groups of GM1 over POPC, independent of the $A\beta_{42}$ oxidation state. However, the binding was more pronounced once the residue Gly29 or Gly33 was oxidized, which seems to be correlated with a reduced β -sheet formation in these two cases compared to the the other two variants. According to our observation, we suggested that $A\beta_{42}$ with oxidized Gly25 residue is as toxic as wild-type $A\beta$, considering β -sheet formation as a marker of toxicity. This study emphasizes that the oxidation underwent by $A\beta$ itself is affecting both its conformation and interaction with the membrane in a way that is dependent on the position of the oxidized glycine residue in the $A\beta$ sequence and on the lipid interaction partner from the membrane. Additionally, the simulation study of $A\beta$ interacting with free lipids in the aqueous phase provided atomic insight into the disorder-to-order transition underwent by $A\beta$, via folding into a helical or β -sheet conformation upon binding to a sufficient number of lipid molecules, a process that we referred to as “complex formation”. A similar observation we also reported upon

dimer formation of A β 42 in solution, which is characterized by a random coil to β -sheet transition. This led us to conclude that A β 's hydrophobicity is not sufficient for its folding by itself, but it can do so following its binding to a hydrophobic interaction partner. This finding is in line with the typical behavior reported for IDPs where conformation switching can be induced by binding of an IDP to an interaction partner such as other proteins, or small molecules.

In the study of A β -lipid complex formation, we also revealed that the lipid molecule bound to A β encourages the peptide to fold into helical conformation once it is binding to a membrane, which dips a bit deeper into the membrane than A β alone, and this might be the first step for membrane insertion. Though the peptide is not fully inserted, the complex seems to be playing a role toward reducing energy barrier for peptide insertion. Keeping this mind, we can conclude that in the other two studies where we observed a close interaction of the peptide with the lipid bilayer, but not insertion is probably due to the fact that the peptide is initially driven by electrostatic interaction to the membrane; and once it is on the membrane surface then it is mainly occupied by the bulky GM1 sugar groups, which in turn reduces the peptide order and attenuates its propensity to fold, which altogether seems to increase the energy barrier toward membrane insertion by A β .

In the study of the macromolecular crowding effect on A β _{16–22} aggregation, particularly the dimer and hexamer formation was studied. The main goal was to follow the oligomerization mechanism in a crowded (concentrated) environment resembling the cell-like conditions. Similar to the neuronal membrane study (Publication I), this study focuses also on the oligomeric species of the A β peptide, as the most toxic species, toward better understanding of AD development. Here, we were able to shine light on the macromolecular crowding effect on A β at the atomistic level of detail, which to the best of our knowledge had not been simulated yet. Furthermore, the usage of standard unbiased MD simulations together with the metadynamics technique enable us to explore the aggregation mechanism (at the hexameric level) and the associated free energy surface (at the dimeric level). A manuscript is under preparation; nonetheless, our preliminary results revealed that oligomer formation, for both dimer and hexamer, is enhanced by the presence of the crowding agents. From the view point of metadynamics, the dimers in the crowded solution are energetically more favorable (i.e. encountered a deeper energy basin) than in the diluted solution. Thus, we speculate that in response

to the addition of crowding agents, the peptide adopts a state that minimizes the overall crowding effect on the peptide. For example, in the case of six $A\beta_{16-22}$, we found that the peptides assemble quickly into tetramers/pentamers to minimize the volume occupied by the peptides.

The simulation study in which we assessed the interaction of monomeric hIAPP wild-type and its variants (H18A, H18K, H18E, H18R) with a lipid bilayer supports our observation from the $A\beta$ studies regarding the role of the hydrophilic interaction in driving close IAPP interaction with the DOPC:DOPS membrane. Moreover, the MD simulations revealed that membrane binding induced the formation of an amphipathic helix in all five-peptides, that we hypothesized to be an intermediate on the way to IAPP amyloid aggregation. Different to $A\beta_{42}$, we observed insertion into the membrane of the helix formed in H18K- and H18R-IAPP. Our simulations were accompanied by experiments performed by our collaboration partners. These experiments confirmed that the membrane-bound helix is indeed a precursor to amyloid aggregation, which occurred in all peptides but H18E-IAPP. This β -sheet formation was accompanied by a reduction in the random coil and α -helix contents. Nonetheless, the helical content remained at 15-20% of the structure. The joint analysis from MD simulations and experiments at the monomeric and aggregate level thus suggests that the membrane binding initially occurs via the helical conformation, which is on pathway to amyloid formation such that once the aggregated IAPP is interacting with the membrane then the peptide is triggering parallel or antiparallel β -sheet formation dependent on the primary sequence. This study emphasizes the relevance of residue 18 in (de)stabilizing the IAPP fibrils which in turn can be a possible target toward inhibiting its toxicity.

In the light of our findings, it is worth mentioning that the all-atom MD simulation technique, similar to any other investigation technique, suffers from its own limitations, such as the high computing time demand that limits the time scales that can be reached by simulations. This needs to be considered while designing a simulation study in order to make reasonable use of it. Enhancement methods have been introduced to the MD method that enable overcoming these limitations, such as HREMD and MetaD, which were also implemented in some of our studies. Nonetheless, all-atom MD simulations employed by our studies provide a detailed microscopic view of the systems under investigation, which prove its usefulness when it comes to study systems of biological

relevance. As a step forward, it is recommended to connect to experimental studies, if time and conditions permit, for a broader perspective.

I believe that the simulation studies presented in this thesis will serve as a template that motivates further studies to address more challenging issues in the field of amyloid proteins in their real biological environment. These studies provide a primary nucleus toward solving the puzzle around amyloid aggregation and its connection to disease, and maybe advancing a possible therapeutic.

Appendix A

Published Articles

A.1 Publication I

Amyloid- β peptide dimers undergo a random coil to β -sheet transition in the aqueous phase but not at the neuronal membrane

Fatafta H., Khaled M., Owen MC., Sayyed-Ahmad A., Strodel B. PNAS., 2021 Sep 28; 118(39):e2106210118. doi: 10.1073/pnas.2106210118.



Amyloid- β peptide dimers undergo a random coil to β -sheet transition in the aqueous phase but not at the neuronal membrane

Hebah Fatafta^a, Mohammed Khaled^a, Michael C. Owen^{b,c}, Abdallah Sayyed-Ahmad^d, and Birgit Strodel^{a,e,1}

^aInstitute of Biological Information Processing (IBI-7: Structural Biochemistry), Forschungszentrum Jülich, 52425 Jülich, Germany; ^bCentral European Institute of Technology, Masaryk University, Brno 625 00, Czech Republic; ^cInstitute of Chemistry, University of Miskolc, 3515 Miskolc-Egyetemváros, Hungary; ^dDepartment of Physics, Birzeit University, 71939 Birzeit, Palestine; and ^eInstitute of Theoretical and Computational Chemistry, Heinrich Heine University Düsseldorf, 40225 Düsseldorf, Germany

Edited by Gerhard Hummer, Max Planck Institute for Biophysics, Frankfurt am Main, Germany, and accepted by Editorial Board Member Angela M. Gronenborn August 16, 2021 (received for review March 31, 2021)

Mounting evidence suggests that the neuronal cell membrane is the main site of oligomer-mediated neuronal toxicity of amyloid- β peptides in Alzheimer's disease. To gain a detailed understanding of the mutual interference of amyloid- β oligomers and the neuronal membrane, we carried out microseconds of all-atom molecular dynamics (MD) simulations on the dimerization of amyloid- β (A β)₄₂ in the aqueous phase and in the presence of a lipid bilayer mimicking the in vivo composition of neuronal membranes. The dimerization in solution is characterized by a random coil to β -sheet transition that seems on pathway to amyloid aggregation, while the interactions with the neuronal membrane decrease the order of the A β ₄₂ dimer by attenuating its propensity to form a β -sheet structure. The main lipid interaction partners of A β ₄₂ are the surface-exposed sugar groups of the gangliosides GM1. As the neurotoxic activity of amyloid oligomers increases with oligomer order, these results suggest that GM1 is neuroprotective against A β -mediated toxicity.

Alzheimer's disease | amyloid- β | neuronal membrane | molecular dynamics | transition network

In Alzheimer's disease (AD), amyloid- β peptide (A β) aggregates into fibrils and subsequently accumulates as plaques within the neural tissue (1). An increasing number of studies suggest that the smaller soluble oligomers formed in the earlier stages of the aggregation process are the main cytotoxic species affecting the severity and progression of AD (2–4). A β dimers have been reported to be the smallest toxic oligomer that affects synaptic plasticity and impairs memory (5, 6). Therefore, a detailed characterization of A β dimerization is an essential step toward developing a better understanding of the aggregation process. However, its transient nature (resulting from its high aggregation tendency), its plasticity, and its equilibrium with both the monomer and higher-order oligomers all make the A β dimer extremely challenging to study experimentally. In fact, a large amount of the experimental studies performed on A β dimers employ some kind of cross-linking to stabilize them (7–9). On the other hand, covalently cross-linked A β dimers are certainly of biological relevance, as such species have been retrieved from the brains of AD patients and their neurotoxicity has been demonstrated (6, 10). Apart from this, recent technological developments, such as advanced single-molecule fluorescence spectroscopy and imaging, opened the way to characterize amyloid oligomers without the need to stabilize them by cross-linking (11, 12). Molecular dynamics (MD) simulations are also able to provide atomic insight into the temporal evolution of the dimer structure without the need of cross-linking (13, 14). Previous simulations of A β dimers were modeled in the aqueous phase only, and thus they lacked essential details from the cellular context. Consideration of the latter is particularly important if one wishes to reveal the mechanism of toxicity that has

been shown to rely on direct contact with the lipid membrane of neurons by A β oligomers (15, 16).

Many studies have been done to understand the consequences of A β -membrane interactions; however, it is extremely difficult to capture these transient interactions with experimental methods. This becomes possible with MD simulations and this problem is addressed in the current work. We use an aggregate of 24 μ s of MD simulations to investigate the dimerization of the full-length A β ₄₂ peptide both in solution and in the presence of a model lipid bilayer including six lipid types to mimic the composition of a neuronal cell membrane (17–19): 38% 1-palmitoyl-2-oleoyl-sn-glycero-3-phosphocholine (POPC), 24% 1-palmitoyl-2-oleoyl-sn-glycero-3-phosphoethanolamine (POPE), 5% 1-palmitoyl-2-oleoyl-sn-glycero-3-phospho-L-serine (POPS), 20% cholesterol (CHOL), 9% sphingomyelin (SM), and 4% monosialotetrahexosylganglioside (GM1) (Fig. 1A). For modeling A β we employ Charmm36m, a force field adjusted for intrinsically disordered proteins (IDPs), to model their preference to adopt extended structures. When applied to monomeric A β , Charmm36m yields more than 80% of the structures in a random coil and extended

Significance

The aggregation of the amyloid- β peptide (A β) into neurotoxic oligomers is central to the development of Alzheimer's disease. One possible source of their toxicity results from interactions of the A β oligomers with the neuronal membrane, damaging membrane integrity and thus neurons. However, molecular details of these interactions are unclear. Here, we contrast the dimerization of A β in solution and at the neuronal membrane. Our results clearly indicate that the sugar moieties of GM1 sequester A β by forming key hydrogen bonds with the peptide, which diverts the configuration of the A β dimers away from damaging β -sheet-rich structures. These findings underline the importance of GM1 in Alzheimer's disease progression and provide a nanoscopic basis for its reported neuroprotective effect.

Author contributions: H.F., M.C.O., and B.S. designed research; H.F., M.K., and M.C.O. performed research; H.F., M.K., and M.C.O. analyzed data; H.F., A.S.-A., and B.S. wrote the paper; and A.S.-A. and B.S. supervised the work.

The authors declare no competing interest.

This article is a PNAS Direct Submission. G.H. is a guest editor invited by the Editorial Board.

This open access article is distributed under Creative Commons Attribution-NonCommercial-NoDerivatives License 4.0 (CC BY-NC-ND).

¹To whom correspondence may be addressed. Email: b.strodel@fz-juelich.de.

This article contains supporting information online at <https://www.pnas.org/lookup/suppl/doi:10.1073/pnas.2106210118/-DCSupplemental>.

Published September 20, 2021.

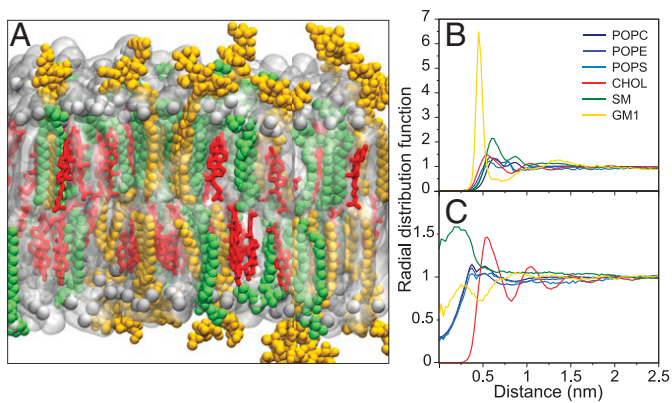


Fig. 1. (A) A snapshot of the neuronal membrane containing 38% POPC, 24% POPE, 5% POPS (collectively shown as gray surface with their phosphorous atoms indicated by gray spheres), 20% CHOL (red sticks), 9% SM (green spheres), and 4% GM1 (yellow spheres). In the following, PC, PE, and PS are synonymously used for POPC, POPE, and POPS, respectively. (B and C) Radial distribution functions for (B) lipid pairings of identical type and (C) lipid-CHOL pairings. The P atoms of PC, PE, PS, and SM and the O atoms of CHOL and GM1 were used as reference atoms for the RDF calculations. The RDFs are averaged over both membrane leaflets. The x axis shows the distances between the respective atom pairs. Since CHOL resides deeper inside the membrane, it is possible that the O atom of CHOL and the reference atoms of the other lipids are above each other, explaining why not all of the RDFs approach zero for $x=0$. The colors of the functions refer to the lipids as indicated in the color key in B. Pairs with RDF > 1 are considered to form clusters.

state, and the remaining ones feature transient β -hairpins, which is in acceptable agreement with experimental data (20). Moreover, Charmm36m outperforms other force fields when it comes to modeling peptide aggregation (21, 22). To the best of our knowledge, this simulation study breaks ground on two fronts: 1) It exceeds the simulation time of previous studies modeling $A\beta$ -membrane interactions by an order of magnitude, and 2) it studies the aggregation of $A\beta$ on a bilayer containing more than three different lipid types. Lipid bilayers of a complexity comparable to the one modeled here have been thus far studied only at the coarse-grained level (23, 24). We also analyze the aggregation pathways by transition networks (25–27), which elucidate the similarities and differences between $A\beta$ dimerization steps both in solution and at the neuronal membrane. We find that the neuronal membrane reduces the dynamics of membrane-bound $A\beta_{42}$ while it also inhibits β -sheet formation. Here, the sugar groups of GM1 form hydrogen bonds with the peptide, thereby reducing the possibilities for other hydrogen bonds to otherwise form. In contrast, the dimerization in the aqueous phase is characterized by a random coil to β -sheet transition, leading to β -sheet structures similar to the ones found in $A\beta$ fibrils.

Results

The Neuronal Membrane Is in a Liquid Ordered Phase. Before we analyze the interaction of $A\beta$ with the neuronal membrane, we determine the characteristics of the latter. The mass density profile of each lipid and water along the membrane z axis (*SI Appendix, Fig. S1*) shows the distribution of the bilayer components, as well as the bilayer thickness. The positions of the headgroups are at similar locations for POPC (PC), POPE (PE), POPS (PS), and SM. CHOL, on the other hand, is shifted toward the hydrophobic core of the bilayer, while GM1 is farther away from the bilayer center, due to the protrusion of the sugar groups from the xy surface of the membrane (Fig. 1A). The headgroup-to-headgroup distance of PC, PE, and PS indicates a bilayer thickness of 4.65 ± 0.03 nm.

We calculated the acyl chain order parameter S_{CH} of the C–H bonds of all the lipid tails (*SI Appendix, Fig. S2*) to gain insight into their arrangement within the membrane. Values of 0.35 to 0.4 for the order parameters of carbon atoms 4 to 10 are reached, which is an increase compared to the order parameters found in other membranes (28, 29). This is due to the effects of cholesterol and sphingomyelin, which are known for their role in increasing lipid order. Notably, we find the acyl chains of GM1 and SM to be the most ordered. We can thus conclude that the neuronal membrane is in the liquid-ordered state, which is in agreement with previous observations (24, 30).

GM1 Forms Ganglioside Clusters. The radial distribution function (RDF) of all possible lipid pairings was calculated to monitor the effect of these pairwise interactions on lipid clustering (Fig. 1B and C and *SI Appendix, Fig. S3*). A distinct RDF peak is seen at ≈ 0.45 nm for the self-clustering of GM1 and pronounced peaks are seen at 0.55 and 0.6 nm for the formation of CHOL and SM clusters, respectively, while all other lipids do not tend to self-associate. The self-clustering of GM1 is considerably stronger than that of the other lipids. Thus, taking the relatively low concentration of GM1 (4%) into account, one can conclude that GM1 has a strong tendency to self-associate that can result in its sorting. No strong clustering between mixed lipid pairs is observed. Notable coassociation is seen only for SM with POPE, CHOL, and GM1. Interestingly, the RDF of PE–PS has a higher peak compared to that of PE–PE and PS–PS, respectively. The dispersion of PS is understandable given that it is negatively charged. The negative charge of both GM1 and PS also explains why these two lipids avoid coclustering.

To elucidate the dominant lipid–lipid interactions underlying the RDFs, the average numbers of hydrogen bonds (H bonds) between the different lipid pairs were evaluated. *SI Appendix, Fig. S4* shows that the sorting of GM1 results from its ability to build a network of H bonds via its sugar headgroups, despite its negative charge. The propensity of SM to form H bonds with itself also gives rise to its self-clustering, whereas the minor self-clustering seen for CHOL is a result of the cholesterol condensing effect. This effect does not result from attractive van der Waals interactions between CHOL molecules, but from a reduced membrane perturbation energy if small cholesterol domains are formed (31). However, such cholesterol clusters are not particularly stable, as evidenced by only a small peak in the RDF for CHOL–CHOL. The coclustering of CHOL and SM is facilitated by H bonds formed between the hydroxyl of CHOL and the amide group of SM, which agrees with previous findings (32). The RDF profile of SM–GM1 can also be explained by H-bond formation. We conclude that H bonds play an essential role in stabilizing lipid clusters within the neuronal membrane.

$A\beta_{42}$ Dimerizes at the Neuronal Membrane and Interacts with GM1.

To understand the effects of the neuronal membrane on the aggregation of $A\beta_{42}$, we analyzed the $6 \times 2 \mu\text{s}$ of MD data in the presence of the lipid bilayer and compared the aggregation to the $6 \times 2 \mu\text{s}$ of MD simulations done in the aqueous phase. We first assess whether and how the two peptides bind to and interact with the membrane.

To follow the association between $A\beta_{42}$ and the neuronal membrane, we calculated the minimum distance of both peptides from the lipid bilayer surface for each of the six simulations (*SI Appendix, Fig. S5*). It can be seen that peptide 1 usually interacts with the membrane at a closer distance than peptide 2 does, which can be explained by the fact that the initial structures of five of the six simulations were selected from the initial 2- μs simulation. This allows us to better elucidate the effects of the membrane on the preferentially membrane-bound

peptide as their mutual interaction time is larger than it would have been if both peptides had the same interaction probability. Nonetheless, both peptides tend to be associated with the membrane as an intact dimer, since if one peptide is >0.5 nm away from the membrane, implying that this peptide is in solution, then very often this is also the case for the other peptide. Fig. 2 shows representative snapshots for the membrane association of A β 42, including one for loose binding in Fig. 2A. Fig. 2B represents the situation where peptide 1 is in close contact with the membrane, while peptide 2 is a bit farther away. The opposite, less prevalent situation with peptide 2 being closer is depicted in Fig. 2C and is less common, while Fig. 2D shows how both peptides can bind tightly to the membrane. Fig. 2 further suggests that A β 42 tends to interact with GM1 instead of the other lipids and that β -sheets are the dominating secondary structure in peptide 2 but not in the more membrane-bound peptide 1. The analysis of the contacts between A β 42 and the various lipids confirms that the peptide has a high tendency to associate with GM1, followed by PC, PE, and PS (SI Appendix, Fig. S6). Here, we emphasize that these contacts are not normalized but absolute values. Considering that only 4% of the lipids are GM1 while the phospholipids make up for more than two-thirds of the membrane, one can thus conclude that A β 42 is highly attracted to GM1. Interestingly, almost no contacts are made with CHOL or SM.

To rationalize the driving force that controls A β 42 interaction with the membrane surface, the interaction energy of each A β 42 residue with each of the lipid components was calculated and partitioned into its electrostatic (E_{Coul}) and Lennard-Jones (E_{LJ}) contributions (Fig. 3). Notably, the lipid interactions of peptide 1 are more favorable than those of peptide 2, agreeing with the observation that peptide 1 interacted more strongly with the membrane. Our results suggest that the major driving force for the association of the peptides to the membrane is the electrostatic attraction to PC, PE, and PS, especially via the highly charged N-terminal region and residues F20 to A30. Residues at the N terminus had the strongest interactions with the membrane, such as D1, E3, and D7 with PE; D1 with PC; and R5 with PS. The latter interaction involves H-bond formation (SI Appendix, Fig. S7), which is enabled via the carboxylate group of PS, whereas the primary ammonium group of PE forms H bonds with D1, E3, and D7. The tertiary ammonium group of PC, on the other hand, does not support H-bond formation, leading to a relatively low H-bond propensity between PC (via its phosphate group) and A β 42. The interactions between GM1 and A β 42 are driven by both Coulomb and Lennard-Jones energies (Fig. 3) and are facilitated by the sugar headgroups of GM1, which protrude

from the membrane and are therefore particularly accessible to A β 42. Moreover, the interactions with GM1 derive from a considerable number of H bonds, which involve almost all residues of both peptides, but particularly those of peptide 1.

No direct interaction between A β 42 and CHOL was observed (SI Appendix, Fig. S6), due to the deeper, unexposed position of CHOL within the membrane. Interestingly, even though SM has the same headgroup as PC, which is also located at a similar position along the bilayer normal, A β 42 hardly interacted with SM. This can be understood by considering the preference of SM to form H bonds with other lipids including itself, which reduces its tendency to create H bonds with the peptide.

The A β 42 Dimer Does Not Affect the Neuronal Membrane. To determine whether the peptides affect the structure of the lipid membrane, we calculated the lipid order parameter for the lipids that are within 0.5 nm of the peptide when adsorbed to the membrane (SI Appendix, Fig. S2). The results suggest no notable change in the lipid order parameter due to the interactions with A β 42. Moreover, only a slight deviation of about ± 0.1 nm was seen in the bilayer thickness (SI Appendix, Fig. S8) at the site of peptide interaction. We thus conclude that the peptides interact only with the lipid headgroups without inserting into the membrane, thereby preventing larger changes in the membrane order and thickness.

Different Aggregation Pathways in Solution and at the Neuronal Membrane. To unravel differences within the aggregation pathways, we computed transition networks (TNs) for the A β 42 dimerization both in the aqueous phase and in the presence of the neuronal membrane. To this end, we characterized the conformations by assigning the aggregate state (monomer or dimer), the number of hydrophobic contacts between the peptides in a dimer, and the number of residues in β -strand conformation as descriptors. To further simplify the TNs, we grouped both the number of hydrophobic contacts and the number of residues in β -strand conformation in blocks of five such that we end up with ranges h1 to h12 and b1 to b6. For example, h1 and b1 stand for hydrophobic contacts and the number of residues in β -strand conformation, respectively, ranging from 1 to 5. The maximum state h12 involves between 56 and 60 hydrophobic contacts and the b6 state means that between 26 and 30 residues per peptide adopted a β -strand conformation.

The resulting TNs (Fig. 4) are characterized by two regions: the monomeric region (on the left side of the TNs) and the dimeric region (in the middle and the right side of the TNs), where the former evolves into the latter. These regions are

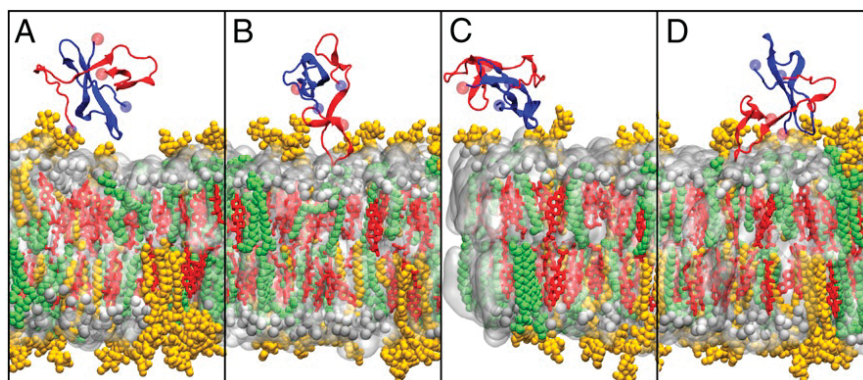


Fig. 2. Snapshots of A β 42 interacting with the neuronal membrane. Peptide 1 and peptide 2 are shown as cartoons in red and blue, respectively, with their termini indicated by spheres (N, light blue; C, light red). The color coding for the membrane is the same as in Fig. 1A. Representative interaction patterns are provided: (A) both peptides being loosely attached to the bilayer surface, (B) peptide 1 being in close interaction with the membrane and peptide 2 being bound to peptide 1, (C) the opposite situation to that in B, and (D) both peptides being in close contact with the membrane.

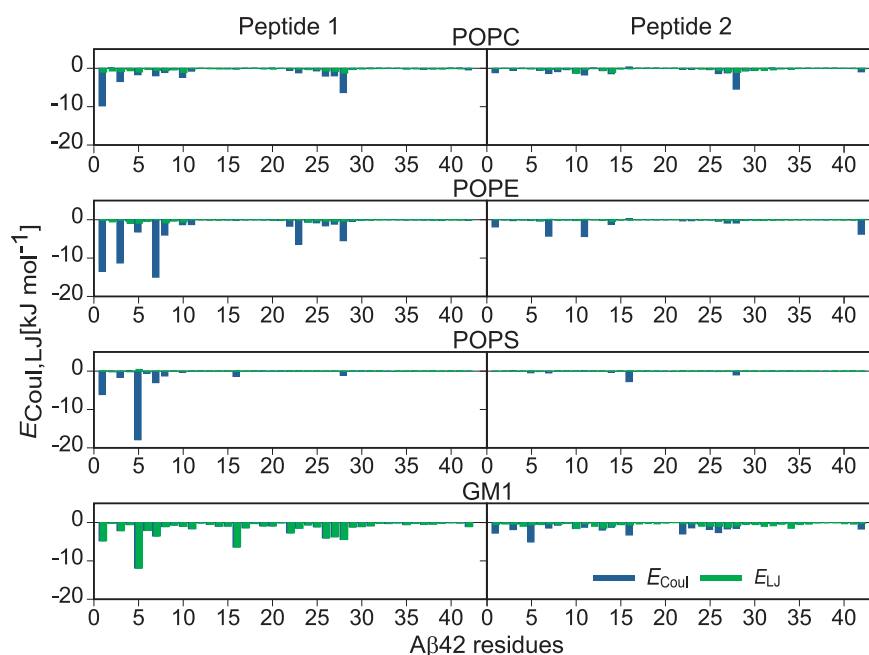


Fig. 3. The average interaction energies of peptide 1 (Left) and peptide 2 (Right) with each lipid of the neuronal membrane. Electrostatic and Lennard-Jones energies are shown in blue and green, respectively. The more negative an energy is, the more attractive is the corresponding interaction.

connected by several bridging nodes, which, on average, are characterized by a higher amount of β -sheet (i.e., larger n in the descriptor b_n) in the case of the solution system. In both TNs, a representative bridging node is indicated by a green circle, [2, h2, b6] for the solution system and [2, h2, b2] for the membrane system, which are further augmented by a characteristic structure. In solution, there are more transitions between monomers and dimers, which indicates a higher number of association and dissociation events. In general, the TN for the solution system exhibits more nodes and transitions.

A closer inspection of both TNs reveals how the two peptides evolve from the monomeric random coil state, which is represented by node [1, 0, 0] with no interpeptide hydrophobic contacts and no residues in β -strand conformation, to dimers with only a few hydrophobic contacts, as present in states [2, h1, b_n]. Here b_n ranges from b_1 to b_6 , indicating an increase in β -strand content as the structure changes along the path through nodes [1, 0, b_n] and [2, 0, b_n]. The dimers with no hydrophobic contacts are so-called encounter complexes, where the minimal distance between the two monomers fell below 4.5 nm, and subsequently form stable dimers by increasing their contact area as interpeptide contacts form. This process stabilizes the dimer and is accompanied by an increase in β -strand content. In solution, the dimers form more interpeptide hydrophobic contacts, reaching states [2, h12, b_6] and [2, h13, b_5] wherein 50 to 70% of all A β 42 residues form a β -sheet. In the presence of the neuronal membrane, both the hydrophobic contact area and β -sheet content are reduced, with the maximal values being [2, h10, b_4] and [2, h9, b_5], explaining the smaller number of nodes in this TN. Some of the interpeptide contacts are replaced by peptide-lipid contacts, which in turn inhibits β -sheet formation. This conclusion is confirmed by the representative structures shown in Fig. 4 and those illustrating the membrane adsorption of the dimer (Fig. 2). The membrane-adsorbed dimer structures are more compact than the dimer structures in solution, which feature extended β -sheets.

Long β -Strands in Solution and Compact A β 42 Structures at the Membrane. To quantify the effect of both aggregation and membrane adsorption on the peptide secondary structure, we deter-

mined the propensity of each residue to adopt a helical conformation, to be part of a β -sheet, or to be in a turn or bend conformation (Fig. 5A). For the dimer both in solution and on the membrane, β -sheet formation is observed. Using the same force field, mostly disordered conformations were sampled for the A β monomer during a 30- μ s MD simulation, with an average β -sheet content of about 15% (20). This rises to 36% for the dimer in solution, which indicates that dimerization causes A β 42 to undergo a disorder-to-order transition with β -sheet folding. The β -sheet content for the membrane-adsorbed dimer is 28% and thus smaller compared to that for the solvated dimer. This decrease is particularly pronounced for peptide 1, which interacts more strongly with the membrane than peptide 2 does. Instead, peptide 1 exhibits more turns, bends, and random coil structures, which suggests that the membrane inhibits β -sheet formation. Also, no pronounced helix formation is observed for the membrane-bound dimer, which one might expect based on NMR results (33) and previous simulation studies of A β that employed implicit membrane models (34, 35). However, a closer inspection of these studies reveals that for helices to be present, the affected A β residues need to be inserted into the hydrophobic membrane core, which did not occur here. It remains to be shown what comes first: helix formation or membrane insertion. In solution, both peptides feature a very similar secondary structure pattern along their primary structure. They display a particularly high propensity for a β -sheet in the regions Q15 to F20 of the central hydrophobic core (CHC) and A30 to V40 from the C-terminal hydrophobic region. This excludes the residue pair G37/G38, which has a tendency to form a turn as previously shown in simulations (36) and NMR spectroscopy (37).

The analysis of the intrapeptide contacts, derived from inter-residue distances (Fig. 6), indicates that in solution long β -hairpins between two antiparallel strands involving residues Y10 to V24 and Q27 to V40 formed in both peptides. These β -hairpins are particularly stable since the β -sheet propensity of the strongly hydrophobic regions 18 VFF 20 and 32 I 34 GL 34 even reaches values above 90%. In previous simulation studies, β -sheet formation upon A β dimerization has also been the prevailing finding (see table 2 of ref. 36 and references therein

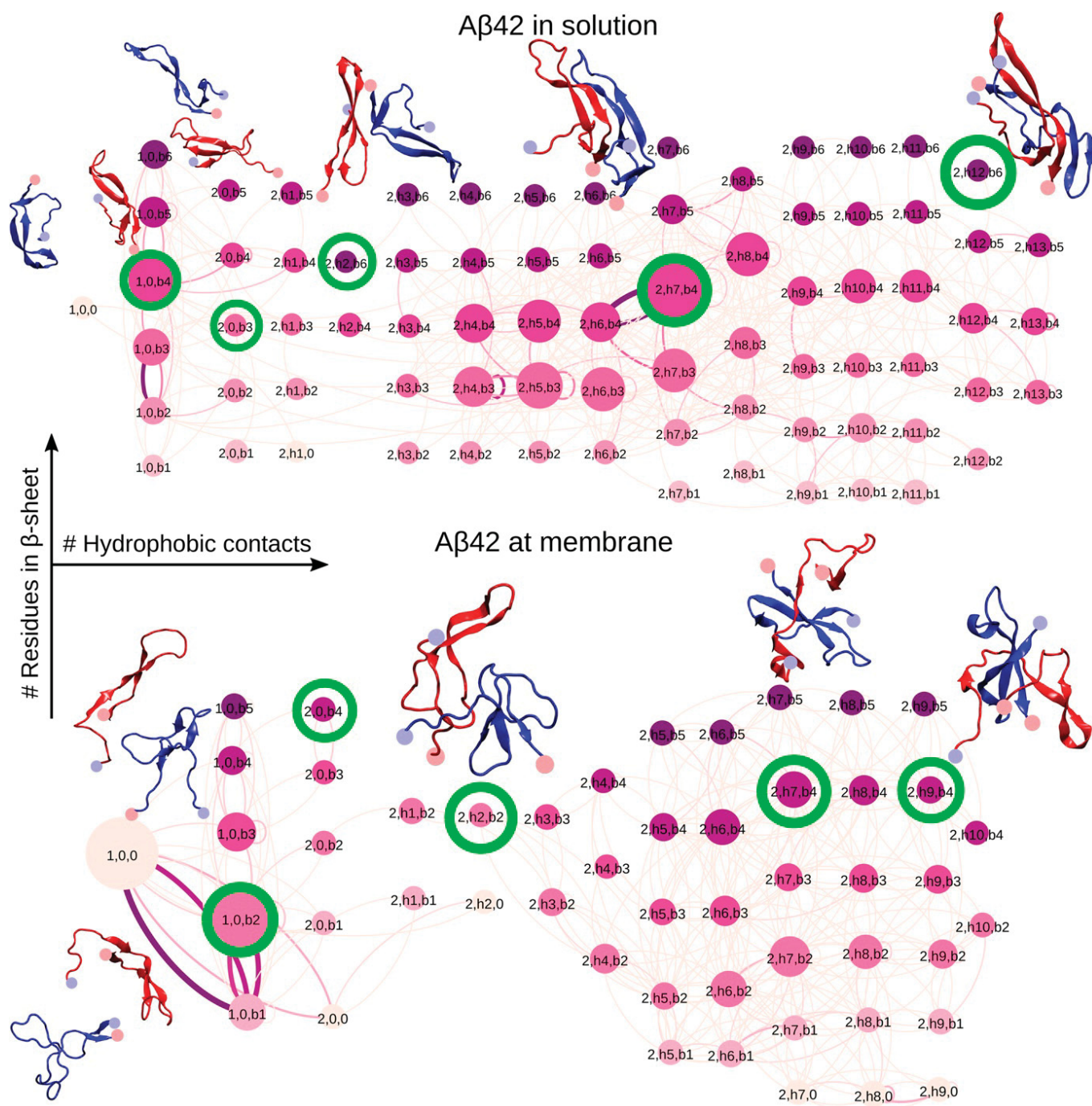


Fig. 4. The TN for A β 42 dimerization in the aqueous phase (*Top*) and in the presence of the neuronal membrane (*Bottom*). Each node is defined by three descriptors: oligomer size, number of interpeptide hydrophobic contacts, and number of residues in β -strand conformation. The last two descriptors are grouped in blocks of five and are named h1 to h12 for hydrophobic contacts and b1 to b6 for the number of residues in β -strand conformation. The nodes are connected by edges that represent transitions between the connected peptide states. The size of the nodes and the thickness of the edges are proportional to the respective state or transition probability. They are colored based on the descriptor reflecting the number of residues in β -strand conformation (from light pink for no β -sheets to dark purple for the maximum amount of β -sheets in b6). For the nodes circled in green representative peptide conformations are shown (see color code in Fig. 2).

as well as refs. 38–41). As found here, the β -sheets are preferentially formed between the C-terminal hydrophobic regions, followed by the involvement of the CHC. However, in most of these previous studies, the β -sheets are shorter and the overall dimer appearance is more compact. This likely resulted from the usage of older force fields, which were not optimized for IDPs and are known to provide too compact IDP conformations (42). Exceptions are a coarse-grained discrete MD study

(38) and a structure-prediction study for transmembrane A β oligomers (35) that yielded similarly extended β -sheets. This is confirmed by comparing the intrapeptide contacts that are present in the different A β 42 dimers, as shown in *SI Appendix, Fig. S9*. *SI Appendix, Fig. S9* further shows that the β -hairpin centered at G25/S26 coincides with the peptide regions that are involved in the cross- β -sheet structure found in U-shaped A β fibrils (43, 44).

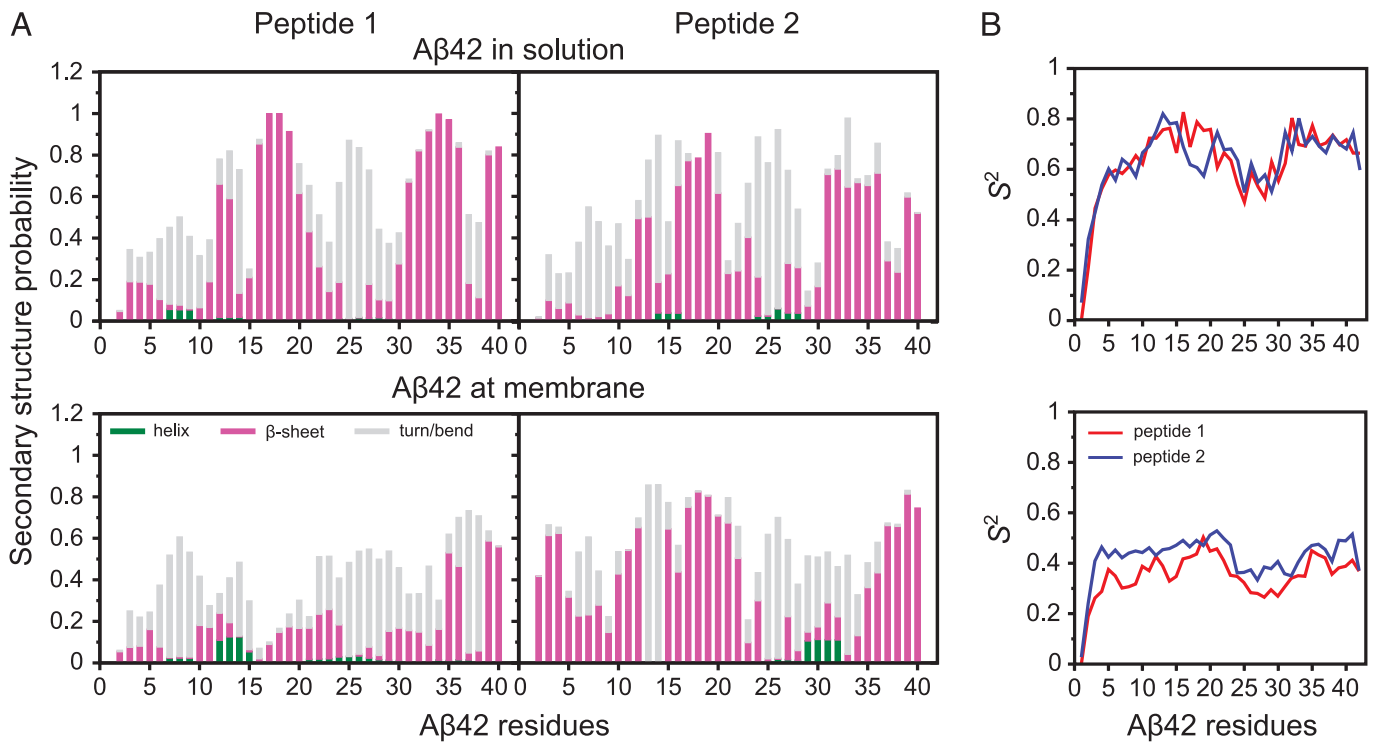


Fig. 5. Structural characteristics of the dimer in the aqueous phase (*Top*) and in the presence of the neuronal membrane (*Bottom*). (A) Probability of secondary structures to form in each residue of the peptides. The bars represent the cumulative secondary structure probabilities consisting of helix (green), β -strand/bridge (magenta), and turn or bend (gray). The difference from 1.0 presents the probability of the random coil state. (B) The average order parameter S^2 of each residue and peptide.

The intrapeptide contacts present in the membrane-adsorbed dimer are more diverse and different in the two peptides. For peptide 2 they reveal the prevalence of two shorter hairpins, one centered at H14 and the other one at G25, and several contacts between N- and C-terminal residues. The more membrane-adsorbed peptide 1, on the other hand, is devoid of noteworthy contacts involving its N-terminal residues. These are the amino acids that preferentially interact with the membrane and are therefore not available for interresidue interactions. In the C-terminal region of peptide 2 the formation of a very short β -hairpin is visible. Overall, the intrapeptide contacts corroborate the conclusion that at the membrane A β 42 adopts more compact conformations with less β -sheet than the dimer in solution.

Dimerization in Solution Is Mainly Driven via the Hydrophobic C-Terminal Region. To obtain an overview of how the two peptides are arranged with respect to each other as dimers, we calculated the interpeptide distances on a per-residue basis. The resulting distance matrices for the two dimer systems (Fig. 6) are almost symmetric with respect to their diagonal and are characterized by areas of high contact density along the diagonal as well as in the upper left and lower right quadrants. Only the D23 to K28 region in both peptides and in both environments does not show a noteworthy contact propensity. This is the same region of the peptide that we assigned a turn or bend conformation (Fig. 5). It can thus be concluded that this bend/turn region does not form the interpeptide interface.

For the dimer in solution, the highest contact density is observed between the two C-terminal regions, A30 to A42, which are the same regions where a high β -propensity was identified. Therefore, these two C-terminal regions not only are involved in intrapeptide β -sheets, but also form an interpeptide β -sheet in solution. This is confirmed when analyzing the residue–residue interaction energies between the two peptides, which involve

Coulomb interactions deriving from backbone H bonds and Lennard-Jones energies originating from interactions between hydrophobic residues (*SI Appendix, Fig. S10*). While the distance matrix does not show a clear preference for either an antiparallel or a parallel β -sheet between the two C-terminal regions, and both arrangements are indeed possible (see the representative conformations for nodes [2, h7, b4] [parallel] and [2, H12, b6] [antiparallel] of the corresponding TN in Fig. 4), the interaction energies indicate that the antiparallel arrangement is favored. This is different from A β fibrils where only parallel β -sheets are found. Other preferred contacts in the dimers form between the CHC of one peptide and the C-terminal region of the other peptide. The fourth area with a certain, yet smaller probability of interpeptide contact is between the CHC regions of both peptides. However, these contacts are weaker than those between the two C-terminal regions, as the corresponding interaction energies are smaller in magnitude (*SI Appendix, Fig. S10*). The dissection of the interaction energies further reveals that attraction between the oppositely charged residues E22/D23 and K28 is involved in the association process, which is in agreement with previous findings (45).

The distance matrix of the membrane-adsorbed dimer looks similar to the one of the dimer in solution. However, the contact areas are more pronounced, indicating less structural diversity in the internal arrangement of the dimers. Second, the area without interpeptide contacts around residues D23 to K28 is larger. This applies to peptide 1 in particular and can be explained by the contacts that this peptide forms with the membrane instead. Third, the order of areas with the highest contact probability is different from those of the solution system. The shortest distances in the membrane-adsorbed dimer are observed between the CHC of peptide 1 and the C-terminal region of peptide 2, followed by the contacts between both CHC regions. However, based on the secondary structure analysis, β -sheet formation between the two peptides is less likely and is largely limited to within peptide

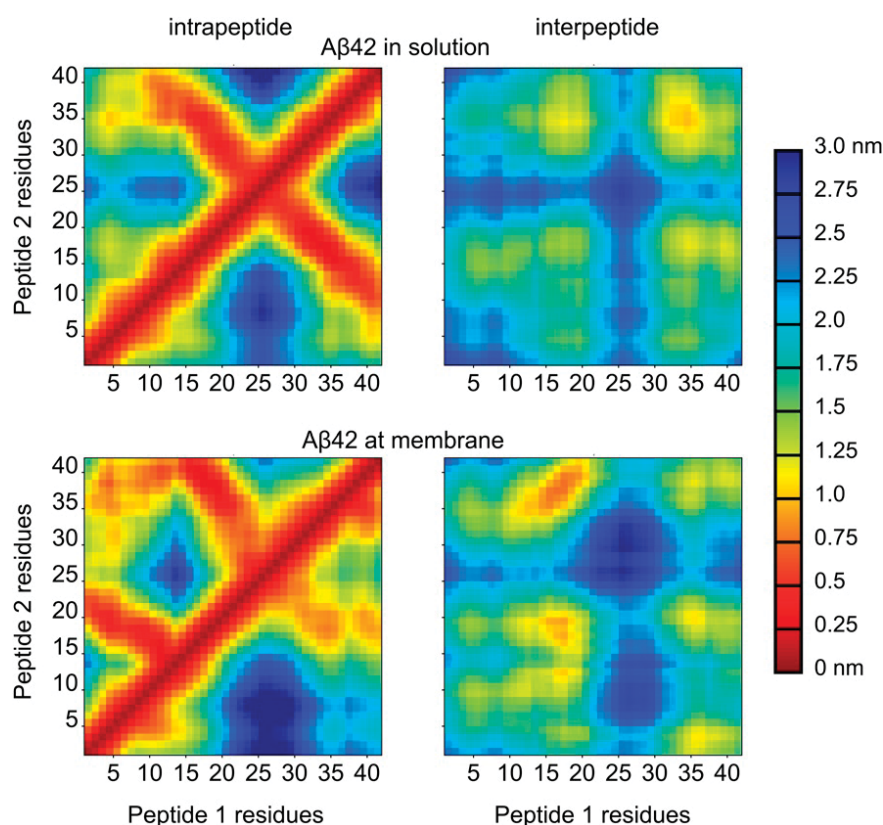


Fig. 6. The distance matrices illustrating intra- and interpeptide contacts between residues for the dimer in the aqueous phase (*Top*) and in the presence of the neuronal membrane (*Bottom*). The intrapeptide contacts within peptide 1 are shown below the main diagonal and those within peptide 2 above it. The interpeptide contacts are shown for peptide 1 and peptide 2 composing the dimer. The color bar on the right indicates the average intra- and interresidue distances (in nanometers).

2. Contacts between the C-terminal region of peptide 1 and the N-terminal region of peptide 2 are also observed. As a result, the latter region exhibits an increased β -sheet propensity, which extends up to residue Y10 (Fig. 5A). It initially was assumed that the N-terminal region of $A\beta$ is always disordered. However, this was later refuted, first by simulations (*SI Appendix, Fig. S9*) and then by cryo-electron microscopy (35, 46). Contacts between the C-terminal regions are of less relevance for the membrane-adsorbed dimer due to the competition between peptide-peptide and peptide-membrane interactions. The ranking of the interpeptide contact preferences is confirmed by the analysis of the interaction energies (*SI Appendix, Fig. S10*). Unlike in solution, attraction between E22/D23 and K28 does not play a role during the dimerization of $A\beta$, which can be explained by the preference of K28 to associate with the membrane.

Reduced Global Motions but Increased Local Disorder in the Membrane-Adsorbed Dimer. To quantify the peptide dynamics, we calculated the S^2 order parameters to monitor the mobility of the N-H bond vectors of the peptide backbone along with the average global rotational correlation times, $\langle\tau\rangle$ (Fig. 5B). These quantities would be directly comparable to those determined by NMR spectroscopy, which, however, are not available yet. The global rotational dynamics of the $A\beta$ 42 dimer in solution occur on the low nanosecond time scale with $\langle\tau\rangle = 20 \pm 10$ ns. The S^2 values reflect the different secondary structure propensities of the various residues. They are above ≈ 0.7 for the residues in a β -conformation, while the more mobile turn region and neighboring residues ranging from E22 to A30 have S^2 values between 0.5 and 0.7, and the disordered N-terminal region has order parameters below 0.5. The comparison to the S^2 values of

the $A\beta$ 40 monomer confirm that the dimer in solution is considerably more folded, since for the monomer all S^2 values are below 0.4 (47). The global rotational dynamics of the $A\beta$ 42 dimer in the presence of the neuronal membrane are by a factor of 5 slower than in solution: $\langle\tau\rangle = 108 \pm 30$ ns. Interestingly, the slower motion is accompanied by decreased order parameters compared to that seen in solution; the S^2 values range from 0.25 to 0.55 (and below 0.25 for the N-terminal residues, similar to the situation in the solution dimer). The overall reduction in S^2 for the membrane-adsorbed dimer implies that the peptides are generally less folded than they are in solution, which agrees with the observed reduction in β -sheet and increase in random coil. Thus, a picture emerges where on the one hand the overall peptide dynamics are reduced due to the adsorption on the membrane, while at the same time the interactions with the membrane reduce the local peptide order as reflected by the S^2 values.

Discussion

In the present study, all-atom MD simulations on the microsecond time scale have been performed to elucidate the mechanism of $A\beta$ 42 dimerization in pure water and in the presence of a neuronal membrane. The consideration of a neuronal membrane consisting of six components (PC, PE, PS, CHOL, SM, and GM1) is a major step forward compared to previous simulation studies on $A\beta$ -membrane interactions, which included three lipid types or fewer. Dimerization was observed in the aqueous phase as well as at the neuronal membrane. However, the resulting dimer structures showed significant differences. Our simulations of $A\beta$ 42 dimerization in solution revealed a coil-to- β transition that is the first step along the amyloid

aggregation pathway. The dimer conformations sampled in solution bear certain similarities to the β -sheets found in the U-shaped A β 42 amyloid fibrils. To our knowledge, a dimer structure with such a high β -sheet content and overall order has never been reported from all-atom MD simulations where the aggregation of A β progresses from disordered monomers into oligomers. We conclude that only the MD sampling of several microseconds and the use of a force field well suited to A β allow the random coil to β -sheet transition to be observed in a simulation (22). Thus, with these simulations we finally shed light on the structural transitions that might lead to nuclei enabling amyloid formation. Our future simulations will test whether the dimers that formed in solution here are indeed on pathway toward amyloid fibrils.

On the neuronal membrane, the dimer conformations are generally less ordered than in solution. The dimerization took place on the membrane, with one of the two peptides being preferentially adsorbed to the membrane and the other one associating with the already membrane-attached peptide without noteworthy interacting with the membrane itself. The directly adsorbed peptide in particular has a higher amount of random coil and less β -sheet. The membrane adsorption is mainly driven by electrostatic interactions between the charged N-terminal residues of A β and the headgroups of PC, PE, and PS, in addition to hydrogen bonding between the sugar moieties of the GM1 lipids and A β 42 residues across its whole primary structure. GM1 is found to form clusters within the neuronal membrane, which are the preferable site for A β to bind to the membrane surface. This is in line with experimental results that revealed GM1 as part of a neuronal membrane to be the main interaction partner of A β , whereas less binding was seen for SM and also PC (48). No insertion of the peptides into the hydrophobic region of the membrane was observed in our simulations. Instead, the interactions with the membrane stiffened both peptides, restricting their conformational diversity compared to the A β 42 dimer simulated in the aqueous phase. Not only did the transition networks reveal a reduction in the number of conformational states, but also the correlation times of the N–H bond vector motions indicated an impaired peptide motion. However, while adsorption was found to have profound effects on the A β 42 dimer, the membrane was only marginally affected.

Our observations are in agreement with a large and diverse set of experimental results. Of special note is a study that analyzed the effects of glucose on A β 42 aggregation (49). In this study, Kedia et al. (49) found that A β 42 forms low-molecular-weight oligomers in the presence of sugars and that these oligomers do not adopt a β -sheet structure. This agrees with our observation that A β 42 dimers that preferentially interact with the glycans of GM1 form fewer β -sheets than A β 42 dimers that form in solution do. Moreover, another study revealed that A β oligomers that are present in the brain interstitial fluid are sequestered from that fluid by strongly binding to GM1, which also prevented the further aggregation of A β (48). We are aware of studies by Ikeda et al. (50) and Matsuzaki (51) that concluded that GM1 exhibits a strong Abeta fibril seeding potential following the formation of β -sheet-rich oligomers on GM1 clusters. However, these clusters are much larger than those formed in our simulations, as Ikeda et al. (50) and Matsuzaki (51) employed ganglioside-rich (>20 mol% vs. the 4 mol% used in our study) membranes, where GM1 forms an interconnected network of micrometer size yielding glycan platforms in liquid-ordered membranes. As elaborated by Hof and coworkers (52), the scenarios for membranes with high and low GM1 contents are not necessarily contradicting each other but rather complementary.

Another finding by the study of Kedia et al. (49) was that the unstructured A β 42 oligomers that formed in the presence of glucose are able to interact with membrane bilayers. Their

diffusion decreased by a factor of about 4 upon membrane adsorption, which agrees nicely with our observation that membrane interactions reduce the dynamics of the dimer. Moreover, no incorporation of the unstructured A β 42 oligomers into the membrane was recorded (49), which also concurs with our findings. We conclude that, if a β -sheet structure should be required for membrane insertion of A β aggregates to occur, GM1 in the neuronal membrane has a neuroprotective effect as it could break the β -sheet structure in the A β dimer. This finding would be in agreement with the neuroprotective and neurogenerative effects reported for GM1 (53–55) and the conclusion that the neurotoxic activity of amyloid oligomers increases with their β -sheet content (8). On the other hand, Selkoe and coworkers (48) found that even though GM1 sequesters A β from the brain interstitial fluid, thereby inhibiting the aggregation of A β , the binding of the peptide to GM1 alone mediates neurotoxic effects. This once more highlights that the interplay between A β , its aggregation, and the neuronal membrane is far from trivial and despite the wealth of already published studies on that matter, further studies are needed to fully solve this puzzle.

Materials and Methods

Setup of the Simulated Systems. The systems modeled are composed of two A β 42 peptides, which were simulated in the aqueous phase and in the presence of the neuronal lipid membrane. The initial A β 42 structures were taken from the most populated clusters from a preceding 3- μ s MD simulation of monomeric A β 42 in solution. The neuronal membrane model composed of 152 PC, 96 PE, 20 PS, 80 CHOL, 36 SM, and 16 GM1 molecules was generated as symmetric lipid bilayer using the CHARMM-GUI interface (56).

The simulated membrane system also contained water layers above the upper and beneath the lower membrane leaflet, using the three-site transferable intermolecular potential (TIP3P) for modeling the water molecules, with sodium and chloride ions added at the physiological concentration of 150 mM. The two A β 42 peptides were placed in the upper water layer at a distance of \approx 2 nm from the equilibrated lipid bilayer surface and at a distance of $>$ 1 nm between the closest atoms from the two peptides. All distances from the peptides to any of the simulation box edges were at least 1.2 nm to avoid interactions between the peptides and their periodic images. The total number of atoms in the modeled membrane system was \approx 160,000 atoms and the box size was about $9.6 \times 9.6 \times 13.6$ nm³. The setup of the system in the aqueous phase was similar, but without a lipid bilayer, resulting in a system size of about $9.2 \times 9.2 \times 6.5$ nm³, and contained \approx 54,760 atoms. This amounts to peptide concentrations of 4 and 6 mM, respectively. This is two to three orders of magnitude higher than the concentrations used in corresponding in vitro experiments. However, it is beyond our computational capabilities to model μ M peptide concentrations at the atomistic level. Moreover, simulations at such low concentrations would most of the time simulate only the diffusion of monomeric peptides (57). We therefore aim to model the oligomerization of A β in a stepwise fashion (57, 58), starting here with simulations of dimers.

MD Simulation Conditions. The all-atom MD simulations were performed using GROMACS/2018.2 (59) along with the CHARMM36m force field for A β 42 (60) and Charmm36 for the lipids (61). Each system was first energy minimized using the steepest-descent algorithm to remove atomic clashes. This was followed by equilibration in the canonical ensemble where a temperature of 310 K was regulated with the velocity-rescale thermostat (62). Next, the system was equilibrated under isobaric-isothermic conditions to obtain a pressure of 1.0 bar, where the pressure was regulated using a semi-isotropic Parrinello–Rahman pressure coupling scheme (63). Periodic boundary conditions were set in all directions. Both the van der Waals and Coulomb force cutoffs were set to 1.2 nm in real space. The particle mesh Ewald (PME) method was applied for calculating the electrostatic interactions. Before we studied the interaction of A β 42 with the neuronal membrane, we equilibrated the membrane without peptides being present for 1 μ s. For A β 42 dimer systems, an initial simulation was run for 2 μ s, from which different snapshots were randomly selected and used as starting structures for the next 5×2 - μ s simulations. For the subsequent analysis, we combined the data from the six independent simulations and derived the results presented in this study.

Analysis of the Lipid Bilayer Properties. For the determination of the order parameter of the lipid acyl chains, S_{CH} , one uses the C–H bond vectors

present in the lipid tails and calculates the orientation of these vectors with respect to the bilayer normal (the z axis) using

$$S_{CH} = \frac{\langle 3\cos^2\theta - 1 \rangle}{2}, \quad [1]$$

where θ is the angle between the C–H bond vector and the bilayer normal. The angular brackets indicate the ensemble average. This calculation was accomplished with a Python script available at <https://github.com/NMRLipids/MATCH> (64).

The mass density profiles along the bilayer normal were calculated using the “gmx density” tool. The distance between the peaks of the total density gives an estimate of the bilayer thickness. Furthermore, the bilayer thickness was calculated as the z-position difference between the P atoms of the lipid headgroups in the upper and lower leaflets using the “gmx distance” tool. The RDF provides information about the probability of finding a particle at a certain distance from another particle. We calculated the radial distribution functions of different lipid pairs in two dimensions (the xy plane) using the “gmx rdf” tool. The hydrogen bonds between different lipid pairs were determined using “gmx hbond.” A hydrogen bond was recorded when the angle between the donor and acceptor bonded hydrogen was between 150 and 180° and the distance between the two atoms was within 0.35 nm.

Analysis of A β 42 Properties. The secondary structure of each A β 42 residue was determined using the “define secondary structure program” (DSSP) (65) invoked via the GROMACS tool “do dssp.” To facilitate a clear representation, the data of similar secondary structures are grouped together: β -strand and β -bridge are combined as β -sheet and β -turn and bend as turn/bend; and the helix includes α , π , and 3_{10} -helices.

For the calculation of the S^2 order parameter we used the MOPS² (Molecular Order Parameter S^2) software developed in ref. 66 to calculate S^2 from the N–H bond vector autocorrelation function. To facilitate the calculation, each trajectory was divided into subtrajectories of $t_{sub} = 100$ ns length. For each of the subtrajectories the S^2 values and the rotational correlation times, τ , were calculated and subsequently averaged over all subtrajectories. The rotational correlation times were further averaged over all residues and both peptides, denoted as $\langle\tau\rangle$, whereas S^2 is provided per residue and peptide. Since $\langle\tau\rangle$ for the membrane system is in the same range as t_{sub} , we checked on the convergence for the S^2 calculation in this case (SI Appendix, Fig. S11).

Transition Networks. For the generation of the TNs to characterize the assembly of peptides into dimers we used the ATRANET (Automated Transition Network) software (<https://github.com/strodel-group/ATRANET>) (27). It defines the oligomerization state by a number of descriptors, depending on the properties of interest. In our case, three descriptors are used: The first one is the oligomer size, which can be 1 in the case of monomer or 2 in

the case of a dimer. To define a dimer, the minimum distance between any atom of peptide 1 and any atom of peptide 2 along with the requirement of this distance to be within 0.45 nm was used. The second descriptor, the number of hydrophobic contacts between both peptides, counts the possible interpeptide atom pairs formed between the hydrophobic amino acids of A β 42 that are within a certain cutoff (also 0.45 nm). The third descriptor is the number of residues in β -strand conformation, which is evaluated using DSSP and averaged over both peptides. Feeding these descriptors to ATRANET leads to a transition matrix that can be visualized using Gephi (67). Snapshots of the representative structures from the transition network were rendered using the visual molecular dynamics (VMD) program (68).

Calculation of A β 42–Bilayer Interactions. The peptide–lipid interactions were analyzed by calculating the interaction energy between each A β 42 residue and the headgroup of each lipid component using “gmx energy.” The “gmx mindist” program was employed to determine the number of contacts between each A β 42 residue and each lipid component in the neuronal membrane. A contact was recorded when the distance between any two nonhydrogen atoms from a residue and a lipid was within 0.5 nm. The H-bond propensity was determined by the number of times an H bond was formed between hydrogen bond donating and accepting atoms in lipid pairs.

Data Availability. The MD trajectories and the analysis scripts are available at Mendeley Data, <https://data.mendeley.com/datasets/92mkp4pk86>. All data resulting from the analysis of this raw data is shown in the main text or SI Appendix.

ACKNOWLEDGMENTS. H.F., M.K., A.S.-A., and B.S. acknowledge funding for this project from the Palestinian-German Science Bridge financed by the German Federal Ministry of Education and Research. B.S. received funding for this project from the Deutsche Forschungsgemeinschaft (German Research Foundation, <https://www.dfg.de/>) through Grant 267205415 (CRC 1208, Project A07). M.C.O. received funding for this project from the European Union’s Horizon 2020 research and innovation programme under the Marie Skłodowska-Curie grant and it is cofinanced by the South Moravian Region under Grant 665860. This article reflects only the authors’ view and the European Union is not responsible for any use that may be made of the information it contains. This research was supported by the European Union and the Hungarian State, cofinanced by the European Regional Development Fund in the framework of the GINOP-2.3.4-15-2016-00004 project, aimed to promote the cooperation between the higher education and the industry. M.C.O. and B.S. gratefully acknowledge the Gauss Centre for Supercomputing (GCS) e.V. (www.gauss-centre.eu) for funding this project by providing computing time on the GCS Supercomputer SuperMUC-NG at Leibniz Supercomputing Centre (<https://www.lrz.de/>). H.F., M.K., and B.S. gratefully acknowledge the computing time granted through Jülich Aachen Research Alliance - High Performance Computing (Projects JICS6C and AMYLOID-MSM) on the supercomputer Jureca at Forschungszentrum Jülich.

1. S. H. Barage, K. D. Sonawane, Amyloid cascade hypothesis: Pathogenesis and therapeutic strategies in Alzheimer’s disease. *Neuropeptides* **52**, 1–18 (2015).
2. C. A. McLean *et al.*, Soluble pool of Abeta amyloid as a determinant of severity of neurodegeneration in Alzheimer’s disease. *Ann. Neurol.* **46**, 860–866 (1999).
3. M. D. Kirkitadze, G. Bitan, D. B. Teplow, Paradigm shifts in Alzheimer’s disease and other neurodegenerative disorders: The emerging role of oligomeric assemblies. *J. Neurosci. Res.* **69**, 567–577 (2002).
4. K. Broersen, F. Rousseau, J. Schymkowitz, The culprit behind amyloid beta peptide related neurotoxicity in Alzheimer’s disease: Oligomer size or conformation? *Alzheimers Res. Ther.* **2**, 12 (2010).
5. A. Müller-Schiffmann *et al.*, Amyloid- β dimers in the absence of plaque pathology impair learning and synaptic plasticity. *Brain* **139**, 509–525 (2016).
6. G. Brinkmalm *et al.*, Identification of neurotoxic cross-linked amyloid- β dimers in the Alzheimer’s brain. *Brain* **142**, 1441–1457 (2019).
7. G. Bitan, D. B. Teplow, Rapid photochemical cross-linking—A new tool for studies of metastable, amyloidogenic protein assemblies. *Acc. Chem. Res.* **37**, 357–364 (2004).
8. K. Ono, M. M. Condron, D. B. Teplow, Structure-neurotoxicity relationships of amyloid beta-protein oligomers. *Proc. Natl. Acad. Sci. U.S.A.* **106**, 14745–14750 (2009).
9. B. O’Nuallain *et al.*, Amyloid beta-protein dimers rapidly form stable synaptotoxic protofibrils. *J. Neurosci.* **30**, 14411–14419 (2010).
10. A. Vázquez de la Torre *et al.*, Direct evidence of the presence of cross-linked β dimers in the brains of Alzheimer’s disease patients. *Anal. Chem.* **90**, 4552–4560 (2018).
11. F. Castello *et al.*, Two-step amyloid aggregation: Sequential lag phase intermediates. *Sci. Rep.* **7**, 40065 (2017).
12. J. Yang *et al.*, Direct observation of oligomerization by single molecule fluorescence reveals a multistep aggregation mechanism for the yeast prion protein ure2. *J. Am. Chem. Soc.* **140**, 2493–2503 (2018).
13. J. Nasica-Labouze *et al.*, Amyloid β protein and Alzheimer’s disease: When computer simulations complement experimental studies. *Chem. Rev.* **115**, 3518–3563 (2015).
14. P. H. Nguyen *et al.*, Amyloid oligomers: A joint experimental/computational perspective on Alzheimer’s disease, Parkinson’s disease, type II diabetes, and amyotrophic lateral sclerosis. *Chem. Rev.* **121**, 2545–2647 (2021).
15. S. J. C. Lee, E. Nam, H. J. Lee, M. G. Savelieff, M. H. Lim, Towards an understanding of amyloid- β oligomers: Characterization, toxicity mechanisms, and inhibitors. *Chem. Soc. Rev.* **46**, 310–323 (2017).
16. M. C. Owen *et al.*, Effects of in vivo conditions on amyloid aggregation. *Chem. Soc. Rev.* **48**, 3946–3996 (2019).
17. Z. Korade, A. K. Kenworthy, Lipid rafts, cholesterol, and the brain. *Neuropharmacology* **55**, 1265–1273 (2008).
18. E. Posse de Chaves, S. Sipione, Sphingolipids and gangliosides of the nervous system in membrane function and dysfunction. *FEBS Lett.* **584**, 1748–1759 (2010).
19. Y. C. Kao, P. C. Ho, Y. K. Tu, I. M. Jou, K. J. Tsai, Lipids and Alzheimer’s disease. *Int. J. Mol. Sci.* **21**, 1505 (2020).
20. A. Paul, S. Samantray, M. Antegnini, M. Khaled, B. Strodel, Thermodynamics and kinetics of the amyloid- β peptide revealed by Markov state models based on MD data in agreement with experiment. *Chem. Sci. (Camb.)* **12**, 6652–6669 (2021).
21. S. Samantray, F. Yin, B. Kav, B. Strodel, Different force fields give rise to different amyloid aggregation pathways in molecular dynamics simulations. *J. Chem. Inf. Model.* **60**, 6462–6475 (2020).
22. B. Strodel, Amyloid aggregation simulations: Challenges, advances and perspectives. *Curr. Opin. Struct. Biol.* **67**, 145–152 (2021).
23. H. Koldso, D. Shorthouse, J. Hélie, M. S. Sansom, Lipid clustering correlates with membrane curvature as revealed by molecular simulations of complex lipid bilayers. *PLoS Comput. Biol.* **10**, e1003911 (2014).
24. H. I. Ingólfsson *et al.*, Computational lipidomics of the neuronal plasma membrane. *Biophys. J.* **113**, 2271–2280 (2017).

25. B. Barz, D. J. Wales, B. Strodel, A kinetic approach to the sequence-aggregation relationship in disease-related protein assembly. *J. Phys. Chem. B* **118**, 1003–1011 (2014).
26. B. Barz, Q. Liao, B. Strodel, Pathways of amyloid- β aggregation depend on oligomer shape. *J. Am. Chem. Soc.* **140**, 319–327 (2018).
27. A. M. Illig, B. Strodel, Performance of Markov state models and transition networks on characterizing amyloid aggregation pathways from MD data. *J. Chem. Theory Comput.* **16**, 7825–7839 (2020).
28. J. P. Jämbeck, A. P. Lyubartsev, An extension and further validation of an all-atomistic force field for biological membranes. *J. Chem. Theory Comput.* **8**, 2938–2948 (2012).
29. I. Ermilova, A. P. Lyubartsev, Extension of the slipids force field to polyunsaturated lipids. *J. Phys. Chem. B* **120**, 12826–12842 (2016).
30. J. Egawa, M. L. Pearn, B. P. Lemkuil, P. M. Patel, B. P. Head, Membrane lipid rafts and neurobiology: Age-related changes in membrane lipids and loss of neuronal function. *J. Physiol.* **594**, 4565–4579 (2016).
31. V. Pata, N. Dan, Effect of membrane characteristics on phase separation and domain formation in cholesterol-lipid mixtures. *Biophys. J.* **88**, 916–924 (2005).
32. H. Ohvo-Rekilä, B. Ramstedt, P. Leppimäki, J. P. Slotte, Cholesterol interactions with phospholipids in membranes. *Prog. Lipid Res.* **41**, 66–97 (2002).
33. M. Coles, W. Bicknell, A. A. Watson, D. P. Fairlie, D. J. Craik, Solution structure of amyloid beta-peptide(1–40) in a water-micelle environment. Is the membrane-spanning domain where we think it is? *Biochemistry* **37**, 11064–11077 (1998).
34. N. Miyashita, J. E. Straub, D. Thirumalai, Structures of β -amyloid peptide 1–40, 1–42, and 1–55 – the 672–726 fragment of app – in a membrane environment with implications for interactions with γ -secretase. *J. Am. Chem. Soc.* **131**, 17843–17852 (2009).
35. B. Strodel, J. W. L. Lee, C. S. Whittleston, D. J. Wales, Transmembrane structures for Alzheimer's A β (1–42) oligomers. *J. Am. Chem. Soc.* **132**, 13300–13312 (2010).
36. L. Nagel-Steger, M. C. Owen, B. Strodel, An account of amyloid oligomers: Facts and figures obtained from experiments and simulations. *ChemBioChem* **17**, 657–676 (2016).
37. T. Kakeshpour *et al.*, A lowly populated, transient β -sheet structure in monomeric a β 1–42 identified by multinuclear NMR of chemical denaturation. *Biophys. Chem.* **270**, 106531 (2020).
38. B. Urbanc *et al.*, Molecular dynamics simulation of amyloid beta dimer formation. *Biophys. J.* **87**, 2310–2321 (2004).
39. S. Côté, R. Laghaei, P. Derreumaux, N. Mousseau, Distinct dimerization for various alloforms of the amyloid-beta protein: A β 1–40, β 1–42, and β 1–40(d23n). *J. Phys. Chem. B* **116**, 4043–4055 (2012).
40. V. H. Man, P. H. Nguyen, P. Derreumaux, High-resolution structures of the amyloid- β –42 dimers from the comparison of four atomistic force fields. *J. Phys. Chem. B* **121**, 5977–5987 (2017).
41. B. Mehrzama, A. Rauk, Exploring amyloid- β dimer structure using molecular dynamics simulations. *J. Phys. Chem. A* **123**, 4658–4670 (2019).
42. S. Rauscher *et al.*, Structural ensembles of intrinsically disordered proteins depend strongly on force field: A comparison to experiment. *J. Chem. Theory Comput.* **11**, 5513–5524 (2015).
43. T. Lührs *et al.*, 3D structure of Alzheimer's amyloid- β (1–42) fibrils. *Proc. Natl. Acad. Sci. U.S.A.* **102**, 17342–17347 (2005).
44. A. K. Paravastu, R. D. Leapman, W. M. Yau, R. Tycko, Molecular structural basis for polymorphism in Alzheimer's beta-amyloid fibrils. *Proc. Natl. Acad. Sci. U.S.A.* **105**, 18349–18354 (2008).
45. B. Tarus, J. E. Straub, D. Thirumalai, Structures and free-energy landscapes of the wild type and mutants of the A β (21–30) peptide are determined by an interplay between intrapeptide electrostatic and hydrophobic interactions. *J. Mol. Biol.* **379**, 815–829 (2008).
46. L. Gremer *et al.*, Fibril structure of amyloid- β (1–42) by cryo-electron microscopy. *Science* **358**, 116–119 (2017).
47. N. Rezaei-Ghaleh, G. Parigi, M. Zweckstetter, Reorientational dynamics of amyloid- β from NMR spin relaxation and molecular simulation. *J. Phys. Chem. Lett.* **10**, 3369–3375 (2019).
48. S. Hong *et al.*, Soluble A β oligomers are rapidly sequestered from brain ISF in vivo and bind GM1 ganglioside on cellular membranes. *Neuron* **82**, 308–319 (2014).
49. N. Kedia, M. Almisry, J. Bieschke, Glucose directs amyloid- β into membrane-active oligomers. *Phys. Chem. Chem. Phys.* **19**, 18036–18046 (2017).
50. K. Ikeda, T. Yamaguchi, S. Fukunaga, M. Hoshino, K. Matsuzaki, Mechanism of amyloid β -protein aggregation mediated by GM1 ganglioside clusters. *Biochemistry* **50**, 6433–6440 (2011).
51. K. Matsuzaki, Formation of toxic amyloid fibrils by amyloid β protein on ganglioside clusters. *Int. J. Alzheimers Dis.* **2011**, 956104 (2011).
52. M. Becbauer, M. Hof, M. Amaro, Impact of GM1 on membrane-mediated aggregation/oligomerization of β -amyloid: Unifying view. *Biophys. J.* **113**, 1194–1199 (2017).
53. T. V. Sokolova, I. O. Zakharova, V. V. Furaev, M. P. Rychkova, N. F. Avrova, Neuroprotective effect of ganglioside GM1 on the cytotoxic action of hydrogen peroxide and amyloid beta-peptide in PC12 cells. *Neurochem. Res.* **32**, 1302–1313 (2007).
54. F. Kreutz *et al.*, Amyloid- β induced toxicity involves ganglioside expression and is sensitive to GM1 neuroprotective action. *Neurochem. Int.* **59**, 648–655 (2011).
55. R. Yang *et al.*, Monosialoanglioside improves memory deficits and relieves oxidative stress in the hippocampus of rat model of Alzheimer's disease. *Neuro. Sci.* **34**, 1447–1451 (2013).
56. J. Lee *et al.*, CHARMM-GUI input generator for NAMD, GROMACS, AMBER, openMM, and CHARMM/openMM simulations using the CHARMM36 additive force field. *J. Chem. Theory Comput.* **12**, 405–413 (2016).
57. M. Carballo-Pacheco, B. Strodel, Advances in the simulation of protein aggregation at the atomistic scale. *J. Phys. Chem. B* **120**, 2991–2999 (2016).
58. U. Sengupta, M. Carballo-Pacheco, B. Strodel, Automated Markov state models for molecular dynamics simulations of aggregation and self-assembly. *J. Chem. Phys.* **150**, 115101 (2019).
59. M. J. Abraham *et al.*, GROMACS: High performance molecular simulations through multi-level parallelism from laptops to supercomputers. *SoftwareX* **1**, 19–25 (2015).
60. J. Huang *et al.*, CHARMM36m: An improved force field for folded and intrinsically disordered proteins. *Nat. Methods* **14**, 71–73 (2017).
61. J. B. Klauda *et al.*, Update of the CHARMM all-atom additive force field for lipids: Validation on six lipid types. *J. Phys. Chem. B* **114**, 7830–7843 (2010).
62. G. Bussi, D. Donadio, M. Parrinello, Canonical sampling through velocity rescaling. *J. Chem. Phys.* **126**, 014101 (2007).
63. H. J. Berendsen, J. Postma, W. F. van Gunsteren, A. DiNola, J. R. Haak, Molecular dynamics with coupling to an external bath. *J. Chem. Phys.* **81**, 3684–3690 (1984).
64. H. Antila *et al.*, Headgroup structure and cation binding in phosphatidylserine lipid bilayers. *J. Phys. Chem. B* **123**, 9066–9079 (2019).
65. Y. Zhang, C. Sagui, Secondary structure assignment for conformationally irregular peptides: Comparison between DSSP, STRIDE and KAKSI. *J. Mol. Graph. Model.* **55**, 72–84 (2015).
66. C. Möckel *et al.*, Integrated NMR, fluorescence, and molecular dynamics benchmark study of protein mechanics and hydrodynamics. *J. Phys. Chem. B* **123**, 1453–1480 (2019).
67. M. Bastian *et al.*, Gephi: An open source software for exploring and manipulating networks. *Proc. Third Int. ICWSM Conf.* **8**, 361–362 (2009).
68. W. Humphrey, A. Dalke, K. Schulten, VMD: Visual molecular dynamics. *J. Mol. Graph.* **14**, 33–38 (1996).

1

2 **Supplementary Information for**

3 **Amyloid- β peptide dimers undergo a random coil to β -sheet transition in the aqueous phase**
4 **but not at the neuronal membran**

5 **Hebah Fatafta, Mohammed Khaled, Michael C. Owen, Abdallah Sayyed-Ahmad, Birgit Strodel**

6 **Corresponding Author name: Birgit Strodel.**

7 **E-mail: b.strodel@fz-juelich.de**

8 **This PDF file includes:**

9 Figs. S1 to S11 (not allowed for Brief Reports)

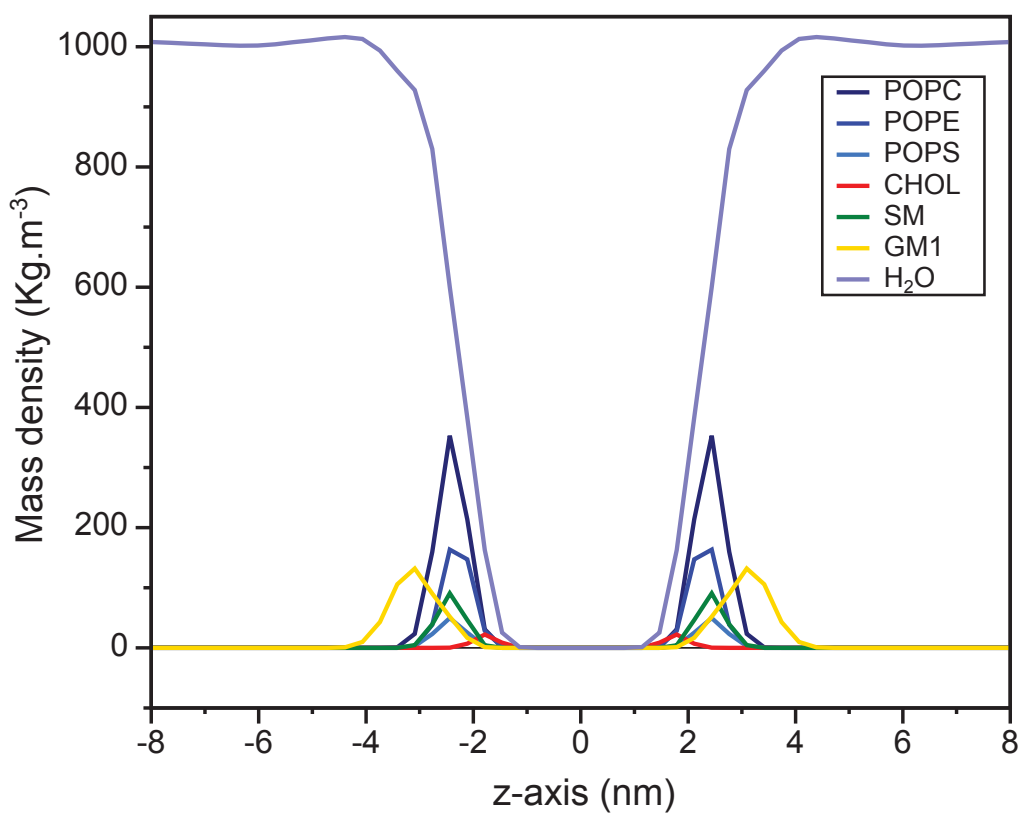


Fig. S1. The average mass density profile of lipids and water along the z -direction corresponding to the bilayer normal. Colors are chosen according to the legend given on the right.

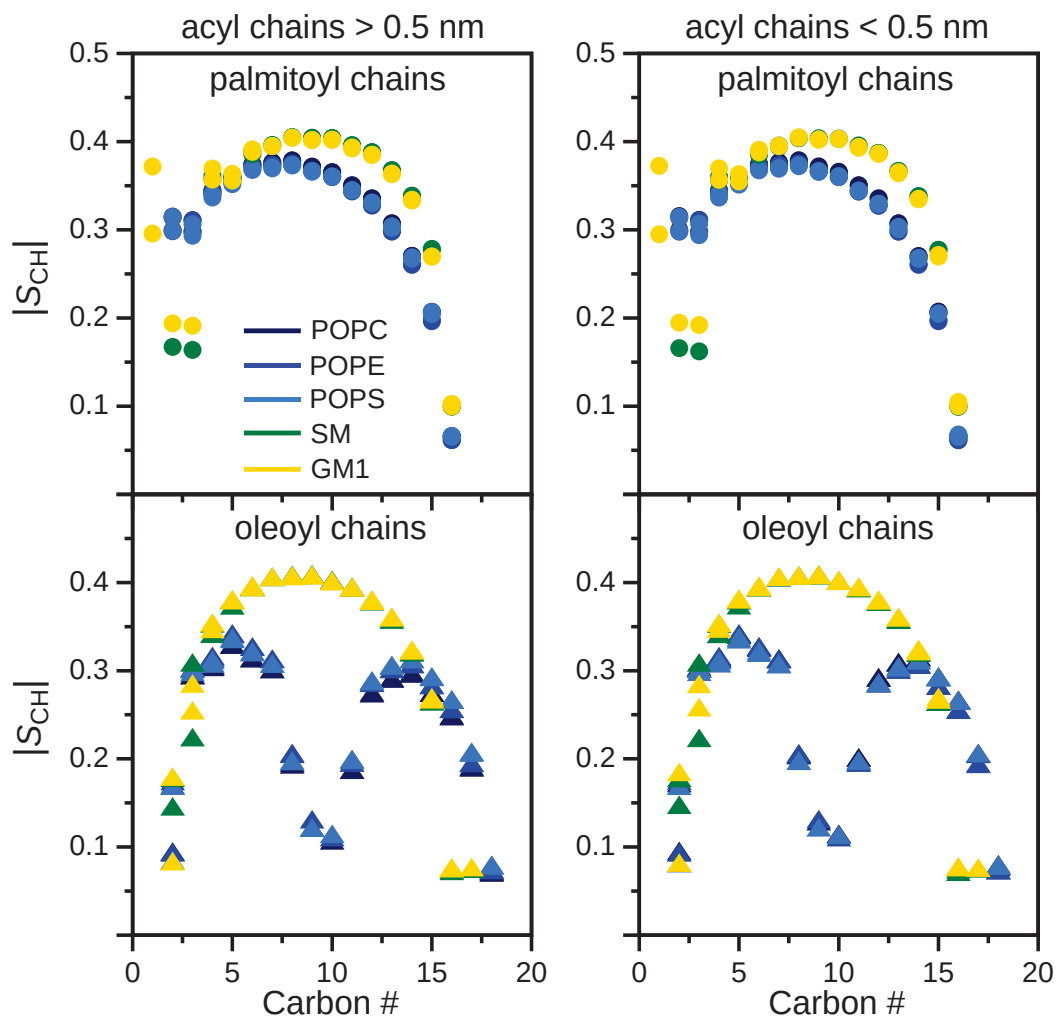


Fig. S2. Average order parameters of the acyl chains (top: palmitoyl chains; bottom: oleoyl chains) of each lipid component of the neuronal membrane, distinguishing between lipids that are more than 0.5 nm away from A β 42 (left) and those within 0.5 nm of the peptide (right).

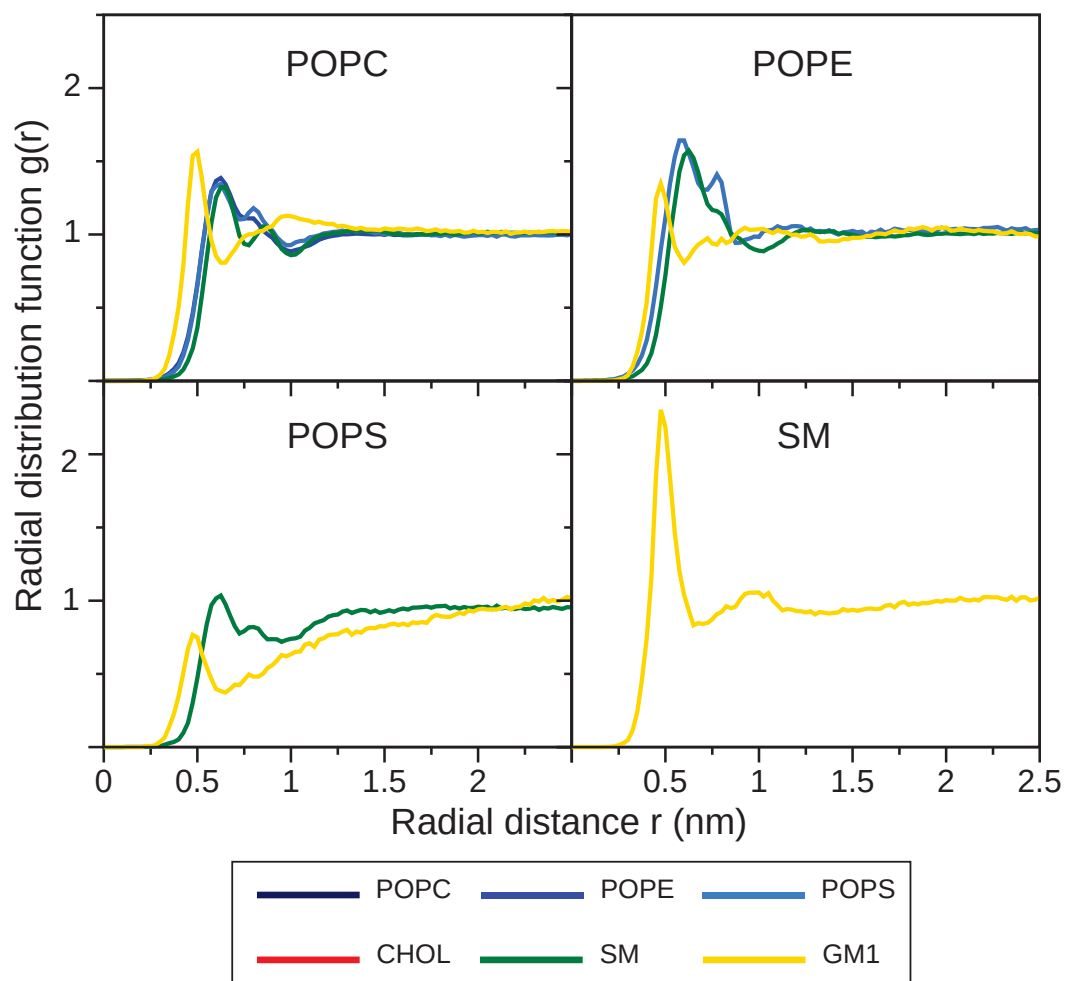


Fig. S3. Radial distribution functions for mixed lipid pairings: (top left) POPC–lipid pairs; (top right) POPE–lipid pairs; (bottom left) POPS–lipid pairs; (bottom right) SM–lipid pairings). Pairings between identical lipid types are shown in the main text in Figure 2A and pairing involving CHOL are presented in Figure 2B. The P atoms of POPC, POPE, POPS, and SM and the O atoms of CHOL and GM1 were used for the RDF calculations. The x -axes show the distances between the respective atom pairs. The colors of the graphs refer to the lipids as indicated in the color key below the plots. Pairs with RDF > 1 are considered to cluster.

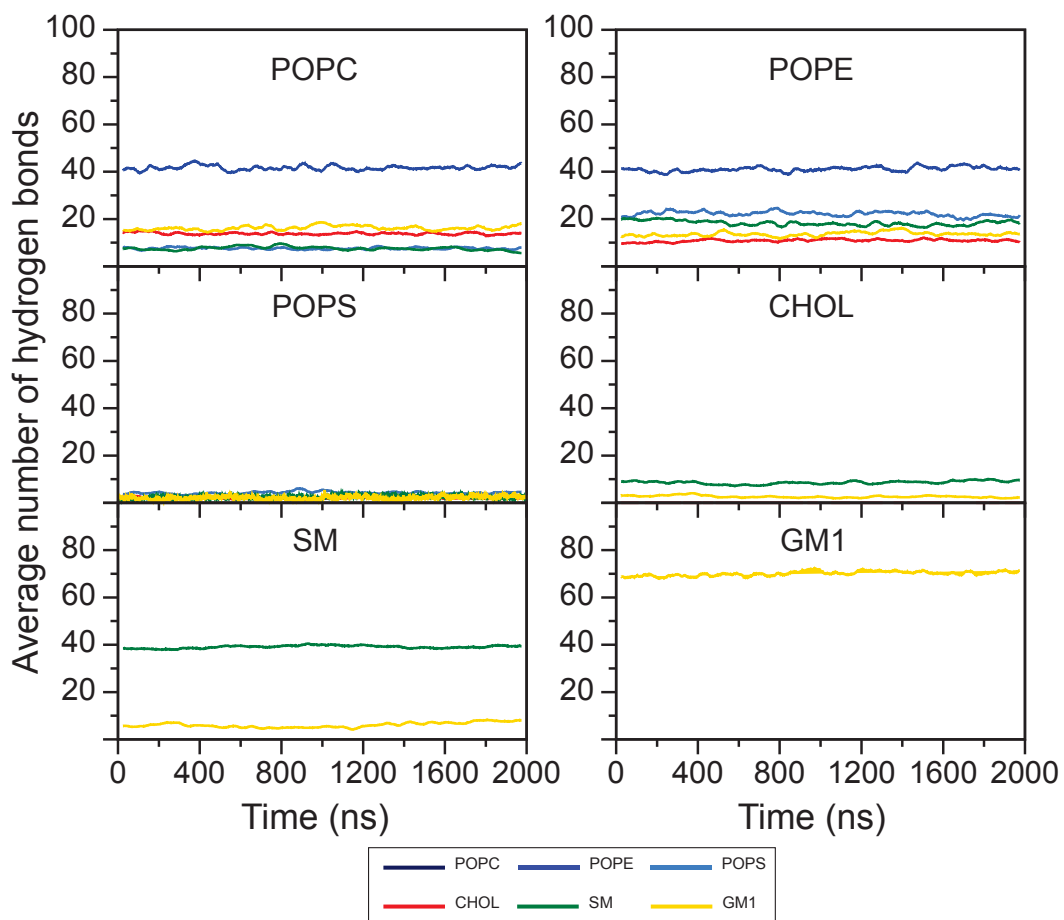


Fig. S4. The average number of hydrogen bonds between different lipid pairs. The colors of the graphs refer to the lipids as indicated in the color key below the plots.

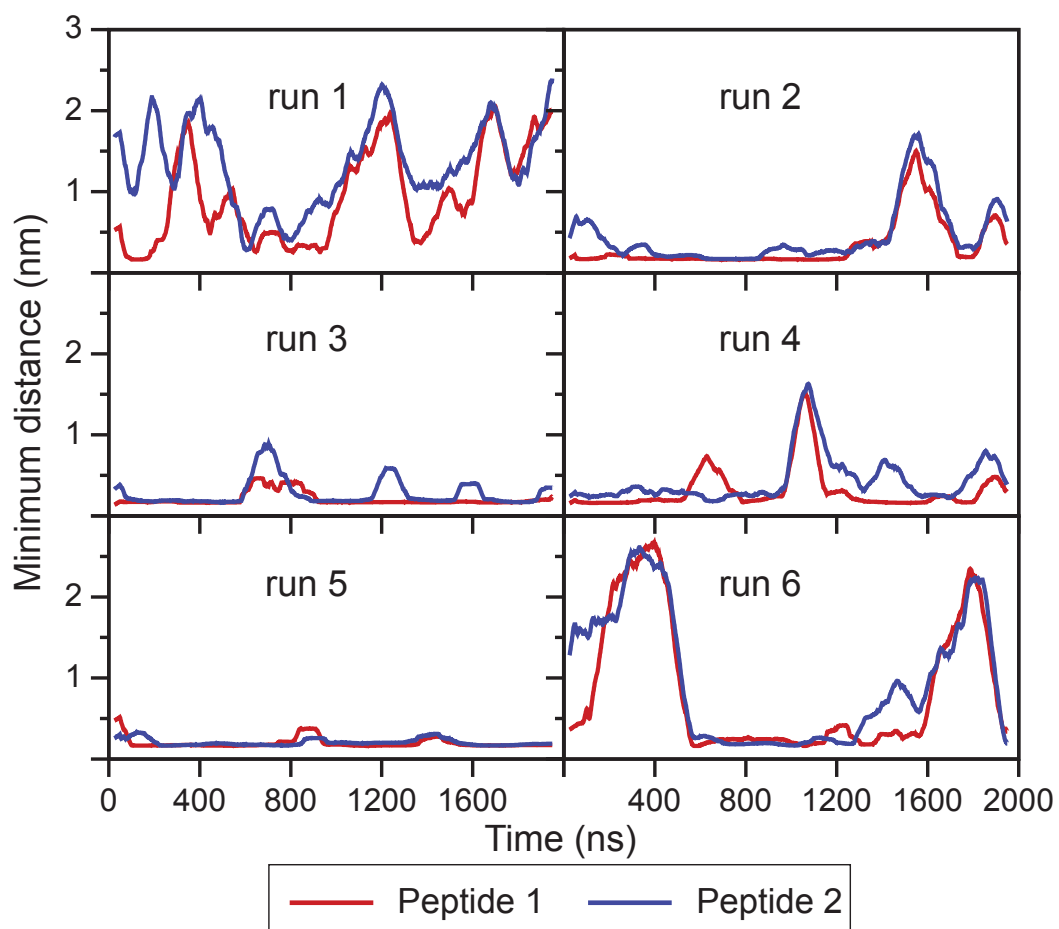


Fig. S5. The average number of A β 42–lipid contacts (and standard error of the mean) calculated for peptide 1 (left) and peptide 2 (right) with each of the components of the neuronal membrane (lipid names shown above the panels).

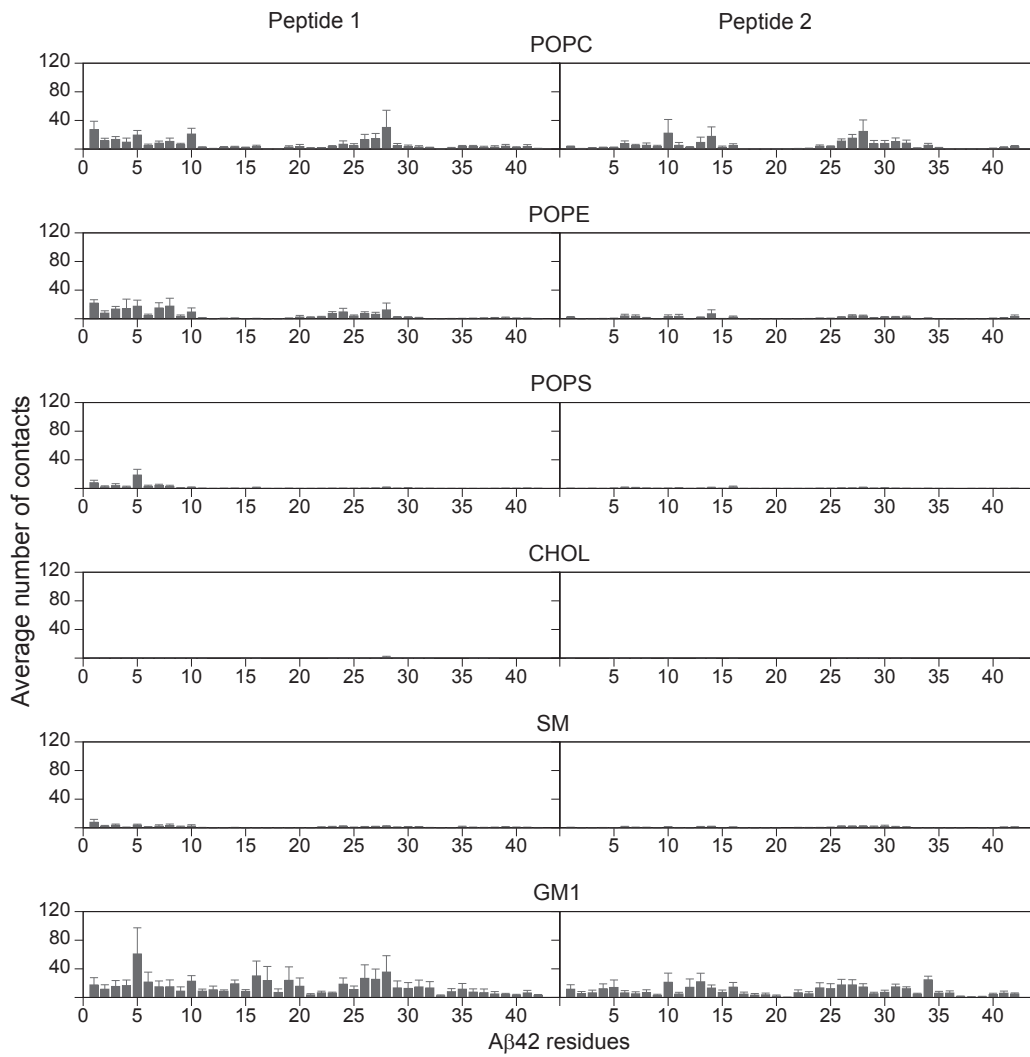


Fig. S6. The average number of A β 42–lipid contacts (and standard error of the mean) calculated for peptide 1 (left) and peptide 2 (right) with each of the components of the neuronal membrane (lipid names shown above the panels).

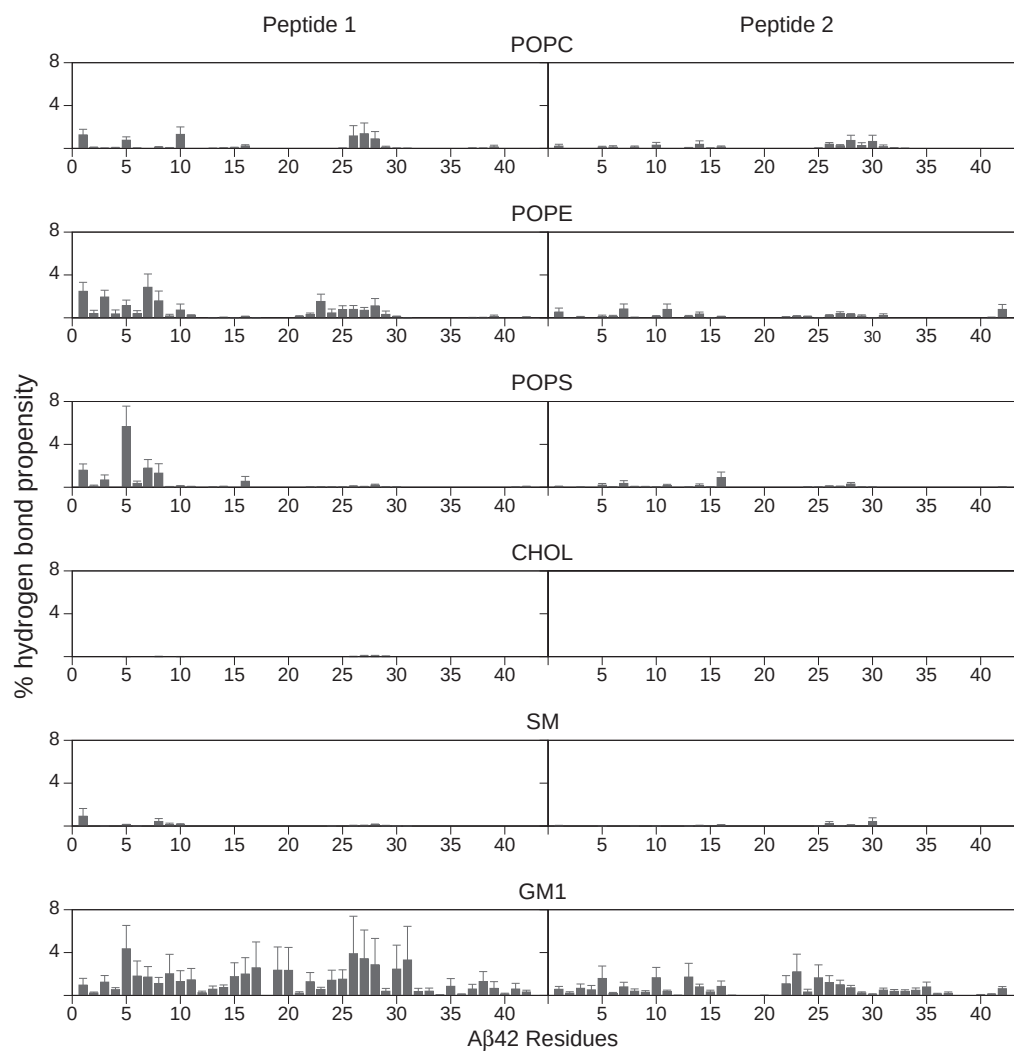


Fig. S7. The average hydrogen bond propensity between A β 42 and lipids (and standard error of the mean) calculated for peptide 1 (left) and peptide 2 (right) with each of the components of the neuronal membrane (lipid names shown above the panels).

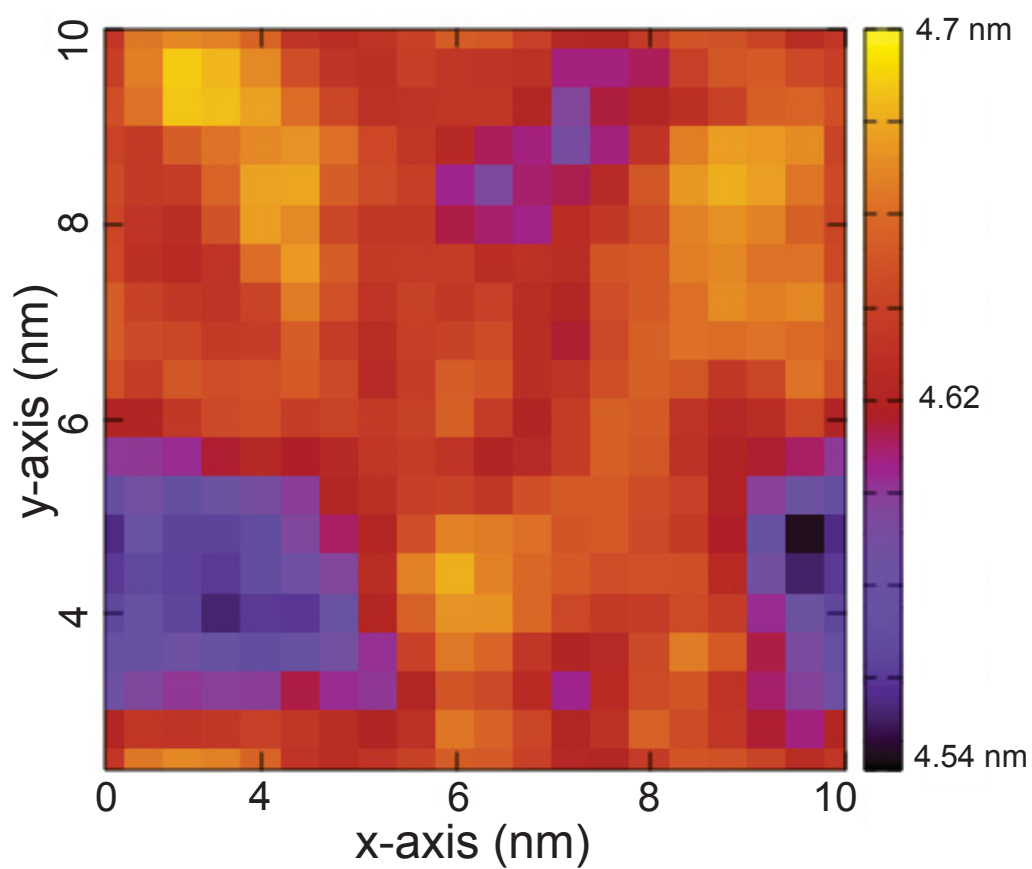


Fig. S8. Average bilayer thickness calculated when the protein is within 0.5 nm of the membrane. The x and the y -axes represent the unit cell dimension in nm. The color bar shows the thickness range in nm.

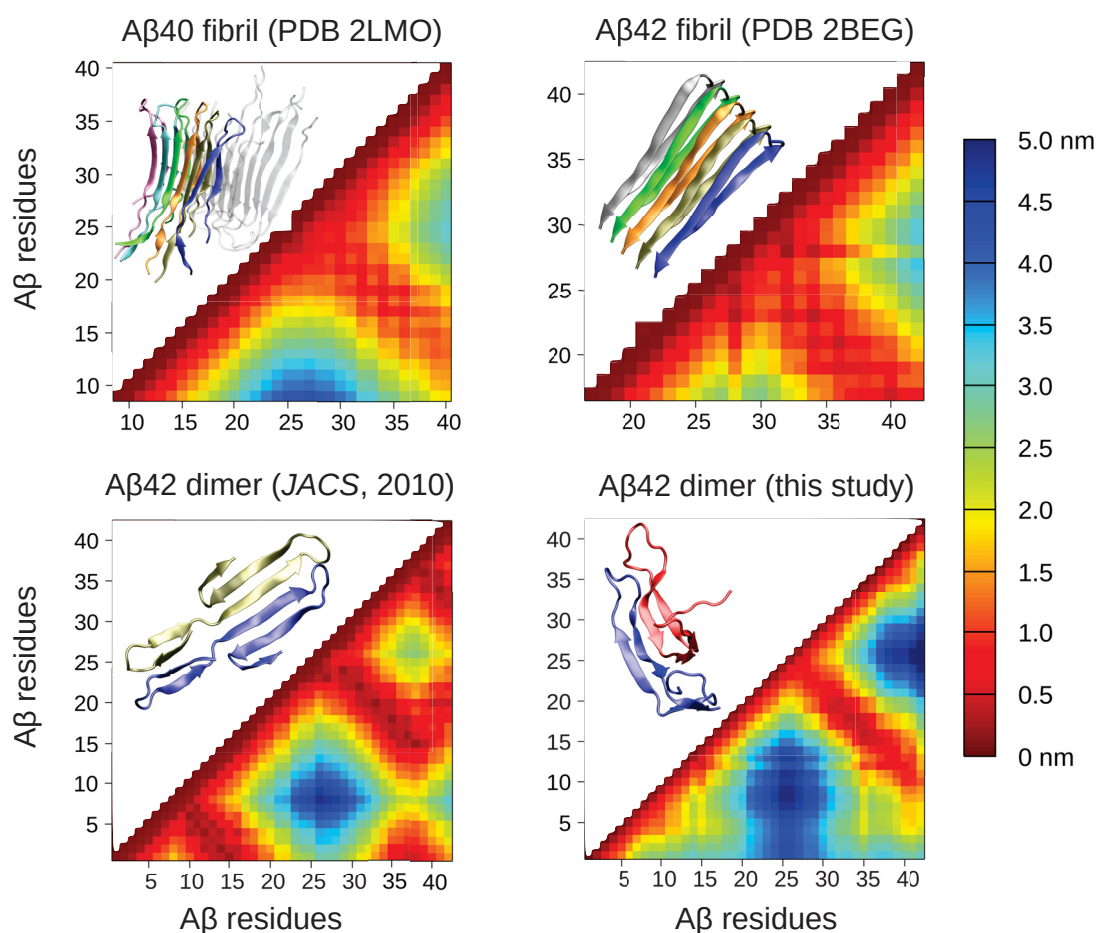


Fig. S9. Comparison of the intrapeptide contacts present in $A\beta$ fibrils (top) and $A\beta$ dimers (bottom). The contacts are provided as minimal distances between the residues of $A\beta$. For the fibrils, the structures from PDB entry 2LMO for $A\beta_{40}$ (ref. 44 in the main text) and PDB entry 2BEG for $A\beta_{42}$ (ref. 43 in the main text) were chosen. Since these fibril models only start with residue 9 for $A\beta_{40}$ and residue 17 for $A\beta_{42}$, the distance presentations are limited to residues G9–V40 and L17–A42, respectively. The corresponding fibril structure is shown as cartoon in the upper left triangle of either plot. The average intrapeptide distance matrix of the $A\beta_{42}$ dimer structures obtained from the MD simulations in solution performed in the current study are shown in the lower right panel. As comparison, the distance matrix of one of the $A\beta_{42}$ dimer structures obtained from a structure prediction approach for transmembrane $A\beta_{42}$ (ref. 46 in the main text) is shown in the lower left panel. Representative dimer structures are shown in both panels. The contacts present in the fibrils and those in the dimers obtained here are very similar for residue numbers $\gtrsim 20$ and are dominated by a β -hairpin centered at G25/S26. Only in the $A\beta_{42}$ fibril (upper right panel), residue D23 forms more contacts with other residues in its vicinity, as it is pointing towards the interior of the fibril in order to enable salt bridge formation with K28. The β -hairpin centered at G25/S26 is also present in the $A\beta_{42}$ dimer model determined by structure prediction for transmembrane $A\beta_{42}$ and is accompanied by two further β -hairpins: an N-terminal one centered at G9/Y10 and a C-terminal one at G37/G38 (lower left panel). These two hairpins are only weakly visible in the distance map for the dimers sampled in the current study (lower right panel).

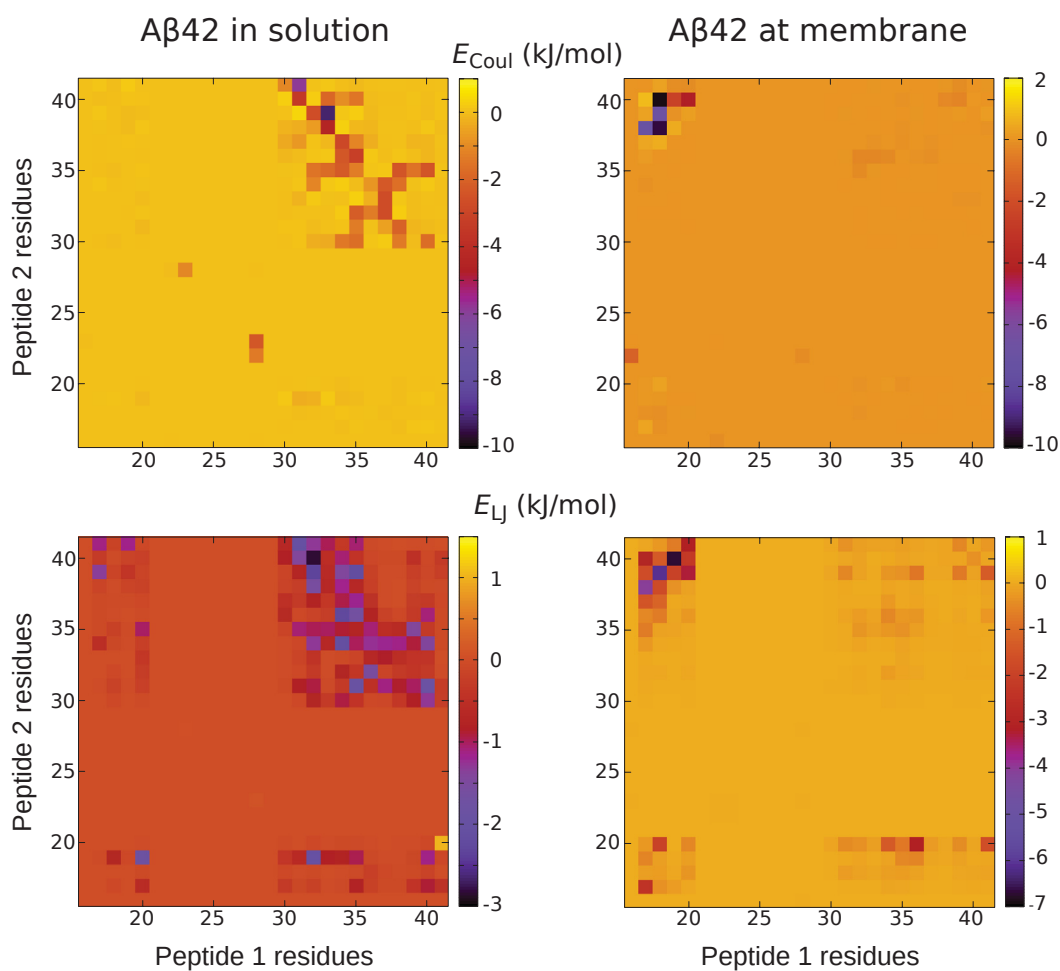


Fig. S10. Average interpeptide interaction energies between residues, decomposed into Coulomb (top) and Lennard-Jones (bottom) interactions, for A β 42 dimers in solution (left) and at the membrane (right). The peptide association in solution is dominated by interactions between the C-terminal regions of both peptides, while the peptides of the membrane-bound dimers mainly interact with each other via the central hydrophobic core of peptide 1 and the C-terminal residues of peptide 2. Please note that results are only shown for residue numbers > 15, as for the N-terminal residues no noteworthy interaction energies were recorded. Moreover, the energy scales in the four plots are slightly different from each other (see color bars) in order to provide a good resolution of the energies.

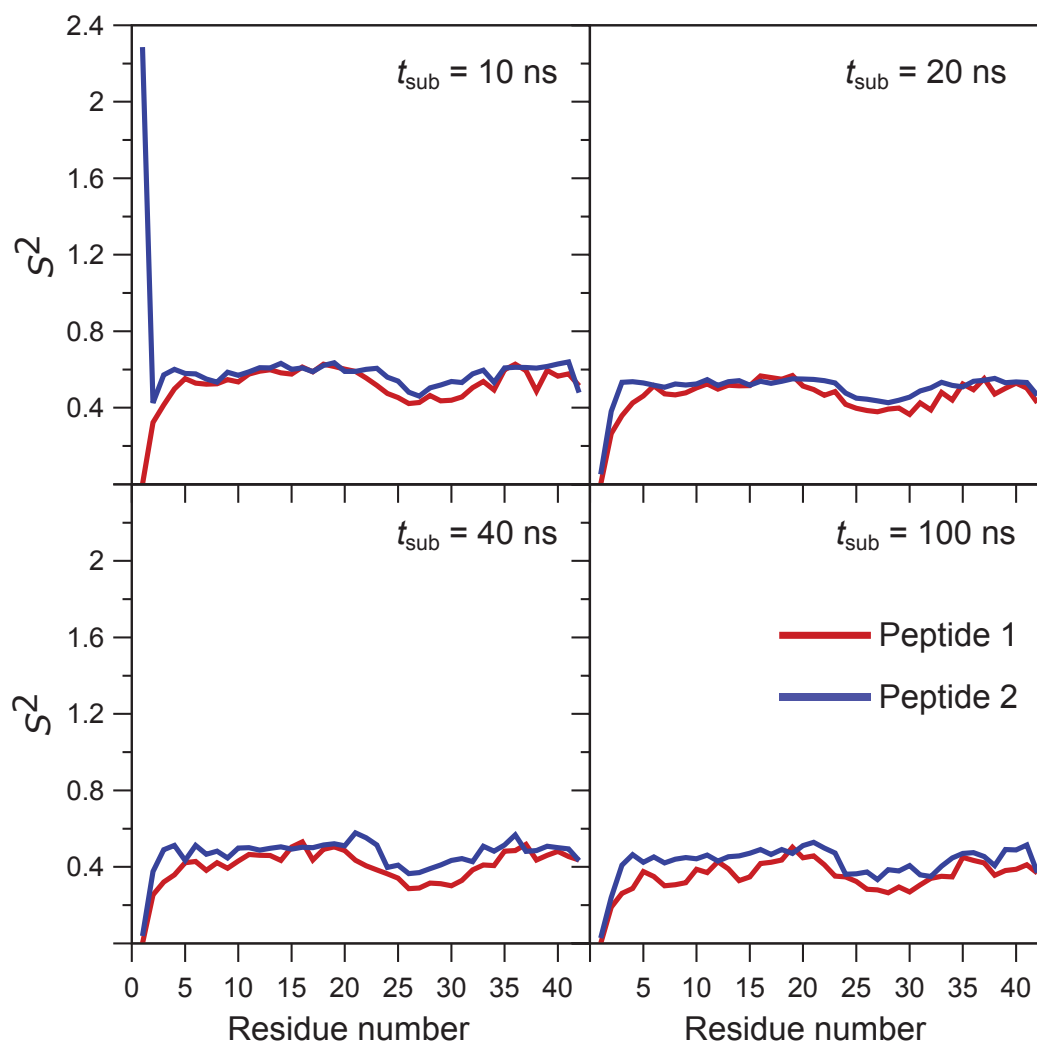


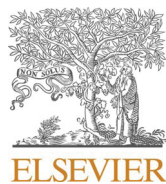
Fig. S11. The average order parameter S^2 of each residue and peptide in the A β 42 dimer at the neuronal membrane. Results are shown for increasing lengths of the subtrajectories, t_{sub} , used for calculating and fitting the N–H bond vector autocorrelation functions. A sufficient level of convergence is reached for $t_{\text{sub}} \geq 40$ ns.

A.2 Publication II

Disorder-to-order transition of the amyloid- β peptide upon lipid binding

Fatafta H., Kav B., Bundschuh B., Loschwitz J., Strodel B. *Biophys Chem.*, 2022

Jan; 280:106700. doi: 10.1016/j.bpc.2021.106700



Disorder-to-order transition of the amyloid- β peptide upon lipid binding

Hebah Fatafta^{a,1}, Batuhan Kav^{a,1}, Bastian F. Bundschuh^b, Jennifer Loschwitz^{a,b},
Birgit Strodel^{a,b,*}

^a Institute of Biological Information Processing (IBI-7: Structural Biochemistry), Forschungszentrum Jülich, 52425 Jülich, Germany

^b Institute of Theoretical and Computational Chemistry, Heinrich Heine University Düsseldorf, Universitätsstrasse 1, 40225 Düsseldorf, Germany

ARTICLE INFO

Keywords:

Amyloid-beta
IDPs
Binding-and-folding process
MD simulations
Amyloid-lipid interactions

ABSTRACT

There is mounting evidence that Alzheimer's disease progression and severity are linked to neuronal membrane damage caused by aggregates of the amyloid- β ($A\beta$) peptide. However, the detailed mechanism behind the membrane damage is not well understood yet. Recently, the lipid-chaperone hypothesis has been put forward, based on which the formation of complexes between $A\beta$ and free lipids enables an easy insertion of $A\beta$ into membranes. In order to test this hypothesis, we performed numerous all-atom molecular dynamics simulations. We studied the complex formation between individual lipids, considering both POPC and DPPC, and $A\beta$ and examined whether the resulting complexes would be able to insert into lipid membranes. Complex formation at a one-to-one ratio was readily observed, yet with minimal effects on $A\beta$'s characteristics. Most importantly, the peptide remains largely disordered in 1:1 complexes, and the complex does not insert into the membrane; instead, it is adsorbed to the membrane surface. The results change considerably once $A\beta$ forms a complex with a POPC cluster composed of three lipid molecules. The hydrophobic interactions between $A\beta$ and the lipid tails cause the peptide to fold into either a helical or a β -sheet structure. These observations provide atomic insight into the disorder-to-order transition that is needed for membrane insertion or amyloid aggregation to proceed.

1. Introduction

Intrinsically disordered proteins (IDPs) are a family of proteins that are generally characterized by lacking a well defined structure. Instead, they are disordered and can adopt a variety of conformations in their physiological environment [1,2]. Interestingly, this disordered nature is essential for IDPs in order to perform diverse biological functions, such as regulation in cell cycling, transcription, and translation [3–6]. Several, if not most, IDPs undergo a function-related disorder-to-order transitions upon binding to a specific interaction partner, allowing them to mediate multiple interactions with different partners in the cell [7–12]. A recent review discussed how such disorder-to-order transitions can be characterized using molecular dynamics (MD) simulations [13]. When misexpressed, mismodified, misprocessed, and/or dysregulated, (IDPs) are connected to the development of various diseases [14], including amyloidosis [15], diabetes [16], and neurodegenerative diseases [17,18] in humans. Notably, many of these diseases are associated with amyloid forming proteins, which are proteins that assemble into pathogenic, insoluble aggregates including oligomers, protofibrils, and

fibrils [19].

One member of the IDP and amyloid-protein families that gained particular attention is the amyloid- β ($A\beta$) peptide, which is strongly linked to the development of Alzheimer's disease (AD) [20,21]. $A\beta$ is generated through the cleavage of the transmembrane amyloid precursor protein [22,23]. It ranges from 39 to 43 amino acids in length, with $A\beta_{42}$ being the predominant alloform in the amyloid fibrils that lead to senile plaques. Moreover, $A\beta_{42}$ is also more toxic than $A\beta_{40}$, which is the most common alloform. Mounting evidence suggests that the toxicity related to $A\beta$ is exerted via abnormal interactions of the $A\beta$ aggregates with the neuronal cell membrane [24,25]. The small-sized amyloid oligomers are found to be more toxic than the mature fibrils [26–28]. Unfortunately, the detailed molecular mechanism of the $A\beta$ -membrane interaction is still not fully resolved. Therefore, further studies aiming to understand these interactions and the resulting membrane-damaging mechanisms are warranted and needed.

Numerous studies that explored $A\beta$ -membrane interactions focused on $A\beta$ in a water-membrane environment. They typically aimed to identify the key players, such as $A\beta$ oligomers or fibrils, and the

* Corresponding author at: Institute of Biological Information Processing (IBI-7: Structural Biochemistry), Forschungszentrum Jülich, 52425 Jülich, Germany.
E-mail address: b.strodel@fz-juelich.de (B. Strodel).

¹ These authors contributed equally.

membrane-damage mechanisms, such as membrane pore formation or detergent-like membrane thinning [29–31]. Common to these studies is that they investigate the behavior of $A\beta$ in a lipid-rich phase, i.e., in the presence of a lipid membrane. However, recent studies demonstrated the crucial role of free lipids, which exist at nanomolar to micromolar concentration in equilibrium with the membrane, in the formation of $A\beta$ -lipid complexes, which enabled an easy membrane insertion for $A\beta$ and also other amyloid proteins [32,33]. Based on these results, La Rosa and coworkers proposed a lipid-chaperone hypothesis as a unifying framework for amyloid-membrane poration [34]. Some experimental and MD studies reported on the stability of peptide-lipid complexes in solution and their role in assisting protein transport into membranes [34,32,35]. In general, lipid-assisted protein transport is overlooked compared to the well documented lipid-carriage by proteins [36–38].

In this study, we perform all-atom MD simulations to investigate two aspects of the lipid-chaperone hypothesis: (i) complex formation between $A\beta_{42}$ and lipid molecules in 1:1 and 1:3 ratios in solution, (ii) interaction of the $A\beta_{42}$ -lipid complexes with pre-assembled lipid membranes. As lipids we chose the most abundant lipids in mammalian cells: 1-palmitoyl-2-oleoyl-sn-glycero-3-phosphocholine (POPC) and 1,2-dipalmitoyl-sn-glycero-3-phosphocholine (DPPC) (Fig. 1). We find that $A\beta_{42}$ forms stable complexes with both lipid molecules. While the peptide remains largely disordered in the 1:1 complexes, it undergoes disordered-to-ordered transitions upon interaction with three lipid molecules. However, on the microsecond timescale of our simulations no membrane insertion is observed for the $A\beta_{42}$ -lipid complexes, while a single lipid can readily integrate into an existing membrane on the same timescale.

2. Methods

2.1. System setup

We performed all-atom MD simulations for three $A\beta_{42}$ -lipid systems: 1:1 complexes in solution, 1:3 complexes in solution, and 1:1 complexes in a membrane environment. For the systems involving 1:1 complexes, we performed two sets of simulations: a reference set and a target set, as described below. The simulations are summarized in Table 1.

2.1.1. 1:1 $A\beta_{42}$ -lipids complexes

We followed the complex formation between $A\beta_{42}$ and a single lipid molecule, either POPC or DPPC, in solution by placing them in a simulation box with an initial minimal distance of 4 nm between them, which was realized with Packmol [39]. This setup defines the target state for the 1:1 complexes, while the reference is a single $A\beta_{42}$ peptide in solution. As starting structure for $A\beta_{42}$ a random-coil conformation was used. It was retrieved from a 30 μ s MD simulation of $A\beta_{40}$ that employed the Amber99SB-UCB force field [40,41]. The two C-terminal residues Ile41 and Ala42 were added to obtain $A\beta_{42}$. Each simulation was run for

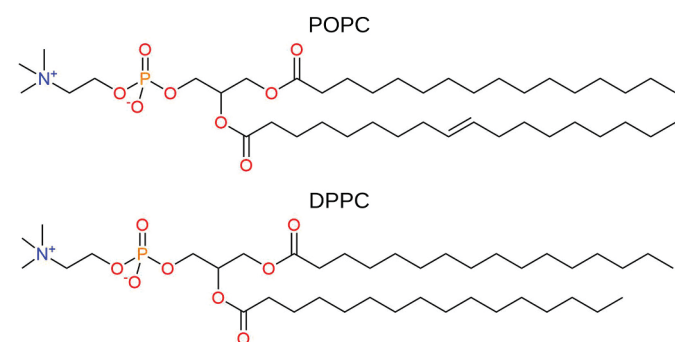


Fig. 1. Chemical 2D-structure of 1-palmitoyl-2-oleoyl-sn-glycero-3-phosphocholine (POPC, top) and 1,2-dipalmitoyl-sn-glycero-3-phosphocholine (DPPC, bottom).

Table 1

Summary of simulations performed in this work.

System	Runs \times length
1 $A\beta_{42}$	$3 \times 1 \mu$ s
1:1 $A\beta_{42}$ -DPPC	$3 \times 1 \mu$ s
1:1 $A\beta_{42}$ -POPC	$3 \times 1 \mu$ s
1:3 $A\beta_{42}$ -POPC	$3 \times 2 \mu$ s
1:1 $A\beta_{42}$ -POPC + POPC membrane	$3 \times 2 \mu$ s
1 $A\beta_{42}$ + POPC membrane	$1 \times 2 \mu$ s
1 POPC + POPC membrane	$1 \times 2 \mu$ s
Total simulation time	25 μs

1 μ s and in triplicate using different initial velocities. The total number of atoms in these systems was $N \approx 50,000$ and the simulation box volume V measured $8.0 \times 8.0 \times 8.0 \text{ nm}^3$.

2.1.2. 1:3 $A\beta_{42}$ -POPC complexes

To study the behavior of $A\beta_{42}$ in the presence of three POPC lipids, we identified the most populated conformation of the 1:1 $A\beta_{42}$ -POPC complex and added two more POPC lipids to it. The two additional POPC molecules were placed randomly using Packmol, with a minimum distance of 4 nm from the existing 1:1 complex and between each other. For this setup, 2 μ s MD simulations were performed in triplicate with different initial velocities. The total number of atoms in these systems was $N \approx 50,000$ and the simulation box volume V measured $8.0 \times 8.0 \times 8.0 \text{ nm}^3$.

2.1.3. 1:1 $A\beta_{42}$ -lipids complexes plus membrane

A lipid bilayer composed of 154 POPC lipids was generated using the CHARMM-GUI interface [42]. The reference set includes two setups: one involving a single $A\beta_{42}$ peptide plus the membrane, the other one including a single POPC lipid plus the membrane. The target system is a 1:1 $A\beta_{42}$ -POPC complex plus the membrane. The peptide, lipid or complex were placed at a minimal distance of 1.0 nm above the bilayer surface in the water layer. All systems were simulated for 2 μ s, and in the case of the target system, the system was simulated in triplicate with different initial velocities. The total number of atoms in these systems was $N \approx 134,000$ atoms and the simulation box volume measured $10.0 \times 10.0 \times 14.0 \text{ nm}^3$.

2.2. Simulation details

The MD simulations were performed using GROMACS version 2018 [43]. $A\beta_{42}$ was modeled using the CHARMM36mW force field [44], as this force field provides acceptable results for the amyloid- β peptide [41] and amyloid aggregation [45]. The CHARMM36 force field [46] was applied to the lipids. All systems were solvated using the TIP3P water model [47,48] and NaCl was added at a physiological concentration of 150 mM. Each system was first energy minimized using the steepest decent algorithm to remove atomic clashes. This was followed by equilibration MD simulations of 0.1 ns length and under NVT conditions where the temperature T was kept at 310 K using a velocity-rescaling thermostat [49]. Next, the systems were equilibrated for 1 ns under NpT conditions to obtain a pressure p of 1.0 bar. The pressure was regulated using the isotropic (for the simulations without a lipid membrane) or semi-isotropic (for the simulations involving a lipid membrane) Parrinello-Rahman pressure coupling scheme [50]. Periodic boundary conditions were applied in all directions and the particle mesh Ewald method [51] was used for calculating the electrostatic interactions. Both the short-range Coulomb interactions and the van der Waals interactions were cut at 1.2 nm in real space.

2.3. Analysis

The analysis of the simulations was performed using a combination of GROMACS tools and the MDTraj library. We calculated the root mean square fluctuations (RMSF) of the $A\beta_{42}$ residues using the GROMACS tool *rmsf*. The secondary structure of the peptide was determined using the DSSP algorithm [52] and time-averages calculated, which are provided as secondary structure propensities. Here, we collectively present α -, π - and 3_{10} -helices as helical propensity, β -bridges are included in the β -strand propensities, and bends and β -turns are collectively shown as turn propensities. The solvent accessible surface area (SASA) of $A\beta_{42}$ was determined using the GROMACS tool *sasa*. We calculated the number of contacts between $A\beta_{42}$ and the lipids, which either form a complex with the peptide or are part of the membrane, using a 0.5 nm distance cutoff between the protein backbone atoms and the lipid atoms (excluding lipid hydrogen atoms). We provide contact probabilities, which are the ratio between the number of MD snapshots with $A\beta_{42}$ -lipid contacts being present and the number of snapshots in the corresponding MD trajectory.

3. Results

3.1. Complex formation between $A\beta_{42}$ and soluble lipids: 1:1 $A\beta_{42}$ -lipid complexes

We investigate the interactions between $A\beta_{42}$ and single POPC or DPPC lipids using unbiased all-atom MD simulations of three distinct systems: a single $A\beta_{42}$ peptide in solution, a single $A\beta_{42}$ peptide with one soluble POPC lipid, and a single $A\beta_{42}$ peptide with one soluble DPPC lipid. For each system, we run three independent simulations, each of which was 1 μ s long. The single $A\beta_{42}$ peptide serves as a reference, to unravel the effects of a POPC or DPPC lipid on the structure of $A\beta_{42}$.

3.1.1. The formation of $A\beta_{42}$ -lipid complexes reduces the peptide flexibility

In all of our simulations involving both an $A\beta_{42}$ peptide and a lipid molecule, a stable protein-lipid complex formed within the first 100 ns and did not dissociate in the rest of the simulations (Fig. S1). This indicates that the lifetimes of these complexes is longer than microseconds. Representative complex snapshots are shown in Fig. 2a and b. To investigate how the complex formation affects the peptide flexibility, we calculated the RMSF of each peptide residue after the $A\beta_{42}$ -lipid complex had formed, and compare these results to the case of a single $A\beta_{42}$ in solution (Fig. 2c). For most residues we observe a reduction in the RMSF upon complex formation. The increase in peptide rigidity is especially pronounced for the hydrophobic regions of $A\beta_{42}$, which are the central hydrophobic core involving residues Leu17–Ala21 and the C-terminal residues Ala30–Ala42. The formation of $A\beta_{42}$ -DPPC complexes imposes more rigidity on $A\beta_{42}$ than complexation with POPC, particularly in the region Asp1–Val24. Furthermore, the calculation of the SASA indicates that the complex formation reduces the peptide's accessibility to the solvent. The SASA values of $A\beta_{42}$ are 45.7 ± 1.3 , 43.9 ± 1.2 and 40.6 ± 1.2 nm² for an individual $A\beta_{42}$ peptide, for $A\beta_{42}$ in complex with a POPC molecule and in complex with a DPPC molecule, respectively. The larger reductions in peptide flexibility and SASA in the case of DPPC as compared to POPC suggest that the interactions between $A\beta_{42}$ and DPPC are stronger and/or involve more $A\beta_{42}$ residues.

3.1.2. Small increase in β -sheet but no helix upon 1:1 complex formation

To characterize the effect of the complex formation on the peptide secondary structure, we calculated both the evolution of the secondary structure per residue (Fig. S2) and the time-averaged secondary structure for the whole peptide (Fig. 2d) and compare the results to the findings for the individual $A\beta_{42}$ peptide. The time-averaged data reveal an increase in turn structures upon complex formation with either lipid. Furthermore, the binding to DPPC, but not POPC, encouraged more

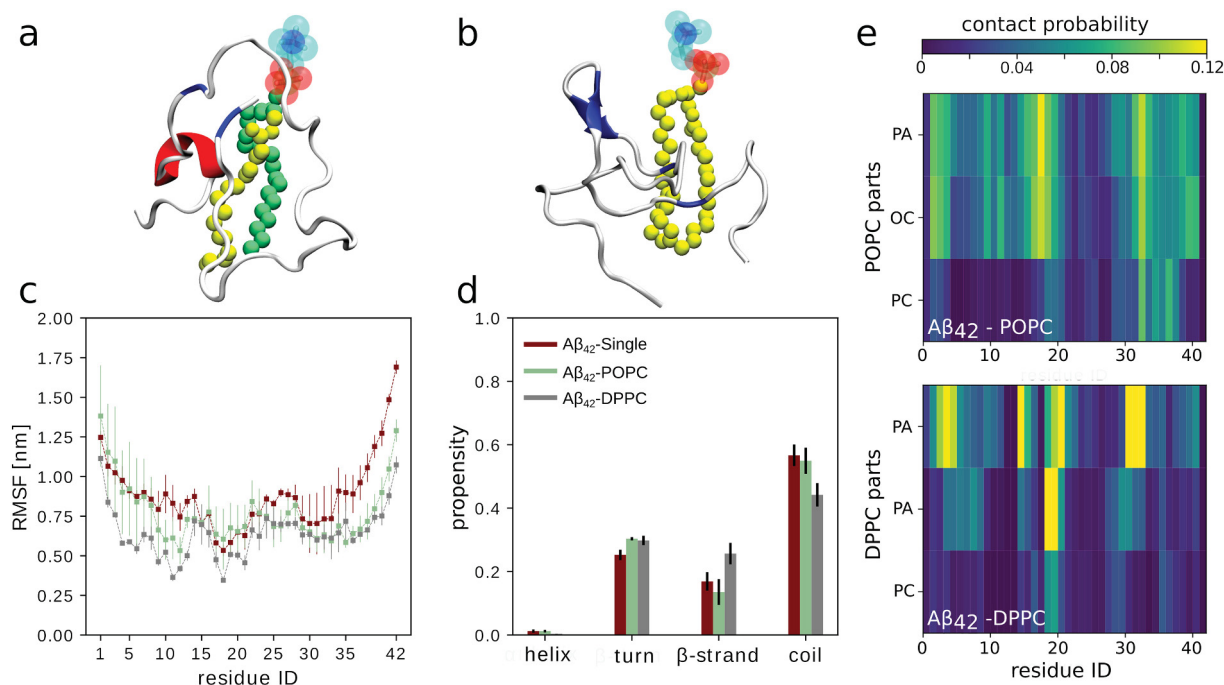


Fig. 2. Summary of the results for the 1:1 $A\beta_{42}$ -lipid complexes. (a) and (b) Snapshot of an $A\beta_{42}$ -POPC and $A\beta_{42}$ -DPPC 1:1 complex, respectively. $A\beta_{42}$ is depicted as cartoon, with the helix being colored in red, β -structures in blue, and the rest in white. POPC and DPPC are shown with spheres, using yellow for the palmitoyl chains, green for the oleoyl chain, red for the phosphatidyl group, and blue for the choline moiety. (c) The average RMSF and (d) the secondary structure propensities of $A\beta_{42}$, where being an individual peptide (red) or in complex with a POPC lipid (green) and DPPC (gray). The values are averaged over three independent runs and error bars represent the standard error of the mean. (e) The average contact probabilities between the $A\beta_{42}$ residues and POPC (top) and DPPC (bottom) in the 1:1 complexes. The lipids are divided into their phosphocholine headgroups (PC) and their tails: the oleoyl (OL) and palmitoyl (PA) chains of POPC and two PA chains in DPPC. The contact probabilities are color-coded according to the color bar at the top. (For interpretation of the references to color in this figure legend, the reader is referred to the web version of this article.)

β -strands to be formed, which happened at the expense of random coil structures. $A\beta_{42}$ shows a very small propensity for helix formation, which almost completely disappears following binding to DPPC. Only the time-evolution plots of the secondary structure shown for each MD simulation (Fig. S2) reveals that also in the presence of DPPC some helical structures existed, yet only for short amounts of time. These plots further disclose that the β -strands that formed in the case of the $A\beta_{42}$ -DPPC complexes are part of a β -sheet that was established in the N-terminal half of the peptide, mainly involving residues Ser8–Phe20 with a turn at His13/His14. This β -sheet was established in all three simulations involving DPPC and in one of the simulations with POPC. However, it was not present in the other two $A\beta_{42}$ -POPC simulations and also not in the simulations of the isolated $A\beta_{42}$ peptide. In the latter, some helix formation is observed in the N-terminal region of $A\beta_{42}$, which disappears upon complex formation with either lipid. In summary, while the time-averaged secondary structure does not indicate large effects on the $A\beta_{42}$ structure, the detailed analysis does show that the $A\beta_{42}$ -lipid interactions change the peptide's structural preferences.

3.1.3. The lipid tails dominate the interaction with $A\beta_{42}$

To elucidate the dominant peptide-lipid interactions, we calculated the contacts between $A\beta_{42}$ residues and the POPC or DPPC lipid. The results in Fig. 2e reflect that the tails of the lipid molecules contribute more to the peptide-lipid contacts than the headgroups. Moreover, both lipid tails of either lipid are involved in contact formation with $A\beta_{42}$. In particular, the oleoyl and the palmitoyl chain of POPC contribute similarly in driving $A\beta_{42}$ -POPC interactions. POPC interacts with many of the $A\beta_{42}$ residues, yet with most of them with a rather low probability, whereas the interaction with DPPC is mainly established by a few but prevailing contacts. In either case, the region Glu22–Gly29, which contains several charged and polar residues and has a tendency to lead to a turn in $A\beta$ conformations, has a very low tendency to interact with the lipids, neither with their headgroups nor the tails. $A\beta_{42}$ binds POPC preferably through residues Ala2–Phe4, Gly9–Glu11, Leu17–Phe30, and

Ile31–Val40, while the binding to DPPC is concentrated on Phe4, Gln15, Val18–Phe20, and Ala30–Ile32. Apart from Gln15, these are all hydrophobic residues, indicating that in the binding with DPPC hydrophobic interactions are more important than in the interaction with the monounsaturated POPC lipid. The $A\beta_{42}$ regions involved in binding to POPC or DPPC are the same residues that exhibit a reduced flexibility.

3.2. Complex formation between $A\beta_{42}$ and soluble lipids: 1:3 $A\beta_{42}$ -lipids complexes

Since the single lipid molecules seem to have no pronounced effects on $A\beta_{42}$, we decided to test whether a few more lipids, which are still in solution and not part of a membrane, can induce structural changes in $A\beta_{42}$. To this end, we added two more POPC lipid molecules to the 1:1 $A\beta_{42}$ -POPC lipid complex, using the most stable 1:1 complex encountered in our simulations as a starting point, and simulated this system three times 2 μ s.

3.2.1. Complex formation with 3 POPC molecules triggers a disorder-to-order transition of $A\beta_{42}$

Similar as for the 1:1 systems, association between the existing 1:1 complex and the two additional POPC molecules is readily observed within the first 50 ns, as revealed by the evolution of the minimal distance between $A\beta_{42}$ and the lipids (Fig. S3). These 1:3 complexes are stable and did not disintegrate in the remainder of the simulations. A major difference between the 1:1 and 1:3 complexes is that in the latter $A\beta_{42}$ underwent a random coil-to-helix transition (in MD run 1) or a random coil-to- β -sheet transition (in MD runs 2 and 3), as the evolution of these structural elements in Fig. 3a shows. In run 1 we observe a high α -helix content, where about 45% of the $A\beta_{42}$ residues adopt a helical conformation after \approx 800 ns of simulation time. Inspection of the helical conformation that formed reveals that it is a helix-kink-helix structure (Fig. 3b), which was stable in the last 200 ns of the simulation. In the other two runs, transient helix formation was observed too, especially in

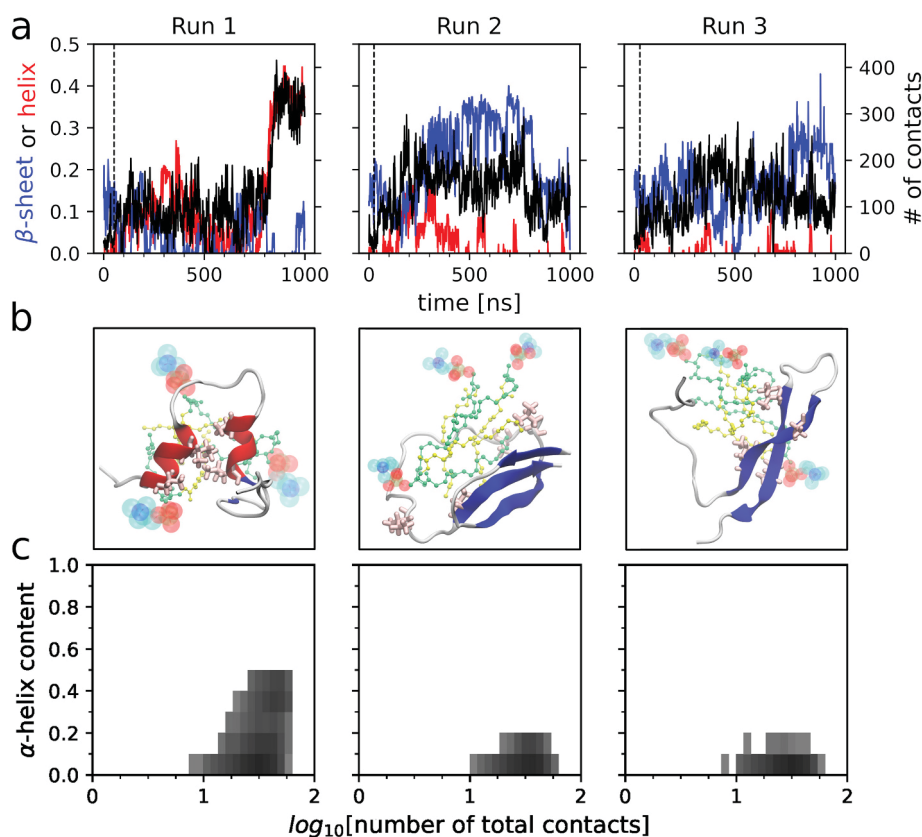


Fig. 3. Summary of the results for the 1:3 $A\beta_{42}$ -POPC complexes. (a) Evolution of the β -sheet (blue) and helix content (red) as well as the number of atom-atom contacts formed between the POPC lipids and $A\beta_{42}$ residues Leu17, Ala21, Ile32, and Val36 obtained from the three simulations of 1:3 $A\beta_{42}$ -POPC complexes. The dashed vertical lines mark time when all three POPC lipids had bound to $A\beta_{42}$. (b) Representative snapshots showing the helix-kink-helix structure that formed at the end of run 1 and β -sheet structures sampled in runs 2 and 3. The peptide is shown as cartoon and the sidechains of Leu17, Ala21, Ile32, and Val36 are explicitly shown. The lipid headgroups are indicated by blue and red spheres, and the oleoyl and palmitoyl chains are represented as ball-and-stick model in green and yellow color, respectively. (c) Two-dimensional histograms of the number of $A\beta_{42}$ -POPC contacts plotted against the α -helix content. The darker the color of a bin, the more likely this contact-helix combination is. (For interpretation of the references to color in this figure legend, the reader is referred to the web version of this article.)

the first 500 ns of run 2, yet in the end the dominating secondary structure were β -sheets. In both run 2 and run 3, at certain times more than 30% of the $A\beta_{42}$ residues are part of a β -sheet. The corresponding structures are shown in Fig. 3b. We can thus conclude that, when $A\beta_{42}$ is surrounded by a sufficient number of lipids, it undergoes a disorder-to-order transition. This is a characteristic of IDPs, which commonly adopt more ordered states upon binding with their targets, which is also known as a coupled binding-and-folding process.

3.2.2. Hydrophobic $A\beta_{42}$ -lipid interactions drive the binding-and-folding process

In order to understand the driving force behind the folding of $A\beta_{42}$ into the helix-kink-helix structure, we calculated the number of contacts formed between the peptide and POPC lipids. The number of these contacts is correlated with the α -helical content (Fig. 3c). For run 1 one can clearly see that the more residues adopt a helical structure, the more contacts between $A\beta_{42}$ and the lipids exist. However, a large number of $A\beta_{42}$ -POPC contacts is not a guarantee for an α -helix to be formed, as for the other two runs, where the helical content did not increase beyond 20%, a similar amount of peptide-lipid contacts were formed. We thus reason that the α -helix content is likely to be correlated with specific residue-POPC contacts, rather than the total number of contacts. In order to test this idea, we calculated the correlation coefficient between the α -helix content and the $A\beta_{42}$ residue-POPC contacts, considering residue singlets, duplets, triplets etc. We increased the number of residue groups until the correlation coefficient did not further improve. For run 1 we find that the contacts between POPC lipids and residues Leu17, Ala21, Ile32, and Val36 have a correlation coefficient of 0.8 with the α -helix content. For run 2, this contact-helix correlation is the highest for the residue pair Leu17 and Ser26, reaching a value of 0.5. Only for run 3, we did not observe any significant correlation (all coefficients < 0.2).

When inspecting the residue-resolved secondary structure evolution, one observes that all the POPC-contacting residues leading to a high correlation coefficient are also part of a helix. This is also highlighted in the representative helix-kink-helix structure that is shown in Fig. 3b. One can see that the helical conformation is stabilized by hydrophobic interactions between the lipid tails and Leu17 and Ala21 of the first helix as well as Ile32 and Val36 of the second helix. To verify this observation, we plotted the evolution of the number of atom-atom contacts formed between POPC and Leu17, Ala21, Ile32, and Val36 along with the evolution of the α -helix content (Fig. 3a). Indeed, from this kind of plot for run 1 we notice that the helical structure is only stable when the mentioned residues are simultaneously in contact with the lipids. In run 2, the amount of these contacts initially rises, leading to a transient increase in the helical content, yet at ≈ 500 ns both the number of these contacts and the helical content drop. Instead, β -sheet structures developed in runs 2 and 3, for which representative structures are shown in Fig. 3b. One can see that β -sheets can develop in different parts of the peptide: between N-terminal and C-terminal residues in run 2 and between hydrophobic stretches that include residues Leu17, Ala21, Ile32, and Val36 in run 3. A difference between the helix-kink-helix structure from run 1 and these two β -sheet structures is that in the latter the three lipids adopted an orientation as in a bilayer, with two of the lipids start forming one leaflet and the third lipid would be part of the opposite leaflet. In run 1, on the other hand, the three lipids rather interact with $A\beta_{42}$ than with themselves. This observation suggests that $A\beta_{42}$ -lipid interactions in solution can encourage α -helix formation, which might in turn cause $A\beta_{42}$ to enter the lipid membrane, as proposed by the lipid-chaperone hypothesis [34], and once fully inserted into the membrane, it converts into β -sheets with the strands being parallel to the lipid tails, as can be seen in Fig. 3b.

3.3. Interaction between the complexes and a lipid bilayer

To examine if the $A\beta_{42}$ -lipid complexes can indeed enhance the peptide insertion into a lipid membrane, we simulated the most stable

$A\beta_{42}$ -POPC lipid complex from the preceding 1:1 complex simulations in the presence of a POPC bilayer. For comparison, we also simulated a single $A\beta_{42}$ peptide and a single POPC lipid placed above a POPC membrane. For the latter, i.e., the reference systems, we performed one 2 μ s MD simulation each, while for the target system we run three independent 2 μ s MD simulations.

3.3.1. A POPC lipid inserts into the membrane but not $A\beta_{42}$

Upon visualizing the trajectories we observed that all simulated entities, i.e., $A\beta_{42}$, a single POPC lipid, and the $A\beta_{42}$ -POPC complex interacted with the lipid bilayer (Fig. S4). After a few attempts, the single POPC lipid even fully inserted into the lipid bilayer after 950 ns of simulation time. We show the intermediate steps occurring during the insertion process in Fig. 4. At $t = 940$ ns, the first contact between the lipid and the membrane, which eventually leads to successful insertion, is established via the palmitoyl chain. This causes the lipid to rotate by $\approx 90^\circ$, aligning it parallel to the membrane surface. Only one nanosecond later, the oleoyl chain has inserted into the headgroup region, making contact with the hydrophobic membrane core. The palmitoyl chain follows suit and also starts inserting into the membrane at $t = 945$ ns. This encourages the full insertion of the POPC lipid into the membrane, which is completed at $t = 950$ ns. Thus, the insertion process itself lasted only 10 ns. Together with the fact, that this event was recorded within a microsecond of simulation time, this indicates that such insertion processes can take place on a (sub)microsecond timescale if a molecule has a high driving force to enter into a membrane. In other words, if $A\beta_{42}$, alone or in complex with a lipid, should have a low free energy barrier to insert into a lipid membrane, we should be able to simulate this event by standard MD simulations.

However, the $A\beta_{42}$ peptide did not insert into the membrane, also not when in complex with a POPC lipid. In these cases, only membrane adsorption is observed. Representative snapshots for these events are shown in Fig. 5a. That no membrane insertion occurred is evident from the average minimum z -coordinate (the bilayer normal is along the z -axis) of the peptide residues (Fig. 5b). We observe that parts of $A\beta_{42}$ when in complex with POPC can insert more deeply into the membrane than the single $A\beta_{42}$ peptide. This insertion is especially pronounced around residue Tyr10 and Gly25-Met35. These involve some of the residue regions that have significant contacts with the oleoyl and palmitoyl chains of the POPC lipid that is in complex with the peptide (Fig. 2e), which suggests that the single lipid is directly involved in the membrane insertion of $A\beta_{42}$. This assumption is further confirmed by the representative snapshot in Fig. 5a (bottom) that shows that the single POPC lipid mediates some of the $A\beta_{42}$ -membrane contacts. Moreover, as $A\beta_{42}$ has an overall charge of -3 , it also screens the electrostatic repulsion between the peptide and the negatively charged phosphate groups of the POPC membrane, enabling a larger contact area between $A\beta_{42}$ and the membrane to be formed. This can be deduced from the insertion depth in Fig. 5b and the representative snapshots in Fig. 5a for the membrane-adsorbed single peptide and the $A\beta_{42}$ -lipid complex, respectively.

The average contacts occurring between $A\beta_{42}$ and the lipid bilayer also reveal more intimate membrane interactions for the $A\beta_{42}$ peptide when in complex with a POPC lipid (Fig. 5c). First of all, in this case $A\beta_{42}$ forms more contacts with the lipid bilayer than an individual $A\beta_{42}$ peptide. These differences are most pronounced in the regions Arg5-Gln15 and Gly25-Met35, which are the same residues that insert most deeply into the membrane in the case of the $A\beta_{42}$ -POPC complex. By far the most contacts are formed by Tyr10, suggesting that this residue might play a key role in the membrane insertion of $A\beta_{42}$. Regarding the single $A\beta_{42}$ peptide, residues Asp1-Arg5 and Gln15-Gly25 are the ones that form more contacts with the lipid bilayer than the other residues, also in comparison to the same residues in the 1:1 complex. These observations clearly demonstrate the different interaction patterns between $A\beta_{42}$ and the POPC bilayer, depending on whether or not $A\beta_{42}$ is in a bound complex with a lipid.

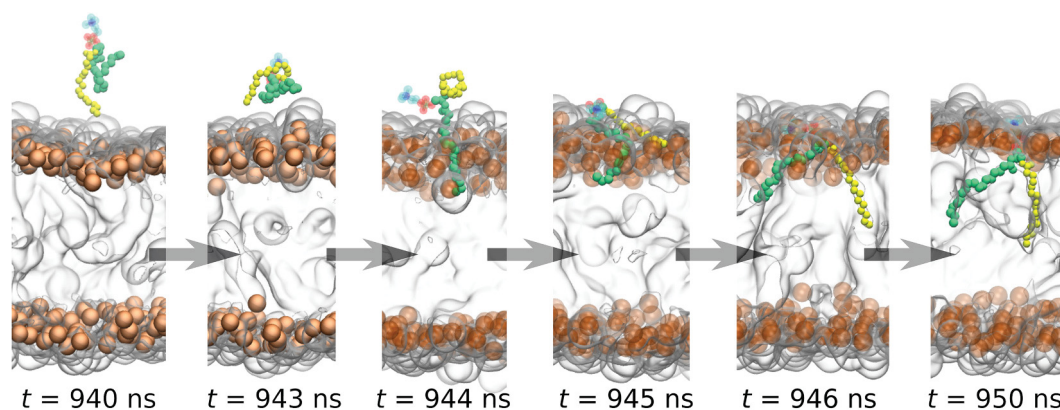


Fig. 4. Snapshots of a POPC molecule inserting into a POPC membrane. At $t = 940$ ns the first contact between the POPC lipid and membrane was established and at $t = 950$ ns the insertion was completed. The oleoyl and palmitoyl chains of the inserting lipid are shown in green and yellow, respectively. The POPC membrane is shown as translucent surface, with the lipid phosphate groups being indicated by orange spheres. (For interpretation of the references to color in this figure legend, the reader is referred to the web version of this article.)

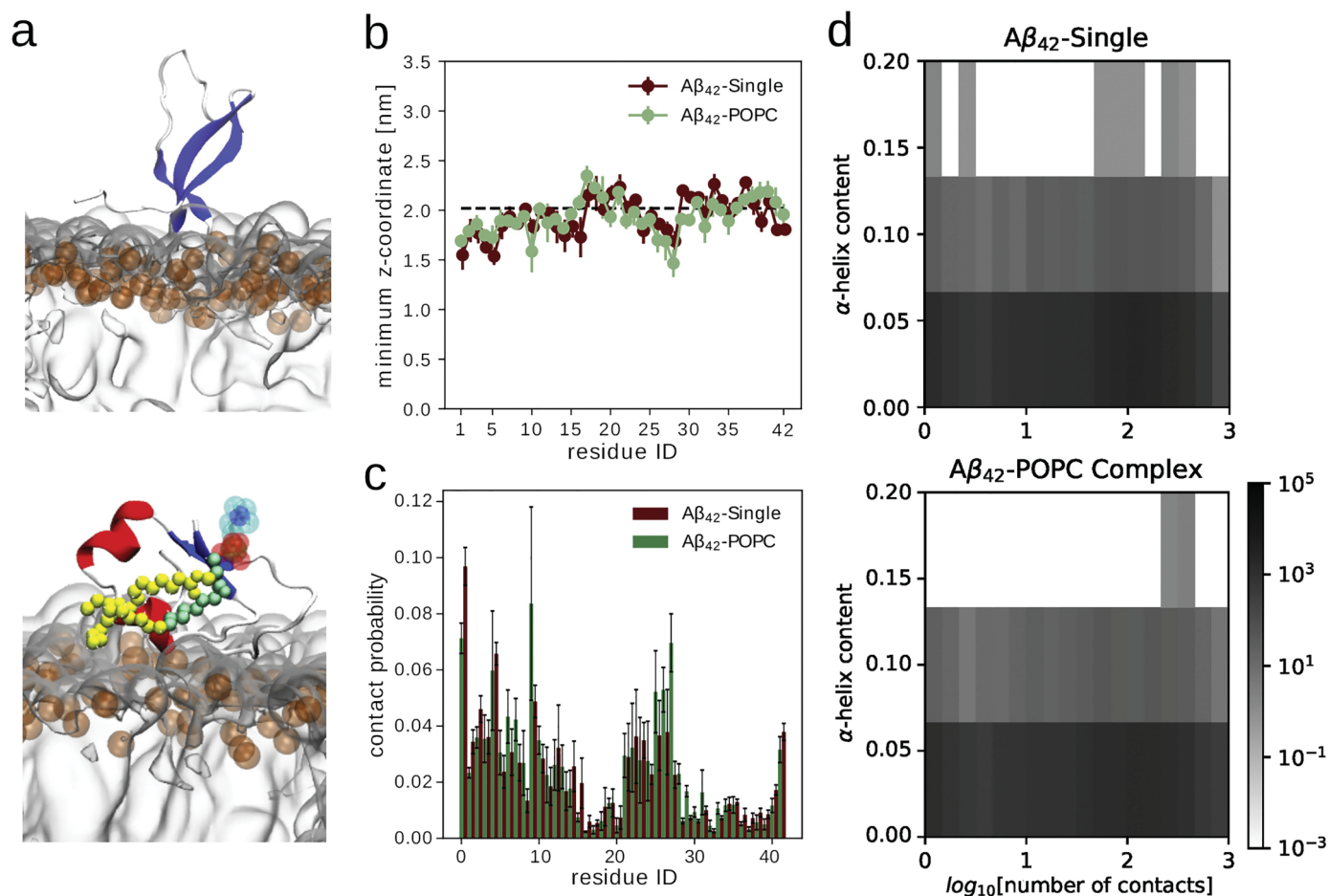


Fig. 5. Summary of the results for the membrane simulations. (a) Snapshots of $A\beta_{42}$ interacting with the POPC membrane, either for the individual peptide (top) or as part of the $A\beta_{42}$ -POPC lipid complex (bottom). The same representations for the peptide, lipid, and membrane as in the previous figures were applied. (b) The minimum z -coordinates of the peptide residues for $A\beta_{42}$ alone (red) and when in complex with a POPC lipid (green). The horizontal dashed line indicates the membrane surface, which is calculated as the half of the distance between the lipid-headgroup density profile peaks. (c) The corresponding probabilities of contact formation between the $A\beta_{42}$ residues and the POPC membrane. The values are averaged over three independent runs and error bars represent the standard error of the mean. (d) Two-dimensional histograms of the number of $A\beta_{42}$ -membrane contacts plotted against the α -helix content. The darker the color of a bin, the more likely this contact-helix combination is (number of occurrences according to the color bar). (For interpretation of the references to color in this figure legend, the reader is referred to the web version of this article.)

3.3.2. The $A\beta_{42}$ -membrane interactions lead to $A\beta_{42}$ folding

The differences between the two systems further manifest themselves in the structural preferences of $A\beta_{42}$. The evolution of the secondary

structure per residue (Fig. S5) reveals a preference for β -sheet formation for the individual $A\beta_{42}$ peptide interacting with the membrane, while in addition to β -sheets also helices form when a POPC lipid is bound to the

membrane-interacting $A\beta_{42}$ peptide. This reinforces the observation from the 1:3 complex simulations that lipid binding to $A\beta_{42}$ can cause a coil-to-helix transition. However, the helical structure encountered in the membrane simulation is different from the helix-kink-helix structure described above. Here, the highest helical propensity resulted between residues Phe20 and Met35, which include the region with the deepest insertion into the membrane. This again suggests that membrane insertion of $A\beta_{42}$ is likely to take place via a helical structure; a possible beginning of this process might be presented by the snapshot shown in Fig. 5a (bottom). Without the extra POPC lipid, very few helices formed in the simulations (Fig. S5). Instead, an increased amount of β -sheets were found compared to the individual peptide or when in complex with a single POPC lipid (Fig. S2). However, the β -sheet structures did not insert into the membrane, but rather adsorbed to its surface, as can be seen in the representative snapshot in Fig. 5a (top).

In order to confirm our observation that helix formation and $A\beta_{42}$ -membrane interactions are indeed correlated, we calculated the helical content and plotted this quantity against the number of contacts that formed between $A\beta_{42}$ and the membrane (Fig. 5d). In both systems the amount of helix increases with increasing $A\beta_{42}$ -membrane contacts. This effect is more pronounced for the $A\beta_{42}$ -POPC complex, where helix formation is already observed when only few contacts between the peptide and the membrane are present. This suggests that the helix formation is a cooperative effect exerted by the single lipid and the membrane on $A\beta_{42}$. This bears similarities with the effects that the three lipids can have on the peptide in a 1:3 complex; however, the amount of helix observed here does not reach beyond 20%, while in run 1 of the 1:3 complex simulations, $\approx 45\%$ of the residues adopted a helical state.

In summary, while no deep membrane insertion of $A\beta_{42}$ was observed here, our results provide evidence on the possible membrane insertion mechanism of the $A\beta_{42}$ peptide, which is likely to proceed via a helical structure and is assisted by bound lipids.

4. Discussion and conclusion

Our simulations revealed the formation of stable complexes between $A\beta_{42}$ and lipids in 1:1 and 1:3 ratios. This observation is in good agreement with the MD studies by La Rosa and coworkers [35,34] who also reported the formation of stable protein-lipid complexes for $A\beta_{40}$, $A\beta_{42}$, human and rat amylin. Our findings highlight that $A\beta_{42}$ remains largely disordered when in complex with only one POPC or DPPC lipid, whereas the binding of three lipid molecules triggers a disorder-order transition upon which the peptide folds into either a helical or β -sheet structure. This observation partly agrees with the findings by La Rosa *et al.* who reported an increase in helical content upon $A\beta$ -lipid complex formation. An α -helical content of 45% developed in one of our triplicate simulations of the 1:3 $A\beta_{42}$ -POPC complexes. It is a helix-kink-helix structure, which is stabilized by hydrophobic interactions between the lipid tails and the hydrophobic residues Leu17, Ala21, Ile32, and Val36. Similar $A\beta$ structures have also been predicted from NMR experiments of the micelle-bound peptide [53–57]. In fact, in our simulations this helical structure is only stable when the mentioned residues were simultaneously in contact with the lipids. This lets us conclude that $A\beta$'s hydrophobicity is not sufficient for its folding by itself, but it can do so following its binding to a hydrophobic interaction partner. This is a typical behavior of IDPs where conformation switching can be induced by binding of an IDP to an interaction partner [13]. Another characteristic of IDPs is that the resulting structure following binding can vary depending on the interaction partner [58]. Such binding plasticity is also found here for $A\beta_{42}$, as it can as well fold into a β -sheet following its binding to three POPC lipids.

The complex stability in solution encouraged us to address its likelihood to drive insertion of $A\beta_{42}$ into a lipid membrane, especially when considering our observation of a single POPC lipid inserting into a POPC membrane within a microsecond of simulation, where the insertion event itself was completed within 10 ns. However, within 2 μ s of our all-atom MD simulations, the peptide did not fully insert into the POPC

membrane, neither when simulated as individual peptide, nor when in complex with a POPC lipid. Nonetheless, the presence of a POPC lipid bound to $A\beta_{42}$ did have some effects on the membrane-bound $A\beta_{42}$. First, it encouraged the formation of a helical structure, whereas without the lipid random coil and β -sheets were the dominating structures. Second, the helical structure in complex with a lipid was able to dip deeper into the membrane than the peptide alone. Despite the absence of full membrane insertion in our simulations, these observations indicate, as suggested by the lipid-chaperone hypothesis [35,34], that $A\beta_{42}$ -lipid complex formation decreases the energy barrier for membrane insertion. Moreover, it encourages $A\beta_{42}$ to fold into a helical structure that seems to be needed for membrane insertion [53–57,59].

For the membrane-bound $A\beta_{42}$ we recorded β -sheet formation when not in complex with an additional lipid. This finding contrasts to our recent study of $A\beta_{42}$ dimerization at a neuronal membrane [60]. While we observed a random coil to β -sheet transition upon dimerization that seems on pathway to amyloid aggregation in solution, the interactions with the neuronal membrane decreased the order of the $A\beta_{42}$ dimer by attenuating its propensity to form a β -sheet structure. This results from the interactions of $A\beta_{42}$ with the surface-exposed sugar groups of the gangliosides GM1, which turned out to be the main interaction partners of $A\beta_{42}$. This shows that in our future studies testing the lipid-chaperone hypothesis, we should and will include more realistic cell membrane models. Moreover, we will also study the effects of $A\beta_{42}$ -lipid complexes with higher lipid ratios, as the current results of the 1:3 complexes already indicate that under these circumstances the lipids have a more pronounced effect. Finally, while our simulations are already on the microsecond timescale, future simulations on the same subject should be even longer, lasting for tens of microseconds, and the application of enhanced sampling methods should be considered too [61,62].

Declaration of Competing Interest

The authors declare that they have no known competing financial interests or personal relationships that could have appeared to influence the work reported in this paper.

Acknowledgments

H.F. and B.S. acknowledge funding for this project from the Palestinian-German Science Bridge financed by the German Federal Ministry of Education and Research. J.L. and B.S. received funding for this project from the Deutsche Forschungsgemeinschaft (German Research Foundation, <https://www.dfg.de/>) through Grant 267205415 (CRC 1208, Project A07). Computational infrastructure and support for performing the MD simulations were provided by the Centre for Information and Media Technology at Heinrich Heine University Düsseldorf.

Appendix A. Supplementary data

Supplementary data to this article can be found online at <https://doi.org/10.1016/j.bpc.2021.106700>.

References

- [1] A.K. Dunker, J.D. Lawson, C.J. Brown, R.M. Williams, P. Romero, J.S. Oh, C. J. Oldfield, A.M. Campen, C.M. Ratliff, K.W. Hipps, et al., Intrinsically disordered protein, *J. Mol. Graphics Modell.* 19 (1) (2001) 26–59.
- [2] D. Eliezer, Biophysical characterization of intrinsically disordered proteins, *Curr. Opin. Struct. Biol.* 19 (1) (2009) 23–30.
- [3] M.-K. Yoon, D.M. Mitrea, L. Ou, R.W. Kriwacki, Cell cycle regulation by the intrinsically disordered proteins p21 and p27, *Biochem. Soc. Trans.* 40 (5) (2012) 981–988.
- [4] A.S. Garza, N. Ahmad, R. Kumar, Role of intrinsically disordered protein regions/ domains in transcriptional regulation, *Life Sci.* 84 (7–8) (2009) 189–193.
- [5] A. Bah, R.M. Vernon, Z. Siddiqui, M. Krzeminski, R. Muhandiram, C. Zhao, N. Sonenberg, L.E. Kay, J.D. Forman-Kay, Folding of an intrinsically disordered protein by phosphorylation as a regulatory switch, *Nature* 519 (7541) (2015) 106–109.
- [6] H.J. Dyson, P.E. Wright, Intrinsically unstructured proteins and their functions, *Nat. Rev. Mol. Cell Biol.* 6 (3) (2005) 197–208.

- [7] K. Rajagopalan, R. Qiu, S.M. Mooney, S. Rao, T. Shiraishi, E. Sacho, H. Huang, E. Shapiro, K.R. Weninger, P. Kulkarni, The stress-response protein prostate-associated gene 4, interacts with c-jun and potentiates its transactivation, *Biochim. Biophys. Acta Mol. Basis Dis.* 1842 (2) (2014) 154–163.
- [8] P. Kulkarni, M.K. Jolly, D. Jia, S.M. Mooney, A. Bhargava, L.T. Kagohara, Y. Chen, P. Hao, Y. He, R.W. Veltri, et al., Phosphorylation-induced conformational dynamics in an intrinsically disordered protein and potential role in phenotypic heterogeneity, *Proc. Natl. Acad. Sci. U.S.A.* 114 (13) (2017) E2644–E2653.
- [9] X. Lin, P. Kulkarni, F. Bocci, N.P. Schafer, S. Roy, M.-Y. Tsai, Y. He, Y. Chen, K. Rajagopalan, S.M. Mooney, et al., Structural and dynamical order of a disordered protein: molecular insights into conformational switching of page4 at the systems level, *Biomolecules* 9 (2) (2019) 77–95.
- [10] D. Parker, K. Ferreri, T. Nakajima, V. LaMorte, R. Evans, S. Koerber, C. Hoeger, M. Montminy, Phosphorylation of creb at ser-133 induces complex formation with creb-binding protein via a direct mechanism, *Mol. Cell. Biol.* 16 (2) (1996) 694–703.
- [11] D. Parker, M. Rivera, T. Zor, A. Henrion-Caude, I. Radhakrishnan, A. Kumar, L. H. Shapiro, P.E. Wright, M. Montminy, P.K. Brindle, Role of secondary structure in discrimination between constitutive and inducible activators, *Mol. Cell. Biol.* 19 (8) (1999) 5601–5607.
- [12] H. Liu, X. Guo, J. Han, R. Luo, H.-F. Chen, Order–disorder transition of intrinsically disordered kinase inducible transactivation domain of creb, *J. Chem. Phys.* 148 (22) (2018) 225101.
- [13] B. Strodel, Energy landscapes of protein aggregation and conformation switching in intrinsically disordered proteins, *J. Mol. Biol.* 433 (20) (2021) 167182.
- [14] P. Kulkarni, V.N. Uversky, Intrinsically disordered proteins in chronic diseases, *Biomolecules* 9 (4) (2019) 147.
- [15] V.N. Uversky, Amyloidogenesis of natively unfolded proteins, *Curr. Alzheimer Res.* 5 (3) (2008) 260–287.
- [16] Z. Du, V.N. Uversky, A comprehensive survey of the roles of highly disordered proteins in type 2 diabetes, *Int. J. Mol. Sci.* 18 (10) (2017) 2010.
- [17] V.N. Uversky, The triple power of d (3): protein intrinsic disorder in degenerative diseases, *Front Biosci. (Landmark Ed)* 19 (2014) 181–258.
- [18] V.N. Uversky, Intrinsic disorder in proteins associated with neurodegenerative diseases, *Front Biosci. (Landmark Ed)* 14 (14) (2009) 5188–5238.
- [19] F. Chiti, C.M. Dobson, Protein misfolding, functional amyloid, and human disease, *Annu. Rev. Biochem.* 75 (2006) 333–366.
- [20] M. Querol-Vilaseca, M. Colom-Cadena, J. Pegueroles, R. Nuñez-Llaves, J. Luque-Cabeceras, L. Muñoz-Llahuna, J. Andilla, O. Belbin, T.L. Spires-Jones, E. Gelpi, et al., Nanoscale structure of amyloid- β plaques in Alzheimer's disease, *Sci. Rep.* 9 (1) (2019) 1–10.
- [21] G.K. Gouras, C.G. Almeida, R.H. Takahashi, Intraneuronal $\alpha\beta$ accumulation and origin of plaques in Alzheimer's disease, *Neurobiol. Aging* 26 (9) (2005) 1235–1244.
- [22] S. Sadigh-Eteghad, B. Sabermarouf, A. Majidi, M. Talebi, M. Farhoudi, J. Mahmoudi, Amyloid-beta: a crucial factor in Alzheimer's disease, *Med. Princ. Prac.* 24 (1) (2015) 1–10.
- [23] P.H. Reddy, M.F. Beal, Amyloid beta, mitochondrial dysfunction and synaptic damage: implications for cognitive decline in aging and Alzheimer's disease, *Trends Mol. Med.* 14 (2) (2008) 45–53.
- [24] S.J.C. Lee, E. Nam, H.J. Lee, M.G. Savelieff, M.H. Lim, Towards an understanding of amyloid- β oligomers: characterization, toxicity mechanisms, and inhibitors, *Chem. Soc. Rev.* 46 (2) (2017) 310–323.
- [25] M.C. Owen, D. Gnut, M. Gao, S.K. W&lquo;arml&rquo;ander, J. Jarvet, A. Gr&lquo;aslund, R. Winter, S. Ebbinghaus, B. Strodel, Effects of in vivo conditions on amyloid aggregation, *Chem. Soc. Rev.* 48 (14) (2019) 3946–3996.
- [26] C.A. McLean, R.A. Cherny, F.W. Fraser, S.J. Fuller, M.J. Smith, K. Vbeyreuther, A. I. Bush, C.L. Masters, Soluble pool of $\alpha\beta$ amyloid as a determinant of severity of neurodegeneration in Alzheimer's disease, *Ann. Neurol.* 46 (6) (1999) 860–866.
- [27] M.D. Kirkitadze, G. Bitan, D.B. Teplow, Paradigm shifts in Alzheimer's disease and other neurodegenerative disorders: the emerging role of oligomeric assemblies, *J. Neurosci. Res.* 69 (5) (2002) 567–577.
- [28] K. Broersen, F. Rousseau, J. Schymkowitz, The culprit behind amyloid beta peptide related neurotoxicity in Alzheimer's disease: oligomer size or conformation? *Alzheimer's Res. Ther.* 2 (4) (2010) 1–14.
- [29] A.D. Korczyn, The amyloid cascade hypothesis, *Alzheimer's Dement.* 4 (3) (2008) 176–178.
- [30] C. Reitz, Alzheimer's disease and the amyloid cascade hypothesis: a critical review, *Int. J. Alzheimer's Dis.* 2012 (2012), 369808.
- [31] E.N. Cline, M.A. Bicca, K.L. Viola, W.L. Klein, The amyloid- β oligomer hypothesis: beginning of the third decade, *J. Alzheimers Dis.* 64 (s1) (2018) S567–S610.
- [32] F. Scollo, C. Tempira, F. Lolicato, M.F. Sciacca, A. Raudino, D. Milardi, C. La Rosa, Phospholipids critical micellar concentrations trigger different mechanisms of intrinsically disordered proteins interaction with model membranes, *J. Phys. Chem. Lett.* 9 (17) (2018) 5125–5129.
- [33] F. Scollo, C. La Rosa, Amyloidogenic intrinsically disordered proteins: new insights into their self-assembly and their interaction with membranes, *Life* 10 (8) (2020) 144.
- [34] M.F. Sciacca, F. Lolicato, C. Tempira, F. Scollo, B.R. Sahoo, M.D. Watson, S. García-Viñuales, D. Milardi, A. Raudino, J.C. Lee, et al., Lipid-chaperone hypothesis: a common molecular mechanism of membrane disruption by intrinsically disordered proteins, *ACS Chem. Neurosci.* 11 (24) (2020) 4336–4350.
- [35] C. La Rosa, S. Scalisi, F. Lolicato, M. Pannuzzo, A. Raudino, Lipid-assisted protein transport: a diffusion–reaction model supported by kinetic experiments and molecular dynamics simulations, *J. Chem. Phys.* 144 (18) (2016) 184901.
- [36] M.B. Rone, J. Fan, V. Papadopoulos, Cholesterol transport in steroid biosynthesis: role of protein-protein interactions and implications in disease states, *Biochim. Biophys. Acta* 1791 (7) (2009) 646–658.
- [37] J. Sandhu, S. Li, L. Fairall, S.G. Pfisterer, J.E. Gurnett, X. Xiao, T.A. Weston, D. Vashi, A. Ferrari, J.L. Orozco, et al., Aster proteins facilitate nonvesicular plasma membrane to ER cholesterol transport in mammalian cells, *Cell* 175 (2) (2018) 514–529.
- [38] M.S. Abreu, L.M. Estronca, M.J. Moreno, W.L. Vaz, Binding of a fluorescent lipid amphiphile to albumin and its transfer to lipid bilayer membranes, *Biophys. J.* 84 (1) (2003) 386–399.
- [39] L. Martínez, R. Andrade, E.G. Birgin, J.M. Martínez, Packmol: a package for building initial configurations for molecular dynamics simulations, *J. Comput. Chem.* 30 (13) (2009) 2157–2164, <https://doi.org/10.1002/jcc.21224>.
- [40] P. Robustelli, S. Piana, D. Shaw, Developing a molecular dynamics force field for both folded and disordered protein states, *Proc. Natl. Acad. Sci. U.S.A.* 115 (2018) 201800690, <https://doi.org/10.1073/pnas.1800690115>.
- [41] A. Paul, S. Samantray, M. Anteghini, B. Strodel, Thermodynamics and kinetics of the amyloid- β peptide revealed by Markov state models based on MD data in agreement with experiment, *Chem. Sci.* 12 (2021) 6652–6669, <https://doi.org/10.1039/D0SC04657D>.
- [42] J. Lee, X. Cheng, J.M. Swails, M.S. Yeom, P.K. Eastman, J.A. Lemkul, S. Wei, J. Buckner, J.C. Jeong, Y. Qi, et al., Charmm-gui input generator for NAMD, GROMACS, Amber, OpenMM, and Charmm/OpenMM simulations using the CHARMM36 additive force field, *J. Chem. Theory Comput.* 12 (1) (2016) 405–413.
- [43] M.J. Abraham, T. Murtola, R. Schulz, S. Páll, J.C. Smith, B. Hess, E. Lindahl, Gromacs: high performance molecular simulations through multi-level parallelism from laptops to supercomputers, *SoftwareX* 1 (2015) 19–25.
- [44] J. Huang, S. Rauscher, G. Nawrocki, R. Ting, M. Feig, B. de Groot, H. Grubm&rdu;uller, A. MacKerell, Charmm36m: an improved force field for folded and intrinsically disordered proteins, *Nat. Meth.* 14 (2017) 71–73, <https://doi.org/10.1038/nmeth.4067>.
- [45] S. Samantray, F. Yin, B. Kav, B. Strodel, Different force fields give rise to different amyloid aggregation pathways in molecular dynamics simulations, *J. Chem. Inf. Model.* 60 (12) (2021) 6462–6475.
- [46] R.W. Pastor, A.D. MacKerell, Development of the CHARMM force field for lipids, *J. Phys. Chem. Lett.* 2 (13) (2011) 1526–1532, <https://doi.org/10.1021/jz200167q>.
- [47] W.L. Jorgensen, J. Chandrasekhar, J.D. Madura, R.W. Impey, M.L. Klein, Comparison of simple potential functions for simulating liquid water, *J. Chem. Phys.* 79 (2) (1983) 926–935, <https://doi.org/10.1063/1.445869>.
- [48] P. Mark, L. Nilsson, Structure and dynamics of the TIP3P, SPC, and SPC/E water models at 298K, *J. Phys. Chem. A* 105 (43) (2001) 9954–9960, <https://doi.org/10.1021/jp003020w>.
- [49] G. Bussi, D. Donadio, M. Parrinello, Canonical sampling through velocity rescaling, *J. Chem. Phys.* 126 (1) (2007) 014101.
- [50] H.J. Berendsen, J.v. Postma, W.F. van Gunsteren, A. DiNola, J.R. Haak, Molecular dynamics with coupling to an external bath, *J. Chem. Phys.* 81 (8) (1984) 3684–3690.
- [51] T. Darden, D. York, L. Pedersen, Particle mesh Ewald: an N-log(N) method for Ewald sums in large systems, *J. Chem. Phys.* 98 (12) (1993) 10089.
- [52] W. Kabsch, C. Sander, Dictionary of protein secondary structure: pattern recognition of hydrogen-bonded and geometrical features, *Biopolymers* 22 (12) (1983) 2577–2637, <https://doi.org/10.1002/bip.360221211>.
- [53] M. Coles, W. Bicknell, A.A. Watson, D.P. Fairlie, D.J. Craik, Solution structure of amyloid β -peptide(1-40) in a water-micelle environment. is the membrane-spanning domain where we think it is? *Biochemistry* 37 (1998) 11064–11077.
- [54] H. Shao, S. Jao, K. Ma, M.G. Zagorski, Solution structures of micelle-bound amyloid beta-(1-40) and beta-(1-42) peptides of Alzheimer's disease, *J. Mol. Biol.* 285 (1999) 755–773.
- [55] J. Jarvet, J. Danielsson, P. Damberg, M. Oleszczuk, A. Gr&lund, Positioning of the Alzheimer abeta(1-40) peptide in SDS micelles using NMR and paramagnetic probes, *J. Biomol. NMR* 39 (2007) 63–72.
- [56] O. Crescenzi, S. Tomaselli, R. Guerrini, S. Salvadori, A.M. D'Ursi, P.A. Temussi, D. Picone, Solution structure of the Alzheimer amyloid β -peptide (1-42) in an apolar microenvironment, *Eur. J. Biochem.* 269 (2002) 5642–5648.
- [57] H. Sticht, P. Bayer, D. Willbold, S. Dames, C. Hilbich, K. Beyreuther, R.W. Frank, P. R&rdu;osch, Structure of amyloid a4-(1-40)-peptide of Alzheimer's disease, *Eur. J. Biochem.* 233 (1995) 293–298.
- [58] V.N. Uversky, A decade and a half of protein intrinsic disorder: biology still waits for physics, *Protein Sci.* 22 (6) (2013) 693–724.
- [59] N. Miyashita, J.E. Straub, D. Thirumalai, Structures of β -amyloid peptide 1-40, 1-42, and 1-55–the 672-726 fragment of app-in a membrane environment with implications for interactions with γ -secretase, *J. Am. Chem. Soc.* 131 (2009) 17843–17852.
- [60] H. Fatafta, M. Khaled, M.C. Owen, A. Sayyed-Ahmad, B. Strodel, Amyloid- β peptide dimers undergo a random coil to β -sheet transition in the aqueous phase but not at the neuronal membrane, *Proc. Natl. Acad. Sci. USA* 118 (2021), <https://doi.org/10.1073/pnas.2106210118> e2106210118.
- [61] M. Carballo-Pacheco, B. Strodel, Advances in the simulation of protein aggregation at the atomistic scale, *J. Phys. Chem. B* 120 (2016) 2991–2999, <https://doi.org/10.1021/acs.jpcc.6b00059>.
- [62] B. Strodel, Amyloid aggregation simulations: challenges, advances and perspectives, *Curr. Opin. Struct. Biol.* 67 (2021) 145–152, <https://doi.org/10.1016/j.sbi.2020.10.019>.

Supporting Information

Disorder-order transition the amyloid- β peptide upon lipid binding

Hebah Fatafta^{1,#}, Batuhan Kav^{1,#}, Bastian F. Bundschuh², Jennifer Loschwitz^{1,2}, Birgit Strodel^{1,2,*}

¹ Institute of Biological Information Processing (IBI-7: Structural Biochemistry), Forschungszentrum Jülich, 52425 Jülich, Germany

² Institute of Theoretical and Computational Chemistry, Heinrich Heine University Düsseldorf, 40225 Düsseldorf, Germany

* Corresponding author: b.strodel@fz-juelich.de

These authors contributed equally.

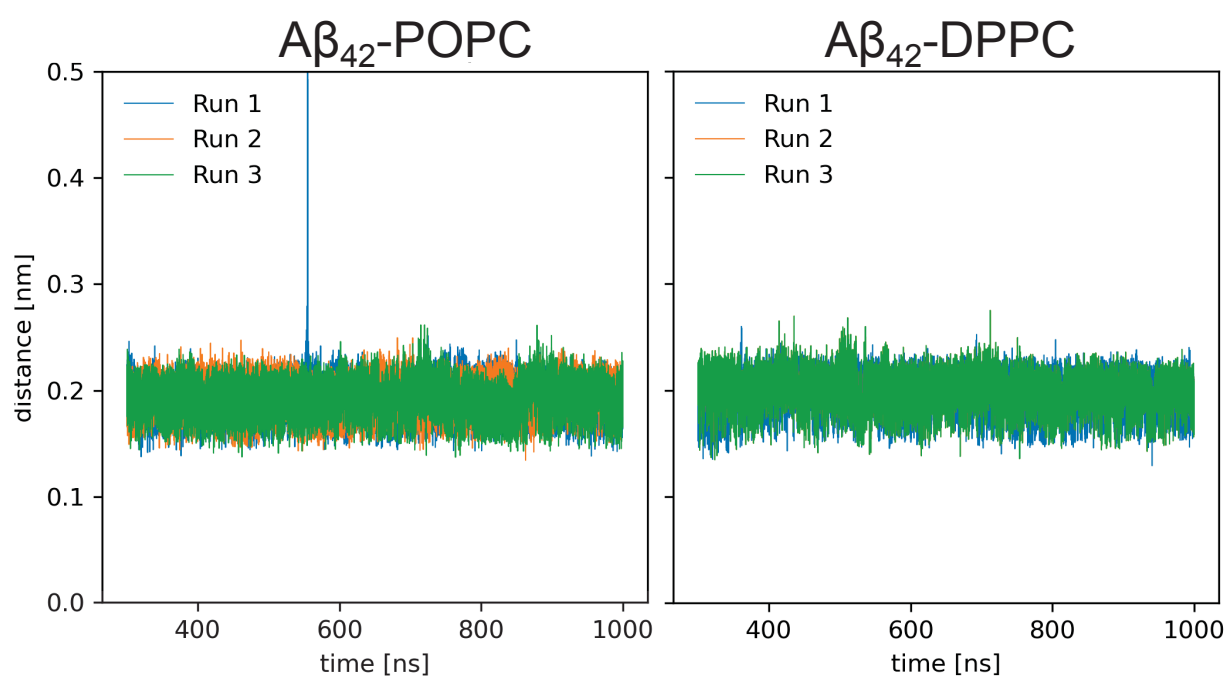


Figure S1: The minimal distance between $A\beta_{42}$ and the POPC lipid (left) and DPPC lipid (right) for each of the three simulations of the 1:1 complexes. The sharp rise in the distance at $t \approx 560$ ns for run 1 involving POPC is due to the periodic boundary conditions applied in the simulations.

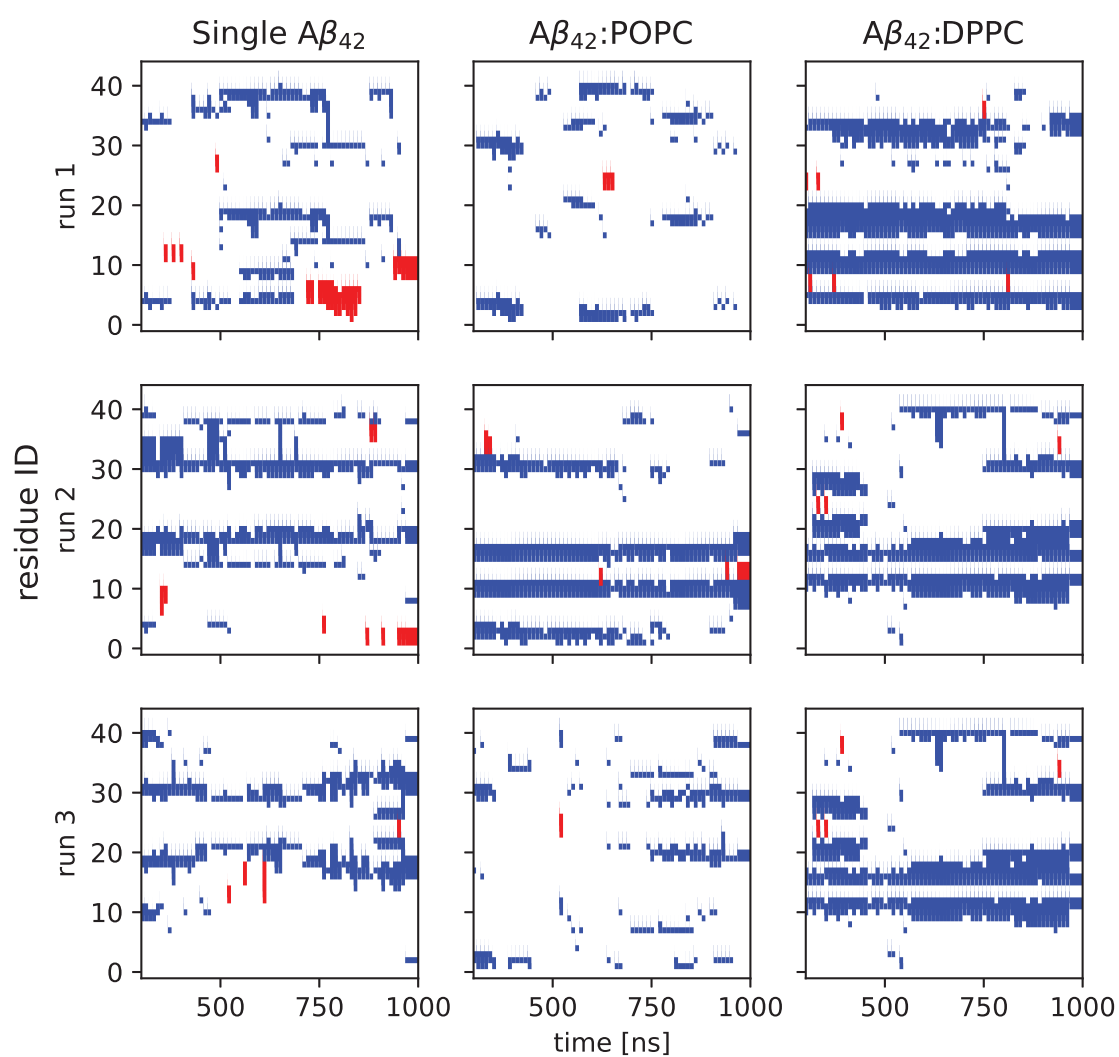


Figure S2: The evolution of the secondary structure for the single $A\beta_{42}$ peptide and the peptide in the $A\beta_{42}$ -POPC and $A\beta_{42}$ -DPPC 1:1 complexes. Every row corresponds to a different run. Helix is shown in red, β -strand/bridge in blue, and all other secondary structures in white.

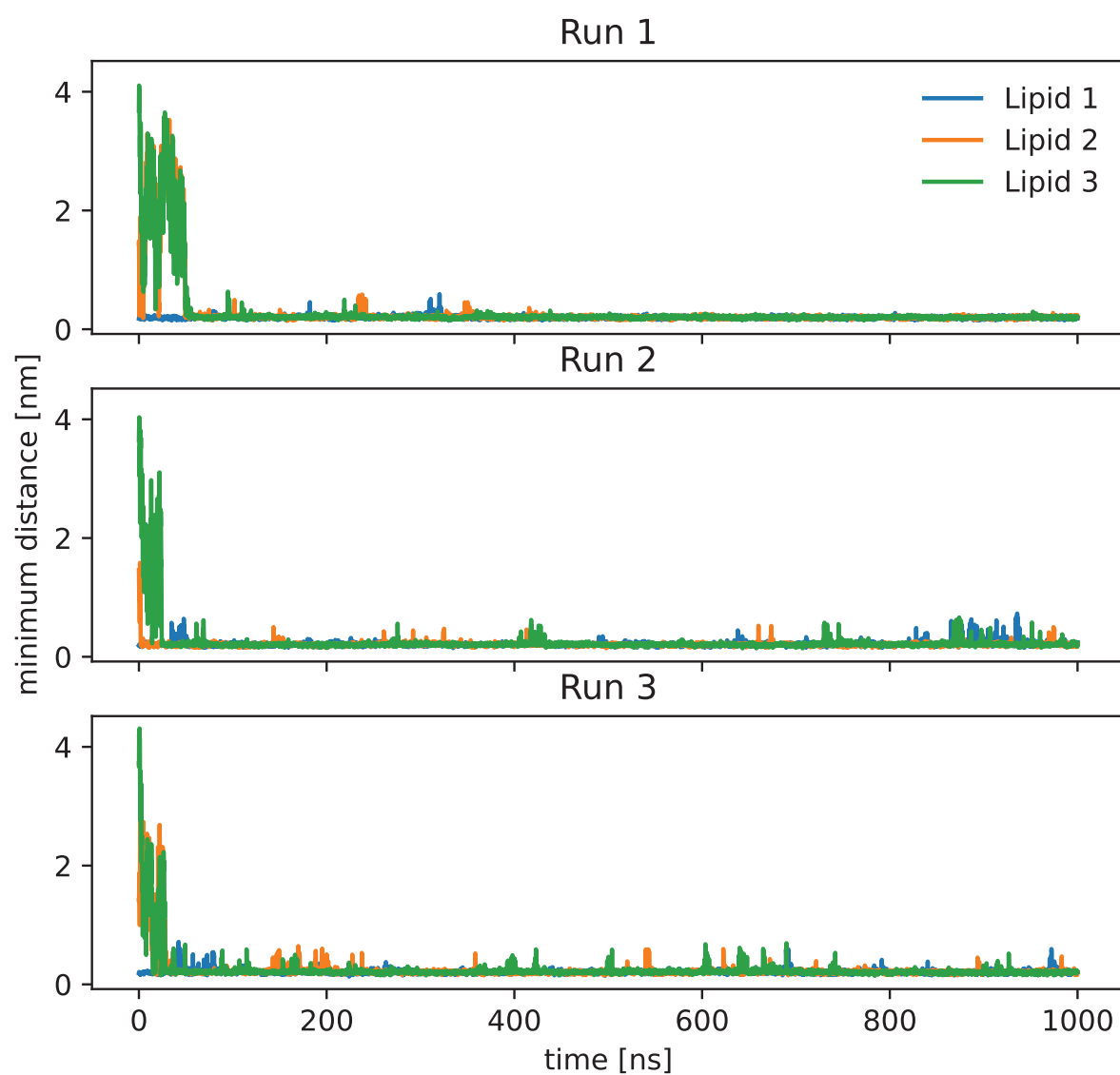


Figure S3: The minimal distance between $A\beta_{42}$ and each of the POPC lipid molecule in the 1:3 complex simulations. Results from top to bottom are for the three different simulation runs.

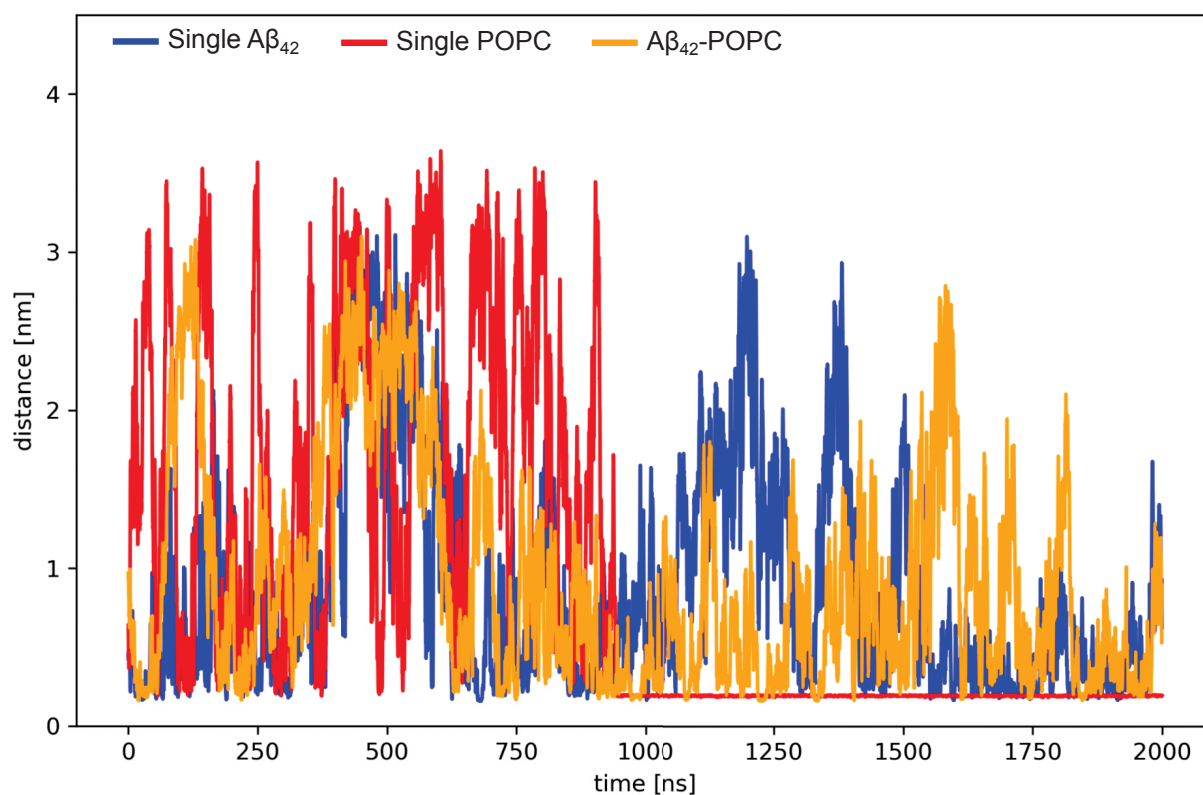


Figure S4: The minimal distances between the POPC membrane and the single A β_{42} peptide (reference simulation), the single POPC lipid molecule (reference simulation), and the A β_{42} -POPC 1:1 complex (one of the three target simulations) are shown.

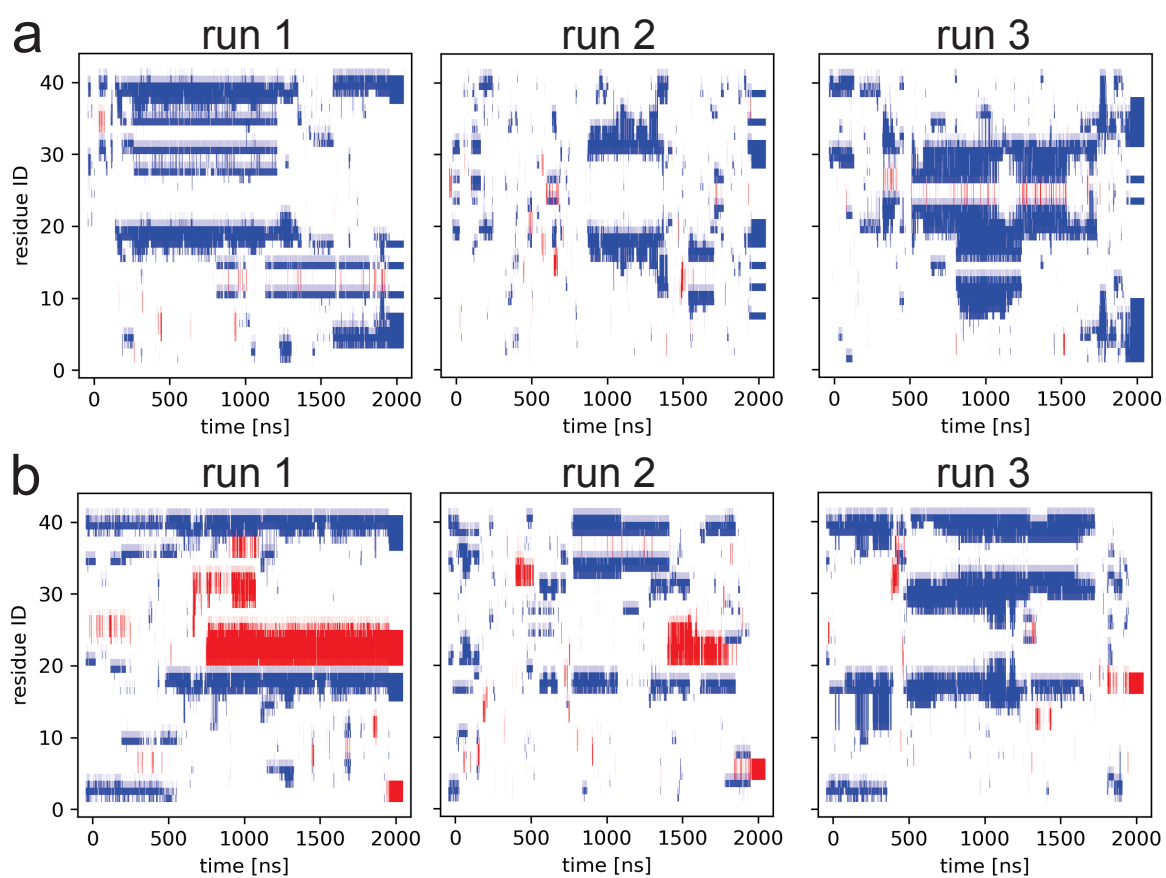


Figure S5: The evolution of the secondary structure for the single $A\beta_{42}$ peptide adsorbed to the POPC membrane (top) and the peptide in membrane-adsorbed $A\beta_{42}$ -POPC 1:1 complex (bottom). Every column corresponds to a different run. Helix is shown in red, β -strand/bridge in blue, and all other secondary structures in white.

A.3 Publication III

Role of Oxidized Gly25, Gly29, and Gly33 Residues on the Interactions of A β 1-42 with Lipid Membranes

Fatafta H., Poojari C., Sayyed-Ahmad A., Strodel B., Owen MC. ACS Chem
Neurosci., 2020 Feb 19;11(4):535-548. doi: 10.1021/acchemneuro.9b00558.

Role of Oxidized Gly25, Gly29, and Gly33 Residues on the Interactions of A β _{1–42} with Lipid Membranes

Hebah Fatafta, Chetan Poojari, Abdallah Sayyed-Ahmad, Birgit Strodel, and Michael C. Owen*

Cite This: *ACS Chem. Neurosci.* 2020, 11, 535–548

Read Online

ACCESS |



Metrics & More



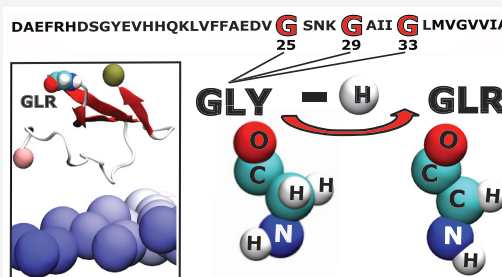
Article Recommendations



Supporting Information

ABSTRACT: Oxidative stress is known to play an important role in the pathogenesis of Alzheimer's disease. Moreover, it is becoming increasingly evident that the plasma membrane of neurons plays a role in modulating the aggregation and toxicity of Alzheimer's amyloid- β peptide ($A\beta$). In this study, the combined and interdependent effects of oxidation and membrane interactions on the 42 residues long $A\beta$ isoform are investigated using molecular simulations. Hamiltonian replica exchange molecular dynamics simulations are utilized to elucidate the impact of selected oxidized glycine residues of $A\beta$ 42 on the interactions of the peptide with a model membrane comprised of 70% POPC, 25% cholesterol, and 5% of the ganglioside GM1. The main findings are that, independent of the oxidation state, $A\beta$ prefers binding to GM1 over POPC, which is further enhanced by the oxidation of Gly29 and Gly33 and reduced the formation of β -sheet. Our results suggest that the differences observed in $A\beta$ 42 conformations and its interaction with a lipid bilayer upon oxidation originate from the position of the oxidized Gly residue with respect to the hydrophobic sequence of $A\beta$ 42 involving the Gly29-XXX-Gly33-XXX-Gly37 motif and from specific interactions between the peptide and the terminal sugar groups of GM1.

KEYWORDS: Amyloid- β peptide, molecular dynamics, membrane simulations, oxidative stress, GM1, peptide membrane interactions



1. INTRODUCTION

Alzheimer's disease (AD) is a neurodegenerative disorder generally affecting persons 65 years and older.¹ With no cure currently available, and the generally increasing life expectancy in most societies, the number of people affected by this disorder is expected to increase in the coming years. Several mechanisms have been proposed as the pathological cause of AD, including genetics, cholinergic, tau, and amyloid hypotheses.^{2–6} Though no hypothesis has been generally accepted, AD brain features substantiate the most widely accepted amyloid cascade hypothesis.⁷ In particular, the AD brain is characterized by the presence of senile plaques. The main component of these plaques is the amyloid- β peptide, which is produced by the cleavage of the amyloid precursor protein (APP) by β and γ secretases.^{8–10} $A\beta$ ranges from 39 to 43 amino acids in length; however, $A\beta$ 42 is predominant in senile plaques and is known to be more toxic than $A\beta$ 40.^{11–13} The primary structure of $A\beta$ 42 is shown in Figure 1. It extends from the unstructured hydrophilic N-terminal region (Asp1 to Lys16) to the hydrophobic C-terminal region (Ala30 to Ala42), and it is linked by central residues (Leu17 to Gly29) that most often form a turn conformation. The central residues have been shown to play a role in membrane insertion and side chain–side chain interactions through a backbone bend that brings the two β -sheets together.^{14–18} In addition, the AD brain is commonly characterized by an increase in oxidative stress.^{19–23} The generation of excess reactive oxygen species

(ROS) or the dysfunction of the antioxidant system can cause an increase in the amount of ROS present in normal cells and subsequently leads to the oxidative stress observed in AD.^{24,25} The ROS are produced either enzymatically (for example to kill invaders in macrophages) or as a side reaction (like respiratory chain) and generally kept at low level but not totally eliminated due to their function. They are necessary to maintain homeostasis in cells and play an important role in signaling. The brain seems to be sensitive to oxidative damage upon oxidative stress due to high dioxygen (the final electron acceptor) consumption in the brain, approximately 20% of the total body consumption.²⁶ It is still controversial whether the accumulation of $A\beta$ increases the level of oxidative stress or that the high level of oxidative stress drives $A\beta$ accumulation.⁶ Studies have shown that $A\beta$ is capable of generating free radicals^{27,28} and shows high affinity to bind metals such as Cu^{2+} and Zn^{2+} .^{29–31}

Though the physiological role of $A\beta$ is not well understood, it was found that $A\beta$ -membrane interactions are essential for $A\beta$ to fulfill its physiological functions. These functions include protecting the body from infections, repairing leaks in the

Received: October 16, 2019

Accepted: January 15, 2020

Published: January 15, 2020

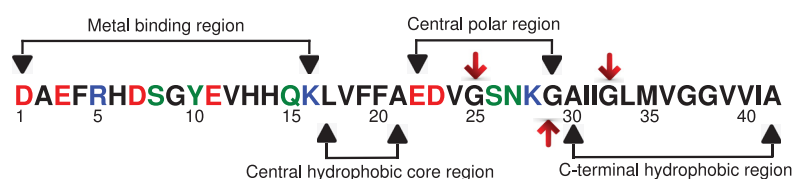


Figure 1. Primary structure of $A\beta_{42}$, showing the acidic residues in red, the basic residues in blue, the hydrophobic residues in black, and the polar residues in green. The residues forming the metal-binding region, the central hydrophobic core, the central polar region, and the C-terminal hydrophobic region are also indicated. Red arrows point to the oxidized glycine residues investigated in this study.

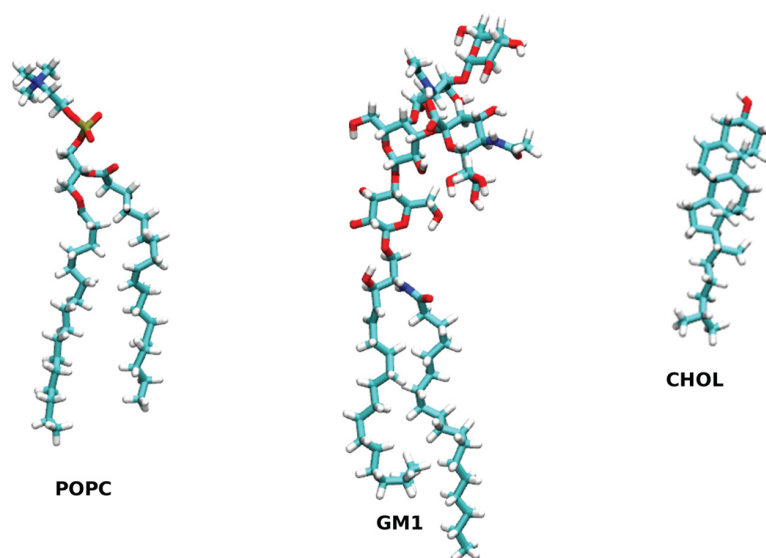


Figure 2. Structures of 1-palmitoyl-2-oleoyl-phosphatidylcholine (POPC), ganglioside (GM1), and cholesterol (CHOL) used in this work. The structures are shown in a licorice representation colored by name, where the oxygen atom is shown in red, the nitrogen atom is shown in blue, the hydrogen atom is shown in white, and the carbon atom is shown in cyan.

blood-brain barrier, promoting recovery from injury, and regulating synaptic function.^{32,33}

Understanding the effect of membrane composition on the conformation of $A\beta$ and its interaction with membranes are essential to explain both its physiological function and its role in AD. For example, from molecular dynamics (MD) simulations it was found that the charge of the lipid headgroup and the structure of the lipid acyl chains determine the stability of $A\beta_{42}$ inserted in zwitterionic POPC and DPPC bilayers and anionic POPG bilayers.¹⁸ The neuronal membrane plays a key role in modulating $A\beta$ aggregation.^{5,34,35} It was found that monosialotetrahexosylganglioside (GM1), the most abundant ganglioside in neurons, affects the conformation of $A\beta$ and its neurotoxicity.³⁶ Moreover, it has been suggested that the initial attachment of amyloid protein to the plasma membrane is first triggered by binding to gangliosides due to their extracellular location.³⁷ Generally, the $A\beta$ -bound GM1 complex has been identified to be present in the AD brain, and it has been found that monomeric $A\beta$ has a high affinity for GM1.^{38,39} Furthermore, it was found that the GM1-binding domain of $A\beta_{42}$ ($A\beta(1-16)$) can inhibit the amyloid pore formation via binding to GM1 and blocking the first step in the pore formation mechanism (a stepwise mechanism controlled by the dual effect of gangliosides and cholesterol).⁴⁰ It was also found that $A\beta$ complex formation is enhanced in lipid bilayers enriched by cholesterol content.^{41,42}

The role of $A\beta$ in oxidative stress related mechanisms of AD progression is still unclear. It was shown that Met35 of $A\beta$

plays a critical role in this redox process.^{43,44} Several studies found that replacing the sulfur atom in Met35 abolished the neurotoxic effect caused by the native peptide.⁴⁴⁻⁴⁷ The neurotoxic fragment $A\beta_{25-35}$ was observed to lose its neurotoxicity when Met35 was removed.^{48,49} It was further hypothesized that the interaction between the proximal residues Gly33 and Met35 in $A\beta_{42}$ accelerates the generation of free radical induced oxidative stress.^{50,51} Moreover, it has been proposed that the hydrophobic C-terminal region is the seed for $A\beta$ aggregation.⁵² This region includes part of the repeated motif GXXXG spanning residues from Gly25 to Gly37.⁵³ Others have shown that Gly33 of this motif plays a key role in $A\beta$ toxicity.^{50,54} It was further reported that modification of Gly33 like mutation not only affects the structure and the hydrophobic surface of the peptide but also affects the neighboring residues and would likely disrupt the interaction between Phe19 and Leu34.

The relationship between glycine residues in the C-terminal region of $A\beta$ and oxidative stress can be explained by the amyloid radical hypothesis. This hypothesis describes how the C atom of glycine residues is susceptible to the loss of an H atom upon oxidation of Met35, which in turn causes the formation of a protein backbone radical, stabilized by the captodative effect,^{55,56} that adopts an extended structure perfect for β -sheet formation.⁵¹ In this hypothesis, Gly33 is predicted to be more susceptible to oxidation by methionine-based sulfuranyl free radical due to the close proximity of these residues in the $A\beta_{42}$ primary structure. Several experimental

studies have been attempted to explore the effect of radicals on proteins, but challenges in locating the center of a radical in protein hinders systematic experimental investigations.^{57,58}

Studies of $A\beta$ peptide often employ shorter $A\beta$ analogs; however, it is essential to explore the full-length monomeric form of $A\beta$ for a comprehensive understanding of its toxicity.^{59,60} Unfortunately, exploring the full-length of $A\beta$ is experimentally challenging due to its high propensity to aggregate. Alternatively, MD simulations can provide insight into the conformational dynamics of $A\beta$ at atomistic resolution and complement experimental findings.^{61,62} Previously, MD simulations have been used to investigate the effect of protein oxidation on protein folding. Owen and co-workers examined the effect of C_α -centered radical formation on the stability of a model helical peptides in different solvent systems.⁶³ Moreover, MD simulations demonstrated the effect of glycine residue radicalization on protein conformation depends both on the protein and the position of the radical.⁶⁴ The effect of radicalization at Gly25 on the $A\beta$ 42 dimer in solution was further investigated by Liao et al.⁶⁵ Although the occurrence of oxidative stress in several neurodegenerative diseases is well-established, there is no computational evidence on the effect of radicalization on peptide-membrane interactions.

Thus, in this study we employ Hamiltonian replica exchange molecular dynamic (HREMD) simulations to understand the effect of oxidizing glycine residues (25, 29, and 33) on the $A\beta$ 42 secondary structure and membrane binding. The structures of 1-palmitoyl-2-oleoyl-phosphatidylcholine (POPC), monosialotetrahexosylganglioside (GM1), and cholesterol (CHOL) used in this membrane are shown in Figure 2. The parameters of the glycy radical (GLR) are taken from our previous study,⁶⁶ and the structure of GLR is shown in Figure S1 in the Supporting Information. HREMD simulations provide an advantage over MD in that it enhances the conformational sampling of the phase space and overcomes the problem of restricting the system to localized low energy regions of the conformational space.⁶⁷

2. RESULTS AND DISCUSSION

Understanding the neuropathology of Alzheimer's disease (AD) is the driving engine for most research in chemical neuroscience and biology. It is thought that the development of Alzheimer's disease (AD) is related to the interactions between amyloid- β ($A\beta$) with neuronal membranes. However, it has also found that the AD brain is characterized by an increase in oxidative stress. This research aims at a better understanding of this complex relationship by examining the effect of oxidizing selected glycine residues in $A\beta$ 42 on its potential toxicity and interaction with a lipid membrane containing the GM1 ganglioside. That would help toward better understanding of this neurodegenerative disorder and its treatment.

2.1. Effect of Bilayer on $A\beta$ 42. **2.1.1. $A\beta$ 42 Insertion Distance.** To see which peptide residues most frequently interacted with the bilayer, we calculated the average distance between the COM of each residues and the average position of each lipid type along the bilayer normal (z -axis). The time-averaged z -position of the phosphorus atom of POPC was used as a reference by setting their average position to zero. The relative position of the hydroxyl oxygen of cholesterol and the COM of the GM1 headgroup are shown in Figure 3. On average, the center of mass of the GM1 headgroups is above

the phosphate group of POPC, while the hydroxy group of cholesterol lies beneath it.

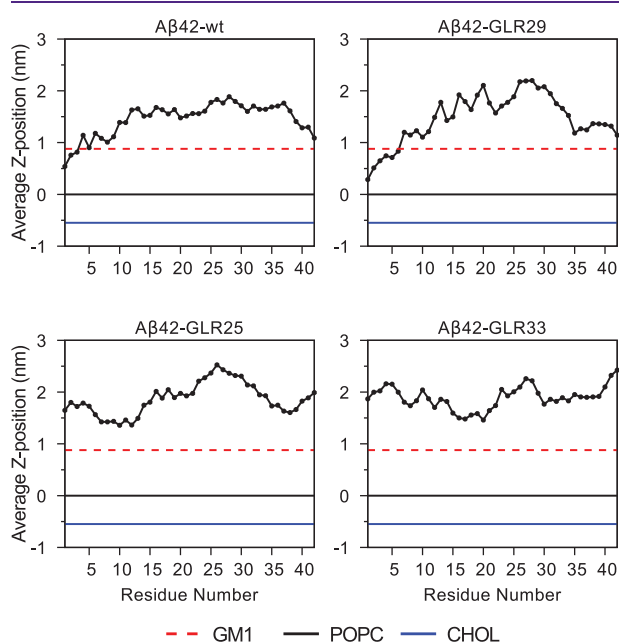


Figure 3. Average insertion distance of each $A\beta$ 42 residue with respect to the POPC and GM1 headgroups and the CHOL hydroxyl group. The headgroups of GM1, POPC, and CHOL are shown in red, black, and blue, respectively.

It can be seen in Figure 3 and Figure 4 that $A\beta$ 42-wt and $A\beta$ 42-GLR29 show similar bilayer interaction profiles, whereas both $A\beta$ 42-GLR25 and $A\beta$ 42-GLR33 had similar interaction profiles. In the wild-type $A\beta$ 42 and $A\beta$ 42-GLR29, Asp1 is closest to the phosphate atoms of the POPC lipids. Its distance from POPC is around 0.5 nm in the former and 0.3 nm in the latter peptide. N-terminal residues Ala2 to Arg5 are the next closest to the bilayer in both cases. The residues in the central polar region (Ser26 to Lys28) were the furthest from the bilayer, whereas residues Ala30, Ile32, Val36, and Gly37 from the C-terminal hydrophobic region of the wt and residues Lys16 and Phe20 of $A\beta$ 42-GLR29 were the next furthest. Despite these similarities, $A\beta$ 42-GLR29 stays slightly closer to the bilayer than the wild-type $A\beta$ 42 does. In the case of $A\beta$ 42-GLR25 and $A\beta$ 42-GLR33, the former is on average the furthest from the bilayer, and this is more pronounced in the N- and C-terminal regions. In the case of $A\beta$ 42-GLR25, the central polar region residues Glu22 to Gly29 are the furthest from the bilayer.

To analyze whether the binding of $A\beta$ 42 to the membrane has an effect on the membrane properties, we first calculated the average bilayer thickness based on the positions of the phosphorus atoms for each simulated system. The average bilayer thickness was found to be about 4.5 nm for all studied systems (see Table S1). This average value was then compared to the local bilayer thickness that was calculated for the snapshots of each trajectory where $A\beta$ 42 was bound to the membrane. To this aim, we utilized the GridMAT-MD tool^{68,69} to calculate the local membrane thickness averaged over all HREMD snapshots containing at least one atom of $A\beta$ 42 within 0.5 nm of the lipid bilayer. The resulting 2D plots (Figure S2) reveal a reduction in the local bilayer thickness to

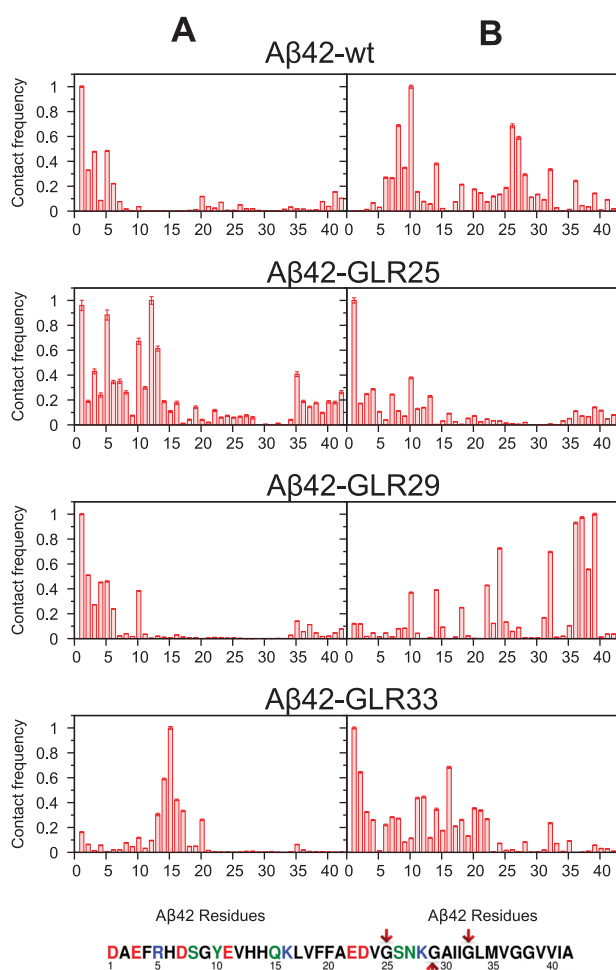


Figure 4. Contact frequency of each $A\beta 42$ residue (and standard deviation of the mean) with POPC (A) and GM1 (B) headgroups. The figure shows the normalized contact frequency in the range 0 to 1, such that 1 means the residue always made contacts with the lipid, and zero means no contacts were made. The sequence of the $A\beta 42$ residues is shown below.

about 4.4 nm or even less upon the interaction of the peptide with the lipid headgroups.

2.1.2. $A\beta 42$ Contacts and Hydrogen Bond with the Bilayer. For a greater understanding of which $A\beta 42$ residues associated with the bilayer, the number of contacts between each $A\beta 42$ residue and the bilayer for the 4 systems was calculated and normalized in the range of 0 to 1, where 0 means that the residue made no contact with the lipid in question, and 1 stands for residues that always remained in contact with lipid (see Figure 4).

The N-terminal residues of $A\beta 42$ -wt made the most contacts with POPC lipids. In this region Asp1 formed the most contacts, followed by Arg5, Glu3, and Ala2, respectively, and then His6, Asp7, and Tyr10 from the metal binding region. Fewer contacts, with a normalized contact frequency of less than 0.2, were observed in the central polar and the C-terminal hydrophobic regions. Similarly, the contacts between $A\beta 42$ -GLR29 residues and POPC were dominated by the N-terminal residues, with a higher membrane affinity shown here in this peptide residues than those in the wild-type. In this region the most contacts were made by Asp1, and the next highest is Ala2,

followed by Arg5, Phe4, and Glu3, respectively, and then Tyr10 in the metal binding region. Fewer contacts (a normalized frequency of less than 0.2) were observed in the C-terminal region, and almost no contacts were made between the bilayer and the central polar and central hydrophobic regions of the peptide. On the other hand, the contacts between $A\beta 42$ -GLR25 and POPC were dominated by residues from the metal binding region. In this region, contacts with residues Asp1, Arg5, Tyr10, Val12, and His13 were most frequent. Fewer contacts, with a normalized frequency of less than 0.5, were observed among the remaining residues in this region and the C-terminal hydrophobic regions. $A\beta 42$ -GLR33 has the lowest affinity for POPC. The most contacts in this peptide were made by residues 13 to 17 from the metal-binding region, with a normalized frequency greater than 0.3.

Most $A\beta 42$ residues showed a propensity to bind GM1 in both the wt and oxidized peptides. However, the contact frequency in the metal-binding region is the highest in $A\beta 42$ -GLR33, followed by $A\beta 42$ -wt, $A\beta 42$ -GLR25, and $A\beta 42$ -GLR29. The central hydrophobic core and the central polar region had the highest affinity for GM1 in $A\beta 42$ -GLR33, followed by $A\beta 42$ -wt, $A\beta 42$ -GLR29, and $A\beta 42$ -GLR25, respectively. These contacts are almost abolished in the case of POPC. The C-terminal hydrophobic region showed the highest frequency to bind GM1 in $A\beta 42$ -GLR29 followed by $A\beta 42$ -wt, $A\beta 42$ -GLR33, and $A\beta 42$ -GLR25, respectively.

Residues Asp1 and Arg5 in the metal-binding region of $A\beta 42$ -wt and both $A\beta 42$ -GLR25 and GLR29 formed hydrogen bonds with POPC, as shown in Figure 5. The propensity to form hydrogen bonds between $A\beta 42$ and POPC is higher in the metal-binding region of $A\beta 42$ -wt and $A\beta 42$ -GLR29 than in $A\beta 42$ -GLR25, while it is less than 10% in some residues within the metal-binding region of $A\beta 42$ -GLR33. On the other hand, no hydrogen bonds formed between POPC and the central polar and C-terminal regions of any of the four $A\beta 42$ peptides.

The propensity of hydrogen bonds to form with GM1 is higher in the case of the oxidized $A\beta 42$ -GLR25, $A\beta 42$ -GLR29, and $A\beta 42$ -GLR33 than in the wt $A\beta 42$. The C-terminal hydrophobic residues of $A\beta 42$ tended to form hydrogen bonds with GM1, which was not the case with POPC. The highest hydrogen bond propensity of the C-terminal hydrophobic residues was observed in $A\beta 42$ -GLR29.

2.1.3. $A\beta 42$ Bilayer Interaction Energy. Next, we analyzed whether the contacts between $A\beta 42$ residues and the lipid bilayer were driven by electrostatic or Lennard-Jones (LJ) interactions. The strongest Coulombic interactions (Figure S3) between POPC and $A\beta 42$ -wt were at Asp1 at $-256 \text{ kJ}\cdot\text{mol}^{-1}$, and the next strongest interacting residue was Arg5; however, the interaction strength at Arg5 was only 1/5 of that at Asp1. The Coulombic interactions between $A\beta 42$ -GLR29 and POPC showed a similar trend as the wt, but the interaction energy of Asp1 was weaker, at around $-150 \text{ kJ}\cdot\text{mol}^{-1}$ and around $-20 \text{ kJ}\cdot\text{mol}^{-1}$ at Tyr10 compared to zero in the wt. The Coulombic interactions between POPC and $A\beta 42$ -GLR25 and $A\beta 42$ -GLR33 are less than $-20 \text{ kJ}\cdot\text{mol}^{-1}$ with residues Asp1 in the former peptide and His13 to Lys16 in the latter peptide. The Coulombic interactions with GM1 were stronger in $A\beta 42$ -GLR25 and $A\beta 42$ -GLR33 compared to $A\beta 42$ -wt and $A\beta 42$ -GLR29. The strongest interaction was with Asp1 in $A\beta 42$ -GLR25 and with Lys16 in $A\beta 42$ -GLR33 with interaction strengths of -104 and $-60 \text{ kJ}\cdot\text{mol}^{-1}$, respectively. The next strongest interaction between GM1 and $A\beta 42$ -GLR33 was with Asp1 at $-50 \text{ kJ}\cdot\text{mol}^{-1}$. Overall, the attractive Coulombic

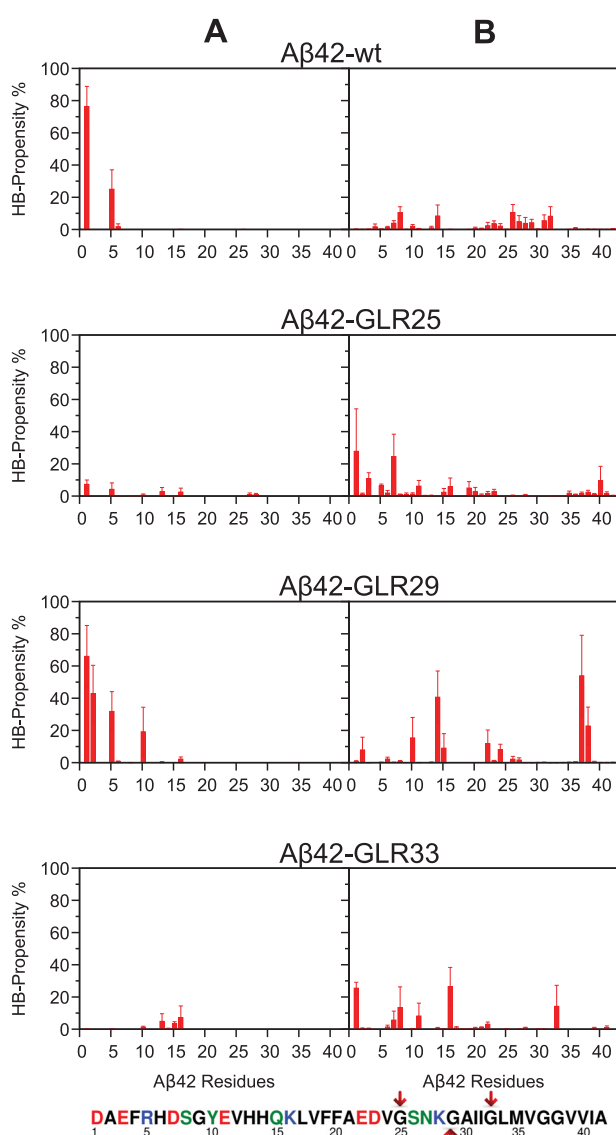


Figure 5. Hydrogen bond propensity (and standard deviation of the mean) of each Aβ42 residue with (A) POPC and (B) GM1 headgroups.

interactions with GM1 were lower in magnitude compared to those with POPC, where no single residue had an average interaction energy below $-104 \text{ kJ}\cdot\text{mol}^{-1}$.

The profile of the LJ interaction energies (Figure 6) between each Aβ42 peptide and the lipids was very similar to that of their respective contact frequency figure (Figure 4). For Aβ42-wt and Aβ42-GLR29 the strongest LJ interactions with POPC were in the N-terminal region of the peptides and averaged between -10 and $-13 \text{ kJ}\cdot\text{mol}^{-1}$. In Aβ42-GLR33 the strongest LJ interactions were with residues His13 to Gln15, whereas residues in the central hydrophobic region averaged between -0.7 and $-11 \text{ kJ}\cdot\text{mol}^{-1}$. Similarly, the strongest LJ interaction with GM1 was on average $-10 \text{ kJ}\cdot\text{mol}^{-1}$ in the C-terminal region of Aβ42-GLR29 and both the metal binding and the central hydrophobic regions of Aβ42-GLR33. The LJ interactions of Aβ42-GLR25 with GM1 averaged less than $-10 \text{ kJ}\cdot\text{mol}^{-1}$ and was dominated by residues from the metal

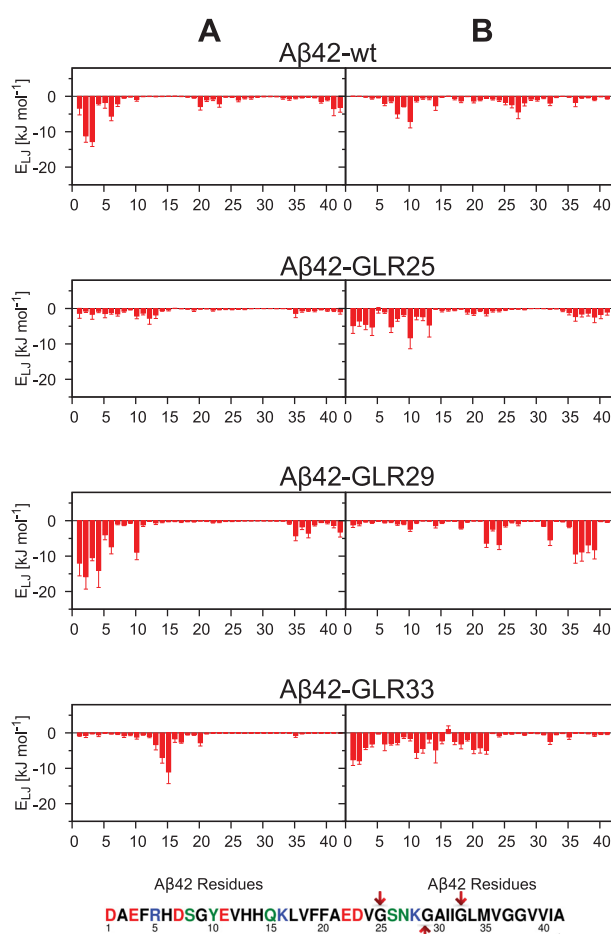


Figure 6. Lennard-Jones interaction energy of each Aβ42 residue (and standard deviation of the mean) between Aβ42 and POPC (A) and GM1 (B) headgroups.

binding and the C-terminal hydrophobic regions. It averaged less than $-5 \text{ kJ}\cdot\text{mol}^{-1}$ in the case of the wt Aβ42.

Furthermore, we examined the effect of solvation on peptide–lipid interactions, to ensure that the stronger the peptide–lipid interaction the lesser the peptide is susceptible to solvation effects. To this aim, the time evolution of the number of water molecules within a 0.5 nm shell from the C atom of the peptide^{70,71} and the minimum distance of the peptide C_α atoms from the lipids were calculated and are jointly shown in Figure S4. A decreasing peptide distance from the lipid (i.e., stronger peptide–lipid interactions) correlates with a reduction in the peptide hydration. Moreover, the highest population of solvating water molecules was present at approximately 3 nm distance of Aβ from the membrane surface, i.e., the initial distance, and it takes around 50 ns for the peptide to move closer to the lipids.

2.2. Aβ42 Structural Properties. **2.2.1. Aβ42 Secondary Structure Assignment.** In the wild-type Aβ, residues Phe4 to Glu11 displayed a β-turn/bend structure. Residues Val12 to Gln15 displayed a helical structure. Residues Lys16 to Ala21 showed a mixture of helical and β-turn/bend structures. Residues Glu22 to Val39 showed a β-turn/bend structure with residues Ile32, Leu34, Val36, and Val39 displaying a mixture of a β-strand/bridge and helical structure. Residues Met35, Val40, and Ile41 showed a β-strand/bridge.

Similar to what was seen in the wild-type, all oxidized $A\beta$ peptides showed a high propensity to form a helical structure in the region Glu11 to Ala21 (Figure 7), with the lowest

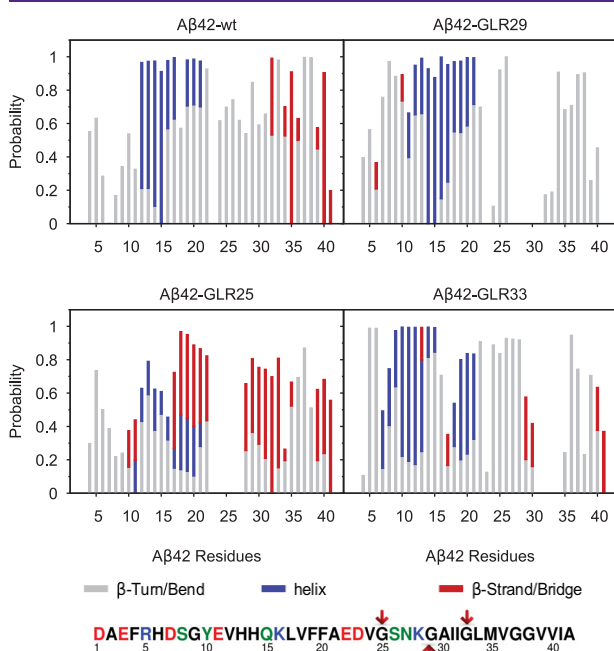


Figure 7. Secondary structure assignment of each $A\beta$ 42 residue in the case of $A\beta$ 42-wt, $A\beta$ 42-GLR25, $A\beta$ 42-GLR29, and $A\beta$ 42-GLR33 in a bilayer compromised of 70% POPC, 25% CHOL, and 5% GM1. The β -turn/bend is shown in silver, the helix is shown in blue, and the β -strand/bridge is shown in red. The figure shows the additive probability of all secondary structures such that the maximum is 1; those residues showing a probability lower than 1 form random coil.

propensity observed in the case of $A\beta$ 42-GLR25. However, an increase in helicity was observed in the case of $A\beta$ 42-GLR33, such that the helical region extended to include residues Asp7 to Ala21 from the central polar and central hydrophobic regions.

The propensity to form a β -strand/bridge was the highest in $A\beta$ 42-GLR25 and $A\beta$ 42-wt. Few residues in $A\beta$ 42-GLR29 and $A\beta$ 42-GLR33 showed a β -strand/bridge structure. This includes residues His6 and Tyr10 in the former peptide and residues His13, Leu17, Gly29, Ala30, Val40, and Ile41 in the latter peptide. On the other hand, all $A\beta$ 42 peptides showed a higher propensity to form a β -turn/bend. Interestingly, residues Asp23 to Asn27 in $A\beta$ 42-GLR25, residues Asn27 to Ile31 in $A\beta$ 42-GLR29, and residues Ile31 to Leu34 in $A\beta$ 42-GLR33 did not show any turn/bend structure.

Moreover, the development of the secondary structure content for all simulations as a function of the simulation time was analyzed and shown in Figure S5. To this aim we utilized the moving window statistics (more about the method can be found in the figure caption) to test the convergence of the secondary structure during the simulation.^{71,72} The figure shows good agreement in the overall trend of the β -sheet propensity over different time windows, and the secondary structure propensity of the peptides apart from $A\beta$ 42-GLR25 converges after 80 ns as no further changes in the β -sheet propensity are observed by the end of the simulations. $A\beta$ 42-GLR25 is more flexible than the other three peptides and thus needs more time for the secondary structure to converge. This

is in line with the previous findings by Liao et al., who found that the flexibility of $A\beta$ 42 increases upon oxidation of Gly25.⁶⁵ Nonetheless, within the last 40 ns of the HREMD simulation also this simulation converged as supported by the nearly stable β -sheet propensity for each of the residues.

2.2.2. $A\beta$ 42 Intramolecular Hydrogen Bond and Contact. Hydrogen bonds present within the peptide backbone, the peptide side chains, and between the peptide backbone and side chains that were present for more than 40% of the time were recorded and listed in Table S2. In the wild-type $A\beta$ 42, backbone–backbone hydrogen bonds were present in the C-terminal region between Ile41 with Gly33 and Leu34, Ile31 with Leu34 and Met35, Gly33 and Met35, and Val36 and Val39, which stabilizes the β -sheet structure. They are also present between residues from the metal binding region such as Glu11 with His14 and Gln15, Val12 and Lys16, His14 with Leu17 and Val18, and Val18 with Ala21 from the central hydrophobic region. In the N-terminal region, backbone–side chain hydrogen bonds formed between Glu3 with Phe4 and Arg5. Moreover, hydrogen bonds formed between the side chain of Glu3 (hydrogen bond acceptor) and the side chain of Arg5 (hydrogen bond donor) from this region. Similarly, a lower number of backbone–backbone hydrogen bonds were present in the $A\beta$ 42-GLR33 metal binding and C-terminal regions. On the other hand, $A\beta$ 42-GLR29 and $A\beta$ 42-GLR25 contained additional backbone–backbone hydrogen bonds that formed within the central hydrophobic core, within the central polar region, and between the C-terminal and the central polar region in the former and within the polar region and between the C-terminal and the central hydrophobic cores of the latter. These bonds exist between residues that either form helices or β -sheets, and such structures are discussed in the next section about the most prevalent $A\beta$ 42 structures. Residues in the N-terminal region did not form backbone to backbone hydrogen bonds in any of these peptides.

The backbone–side chain hydrogen bonds formed most often in $A\beta$ 42-GLR33. However, Phe4 formed a hydrogen bond with Glu3 and Arg5 in all peptides except $A\beta$ 42-GLR25, which did not form any backbone–side chain hydrogen bonds. The hydrogen bonds involving side chains in $A\beta$ 42-GLR29 were similar to those observed in $A\beta$ 42-wt as is shown in Table S2. However, $A\beta$ 42-GLR33 formed an additional hydrogen bond between Ser26 and Asp23, and $A\beta$ 42-GLR25 did not form side chain to side chain hydrogen bonds.

The contact map between the $A\beta$ 42 residues is shown in Figure 8. Regions marked in red indicate residues in close contact (within 0.25 nm of each other), and regions marked in blue stand for residues that display little to no contact. Based on this assignment, one can explain the red main diagonal seen in all contact maps, as it represents the contact of a residue with itself and its neighboring residues. Of interest are those islands of red color that spread in almost all contact maps. Considering the contact map of $A\beta$ 42-GLR25, these light-orange-colored islands are arranged in cross diagonals between residues 28–34 with residues 14–24, illustrating the formation of β -sheets. Similar diagonals are observed in the other peptides but with some distortion, indicating that no β -sheet formation took place, and to a lesser degree in the following order $A\beta$ 42-GL29 > $A\beta$ 42-GL33 > $A\beta$ 42-wt.

2.2.3. The Most Prevalent $A\beta$ 42 Structures. To substantiate the secondary structure and contact map analysis, we clustered the $A\beta$ structures using the algorithm developed by Daura et al. The top cluster of each system is presented in Figure 9, while

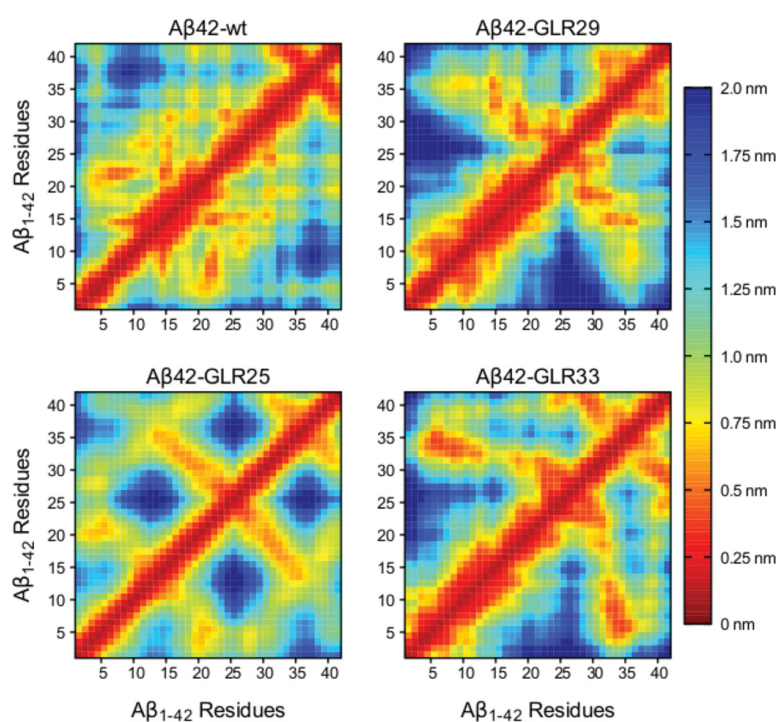


Figure 8. Contact map of each $A\beta_{42}$ residue in the case of $A\beta_{42}$ -wt, $A\beta_{42}$ -GLR25, $A\beta_{42}$ -GLR29, and $A\beta_{42}$ -GLR33 in a bilayer comprised of 70% POPC, 25% CHOL, and 5% GM1. The color box to the right shows the corresponding distance (in nm) to color present in the contact map.

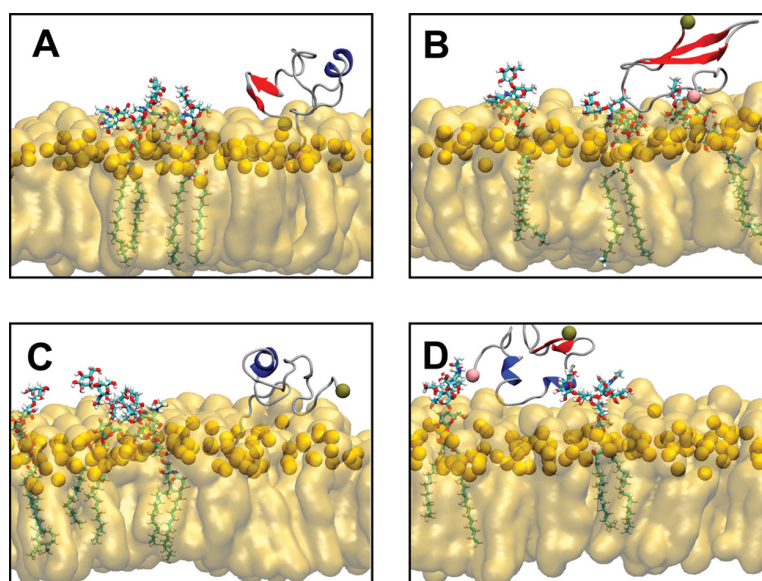


Figure 9. Central structure of the largest cluster: (A) $A\beta_{42}$ -wt (46.7%), (B) $A\beta_{42}$ -GLR25 (33.8%), (C) $A\beta_{42}$ -GLR29 (56.5%), and (D) $A\beta_{42}$ -GLR33 (65.6%). In each rendered image the lipids are colored by orange. The phosphate atom of POPC is in orange, and the N- and C-terminals of $A\beta_{42}$ are shown in pink and tan spheres, respectively. The protein β sheet is shown in red, the helix is shown in blue, and coil and turn are shown in silver.

the structures in the second and third-largest clusters are shown in Figures S6 and S7. The three highest populated $A\beta_{42}$ -wt clusters represented 46.7%, 23.7%, and 9.5% of all structures, respectively (Figure 9A, Figure S6A, and Figure S7A). From the N-terminus to the C-terminus, the secondary structure of the largest and second-largest clusters alternated from random coil to turn, followed by helix at Val12 to Leu17, and then a turn to the antiparallel β -sheet (on either sides of a

turn centered at Gly38) at the C-terminal. There were no β -sheets in the third-largest cluster; however, $A\beta_{42}$ contained coil, turn, and helix. The N-terminus was embedded more deeply into the bilayer in the largest and third-largest clusters and was least embedded in the second-largest cluster. The three most populated structures found in $A\beta_{42}$ -GLR25 represented 33.8%, 18.4%, and 9.4% of all structures, respectively, and are shown in Figure 9B, Figure S6B, and

Figure S7B. The β -sheet structure was observed only in the largest and second-largest clusters; however, a much higher β -sheet content can be seen in these clusters. In addition to the β -sheet at the C-terminal, a β -sheet was observed at the central hydrophobic and polar region (residues Leu17 to Asp23 and Lys28 to Leu34) in the largest cluster and at the metal binding region (Gly9 to Val12) in the second-largest cluster. A helical structure was only observed in the second- and the third-largest clusters. The N-terminus is closer to the bilayer in the largest cluster, while the C-terminus is close to the bilayer in both the second- and third-largest clusters. In the case of A β 42-GLR29, the three representative structures representing 56.5%, 19.3%, and 3.8% of the total number of structures, respectively, are shown in Figure 9C, Figure S6C, and Figure S7C. No β -sheets were observed in any of the three clusters. However, a helical structure was seen in all clusters. Moreover, much more helical content was seen as the helical structure extends to include Glu11 to Glu22 and His13 to Ala21 in the second- and the third-largest clusters, respectively. The N-terminus is embedded in the bilayer in all three clusters, while the C-terminus is only embedded in the second-largest cluster. Figure 9D, Figure S6D, and Figure S7D show the three most populated structures in the presence of A β 42-GLR33, which represent 65.6%, 16%, and 5.2% of the total structures, respectively. In this case the C-terminal β -sheet was observed only in the largest cluster. A helical structure was observed in both the largest and second-largest cluster. There were no helices and no β -sheet in the third-largest cluster. The N-terminus is close to the bilayer in the second-largest cluster, while both the N- and C-terminus residues interact with the solvent in both the largest and the third-largest clusters.

2.3. Discussion. **2.3.1. Effect of Bilayer on A β 42.** The insertion data in Figure 3, which shows the time-averaged distance between each A β 42 residue and the bilayer, revealed following order of membrane insertion: A β 42-wt > A β 42-GLR29 > A β 42-GLR25 > A β 42-GLR33. The detailed interactions of A β 42 residues with the bilayer are shown more quantitatively in the peptide-bilayer contacts (Figure 4). Interactions between A β 42 and the bilayer occur primarily between the N-terminus and the POPC headgroups, while the remaining residues make more contact with GM1. A β 42-GLR25 makes the least contact with GM1 as the normalized frequency is generally less than 0.5, which can indicate why it has the tendency to adopt the β -sheet conformation while on the membrane surface. As shown in Figure 4, the contact between peptides and GM1 is ranked in the order of A β 42-GLR29 > A β 42-GLR33 > A β 42-wt > A β 42-GLR25. Contacts observed at the N-terminus especially with Asp1 and Arg5 were driven by hydrogen bonds that formed between the amino acid residues and the lipids. The propensity of hydrogen bonds to form between A β 42 and GM1 are on the order of A β 42-GLR29 > A β 42-GLR33 > A β 42-GLR25 > A β 42-wt. The hydrogen bond propensity with POPC was limited to residues from the N-terminal metal-binding region, with Asp1 and Arg5 as the main hydrogen bond forming residues. This is expected to be the cause that drives the N-terminus to be close to the bilayer headgroup as can be seen from the insertion data in Figure 3. Here, A β 42-wt and A β 42-GLR29 showed a higher hydrogen bond propensity with POPC than A β 42-GLR25 and A β 42-GLR33. It is not surprising that A β 42 residues that form a hydrogen bond with the bilayer were also shown to be the strong energetic contribution to interactions between each peptide and the lipid bilayer. The interactions between each

A β 42 residue and the lipid bilayer were divided into their Coulombic and Lennard-Jones contributions. Overall, it can be seen from Figures 6 and S3 that the A β -bilayer interaction is mostly hydrophobic in nature, since most residues interacted with the bilayer via the Lennard-Jones interaction. However, Coulombic interactions played a major role in the case of Asp1 and Arg5 residues in both A β 42-wt and A β 42-GLR29, which is expected due to their tendency to form hydrogen bonds with POPC.

The observation that A β 42 formed the most contacts with GM1 can be attributed to the large headgroup of GM1 containing five sugar groups (Figure S8) that tend to lie on the membrane surface, thus providing a platform for hydrogen bonding with A β 42 through its sugar headgroups (Figure 4). It should be noted that with 5% GM1 in the bilayer there were only 7 GM1 lipids in each leaflet. Despite this low GM1 content, as can be seen from the most populated clusters (Figures 9, S6, and S7), A β 42 has a preference to bind to GM1 and in some cases even to two GM1 molecules at the same time due to the possibility of hydrogen bonding to the pentasaccharide GM1 headgroup. In order to further elucidate the A β 42-GM1 binding, we dissected these interactions into their contributions per sugar ring. The representative snapshot in Figure S9 and the contact probability in Figure S10 show that independent of the oxidation state of A β 42, the peptide made the most contacts with the sugar groups furthest away from the membrane surface, that is the terminal β -D-galactose (Gal'), the N-acetyl- β -D-galactosamine (GalNAc), and the N-acetyl- α -neuraminidate (Neu). Apart from A β 42-GLR25, the other three A β 42 variants preferred binding to Neu, while A β 42-GLR25 formed more contacts with Gal'. The contact probability of A β 42-wt and A β 42-GLR25 with GalNAc is also considerably high, leading to some contacts with the adjacent Gal, while A β 42-GLR29 and A β 42-GLR33 formed only a few contacts with GalNAc. Figure S11 confirms that in all cases the contacts between A β 42 and the sugar groups are driven by hydrogen-bond formation, which, however, does not only involve Coulomb but also Lennard-Jones interactions (Figure S12). The formation of hydrogen bonds of A β 42 with GM1 prevents the peptide from forming intrapeptide hydrogen bonds as needed for secondary structure formation, e.g., the formation of β -sheets and α -helices. This is indeed the case as the numerous snapshots in Figures 9, S6, and S7 reveal: at the A β 42-GM1 binding sites, no β -sheet or α -helix is found. However, the binding of A β 42 to GM1 keeps A β 42, or at least parts of it, somewhat above the membrane surface (Figure 3), which in turn encourages β -sheet formation as seen for A β 42-GLR25 in Figure 9B or helix formation as observed for A β 42-GLR33 in Figure 9D. The higher amount of structure formation of membrane-associated A β 42 compared to the solution state can thus be considered to be a consequence of the reduction in conformational flexibility on the membrane surface, while leaving A β 42 enough conformational freedom and also possibilities for intrapeptide hydrogen-bond formation needed for β -sheet or helix formation.

2.3.2. Effect on A β 42 Secondary Structure. The secondary structure of A β 42 has similar secondary structure elements in each system, particularly in the helical central polar region (Val12 to Ala21). This region remained helical in all peptides, though it is extended to include residues Asp7 to Ala21 in A β 42-GLR33. As evidenced by the membrane contacts, hydrogen bonding, and interaction energies, the conformation of A β 42 in the N-terminal region was not affected by the

interaction with POPC. This is because A β 42-GLR25 showed higher contact frequency with POPC in the N-terminal compared to A β 42-GLR33; however, both peptides showed no tendency to form β -sheets in the N-terminal region. The same is applied to A β 42-GLR29 and A β 42-wt. On the other hand, the interaction with GM1 affected the formation of β -sheets. It was observed that A β 42-GLR29 and A β 42-GLR33 showed the highest number of contacts with GM1 when compared to A β 42-wt and A β 42-GLR25, but these peptides had a lower tendency to form β -sheets, which is in agreement with the finding of Mandel et al. on A β 40.⁷³ This is also confirmed by the insertion data (Figure 3) which shows that A β 42-wt and A β 42-GLR25 behave differently with respect to the bilayer, with both peptides having a lower tendency to bind to GM1 (Figure 4) than A β 42-GLR29 and A β 42-GLR33 do.

The assignment of the secondary structure is shown in Figure 7, and it mirrors what is seen in the most populated clusters as shown in Figure 9. The intrapeptide backbone hydrogen bonds indicate a structure that is very similar to that of a β -sheet in the most populated clusters for these two systems.

2.3.3. Comparison with Other Studies. It is known from experimental findings and MD simulations that A β 42 is an intrinsically disordered protein, containing all possible secondary structures.^{9,74–77} It has also been shown that the C-terminal β -sheet is the seed for further A β aggregation into a β -sheet rich structure.⁷⁴ Moreover, the importance of the total β -strand content for controlling the aggregation rates was pointed out in an MD study by Man et al.⁷⁸ In our study we observed a C-terminal β -sheet in the case of A β 42-wt and A β 42-GLR25 especially in two regions, Val39-Ile41 and Ala30-Val36. We also found that there is a β -sheet forming propensity in the regions of Leu17 to Glu22 and Tyr10 to Glu11 in A β 42-GLR25. However, the β -sheet forming propensity in the C-terminal hydrophobic region was very low in the cases of A β 42-GLR29 and A β 42-GLR33, which might be explained by the findings of Fonte et al.⁵³ and Harmeier et al.⁵⁴ Fonte et al. found experimentally that changes in the glycine zipper Gly29-XXX-Gly33-XXX-Gly37 motif prevent the formation of toxic oligomers as they observed a reduction in A β toxicity upon the substitution of Gly37 with leucine.⁵³ It was also found by Harmeier et al. that the substitution of Gly33, which is both at the end of one and at the start of the next GXXXG interaction motif, causes the formation of less toxic oligomers. Based on that, we suggest that the stability of the C-terminal β -sheet in A β 42-GLR25 might be attributed to the fact that Gly25 does not disrupt the zipper motif.

According to our findings, the effect of radicalization of the Gly residue on the structure of A β 42 depends on the position of the oxidized Gly residue within the C-terminal hydrophobic region of A β . This is supported by the MD study of Owen and co-workers on three fast folding miniproteins, where it was also found that the denaturing effect of the Gly radicals depended on the position of the radical.⁶⁴ Structural changes in the protein upon Gly oxidation were more pronounced in the α -helix rich protein than in the β -sheet rich one due to the flat geometry of the radical (Figure S1).⁶⁴ This may even cause the formation of a β -sheet as Owen et al. showed in an MD study of a short helical peptide that underwent a transition to a β -sheet conformation upon radical formation.⁶³

It has been shown experimentally that A β interacts strongly with lipid bilayers comprised of phosphatidylcholine headgroups.^{79,80} In our study we found that this interaction is

mediated by hydrogen bonds with the positively charged N-terminal Asp1 and the side chain of Arg5. Furthermore, we found that such tight interactions have no effect on the A β secondary structure, which is in agreement with the experimental findings that binding of A β to PC-containing bilayers does not affect the secondary structure of the A β peptide at low concentrations.^{81,82} Our results showed how the bulky GM1 headgroups cover a large area of the membrane even with only 7 GM1 lipids in each bilayer leaflet, and the peptide is more likely to bind to the GM1 headgroups, especially to the terminal saccharide residues, than to the POPC headgroups. This agrees with the findings by Manna et al., who concluded that the GM1 headgroups act as a scaffold for A β binding through sugar-specific interactions.⁸³ They further observed the formation of a C-terminal β -hairpin upon binding of A β 42 to GM1, which is also in line with our results. However, it should be noted that another study found that the binding of A β 40 to GM1 headgroups induces the formation of a helix on the C-terminal side of the peptide.⁸⁴ We also observed helix formation upon GM1 binding, which, however, occurred preferentially between residues 10 and 21 of A β 42. This includes the region from 17 to 21 that was already identified as helical for A β 40 in solution.⁸⁵ From an experimental study it was followed that low concentrations of GM1, i.e., physiological concentration of GM1 that ranged from 2–4% of the total lipid content of the membrane,⁸⁶ enhance the formation of β -sheets but prevent A β oligomerization.⁸⁷ Other experiments further showed that the higher the concentrations of GM1 (but less physiologically relevant), the higher the β -sheet content of A β becomes.⁸⁸

3. CONCLUSION

Understanding the interplay between oxidative stress and A β neurotoxicity requires exploring the conformation of oxidized A β peptides. Based on our MD simulations of A β 42 and its oxidized variants in interplay with a model membrane bilayer, we found that A β 42-GLR25 is potentially as toxic as A β 42-wt, assuming that β -sheet formation in A β is connected to its toxicity,¹² whereas A β 42-GLR29 and A β 42-GLR33 showed less β -sheet forming propensity. We also revealed that the sugar moiety of GM1 affects the interaction between A β 42 and the membrane. A β has a high tendency to interact with GM1 (especially A β 42-GLR29 and A β 42-GLR33), and once this happens the propensity of the peptide to form β -sheet is greatly reduced as A β , instead of forming intrapeptide hydrogen bonds, interacts with GM1 through hydrogen bonds. Moreover, the interaction with GM1 also reduces the number of contacts and hydrogen bonds that the peptide makes with POPC. On the other hand, the insertion of the peptide into the bilayer is enhanced by its interaction with POPC; A β 42-wt and A β 42-GLR29 showed the highest number of contacts with POPC, and therefore these peptides interact most closely with the bilayer. Our results suggest that the differences observed in A β conformation and interaction with the bilayer upon the oxidation of different glycine residues might be attributed in part to the position of these residues within the C-terminal hydrophobic region of A β and its subsequent interaction with GM1. Further studies should test this observation and further determine the role of oxidation in A β -mediated AD toxicity.

4. METHODS

4.1. Model System and System Equilibration. The starting structures for the wild-type (wt) and oxidized (Gly25, Gly29, Gly33) $A\beta$ peptides were obtained from 1 μ s simulations, using the final snapshots of these simulations (Figure S13). These simulations had begun with the structure of $A\beta$ 42 as determined by NMR spectroscopy (PDB ID: 1Z0Q).⁸⁹ The N- and C-terminals were the free amino (NH_3^+) and carboxyl (COO^-) groups, respectively, and thus each peptide carried an overall charge of -3 . The oxidized $A\beta$ 42 peptides will be henceforth referred to as $A\beta$ 42-GLR25, $A\beta$ 42-GLR29, and $A\beta$ 42-GLR33. The four peptides were placed 3.5 nm above a symmetric membrane composed of 202 POPC, 72 CHOL, and 14 GM1 lipids. Each system was solvated with the TIP3P water model⁹⁰ and neutralized with 17 Na^+ ions. In addition, 150 mM NaCl was added to mimic the physiological concentration of these ions. The exact numbers of each molecule present in each system are listed in Table 1. All interactions among system constituents were described using OPLS-AA force field parameters.^{66,91–93} All MD simulations were carried out using the GROMACS 4.6 simulation package.⁹⁴

Table 1. Molecular Composition of the Four Membrane Systems: $A\beta$ 42-wt, $A\beta$ 42-GLR25, $A\beta$ 42-GLR29, and $A\beta$ 42-GLR33

bilayer system	number of molecules						water
	peptide	lipids			ions		
		$A\beta$ 42	POPC	CHOL	GM1	Na^+	
$A\beta$ 42-wt	1	202	72	14	69	52	19301
$A\beta$ 42-GLR25	1	202	72	14	69	52	19289
$A\beta$ 42-GLR29	1	202	72	14	69	52	19293
$A\beta$ 42-GLR33	1	202	72	14	69	52	19259

The systems were energy minimized using the steepest descent algorithm to remove all atomic clashes.^{95,96} This was followed by an equilibration under NVT conditions for 1 ns, where the reference temperature of 310 K was regulated with the velocity-rescale thermostat⁹⁷ and the time constant was set to 0.1 ps. During minimization and initial equilibration stages, the heavy atoms of protein and lipids were subjected to position restraints with a force constant of 1000 $\text{kJ/mol} \cdot \text{nm}^2$. Next, the system was equilibrated under NPT conditions for 10 ns to obtain a pressure of 1.0 bar. The pressure was regulated using a semi-isotropic Parrinello–Rahman pressure coupling scheme^{98–100} with a time constant of 5 ps and isothermal compressibility of $4.5 \times 10^{-5} \text{ bar}^{-1}$. The temperature of 310 K was maintained with a Nosé–Hoover thermostat^{101–104} with a time constant of 0.5 ps, while the position restraints on the protein and lipids were still on. The particle Mesh Ewald (PME)^{105,106} method was used to account for the electrostatic interactions within the system. Both the short-range interactions, with a van der Waals cutoff of 1.0 nm (real space), and the long-range (Fourier) electrostatics were used under the periodicity assumption, and the periodic boundary conditions were set in all directions. All bonds were constrained using the LINCS algorithm.¹⁰⁷

4.2. Hamiltonian Replica Exchange MD (HREMD) Simulations. For the final production run, the input parameters were the same as those under NPT conditions, except that the position restraints were switched off. To accelerate conformational sampling, we employed the HREMD protocol for the systems described in the previous section using the protocol introduced in ref 108. System coordinates and input parameters (without restraints) from the NPT equilibration served as the initial input to generate the postprocessed topology files required for the HREMD simulations. The system was split into hot ($A\beta$ peptide) and cold (the rest of the system) regions, where the interactions within the hot region and between the hot region and the cold region were enhanced by scaling the force field terms for the proper dihedrals, Lennard-Jones parameters, and electrostatic interactions. HREMD simulations were performed using 14 replicas with λ values ranging from 1 to 0.5, and replica

exchanges were attempted every 2 ps. Each system was simulated for 200 ns per λ value with the average exchange acceptance ratio of 0.13. All simulations were carried out with GROMACS 4.6 patched to PLUMED 2.2.¹⁰⁹

4.3. Analysis Methods. **4.3.1. Bilayer–Peptide Interactions.** The analysis of each system began when $A\beta$ was within 0.5 nm of the bilayer. All analysis programs mentioned in this section are included in the GROMACS 2018.2 program package.^{110–113} The “gmj traj” program was used to measure the insertion distance of $A\beta$ 42 by computing the center of mass (COM) of each residue, and the average vertical position of the phosphorus atoms of phospholipids was taken along the z-axis. The “gmj mindist” program was employed to determine the number of contacts between each $A\beta$ 42 residue and each POPC or GM1 lipid. A contact was recorded when the distance between any two non-hydrogen atoms from the residue and lipid in question was within 0.5 nm. Then the number of contacts was normalized in the range of 0 to 1. The hydrogen bond propensity was determined by the number of times a hydrogen bond was formed between hydrogen bond donating and accepting atoms in $A\beta$ 42 and each lipid type using the “gmj hbond” program. A hydrogen bond was recorded when the angle between the donor and acceptor bonded hydrogen was between 150 and 180 deg and the distance between the two atoms was within 0.35 nm. The “gmj energy” program was used to calculate the interactions energy between each $A\beta$ residue and the headgroup of POPC or GM1.

4.3.2. $A\beta$ 42 Structure. The secondary structure of each $A\beta$ 42 residue was determined using the *define secondary structure program* (do_dssp).¹¹⁴ To facilitate a clear representation, the data of similar secondary structures are grouped together; β -strand and β -bridge are combined as β -strand/bridge, β -turn and bend are combined as β -turn/bend, and helix includes α , π , and 3_{10} helices. Hydrogen bonds within the peptide backbone, between the backbone and side chains, and between the side chains were counted by applying the same method used for counting the peptide–lipid hydrogen bonds. Representative $A\beta$ 42 structures were obtained by the “gmj cluster” program using the method of Daura et al.¹¹⁵ and a cutoff of 0.25 nm for clustering. The conformation and membrane interactions of the central structure of the three largest clusters were rendered using the VMD program.¹¹⁶

■ ASSOCIATED CONTENT

Supporting Information

The Supporting Information is available free of charge at <https://pubs.acs.org/doi/10.1021/acscchemneuro.9b00558>.

Figures and tables explaining structure used in study and enhancing analysis (PDF)

■ AUTHOR INFORMATION

Corresponding Author

Michael C. Owen – CEITEC – Central European Institute of Technology, Masaryk University, Brno 625 00, Czech Republic; orcid.org/0000-0001-9076-7114; Email: michaelowen27@gmail.com

Authors

Hebah Fatafta – Institute of Biological Information Processing (IBI-7: Structural Biochemistry), Forschungszentrum Jülich, 52425 Jülich, Germany

Chetan Poojari – Department of Physics, University of Helsinki, FI-00014 Helsinki, Finland; Theoretical Physics and Center for Biophysics, Saarland University, 66123 Saarbrücken, Germany

Abdallah Sayyed-Ahmad – Department of Physics, Birzeit University, Birzeit 71939, Palestine; orcid.org/0000-0003-2415-8403

Birgit Strodel – Institute of Biological Information Processing (IBI-7: Structural Biochemistry), Forschungszentrum Jülich,

52425 Jülich, Germany; Institute of Theoretical and Computational Chemistry, Heinrich Heine University Düsseldorf, 40225 Düsseldorf, Germany; orcid.org/0000-0002-8734-7765

Complete contact information is available at:
<https://pubs.acs.org/10.1021/acschemneuro.9b00558>

Author Contributions

All authors made a significant contribution to this manuscript. The contribution of each author is as follows: H.F. analyzed simulation data, prepared figures, presented data, and wrote the manuscript. C.P. designed the study, set up simulations, and wrote the manuscript. A.S.-A. provided study funding and wrote the manuscript. B.S. provided study funding, interpreted simulation data, and wrote the manuscript. M.C.O. designed the study, provided study funding, carried out simulations, and wrote the manuscript.

Notes

This article reflects only the author's (M.C.O.) view, and the EU is not responsible for any use that may be made of the information it contains.

The authors declare no competing financial interest.

ACKNOWLEDGMENTS

H.F., A.S.-A., and B.S. acknowledge funding for this project from the Palestinian-German Science Bridge financed by the German Federal Ministry of Education and Research (BMBF). H.F. and B.S. gratefully acknowledge the computing time granted through JARA-HPC (project JICS6C) on the supercomputer JURECA at Forschungszentrum Jülich. This project has received funding from the European Union's Horizon 2020 research and innovation programme under the Marie Skłodowska-Curie grant agreement no. 665860, and it is cofinanced by the South Moravian Region. M.C.O. also thanks the Helmholtz Postdoc Programme. Access to computing and storage facilities owned by parties and projects contributing to the National Grid Infrastructure MetaCentrum provided under the programme "Projects of Large Research, Development, and Innovations Infrastructures" (CESNET LM2015042) is greatly appreciated.

REFERENCES

- (1) Burns, A., and Iliffe, S. (2009) Alzheimer's disease. *Br. Med. J.* 338, 467–471.
- (2) Förstl, H., and Kurz, A. (1999) Clinical features of Alzheimer's disease. *Eur. Arch. Psy. Clin. N.* 249, 288–290.
- (3) Niu, Z., Zhang, Z., Zhao, W., and Yang, J. (2018) Interactions between amyloid β peptide and lipid membranes. *Biochim. Biophys. Acta, Biomembr.* 1860, 1663–1669.
- (4) Rangachari, V., Dean, D. N., Rana, P., Vaidya, A., and Ghosh, P. (2018) Cause and consequence of $A\beta$ -Lipid interactions in Alzheimer disease pathogenesis. *Biochim. Biophys. Acta, Biomembr.* 1860, 1652–1662.
- (5) Cheng, Q., Hu, Z.-W., Doherty, K. E., Tobin-Miyaji, Y. J., and Qiang, W. (2018) The on-fibrillation-pathway membrane content leakage and off-fibrillation-pathway lipid mixing induced by 40-residue β -amyloid peptides in biologically relevant model liposomes. *Biochim. Biophys. Acta, Biomembr.* 1860, 1670–1680.
- (6) Owen, M. C., Gnutt, D., Gao, M., Wärmländer, S. K., Jarvet, J., Gräslund, A., Winter, R., Ebbinghaus, S., and Strodel, B. (2019) Effects of in vivo conditions on amyloid aggregation. *Chem. Soc. Rev.* 48, 3946–3996.
- (7) Hardy, J. A., and Higgins, G. A. (1992) Alzheimer's disease: the amyloid cascade hypothesis. *Science* 256, 184–186.

- (8) Cheng, R. P., Gellman, S. H., and DeGrado, W. F. (2001) β -Peptides: from structure to function. *Chem. Rev.* 101, 3219–3232.
- (9) Lührs, T., Ritter, C., Adrian, M., Riek-Loher, D., Bohrmann, B., Döbeli, H., Schubert, D., and Riek, R. (2005) 3D structure of Alzheimer's amyloid- β (1–42) fibrils. *Proc. Natl. Acad. Sci. U. S. A.* 102, 17342–17347.
- (10) Kael, M. A., Weber, D. K., Separovic, F., and Sani, M.-A. (2018) Aggregation kinetics in the presence of brain lipids of $A\beta$ (1–40) cleaved from a soluble fusion protein. *Biochim. Biophys. Acta, Biomembr.* 1860, 1681–1686.
- (11) Marshall, K. E., Vadukul, D. M., Dahal, L., Theisen, A., Fowler, M. W., Al-Hilaly, Y., Ford, L., Kemeses, G., Day, I. J., Staras, K., and Serpell, L. C. (2016) A critical role for the self-assembly of Amyloid- β 1–42 in neurodegeneration. *Sci. Rep.* 6, 30182.
- (12) Ono, K., Condron, M. M., and Teplow, D. B. (2009) Structure–neurotoxicity relationships of amyloid β -protein oligomers. *Proc. Natl. Acad. Sci. U. S. A.* 106, 14745–14750.
- (13) El-Agnaf, O. M., Mahil, D. S., Patel, B. P., and Austen, B. M. (2000) Oligomerization and toxicity of β -amyloid-42 implicated in Alzheimer's disease. *Biochem. Biophys. Res. Commun.* 273, 1003–1007.
- (14) Petkova, A. T., Ishii, Y., Balbach, J. J., Antzutkin, O. N., Leapman, R. D., Delaglio, F., and Tycko, R. (2002) A structural model for Alzheimer's β -amyloid fibrils based on experimental constraints from solid state NMR. *Proc. Natl. Acad. Sci. U. S. A.* 99, 16742–16747.
- (15) Kim, W., and Hecht, M. H. (2006) Generic hydrophobic residues are sufficient to promote aggregation of the Alzheimer's $A\beta$ 42 peptide. *Proc. Natl. Acad. Sci. U. S. A.* 103, 15824–15829.
- (16) Cukalevski, R., Boland, B., Frohm, B., Thulin, E., Walsh, D., and Linse, S. (2012) Role of aromatic side chains in amyloid β -protein aggregation. *ACS Chem. Neurosci.* 3, 1008–1016.
- (17) Poojari, C., Kukul, A., and Strodel, B. (2013) How the amyloid- β peptide and membranes affect each other: An extensive simulation study. *Biochim. Biophys. Acta, Biomembr.* 1828, 327–339.
- (18) Poojari, C., and Strodel, B. (2013) Stability of transmembrane amyloid β -peptide and membrane integrity tested by molecular modeling of site-specific $A\beta$ 42 mutations. *PLoS One* 8, e78399.
- (19) Varadarajan, S., Yatin, S., Aksenova, M., and Butterfield, D. A. (2000) Alzheimer's amyloid β -peptide-associated free radical oxidative stress and neurotoxicity. *J. Struct. Biol.* 130, 184–208.
- (20) Butterfield, D. A., and Lauderback, C. M. (2002) Lipid peroxidation and protein oxidation in Alzheimer's disease brain: potential causes and consequences involving amyloid β -peptide-associated free radical oxidative stress. *Free Radical Biol. Med.* 32, 1050–1060.
- (21) Drake, J., Link, C. D., and Butterfield, D. A. (2003) Oxidative stress precedes fibrillar deposition of Alzheimer's disease amyloid β -peptide (1–42) in a transgenic *Caenorhabditis elegans* model. *Neurobiol. Aging* 24, 415–420.
- (22) Butterfield, D. A. (2004) Proteomics: a new approach to investigate oxidative stress in Alzheimer's disease brain. *Brain Res.* 1000, 1–7.
- (23) Sultana, R., and Butterfield, D. A. (2010) Role of oxidative stress in the progression of Alzheimer's disease. *J. Alzheimer's Dis.* 19, 341–353.
- (24) Huang, W.-J., Zhang, X., and Chen, W.-W. (2016) Role of oxidative stress in Alzheimer's disease. *Biomed. Rep.* 4, 519–522.
- (25) Brown, D. R. (2005) Neurodegeneration and oxidative stress: prion disease results from loss of antioxidant defence. *Folia Neuropathol.* 43, 229–243.
- (26) Cheignon, C., Tomas, M., Bonnefont-Rousselot, D., Faller, P., Hureau, C., and Collin, F. (2018) Oxidative stress and the amyloid beta peptide in Alzheimer's disease. *Redox Biol.* 14, 450–464.
- (27) Smith, D. G., Cappai, R., and Barnham, K. J. (2007) The redox chemistry of the Alzheimer's disease amyloid β peptide. *Biochim. Biophys. Acta, Biomembr.* 1768, 1976–1990.
- (28) Zhao, Y., and Zhao, B. (2013) Oxidative stress and the pathogenesis of Alzheimer's disease. *Oxid. Med. Cell. Longevity* 2013 (2013), 316523.

- (29) Minicozzi, V., Stellato, F., Comai, M., Dalla Serra, M., Potrich, C., Meyer-Klaucke, W., and Morante, S. (2008) Identifying the minimal copper- and zinc-binding site sequence in amyloid- β peptides. *J. Biol. Chem.* 283, 10784–10792.
- (30) Marino, T., Russo, N., Toscano, M., and Pavelka, M. (2010) On the metal ion (Zn^{2+} , Cu^{2+}) coordination with beta-amyloid peptide: DFT computational study. *Interdiscip. Sci.: Comput. Life Sci.* 2, 57–69.
- (31) Roberts, B. R., Ryan, T. M., Bush, A. I., Masters, C. L., and Duce, J. A. (2012) The role of metallobiology and amyloid- β peptides in Alzheimer's disease. *J. Neurochem.* 120, 149–166.
- (32) Pearson, H. A., and Peers, C. (2006) Physiological roles for amyloid β peptides. *J. Physiol. (Oxford, U. K.)* 575, 5–10.
- (33) Brothers, H. M., Gosztyla, M. L., and Robinson, S. R. (2018) The Physiological Roles of Amyloid- β Peptide Hint at New Ways to Treat Alzheimer's Disease. *Front. Aging Neurosci.* 10, 118.
- (34) Michikawa, M., Gong, J.-S., Fan, Q.-W., Sawamura, N., and Yanagisawa, K. (2001) A novel action of Alzheimer's amyloid β -protein ($A\beta$): oligomeric $A\beta$ promotes lipid release. *J. Neurosci.* 21, 7226–7235.
- (35) Koudinova, N. V., Koudinov, A. R., and Yavin, E. (2000) Alzheimer's $A\beta$ 1–40 Peptide Modulates Lipid Synthesis in Neuronal Cultures and Intact Rat Fetal Brain Under Normoxic and Oxidative Stress Conditions. *Neurochem. Res.* 25, 653–660.
- (36) Yanagisawa, K., Odaka, A., Suzuki, N., and Ihara, Y. (1995) GM1 ganglioside-bound amyloid β -protein ($A\beta$): A possible form of preamyloid in Alzheimer's disease. *Nat. Med. (N. Y., NY, U. S.)* 1, 1062.
- (37) Di Scala, C., Chahinian, H., Yahi, N., Garmy, N., and Fantini, J. (2014) Interaction of Alzheimer's β -amyloid peptides with cholesterol: mechanistic insights into amyloid pore formation. *Biochemistry* 53, 4489–4502.
- (38) Kakio, A., Nishimoto, S.-i., Yanagisawa, K., Kozutsumi, Y., and Matsuzaki, K. (2002) Interactions of amyloid β -protein with various gangliosides in raft-like membranes: importance of GM1 ganglioside-bound form as an endogenous seed for Alzheimer amyloid. *Biochemistry* 41, 7385–7390.
- (39) Thomaier, M., Gremer, L., Dammers, C., Fabig, J., Neudecker, P., and Willbold, D. (2016) High-affinity binding of monomeric but not oligomeric amyloid- β to ganglioside GM1 containing nanodiscs. *Biochemistry* 55, 6662–6672.
- (40) Di Scala, C., Yahi, N., Boutemour, S., Flores, A., Rodriguez, L., Chahinian, H., and Fantini, J. (2016) Common molecular mechanism of amyloid pore formation by Alzheimer's β -amyloid peptide and α -synuclein. *Sci. Rep.* 6, 28781.
- (41) Eckert, G. P., Kirsch, C., Leutz, S., Wood, W. G., and Müller, W. E. (2003) Cholesterol modulates amyloid beta-peptide's membrane interactions. *Pharmacopsychiatry* 36, 136–143.
- (42) Fantini, J., Yahi, N., and Garmy, N. (2013) Cholesterol accelerates the binding of Alzheimer's β -amyloid peptide to ganglioside GM1 through a universal hydrogen-bond-dependent sterol tuning of glycolipid conformation. *Front. Physiol.* 4, 120.
- (43) Cui, Z. J., Han, Z. Q., and Li, Z. Y. (2012) Modulating protein activity and cellular function by methionine residue oxidation. *Amino Acids* 43, 505–517.
- (44) Butterfield, D. A., and Kanski, J. (2002) Methionine residue 35 is critical for the oxidative stress and neurotoxic properties of Alzheimer's amyloid β -peptide 1–42. *Peptides* 23, 1299–1309.
- (45) Butterfield, D. A., and Boyd-Kimball, D. (2005) The critical role of methionine 35 in Alzheimer's amyloid β -peptide (1–42)-induced oxidative stress and neurotoxicity. *Biochim. Biophys. Acta, Proteins Proteomics* 1703, 149–156.
- (46) Butterfield, D. A., and Sultana, R. (2011) Methionine-35 of $A\beta$ (1–42): importance for oxidative stress in Alzheimer disease. *J. Amino Acids* 2011, 198430.
- (47) Boyd-Kimball, D., Sultana, R., Mohammad-Abdul, H., and Butterfield, D. A. (2005) Neurotoxicity and oxidative stress in DIM-substituted Alzheimer's $A\beta$ (1–42): relevance to N-terminal methionine chemistry in small model peptides. *Peptides* 26, 665–673.
- (48) Varadarajan, S., Kanski, J., Aksenova, M., Lauderback, C., and Butterfield, D. A. (2001) Different Mechanisms of Oxidative Stress and Neurotoxicity for Alzheimer's $A\beta$ (1–42) and $A\beta$ (25–35). *J. Am. Chem. Soc.* 123, 5625–5631.
- (49) Varadarajan, S., Yatin, S., Kanski, J., Jahanshahi, F., and Butterfield, D. A. (1999) Methionine residue 35 is important in amyloid β -peptide-associated free radical oxidative stress. *Brain Res. Bull.* 50, 133–141.
- (50) Kanski, J., Varadarajan, S., Aksenova, M., and Butterfield, D. A. (2002) Role of glycine-33 and methionine-35 in Alzheimer's amyloid β -peptide 1–42-associated oxidative stress and neurotoxicity. *Biochim. Biophys. Acta, Mol. Basis Dis.* 1586, 190–198.
- (51) Rauk, A., Armstrong, D. A., and Fairlie, D. P. (2000) Is oxidative damage by β -amyloid and prion peptides mediated by hydrogen atom transfer from glycine α -carbon to methionine sulfur within β -sheets? *J. Am. Chem. Soc.* 122, 9761–9767.
- (52) Mazzitelli, S., Filipello, F., Rasile, M., Lauranzano, E., Starvaggi-Cucuzza, C., Tamborini, M., Pozzi, D., Barajon, I., Giorgino, T., Natalello, A., and Matteoli, M. (2016) Amyloid- β 1–24 C-terminal truncated fragment promotes amyloid- β 1–42 aggregate formation in the healthy brain. *Acta Neuropathol. Commun.* 4, 110.
- (53) Fonte, V., Dostal, V., Roberts, C. M., Gonzales, P., Lacor, P., Magrane, J., Dingwell, N., Fan, E. Y., Silverman, M. A., Stein, G. H., and Link, C. D. (2011) A glycine zipper motif mediates the formation of toxic β -amyloid oligomers in vitro and in vivo. *Mol. Neurodegener.* 6, 61.
- (54) Harmeier, A., Wozny, C., Rost, B. R., Munter, L.-M., Hua, H., Georgiev, O., Beyermann, M., Hildebrand, P. W., Weise, C., Schaffner, W., and Schmitz, D. (2009) Role of amyloid- β glycine 33 in oligomerization, toxicity, and neuronal plasticity. *J. Neurosci.* 29, 7582–7590.
- (55) Stuyver, T., Danovich, D., and Shaik, S. (2019) Captodative Substitution Enhances the Diradical Character of Compounds, Reduces Aromaticity, and Controls Single-Molecule Conductivity Patterns: A Valence Bond Study. *J. Phys. Chem. A* 123, 7133–7141.
- (56) Viehe, H. G., Janousek, Z., Merenyi, R., and Stella, L. (1985) The captodative effect. *Acc. Chem. Res.* 18, 148–154.
- (57) Green, M. C., Stelzleni, S., and Francisco, J. S. (2013) Spectral Marker for Ca Damage in Beta Peptides. *J. Phys. Chem. A* 117, 550–565.
- (58) Davies, M. J. (2005) The oxidative environment and protein damage. *Biochim. Biophys. Acta, Proteins Proteomics* 1703, 93–109.
- (59) Song, Y., Li, P., Liu, L., Bortolini, C., and Dong, M. (2018) Nanostructural Differentiation and Toxicity of Amyloid- β 25–35 Aggregates Emerge from Distinct Secondary Conformation. *Sci. Rep.* 8, 765.
- (60) Hughes, E., Burke, R. M., and Doig, A. J. (2000) Inhibition of Toxicity in the β -Amyloid Peptide Fragment β -(25–35) Using N-Methylated Derivatives A GENERAL STRATEGY TO PREVENT AMYLOID FORMATION. *J. Biol. Chem.* 275, 25109–25115.
- (61) Karplus, M., and McCammon, J. A. (2002) Molecular dynamics simulations of biomolecules. *Nat. Struct. Biol.* 9, 646.
- (62) Dror, R. O., Jensen, M. Ø., Borhani, D. W., and Shaw, D. E. (2010) Exploring atomic resolution physiology on a femtosecond to millisecond timescale using molecular dynamics simulations. *J. Gen. Physiol.* 135, 555–562.
- (63) Owen, M. C., Strodel, B., Csizmadia, I. G., and Viskolcz, B. (2016) Radical formation initiates solvent-dependent unfolding and β -sheet formation in a model helical peptide. *J. Phys. Chem. B* 120, 4878–4889.
- (64) Owen, M. C., Csizmadia, I. G., Viskolcz, B., and Strodel, B. (2017) Protein stability and unfolding following glycine radical formation. *Molecules* 22, 655.
- (65) Liao, Q., Owen, M. C., Bali, S., Barz, B., and Strodel, B. (2018) $A\beta$ under stress: the effects of acidosis, Cu^{2+} -binding, and oxidation on amyloid β -peptide dimers. *Chem. Commun. (Cambridge, U. K.)* 54, 7766–7769.

- (66) Komáromi, I., Owen, M. C., Murphy, R. F., and Lovas, S. (2008) Development of glycol radical parameters for the OPLS-AA/L force field. *J. Comput. Chem.* 29, 1999–2009.
- (67) Meli, M., and Colombo, G. (2013) A Hamiltonian replica exchange molecular dynamics (MD) method for the study of folding, based on the analysis of the stabilization determinants of proteins. *Int. J. Mol. Sci.* 14, 12157–12169.
- (68) Allen, W. J., Lemkul, J. A., and Bevan, D. R. (2009) GridMAT-MD: a grid-based membrane analysis tool for use with molecular dynamics. *J. Comput. Chem.* 30, 1952–1958.
- (69) Gapsys, V., de Groot, B. L., and Briones, R. (2013) Computational analysis of local membrane properties. *J. Comput.-Aided Mol. Des.* 27, 845–858.
- (70) Persson, F., Söderhjelm, P., and Halle, B. (2018) The geometry of protein hydration. *J. Chem. Phys.* 148, 215101.
- (71) Fox, S. J., Lakshminarayanan, R., Beuerman, R. W., Li, J., and Verma, C. S. (2018) Conformational Transitions of Melittin between Aqueous and Lipid Phases: Comparison of Simulations with Experiments. *J. Phys. Chem. B* 122, 8698–8705.
- (72) Matthes, D., and De Groot, B. L. (2009) Secondary structure propensities in peptide folding simulations: a systematic comparison of molecular mechanics interaction schemes. *Biophys. J.* 97, 599–608.
- (73) Mandal, P. K., and Pettegrew, J. W. (2004) Alzheimer's disease: NMR studies of asialo (GM1) and trisialo (GT1b) ganglioside interactions with A β (1–40) peptide in a membrane mimic environment. *Neurochem. Res.* 29, 447–453.
- (74) Rosenman, D. J., Connors, C. R., Chen, W., Wang, C., and García, A. E. (2013) A β monomers transiently sample oligomer and fibril-like configurations: Ensemble characterization using a combined MD/NMR approach. *J. Mol. Biol.* 425, 3338–3359.
- (75) Fawzi, N. L., Phillips, A. H., Ruscio, J. Z., Doucleff, M., Wemmer, D. E., and Head-Gordon, T. (2008) Structure and dynamics of the A β 21–30 peptide from the interplay of NMR experiments and molecular simulations. *J. Am. Chem. Soc.* 130, 6145–6158.
- (76) Carballo-Pacheco, M., and Strodel, B. (2017) Comparison of force fields for Alzheimer's A: A case study for intrinsically disordered proteins. *Protein Sci.* 26, 174–185.
- (77) Nasic-Labouze, J., Nguyen, P. H., Sterpone, F., Berthoumieu, O., Buchete, N.-V., Cote, S., De Simone, A., Doig, A. J., Faller, P., Garcia, A., and Laio, A. (2015) Amyloid β protein and Alzheimer's disease: When computer simulations complement experimental studies. *Chem. Rev. (Washington, DC, U. S.)* 115, 3518–3563.
- (78) Man, V. H., He, X., Derreumaux, P., Ji, B., Xie, X.-Q., Nguyen, P. H., and Wang, J. (2019) Effects of All-Atom Molecular Mechanics Force Fields on Amyloid Peptide Assembly: The Case of A β 16–22 Dimer. *J. Chem. Theory Comput.* 15, 1440–1452.
- (79) Ding, H., Schauerte, J. A., Steel, D. G., and Gafni, A. (2012) β -amyloid (1–40) peptide interactions with supported phospholipid membranes: A single-molecule study. *Biophys. J.* 103, 1500–1509.
- (80) Korshavn, K. J., Satriano, C., Lin, Y., Zhang, R., Dulchavsky, M., Bhunia, A., Ivanova, M. I., Lee, Y.-H., La Rosa, C., Lim, M. H., and Ramamoorthy, A. (2017) Reduced lipid bilayer thickness regulates the aggregation and cytotoxicity of amyloid- β . *J. Biol. Chem.* 292, 4638–4650.
- (81) Qiang, W., Yau, W.-M., and Schulte, J. (2015) Fibrillation of β amyloid peptides in the presence of phospholipid bilayers and the consequent membrane disruption. *Biochim. Biophys. Acta, Biomembr.* 1848, 266–276.
- (82) Terzi, E., Hölzemann, G., and Seelig, J. (1995) Self-association of β -amyloid peptide (1–40) in solution and binding to lipid membranes. *J. Mol. Biol.* 252, 633–642.
- (83) Manna, M., and Mukhopadhyay, C. (2013) Binding, conformational transition and dimerization of amyloid- β peptide on GM1-containing ternary membrane: insights from molecular dynamics simulation. *PLoS One* 8, e71308.
- (84) Tachi, Y., Okamoto, Y., and Okumura, H. (2019) Conformational Change of Amyloid- β 40 in Association with Binding to GM1-Glycan Cluster. *Sci. Rep.* 9, 6853.
- (85) Vivekanandan, S., Brender, J. R., Lee, S. Y., and Ramamoorthy, A. (2011) A partially folded structure of amyloid-beta (1–40) in an aqueous environment. *Biochem. Biophys. Res. Commun.* 411, 312–316.
- (86) Ledeen, R. (1978) Ganglioside structures and distribution: are they localized at the nerve ending? *J. Supramol. Struct.* 8, 1–17.
- (87) Amaro, M., Šachl, R., Aydogan, G., Mikhalyov, I. I., Vácha, R., and Hof, M. (2016) GM1 Ganglioside Inhibits β -Amyloid Oligomerization Induced by Sphingomyelin. *Angew. Chem., Int. Ed.* 55, 9411–9415.
- (88) Ariga, T., McDonald, M. P., and Robert, K. Y. (2008) Thematic Review Series: Sphingolipids. Role of ganglioside metabolism in the pathogenesis of Alzheimer's disease—a review. *J. Lipid Res.* 49, 1157–1175.
- (89) Tomaselli, S., Esposito, V., Vangone, P., van Nuland, N. A., Bonvin, A. M., Guerrini, R., Tancredi, T., Temussi, P. A., and Picone, D. (2006) The α -to- β conformational transition of Alzheimer's A β (1–42) peptide in aqueous media is reversible: A step by step conformational analysis suggests the location of β conformation seeding. *ChemBioChem* 7, 257–267.
- (90) Jorgensen, W. L., Chandrasekhar, J., Madura, J. D., Impey, R. W., and Klein, M. L. (1983) Comparison of simple potential functions for simulating liquid water. *J. Chem. Phys.* 79, 926–935.
- (91) Kaminski, G. A., Friesner, R. A., Tirado-Rives, J., and Jorgensen, W. L. (2001) Evaluation and reparametrization of the OPLS-AA force field for proteins via comparison with accurate quantum chemical calculations on peptides. *J. Phys. Chem. B* 105, 6474–6487.
- (92) Kulig, W., Pasenkiewicz-Gierula, M., and Róg, T. (2015) Topologies, structures and parameter files for lipid simulations in GROMACS with the OPLS-aa force field: DPPC, POPC, DOPC, PEPC, and cholesterol. *Data Brief* 5, 333–336.
- (93) Maciejewski, A., Pasenkiewicz-Gierula, M., Cramariuc, O., Vattulainen, I., and Rog, T. (2014) Refined OPLS all-atom force field for saturated phosphatidylcholine bilayers at full hydration. *J. Phys. Chem. B* 118, 4571–4581.
- (94) Hess, B., Kutzner, C., van der Spoel, D., and Lindahl, E. (2008) GROMACS 4: algorithms for highly efficient, load-balanced, and scalable molecular simulation. *J. Chem. Theory Comput.* 4, 435–447.
- (95) Zhang, J. (2015) The Hybrid Idea of (Energy Minimization) Optimization Methods Applied to Study Prion Protein Structures Focusing on the beta-2-alpha2 Loop. *Biochem. Pharmacol. (Los Angeles, CA, U. S.)* 4, 1000175.
- (96) Müller, K., and Brown, L. D. (1979) Location of saddle points and minimum energy paths by a constrained simplex optimization procedure. *Theor. Chim. Acta* 53, 75–93.
- (97) Bussi, G., Donadio, D., and Parrinello, M. (2007) Canonical sampling through velocity rescaling. *J. Chem. Phys.* 126, 014101.
- (98) Parrinello, M., and Rahman, A. (1980) Crystal structure and pair potentials: A molecular-dynamics study. *Phys. Rev. Lett.* 45, 1196.
- (99) Parrinello, M., and Rahman, A. (1981) Polymorphic transitions in single crystals: A new molecular dynamics method. *J. Appl. Phys. (Melville, NY, U. S.)* 52, 7182–7190.
- (100) Parrinello, M., and Rahman, A. (1982) Strain fluctuations and elastic constants. *J. Chem. Phys.* 76, 2662–2666.
- (101) Nosé, S. (1984) A unified formulation of the constant temperature molecular dynamics methods. *J. Chem. Phys.* 81, 511–519.
- (102) Nosé, S. (1986) An extension of the canonical ensemble molecular dynamics method. *Mol. Phys.* 57, 187–191.
- (103) NOSE, S. U. I. (2002) A molecular dynamics method for simulations in the canonical ensemble. *Mol. Phys.* 100, 191–198.
- (104) Hoover, W. G. (1985) Canonical dynamics: Equilibrium phase-space distributions. *Phys. Rev. A: At., Mol., Opt. Phys.* 31, 1695.
- (105) Darden, T., York, D., and Pedersen, L. (1993) Particle mesh Ewald: An N-log(N) method for Ewald sums in large systems. *J. Chem. Phys.* 98, 10089–10092.
- (106) Essmann, U., Perera, L., Berkowitz, M. L., Darden, T., Lee, H., and Pedersen, L. G. (1995) A smooth particle mesh Ewald method. *J. Chem. Phys.* 103, 8577–8593.

- (107) Hess, B., Bekker, H., Berendsen, H. J., and Fraaije, J. G. (1997) LINCS: a linear constraint solver for molecular simulations. *J. Comput. Chem.* *18*, 1463–1472.
- (108) Bussi, G. (2014) Hamiltonian replica exchange in GROMACS: a flexible implementation. *Mol. Phys.* *112*, 379–384.
- (109) Tribello, G. A., Bonomi, M., Branduardi, D., Camilloni, C., and Bussi, G. (2014) PLUMED 2: New feathers for an old bird. *Comput. Phys. Commun.* *185*, 604–613.
- (110) Abraham, M. J., Lindahl, E., Hess, B., and van der Spoel, D., and the GROMACS development team (2018) *GROMACS User Manual*, version 2018.2. www.gromacs.org (accessed Jan 21, 2020).
- (111) Abraham, M. J., Murtola, T., Schulz, R., Páll, S., Smith, J. C., Hess, B., and Lindahl, E. (2015) GROMACS: High performance molecular simulations through multi-level parallelism from laptops to supercomputers. *SoftwareX* *1*, 19–25.
- (112) Páll, S., Abraham, M. J., Kutzner, C., Hess, B., and Lindahl, E. (2015) *Solving Software Challenges for Exascale. International Conference on Exascale Applications and Software, Stockholm, Sweden, April 2–3, 2014* (Laure, S. M., Ed.) pp 3–27, Springer, Cham.
- (113) Pronk, S., Páll, S., Schulz, R., Larsson, P., Bjelkmar, P., Apostolov, R., Shirts, M. R., Smith, J. C., Kasson, P. M., van der Spoel, D., and Hess, B. (2013) GROMACS 4.5: a high-throughput and highly parallel open source molecular simulation toolkit. *Bioinformatics* *29*, 845–854.
- (114) Kabsch, W., and Sander, C. (1983) Dictionary of protein secondary structure: pattern recognition of hydrogen-bonded and geometrical features. *Biopolymers* *22*, 2577–2637.
- (115) Daura, X., Gademann, K., Jaun, B., Seebach, D., van Gunsteren, W. F., and Mark, A. E. (1999) Peptide folding: when simulation meets experiment. *Angew. Chem., Int. Ed.* *38*, 236–240.
- (116) Humphrey, W., Dalke, A., and Schulten, K. (1996) VMD: visual molecular dynamics. *J. Mol. Graphics* *14*, 33–38.

■ NOTE ADDED AFTER ASAP PUBLICATION

Due to a production error, this paper was published on the Web on January 30, 2020, with the wrong Supporting Information file. The corrected version was reposted on February 3, 2020.

Supporting Information

Role of Oxidized Gly25, Gly29 and Gly33 residues on the interactions of $A\beta_{1-42}$ with lipid Membranes

Hebah Fatafta,[†] Chetan Poojari,^{‡,¶} Abdallah Sayyed-Ahmad,[§] Birgit Strodel,^{†,||}
and Michael C. Owen^{*,⊥}

[†]*Institute of Biological Information Processing (IBI-7: Structural Biochemistry),
Forschungszentrum Jülich, 52425 Jülich, Germany*

[‡]*Department of Physics, University of Helsinki, P.O. Box 64, FI-00014, Helsinki, Finland*

[¶]*Theoretical Physics and Center for Biophysics, Saarland University, Campus E2 6, 66123
Saarbrücken, Germany*

[§]*Department of Physics, Birzeit University, Birzeit, Palestine*

^{||}*Institute of Theoretical and Computational Chemistry, Heinrich Heine University
Düsseldorf, 40225, Düsseldorf, Germany*

[⊥]*CEITEC – Central European Institute of Technology, Masaryk University, Kamenice
753/5, Brno 625 00, Czech Republic*

E-mail: michaelowen27@gmail.com

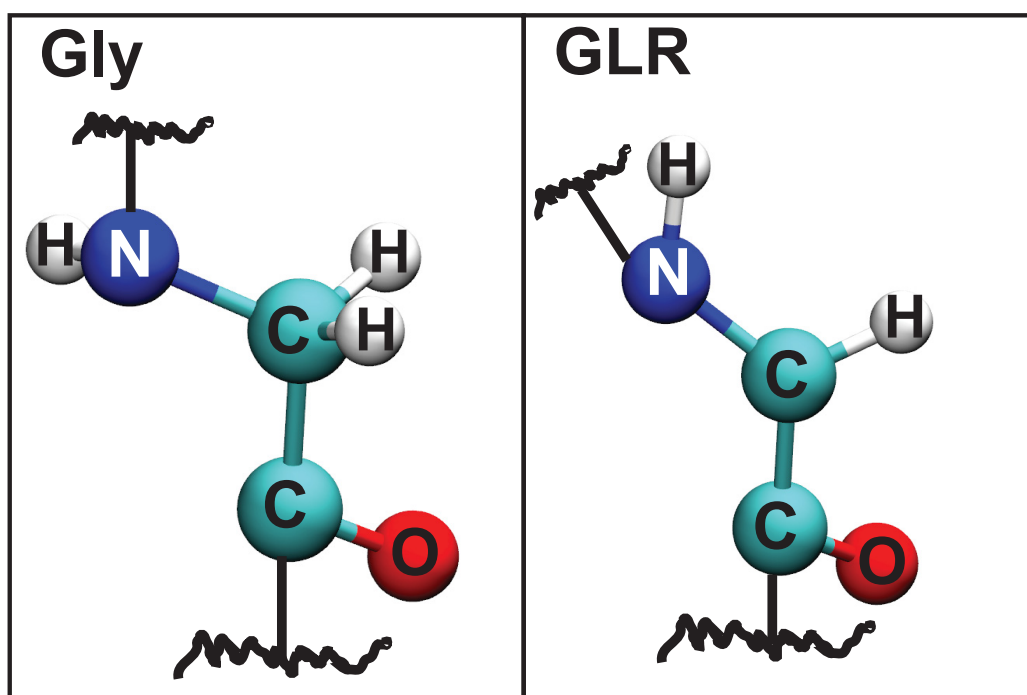


Figure S1: Structure of (A) glycine (Gly) (B) radical glycine (GLR) residue taken from A β 42 peptide. The figure shows that oxidized glycine is missing H-atom at the C $_{\alpha}$ and the backbone atoms lie in a plane. The carbon atoms are shown as cyan, hydrogen as white, oxygen as red, and nitrogen as blue spheres.

Table S1: Average bilayer P-P thickness

System	Average thickness (nm)
A β 42-wt	4.522 \pm 0.001
A β 42-GLR25	4.515 \pm 0.001
A β 42-GLR29	4.497 \pm 0.001
A β 42-GLR33	4.520 \pm 0.001

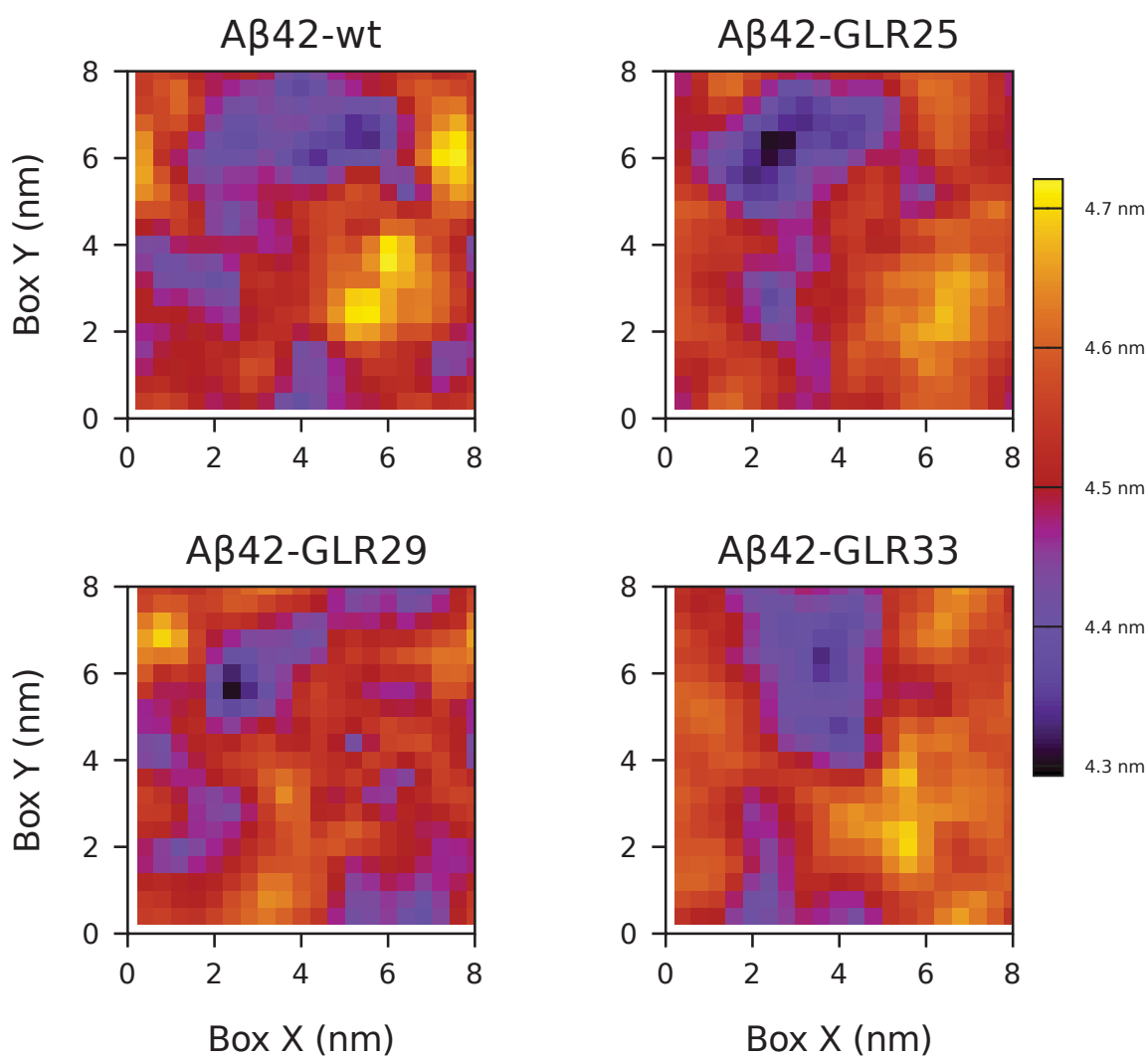


Figure S2: Average bilayer thickness calculated when the protein is closely interacting with the lipid bilayer (i.e., A β 42 within 0.5 nm of the membrane). The x and y axes represent the unit cell dimensions in nm. The thickness was calculated with a 0.4 nm resolution in each dimension. The color box to the right shows the thickness range in nm.

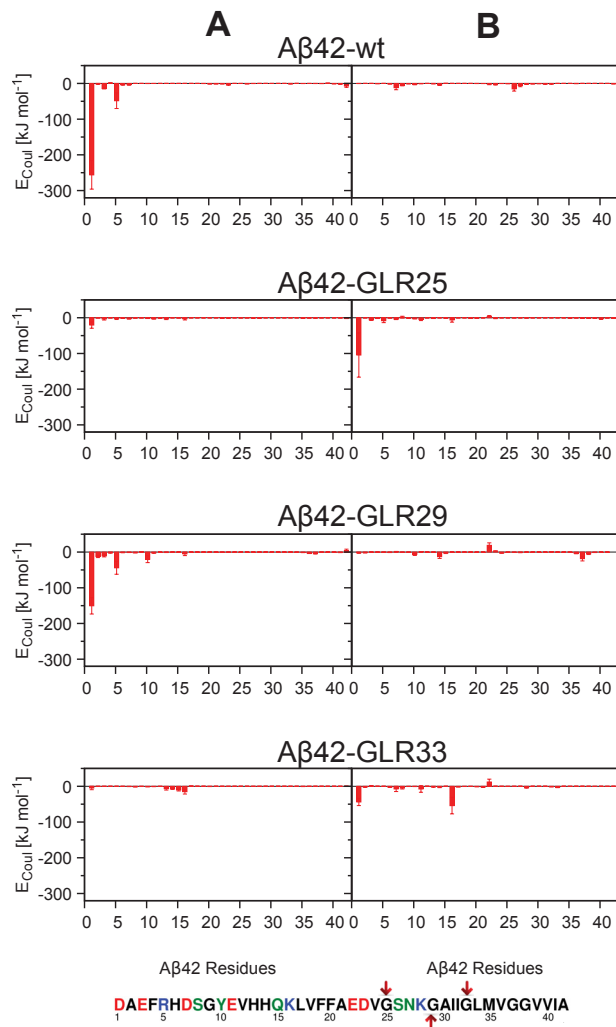


Figure S3: Coulombic interaction energy of each Aβ42 residue (and standard deviation of the mean) between Aβ42 and POPC (A) and GM1 (B) headgroups.

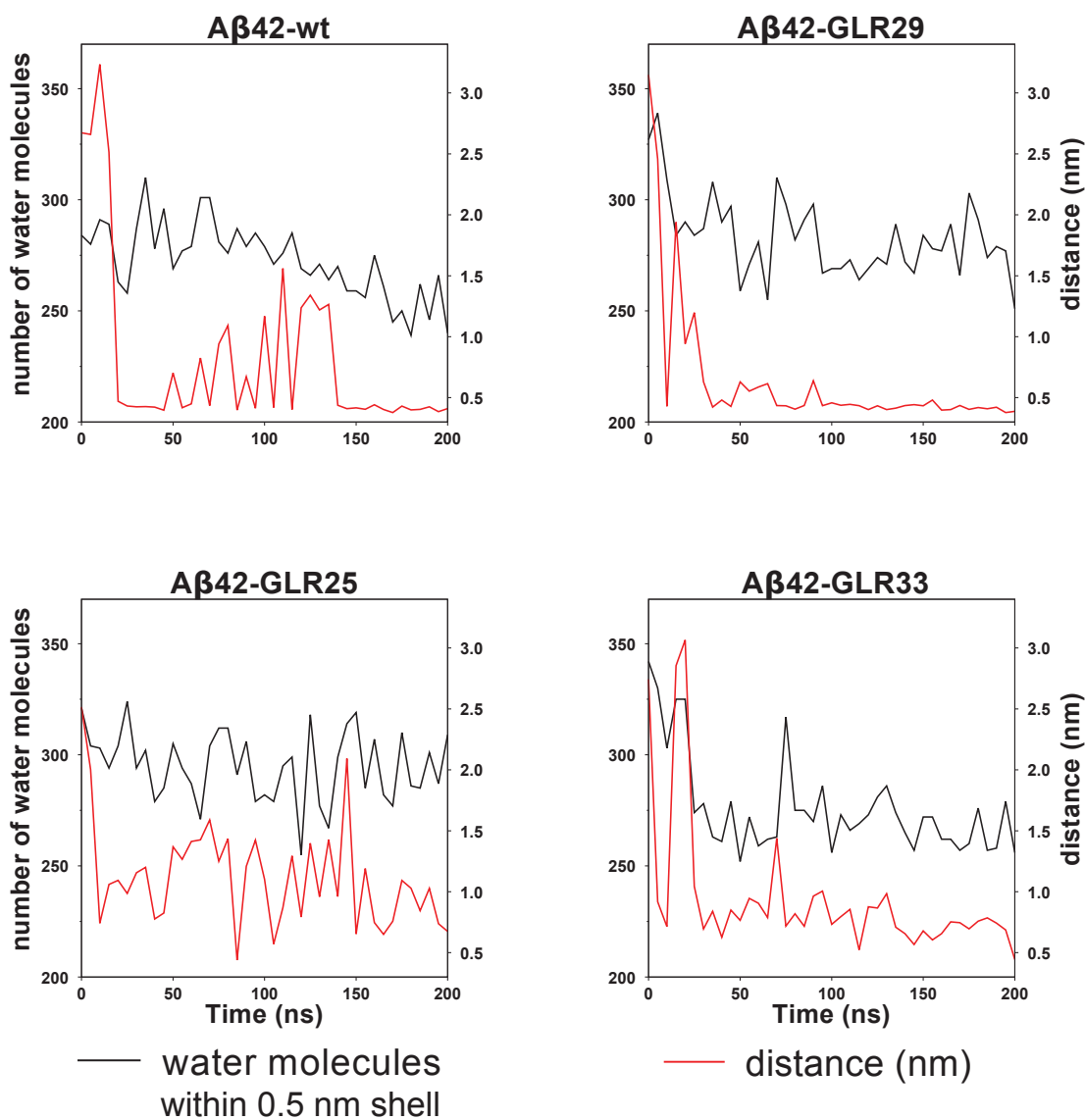


Figure S4: Number of water molecules within a 0.5 nm shell from the peptide C atoms (black, left y -axis) and the minimum distance between the peptide C_{α} atoms and the phosphorous atoms of the lipid bilayer (red, right y -axis) calculated as a function of time for all systems.

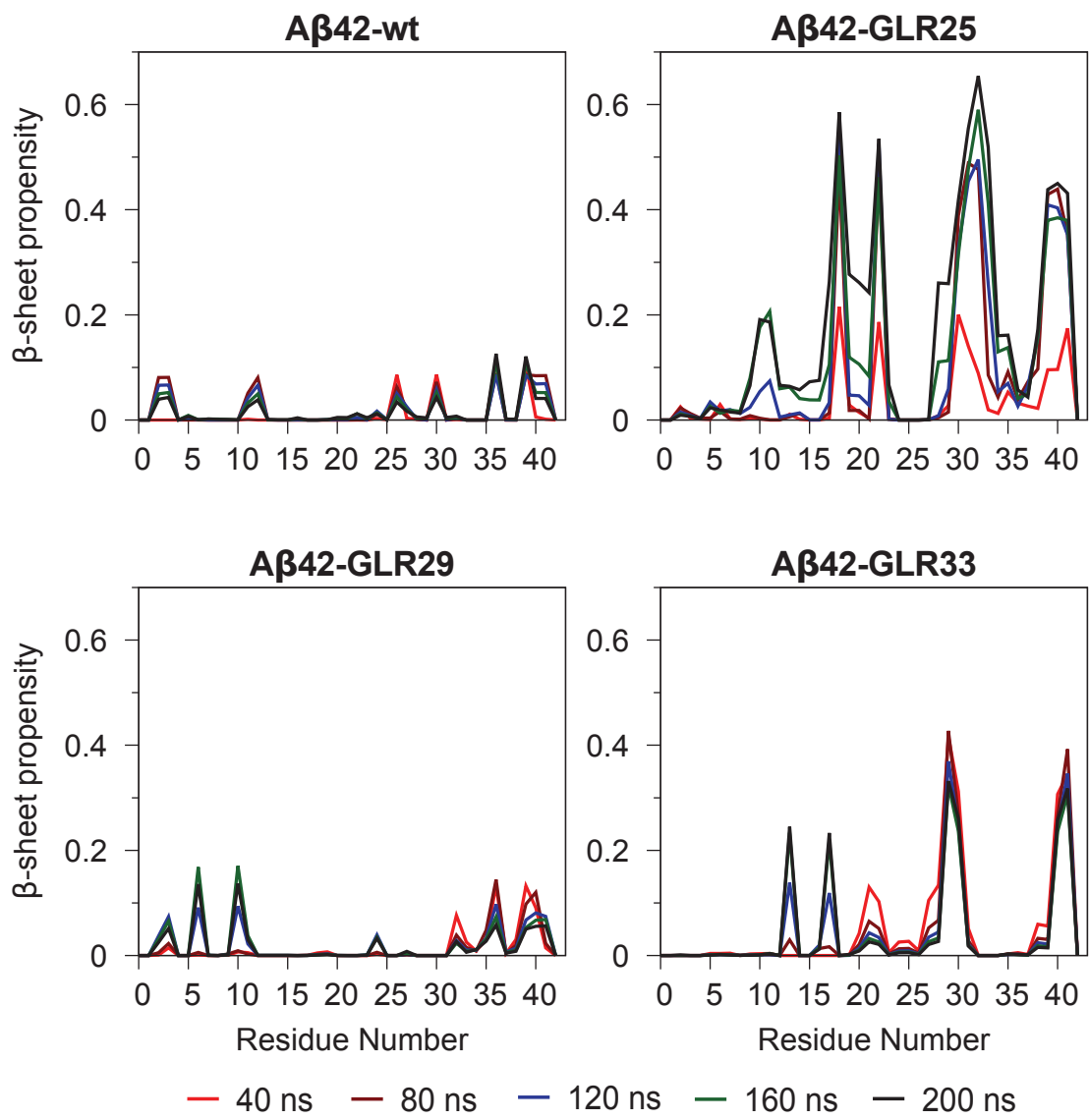


Figure S5: β -sheet propensity of each residue calculated for the 200 ns simulations using moving time windows (40 ns, 80 ns, 120 ns, 160 ns, and 200 ns, with an increment of 40 ns between successive windows).

Table S2: Intrapeptide hydrogen bonds in the four membrane systems, A β 42-wt, A β 42-GLR25, A β 42-GLR29, A β 42-GLR33.

Hydrogen Bonds Within A β 42									
system	backbone to backbone			backbone to side chain			side chain to side chain		
	Donor	Acceptor	%	Donor	Acceptor	%	Donor	Acceptor	%
A β -wt	His14(N)	Glu11(O)	51.3	Phe4(N)	Glu3(OE2)	47.9	Arg5(NE)	Glu3(OE2)	75.8
	Gln15(N)	Glu11(O)	80.4	Arg5(N)	Glu3(OE2)	72.8	Arg5(NH2)	Glu3(OE1)	75.1
	Lys16(N)	Val12(O)	43.0	Ser8(N)	Glu22(OE1)	49.6			
	Leu17(N)	His14(O)	71.8						
	Val18(N)	His14(O)	41.3						
	Ala21(N)	Val18(O)	87.0						
	Leu34(N)	Ile31(O)	66.5						
	Met35(N)	Ile31(O)	44.0						
	Gly33(N)	Met35(O)	42.9						
	Gly33(N)	Ile41(O)	44.2						
	Val36(N)	Val39(O)	84.7						
	Ile41(N)	Leu34(O)	92.8						
	A β -GL25	Leu17(N)	Gly33(O)	41.8					
Gly33(N)		Leu17(O)	44.9						
Phe19(N)		Ile31(O)	44.8						
Ile31(N)		Phe19(O)	44.2						
Asn27(N)		Val24(O)	68.6						
Ile32(N)		Val40(O)	41.3						
Val40(N)		Ile32(O)	41.5						
Leu34(N)		Gly38(O)	40.1						
A β -GL29	Asp7(N)	Gly9(O)	48.8	Phe4(N)	Glu3(OE1)	59.2	Arg5(NE)	Glu3(OE1)	61.5
	Lys16(N)	His13(O)	70.8	Arg5(N)	Glu3(OE1)	63.9	Arg5(NH2)	Glu3(OE2)	66.3
	Leu17(N)	His13(O)	49.2	Gly25(N)	Asp23(OD1)	42.6			
	Val18(N)	His14(O)	59.1						
	Phe19(N)	Lys16(O)	43.2						
	Phe20(N)	Leu17(O)	80.9						
	Ala21(N)	Leu17(O)	58.3						
	GLR29(N)	Glu22(O)	44.8						
	Val24(N)	Asn27(O)	44.7						
	Ala30(N)	Lys28(O)	44.0						
	Ile32(N)	GLR29(O)	44.0						
	Val40(N)	Ile31(O)	53.5						
	A β -GL33	Val12(N)	Gly9(O)	58.4	Phe4(N)	Glu3(OE2)	67.4	Arg5(NE)	Glu3(OE2)
His13(N)		Gly9(O)	40.7	Ser8(OG)	Phe4(O)	44.2	Arg5(NH2)	Glu3(OE1)	71.1
Ala21(N)		Val18(O)	46.2	Arg5(N)	Glu3(OE2)	71.0	Ser26(OG)	Asp23(OD2)	78.8
Ala30(N)		Val40(O)	60.6	Gly25(N)	Asp23(OD2)	75.8			
Leu34(N)		Ile32(O)	62.6	Ser26(N)	Asp23(OD1)	65.0			
Val39(N)		Ala30(O)	46.6	Ser26(N)	Asp23(OD2)	52.2			
				Asn27(N)	Asp23(OD1)	70.6			
				lys28(N)	Asp23(OD1)	71.1			
				Gly29(N)	Asp23(OD1)	64.9			
				Met35(N)	His16(ND1)	62.1			

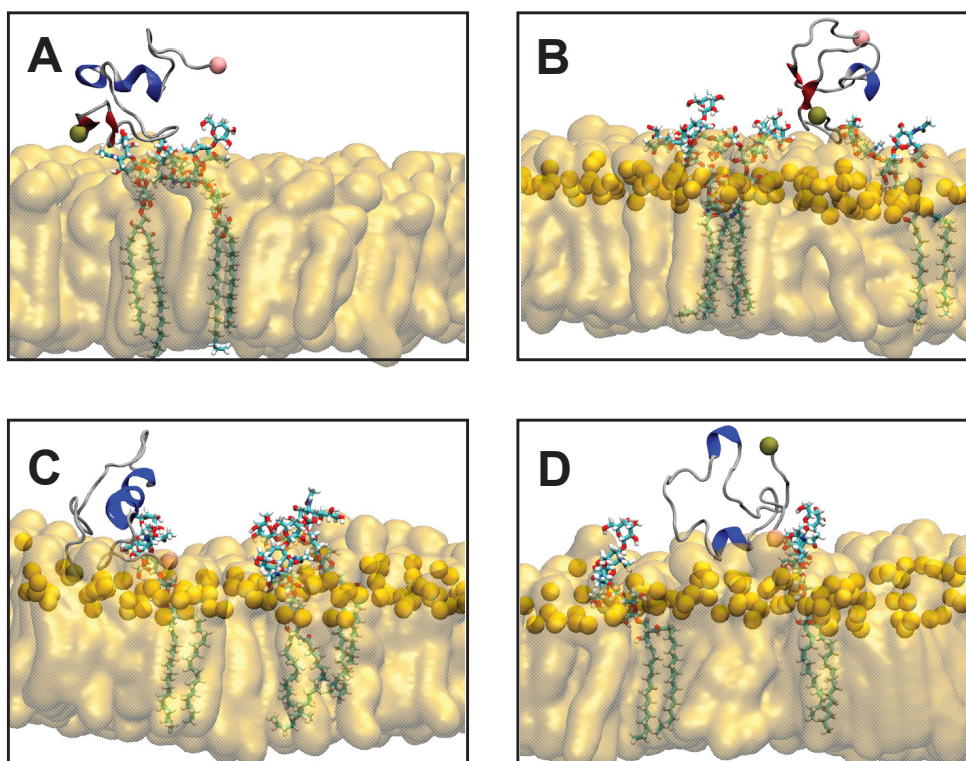


Figure S6: Central structure of the second largest cluster: (A) $A\beta_{42}$ -wt (23.7%), (B) $A\beta_{42}$ -GLR25 (18.4%), (C) $A\beta_{42}$ -GLR29 (19.3%), and (D) $A\beta_{42}$ -GLR33 (16%). In each rendered image the lipids are colored by orange. The phosphate atom of POPC is in orange, the N- and C- terminals of $A\beta_{42}$ are shown in pink and tan spheres, respectively. The protein β sheet is shown in red, the helix is shown in blue, and coil and turn are shown in silver.

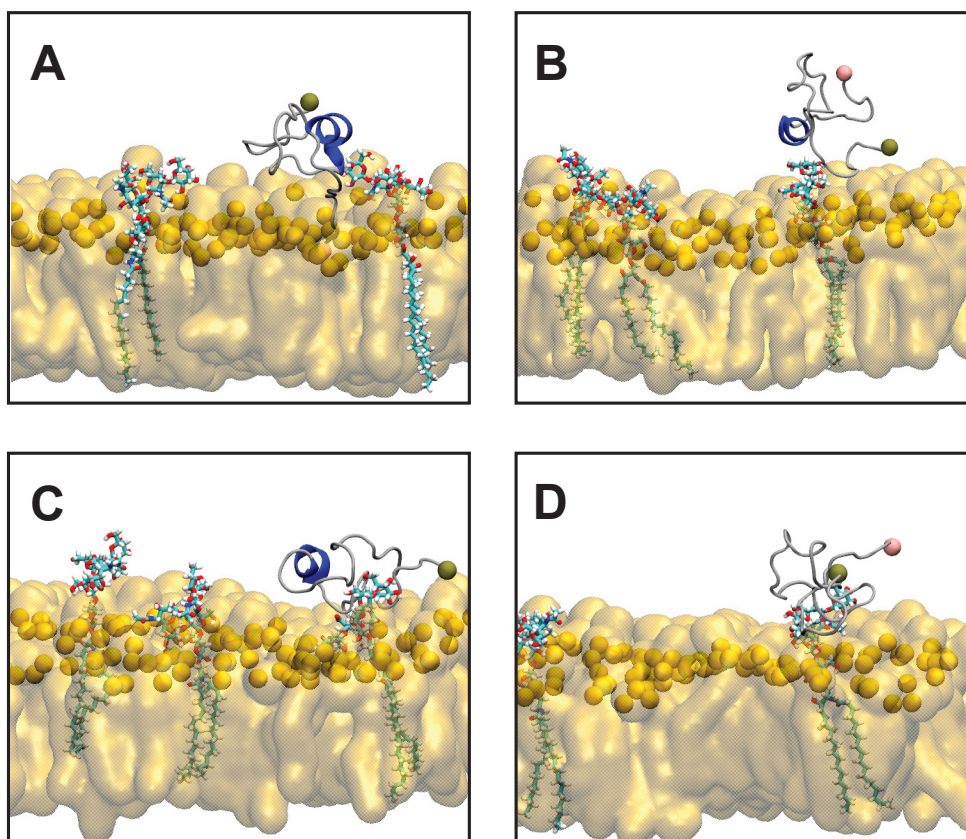


Figure S7: Central structure of the third largest cluster: (A) A β 42-wt (9.5%), (B) A β 42-GLR25 (9.4%), (C) A β 42-GLR29 (3.8%), and A β 42-GLR33 (5.2%). In each rendered image the lipids are colored by orange. The phosphate atom of POPC is in orange, the N- and C-terminals of A β 42 are shown in pink and tan spheres, respectively. The protein β sheet is shown in red, the helix is shown in blue, coil and turn are shown in silver.

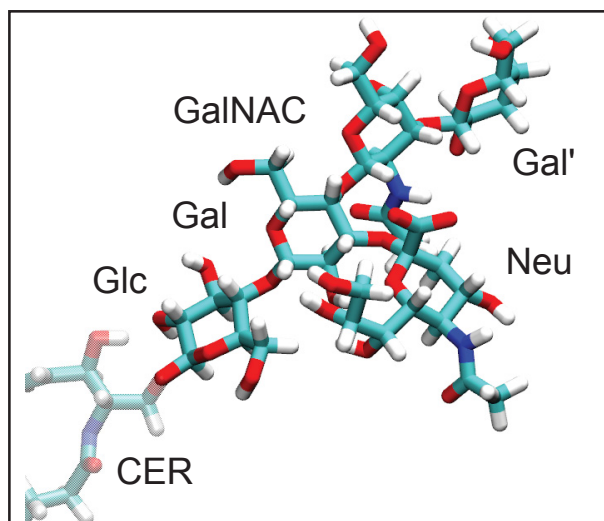


Figure S8: Sugar residues of GM1; β -D-glucose (Glc), β -D-galactose (Gal), N-acetyl- β -D-galactosamine (GalNAC), β -D-galactose (Gal') N-acetyl- α -neuraminidate (Neu). CER represents the lipid ceramide moiety connected to Glc. The oxygen atom is shown in red, the nitrogen atom is shown in blue and the carbon atom is shown in cyan.

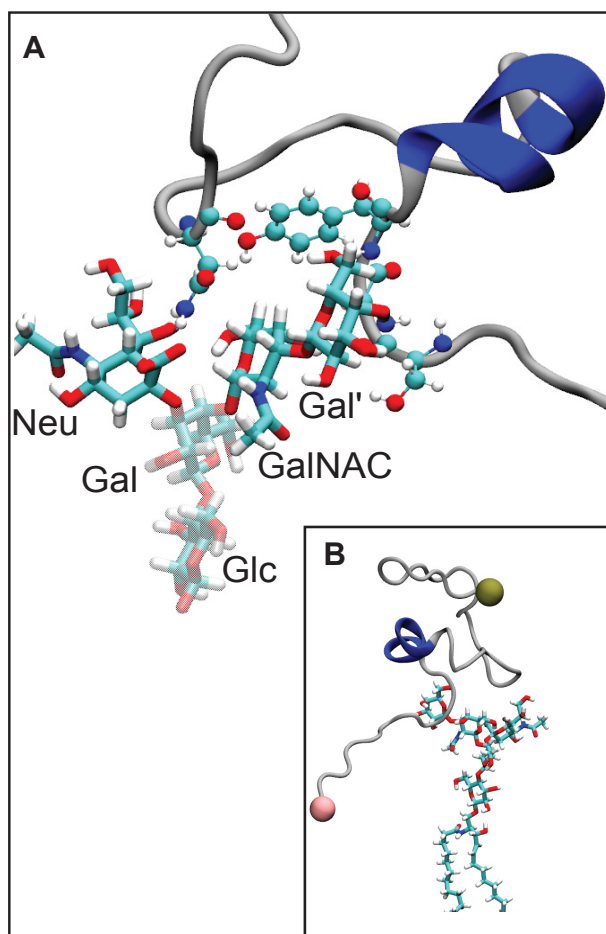


Figure S9: (A) Schematic representation of protein interaction with GM1 residue. (B) Zoom in to the region where protein interacting with sugar moiety of GM1 lipid.

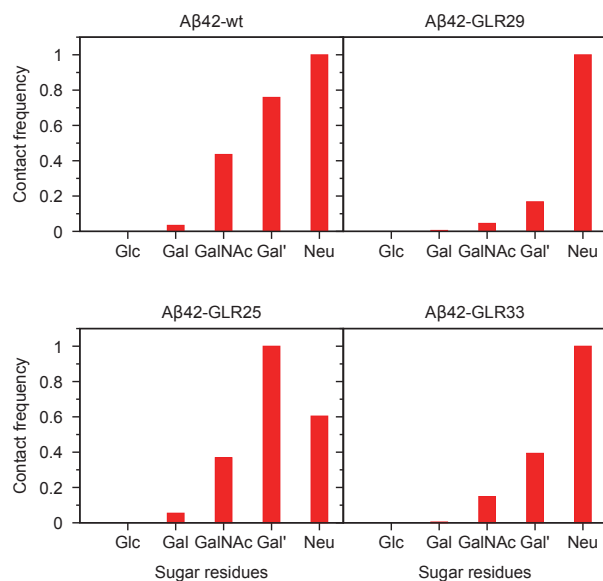


Figure S10: Contact frequency of each GM1 sugar residue with Aβ42 peptide. The sugar residues shown on the x-axis are β -D-glucose (Glc), β -D-galactose (Gal), N-acetyl- β -D-galactosamine (GalNAc), β -D-galactose (Gal') N-acetyl- α -neuraminidate (Neu). The figure shows normalized contact frequency in the range 0 to 1, such that 1 means the residue always made contact with the lipid and zero means no contact were made.

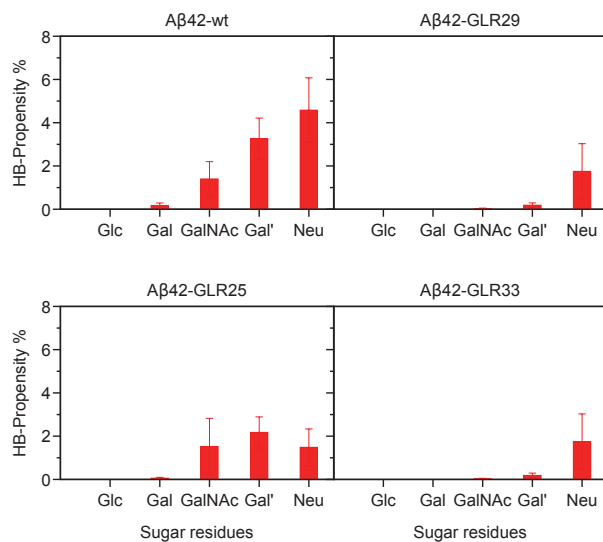


Figure S11: Hydrogen bond propensity (and standard deviation of the mean) of each sugar residue with Aβ42 peptide.

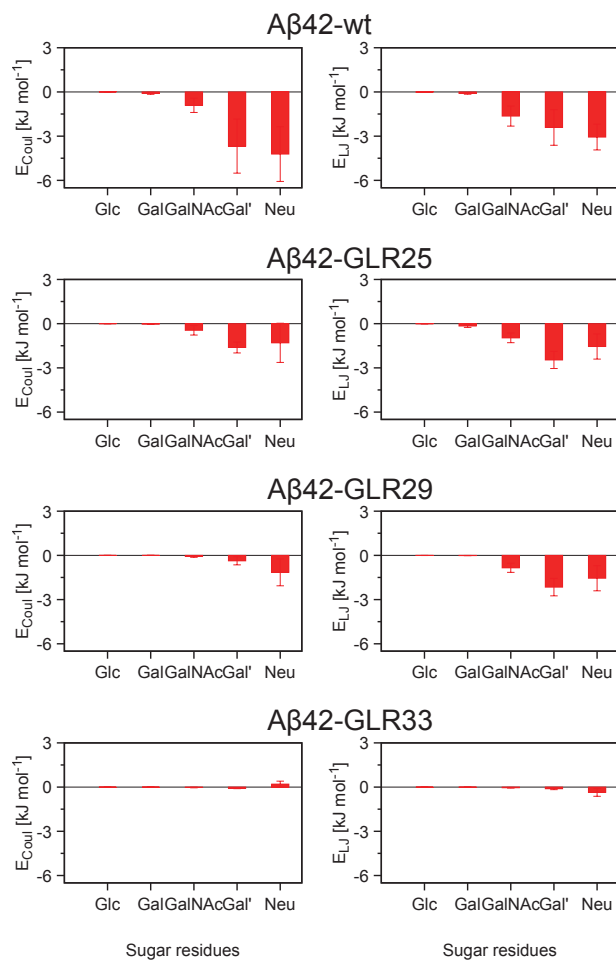


Figure S12: Coulombic (left) and Lennard-Jones (right) interaction energy of each sugar residue (and standard deviation of the mean) with Aβ42 peptide.

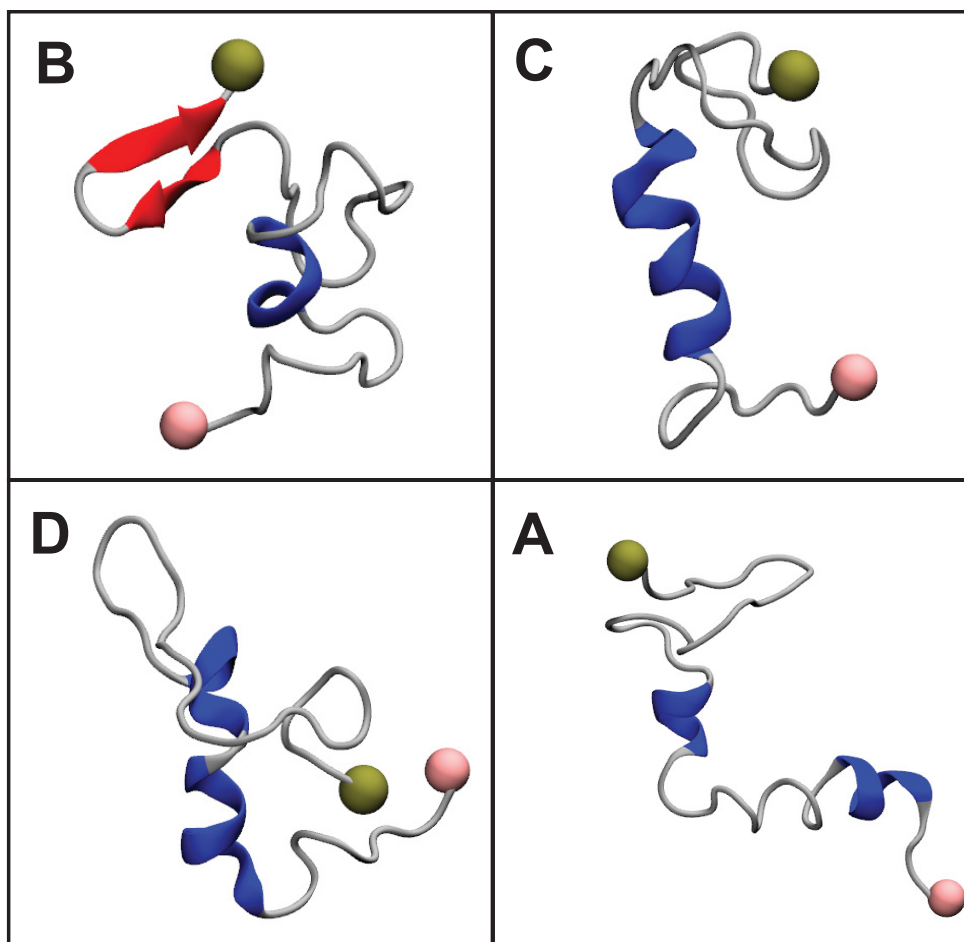


Figure S13: Starting structure of $A\beta_{42}$ peptide obtained from the final snapshots of a $1 \mu\text{s}$ simulation. (A) $A\beta_{42}$ -wt, (B) $A\beta_{42}$ -GLR25, (C) $A\beta_{42}$ -GLR29, and (D) $A\beta_{42}$ -GLR33. The N- and C- terminals of $A\beta_{42}$ are shown in pink and tan spheres, respectively. The protein β sheet is shown in red, the helix is shown in blue, and coil and turn are shown in silver.

A.4 Manuscript IV

**Atomistic simulations of macromolecular crowding effect on $A\beta_{16-22}$
aggregation**

Fatafta H., Strodel B., Sayyed-Ahmad A. Manuscript in preparation.

Atomistic simulations of macromolecular crowding effect on $A\beta_{16-22}$ aggregation

Hebah Fatafta¹ and Birgit Strodel^{1, 2} Abdallah Sayyed-Ahmad^{3, *}

¹Institute of Biological Information Processing (IBI-7: Structural Biochemistry), Forschungszentrum Jülich, 52425 Jülich, Germany

²Institute of Theoretical and Computational Chemistry, Heinrich Heine University Düsseldorf, 40225, Düsseldorf, Germany

³Department of Physics, Birzeit University, Birzeit, Palestine

*Corresponding author: asayyeda@birzeit.edu

March 18, 2022

1 Abstract

Amyloid- β peptide aggregation occurs in cellular environments that are densely crowded by other macromolecules. However, the extent of how such crowded environments affect the peptide aggregation is not fully explored. Here, atomistic molecular dynamic simulations applied to a peptide/crowder system are used to investigate how macromolecular crowding affects the aggregation kinetics of $A\beta_{16-22}$ using simple hard sphere crowders at a crowder volume fraction of 0.3. Our simulations show that the macromolecular crowding enhances the aggregation kinetics of $A\beta_{16-22}$ both on the dimer and hexamer formation. Moreover, the presence of the crowders enhances the formation of an energetically favorable state by the excluded volume effect.

2 Introduction

It is becoming increasingly evident that the aggregation of amyloid- β ($A\beta$) peptide is strongly linked to the progression and development of Alzheimer's disease, especially the $A\beta_{40}$ and $A\beta_{42}$ alloforms [1, 2]. It has been longstanding that the amyloid oligomers rather than the matured fibrils are responsible for the disease progression and severity [3, 4, 5]. Importantly, progress in a better understanding of disease development inspires further research toward understanding the details of its aggregation mechanism. However, most studies applied to probe the assembly process of $A\beta$ peptide have been performed in a diluted aqueous solution, which doesn't correspond to the actual complexity of the real cellular environment. In fact, the intracellular and extracellular environments in the human brain are quite crowded with a variety of macromolecules that occupy (7-40)% of the total volume [6]. Thus, *in vitro* investigations of $A\beta$ don't capture the influence of biomolecules, that would occur *in vivo*, on its assembly [7, 8]. This was further supported by the findings that the extent to which $A\beta$ forms oligomer/fibril in a crowded environment differs by orders of magnitude from that *in vitro* [9].

The effect of macromolecular crowding on protein aggregation has been the subject of a number of experimental studies. In the laboratory, macromolecular crowding have been replicated using concentrated solutions of various synthetic (polyethylene glycol (PEG), sugar-based polymers such as Ficoll and dextran) and biological (such as lysozyme, bovine serum albumin, sucrose) polymers as model crowding agents to investigate their effect on different protein aggregation/fibrillation mechanisms such as apolipoprotein C-II (apo-CII), human insulin, α -synuclein, $A\beta_{40}$ and $A\beta_{42}$. Overall, these studies revealed that the volume excluded effect is the most relevant that

plays a key role in affecting protein behavior. In agreement with the theoretical models that have been pioneered by Minton and accounting for the excluded volume effects [10, 11]. Accordingly, the crowders behave as inert molecules that do not interact with proteins and rather limit the accessible space, thus reducing the conformational entropy and favoring the formation of folded proteins [12, 13, 14, 15, 16]. However, recent experiments showed that inert crowders can also interact with proteins, affecting their stability, yielding varied results depending on the crowder type and size [17, 18, 19]. For example, It has been reported that the synthetic PEG crowders are less inert than dextran and glucose crowders, as a destabilization of ubiquitin protein was observed in its presence compared to enthalpy stabilization by the other two [20]. To this end, crowders have been recognized with a dual nature when it comes to their effect on protein aggregation. On the one hand, it can enhance the protein aggregation via the excluding volume effect but on the other hand, it can also form soft interactions with the solute protein making it difficult to predict the final result of the crowding. In spite of that, research on IDPs in a cell-like crowded environment is rare. Experimental investigations in this regard give an oversimplified view of macromolecular crowding effects on IDPs, as the effect is impeded by the dynamic and transient nature of IDPs that is difficult to capture experimentally. Theoretical calculations, particularly molecular dynamics (MD) simulations can complement the experiment [21, 22], especially with the power of MD simulations in giving direct access to molecular-level details in a carefully controlled environment. Applications of this approach to study the effect of macromolecular crowding on protein aggregation have been performed by O’Brein et al. using atomistic MD simulations [23], Mango et al. using coarse-grained (CG) simulations [24], and Co et al. [25] using Monte Carlo simulations applied to study the oligomerization of a 10-residue fragment of transthyretin (TTR), 10-bead coarse-grained polypeptide and a toy model, respectively. The overall emerged picture from these studies revealed that proteins in a crowded environment have high energy penalties associated with forming aggregates that are not highly compact so the number of kinetic pathways will be smaller compared to proteins in a diluted solution. The same idea applies to amyloidogenic proteins, as they are expected to be sensitive to the presence of crowding agents that promote their folding and compaction. This was reported by discontinuous molecular dynamic (DMD) simulations applied to 192 A β _{16–22} at the CG-level [26]. It has also been pointed out using Langevin dynamics simulations of a 10 beads amyloid peptide that the net effect of crowding on peptide assembly is the result of competition between oligomer stabilization and solution viscosity [24].

In this study, we focus on the small A β oligomers as they have been

identified as toxic agents in AD, particularly the dimer and the hexamer of $A\beta_{16-22}$ fragment, which has been shown to be a key sequence in the formation of $A\beta$ oligomers and fibrils, and has the ability to form fibrils on its own [27, 28, 29]. To this end, we perform all-atom MD simulations to investigate the crowding effect on the hexamer formation of $A\beta_{16-22}$ in a crowded and diluted aqueous solution. Additionally, we perform metadynamics simulations to study the crowding effect on the free energy profile and the kinetics of $A\beta_{16-22}$ dimerization in a crowded and diluted aqueous solution. All was done using a spherical model of repulsive spherical crowders of diameter 1.3 nm at 30% volume concentration together with the short fragment $A\beta_{16-22}$. We believe that the unique contribution of this simulation study is that it provide atomistic insight into the molecular crowding effect on $A\beta$, which to the best to our knowledge has not been done yet. Previous simulation studies used coarse-grained model (CG) and performed discontinuous molecular dynamics (DMD) [26] or Langevin dynamics simulations [24]. Our simulations revealed that the presence of crowders tends to enhance hexamer formation by forcing the peptides to collapse into oligomeric conformations quickly, which then evolve to hexameric conformation toward the end of the simulation. Moreover, our metadynamics simulations of the two $A\beta_{16-22}$ peptides shed light on the role played by crowders in enhancing the aggregate formation, as it reflects that the presence of crowders enhances the formation of the energetically favorable dimer.

3 Results

3.1 Crowding effect on the hexamer formation

We investigate the effect of the crowder on the hexamer formation of $A\beta_{16-22}$ using unbiased all-atom classical molecular dynamics simulations. To this end, we have simulated two systems: six $A\beta_{16-22}$ peptides in crowded solution with crowder volume fraction of 30%, and six $A\beta_{16-22}$ peptides in diluted solution without crowders. For each system, we have run three independent molecular dynamics simulations, each of which is 1.5 μ s long. The system with $A\beta_{16-22}$ in diluted solution serves as a reference, to unravel the effect of the crowder presence on the aggregation process.

3.1.1 Effect of crowders on oligomerization kinetics

Our simulations of the six $A\beta_{16-22}$ peptides in the crowded solution revealed that the presence of crowders enhances the formation of the hexamer compared to simulations without crowders, as revealed by the time evolution of

the oligomerization state in Fig. 1. The figure also shows that the peptides with crowders evolve to hexamer after 500 ns of the simulation time, in all three simulations (see Fig. 1b), such that the resulting hexamer is stable with no further dissociation to a small size oligomers. On the other hand, the peptides without crowders do not evolve smoothly into hexamer, some dissociation events can still be seen toward the end of the simulation as shown from the three different runs. In run 1 and 3 the six peptides assemble into a hexamer at 1.0 μ s and 750 ns respectively, upon which they remain in the hexameric form but this is not seen from run 2, where peptides experience more association and dissociation events (see Fig. 1a). This observation highlights that the assembly process take longer to occur in the diluted solution but once a hexamer forms then it is more preferable state, in which peptides likely to remain without further dissociation.

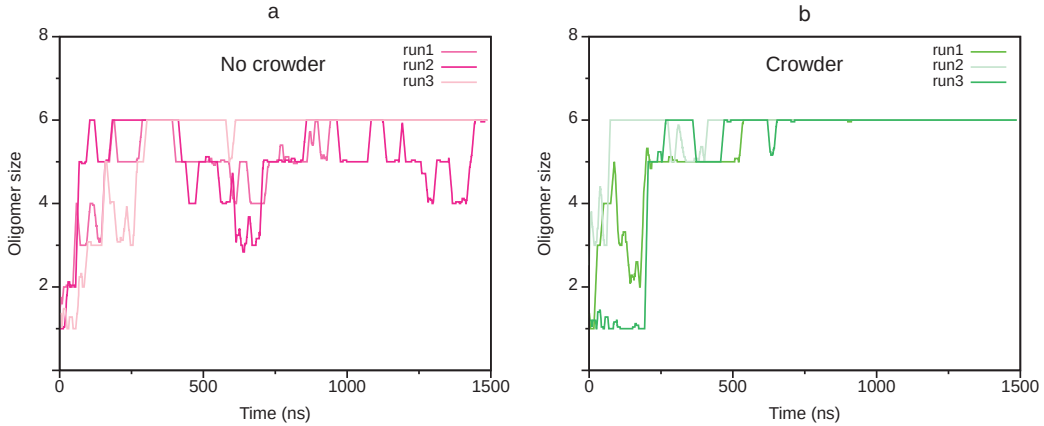


Figure 1: The time evolution of the oligomerization state from each of the triplicate simulations of six $A\beta_{16-22}$ without crowders (a), and with crowders (b). The color of each run as indicated by the color code.

It is evident that the presence of crowders not only dramatically decreases the time scale of aggregation (see Fig. 1) but also affect the aggregation mechanisms. In the simulations without crowders, a hexamer forms through nucleation mechanism. In contrast, the simulations with crowders results in a rapid formation of hexamer that was preceded by the formation of small sized oligomers. Even these oligomers seem to be formed through fast collapse of peptides being rapidly forced together such that they quickly arrange into tetramer or pentamer but not dimer.

Fig. 2 shows snapshots summarizing the aggregates that we observe as final configuration in our simulations of $A\beta_{16-22}$ without crowders (top row) and in the presence of crowders (bottom row). The snapshots with crowders

revealed hexamer with nice β -sheets in Fig. 2c, whereas β -sheet with a small number of peptides per sheet or peptides with a random coil is seen in snapshots Fig. 2a and b. In contrast, with no crowders the snapshots revealed hexamer with β -sheets that contain a small number of peptides per sheet or peptide with random coil is seen in all snapshots Fig. 2(d-f).

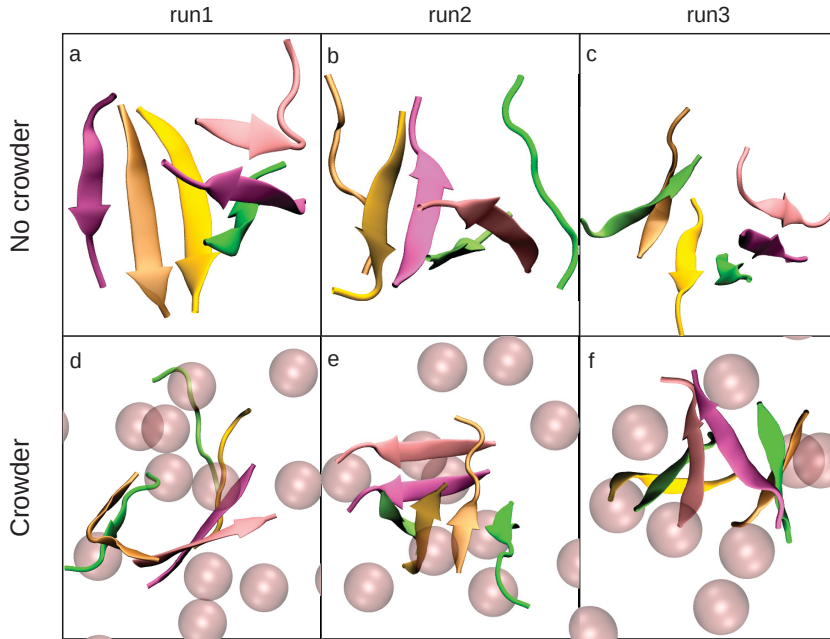


Figure 2: Representative snapshots of the last frame from the simulation of six $A\beta_{16-22}$ with no crowders (top row a-c), and the system with crowders (bottom row d-f). $A\beta$ peptides are shown as cartoon and colored as indicated in the figure, with the crowders indicated by light pink spheres.

3.1.2 Effect of crowders on β -sheet formation

Next, we analyze the effect of crowders on the formation of β -sheets, which results from the association of monomers. To this end, we calculate the time-averaged secondary structure for the peptides with crowders (Fig. 3) and compare the results to the findings for peptides without crowders. The time-averaged data revealed that the presence of crowders enhances the β -sheet formation at the expense of random coil and turn conformation compared to simulations without crowders. The helical content is negligible in both cases.

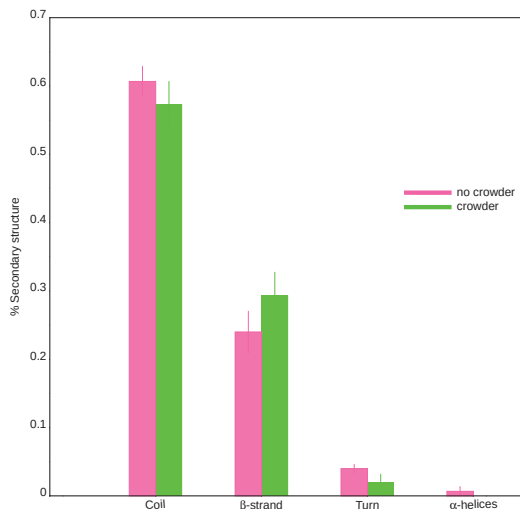


Figure 3: The average secondary structure content in the case of simulation without crowders (pink) and simulation with crowders (green). From left to right, the coil, the β -sheet, the bend-turn and the α -helical contents are shown.

3.1.3 Crowders- $A\beta_{16-22}$ interaction

To figure out how the peptide and the crowder interact during the simulation, the number of contacts is evaluated and shown as average results from each monomer (Fig. 4a). The figure shows that almost all peptides bind the crowder to the same level. However, looking at the contact with peptide residues (Fig. 4b) one see that highest contact is made with residues Leu3 - Phe 6, with slight differences among different monomers.

3.2 Crowding effect on the dimer formation

In order to interpret the change in the free energy associated with the transition from a monomer to an oligomer in the presence of the spherical crowders, we simulated two $A\beta_{16-22}$ peptides in solution with and without the presence of crowders. Similar to hexamer simulations, the system without crowders serves as our reference. For each system, we run metadynamics MD simulation each of $3 \mu\text{s}$. The metadynamics bias was applied to two configurational collective variables (CVs): the distance between the center of mass of the peptides r_{com} and the number of peptide-peptide contacts N_{contacts} .

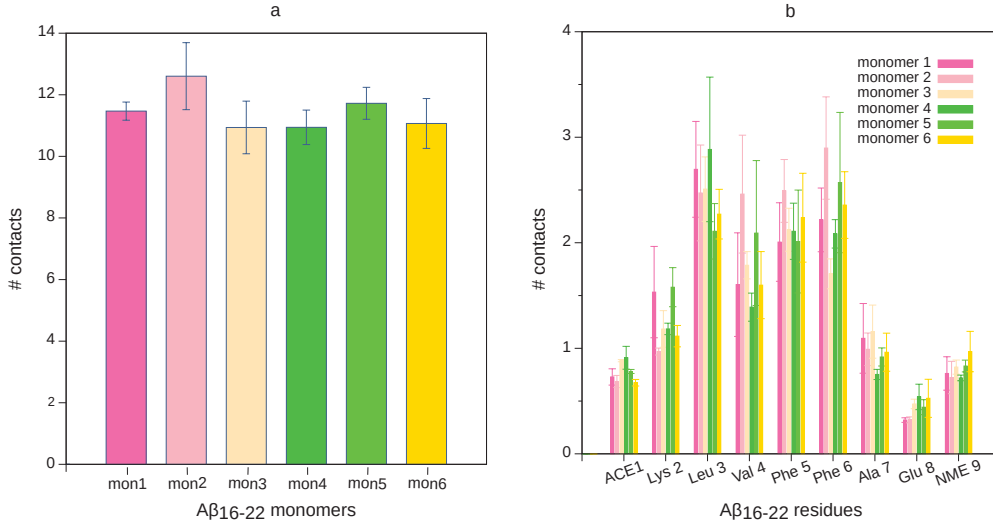


Figure 4: The average number of contacts between A β_{16-22} monomers and the crowder (a), and between A β_{16-22} residues and the crowder (b). The legend show monomers color.

3.2.1 Effect of crowders on the free energy landscape

The ability to compute the free energy (FES) as a function of multiple CVs is the most important practical advantage of metadynamics with respect to other enhanced simulation methods. Therefore, we took the advantage and analyze the 2-dimensional 2D-FES (Fig. 5a and b) and the 1-dimensional 1D-FES (Fig. 5c and d) as a function of the respective CVs, r_{com} and N_{contacts} . A major finding is that the presence of crowders encourages dimer formation, which can be deduced from the deep energy minimum as a function of the CVs.

The 2D-FES of the dimerization process as a function of r_{com} and N_{contacts} is reported in Fig. 5a and b. The free energy landscape revealed a deep basin at $r_{\text{com}} < 0.5$ nm for both dimerization process, with and without crowders, however the basin extension along the N_{contacts} is different. It is clear that the position of the basin indicates that peptide-peptide interaction is favored but its extension along the N_{contacts} suggests that several conformations are likely to be thermodynamically accessible by the dimer in the presence of crowders compared to it without crowders, i.e. the presence of crowders drive dimerization with a broad basin of structural ensemble compared to dimer formation without crowders (see Fig. 6). The figure shows the structural ensemble selected from a time window in the phase space at which $r_{\text{com}} = 0.5$

nm, which is of lowest FES. The figure reflects different snapshots from the beginning of the selected time window (t_0), passing the first observation of the β -sheet (t_{start}), to the middle of the time window (t_{mid}), reaching the end of the time window (t_{end}). It is clear, that the structural ensemble for the dimer in the presence of crowders (Fig. 6 (a-d)) is more diverse (with parallel and anti-parallel β -sheets) than it for dimer without crowders (Fig. 6 (e-h)). Moreover, the dimer with crowders reveals β -sheet that contains more residues compared to the no crowder case.

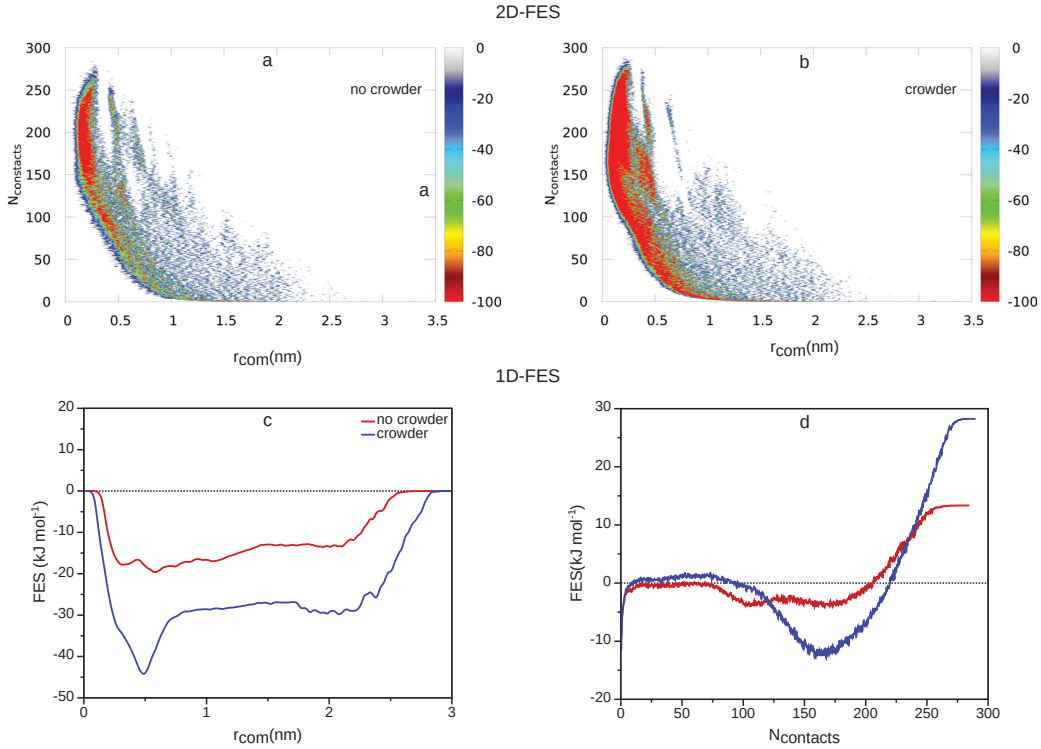


Figure 5: The 2D dimensional free energy surface (FES) (top row) calculated from metadynamics simulation of $A\beta_{16-22}$ simulated without (a) and with crowder (b). The one dimensional FES (bottom row) is shown as a function of collective variables; the center of mass distance between peptide units ($r_{\text{com}}(\text{nm})$) (c), and the number of contacts between the peptide (N_{contacts}) (d).

Furthermore, our analysis of the 1D-FES indicated that FES (r_{com}) for the dimer with crowders explores the deepest energy minimum at $r_{\text{com}} \approx 0.5$ nm with FES of -43 kJ/mol compared to a less well-defined minimum with FES ≈ -28 kJ/mol for the dimer without crowders (Fig. 7c). Similarly, a deep energy minimum at $N_{\text{contacts}} \approx 170$ is seen for the dimer with crowders

compared to a less well-defined minimum without crowders (Fig. 7d). Apart from the deepest energy minimum of FES (r_{com}), both the dimer with and without crowders explore another energy minima at $r_{\text{com}} \approx 2.2$ nm (see Fig. 7c).

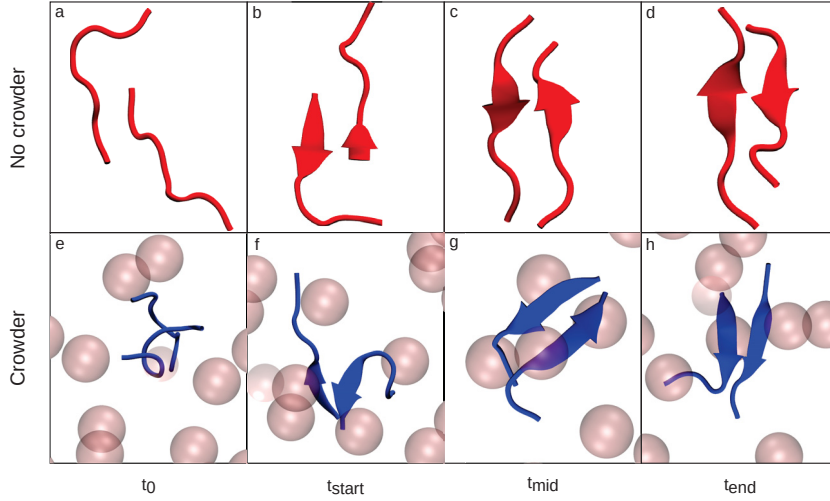


Figure 6: Snapshots of the dimer formed in solution without crowders (top) and with crowders (bottom), the dimers are shown in cartoon representation and colored in red and blue, respectively. The snapshots are taken from the energy basin with the lowest FES(r_{com}) at $r=0.5$ nm. The snapshot with t_0 represents the peptide conformation at the starting of the time window, t_{start} represents the first observation of β -sheet, t_{mid} represents a snapshot from the middle of the time window and lastly t_{end} represents a snapshot at the end of the time window.

3.2.2 Assessing metadynamics

The time evolution of the metadynamics CVs revealed that r_{com} and N_{contacts} looks diffusive in the entire CVs space as shown in Fig. 7c and d. The evolution of r_{com} , which correspond to the center of mass distance of peptides with crowders, revealed that the simulation starts in the minimum on the left ($r_{\text{com}} = 2$ nm) (Fig. 7d). The first minimum is filled until ≈ 500 ns, and then the system moves to the second minimum ($r_{\text{com}} = 0.5$ nm). After the second minimum is also filled at around $1 \mu\text{s}$, the system oscillates with equivalent probabilities between the two minima, until the simulation is completed. In the same way, the figure further shows the diffusivity of the other CVs for dimer with and without crowders. This reflects that the metadynamics

simulations allow exploring new reaction pathways as the system tends to escape the minima passing through the lowest free energy saddle point.

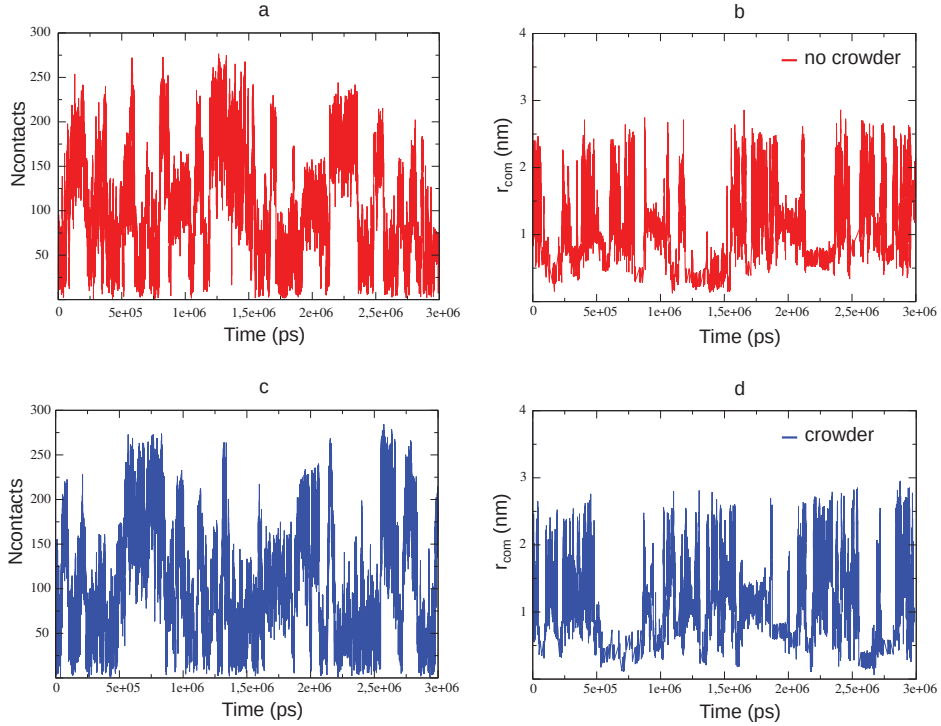


Figure 7: The time evolution of the collective variable. Results from dimer simulated without crowders are shown top whereas those with crowders are bottom. The left column shows the N_{contacts} , and the right one shows r_{com} (nm).

4 Discussion and Conclusions

Using the combination of unbiased all-atom MD simulations and metadynamics simulations, we have been able to shed light on the macromolecular crowding effect on small $A\beta_{16-22}$ oligomeric species, that have been identified as the toxic agents in Alzheimer’s disease, at the atomistic level. Although previous studies on similar systems but with larger number of $A\beta_{16-22}$ peptides have been performed, they were performed at the coarse-grained level using discontinuous molecular dynamics (DMD) or Langevin dynamics simulation. We are not aware of any simulation that match the realism of the species involved in this simulations at the atomistic level.

The oligomerization mechanism observed in our simulations of six $A\beta_{16-22}$ peptides in the presence of spherical crowders deviates from the step-wise growth mechanism, that is well reported for $A\beta$ peptides, in which monomers comes together one by one forming the nucleus (i.e. forming dimers, trimers, tetramers etc) that can further elongate to form amyloid fibrils. Additionally, our results revealed that the aggregation mechanisms with crowders differ from it without crowders, such that in the former a fast collapse of peptide into tetramer or pentamer is first encountered after which a stable hexamer is formed. We speculate that the presence of the crowders affects the interstitial space available for the peptides in away that force them to come together quickly in the form of oligomeric species that later assemble into hexameric.

We have also presented a free energy analysis of dimers in the presence and absence of crowders. Our simulations revealed that the presence of crowders drives the formation of the dimer that is more energetically favorable as compared to simulations without crowders. The structural conformation of such favorable dimer is characterized by high number of contacts and low com distance between the peptides revealing its compactness.

Summarizing thus far, the presence of crowders tends to enhance hexamer formation through forcing the peptides to collapse into oligomeric conformations quickly, which then evolve to hexameric conformation to the end of the simulation. Based on our findings from metadynamics, we suggest that the presence of crowders enhances the formation of energetically favorable state by the excluded volume effect. This could be the scenario beyond its enhancing effect on the aggregation kinetics. In this regard, our findings agree with Munishkina et al. experimental findings [30] that, in the presence of crowders, specific oligomer and fibril aggregation pathways are preferred because of the favorability of specific peptide structures and the fact that they maybe more energetically favorable than others. Moreover, our observations are in agreement with a large and diverse set of simulation studies. Of note, is the simulation study by O'Brien et al. who reported that the addition of crowders of any size or concentration will enhance aggregation and as the crowder size increase the level of enhancement diminishes [23]. Another study by Latshaw et al. [26] revealed that at the CG level, the crowder increases the rate of oligomer formation and that small sized crowder of 5 Å enhances hexamer formation of $A\beta_{16-22}$.

In this study, we have limited ourselves to spherical crowders but future studies with crowders represented as polymer chains or more real crowding molecules might increase the relevance of our simulations.

5 Methods

5.1 Crowder model

The crowders in our simulations are modeled as neutral spherical particles with a diameter of 1.3 nm, that interacts with peptides and with each other by mean of the Lennard-jones potential. The interaction between crowders is modeled being repulsive so that they do not self-assemble during the simulation. For this, force field parameters for the crowder were developed and implemented into GROMACS.

5.2 Simulation setup and protocol

The systems modeled are composed of two $A\beta_{16-22}$ peptides, which were simulated in the aqueous phase and in the presence and absence of crowders. The initial $A\beta_{16-22}$ structures were taken from the most populated clusters from a preceding MD simulation of $A\beta_{16-22}$ in solution.

The simulated system also contained TIP3P water model with sodium and chloride ions at the physiological concentration of 150 mM. The two $A\beta_{16-22}$ peptides were placed randomly in water layer at a distance of >1 nm between the closest atoms from the two peptides. All distances from the peptides to any of the simulation box edges was at least 1.2 nm to avoid interactions between the peptides with their periodic images. The total number of atoms in the modeled dimer system was $\approx 33,400$ atoms and the box size was about $6.99 \times 6.99 \times 6.99$ nm³. The setup of the hexamer system in the aqueous phase was similar, but with six $A\beta_{16-22}$ monomers, resulting in a system size of about $9.8 \times 9.8 \times 9.8$ nm³ and contained $\approx 97,583$ atoms.

The metadynamics simulation were performed using GROMACS MD code [31] with plumed plugin [32]. The all-atom MD simulations were performed using GROMACS/2018.2[31] along with the CHARMM36m force field [33, 34]. Each system was first energy minimized using the steepest decent algorithm to remove atomic clashes. This was followed by equilibration under NVT conditions where a temperature of 310 K was regulated with the velocity-rescale thermostat [35]. Next, the system was equilibrated under NpT conditions to obtain a pressure of 1.0 bar, where the pressure was regulated using isotropic Parrinello-Rahman pressure coupling scheme [36]. Periodic boundary conditions were set in all directions. Both the van der Waals and Coulomb force cutoffs were set to 1.2 nm in real space. The particle mesh Ewald (PME) method was applied for calculating the electrostatic interactions. For $A\beta_{16-22}$ hexamer systems, an initial simulation was

run for 1.5 μ s, then another two simulations with different starting velocity were run each for 1.5 μ s. For the subsequent analysis, we combined the data from the three independent simulations and derived the results presented in this study. For metadynamics simulation of A β_{16-22} dimer, simulations were run for 3 μ s for dimers with and without crowders.

References

- [1] Querol-Vilaseca, M. *et al.* Nanoscale structure of amyloid- β plaques in alzheimer’s disease. *Scientific reports* **9**, 1–10 (2019).
- [2] Gouras, G. K., Almeida, C. G. & Takahashi, R. H. Intraneuronal a β accumulation and origin of plaques in alzheimer’s disease. *Neurobiology of aging* **26**, 1235–1244 (2005).
- [3] Broersen, K., Rousseau, F. & Schymkowitz, J. The culprit behind amyloid beta peptide related neurotoxicity in alzheimer’s disease: oligomer size or conformation? *Alzheimer’s research & therapy* **2**, 1–14 (2010).
- [4] McLean, C. A. *et al.* Soluble pool of a β amyloid as a determinant of severity of neurodegeneration in alzheimer’s disease. *Annals of neurology* **46**, 860–866 (1999).
- [5] Kirkitadze, M. D., Bitan, G. & Teplow, D. B. Paradigm shifts in alzheimer’s disease and other neurodegenerative disorders: the emerging role of oligomeric assemblies. *Journal of neuroscience research* **69**, 567–577 (2002).
- [6] Fulton, A. B. How crowded is the cytoplasm? *Cell* **30**, 345–347 (1982).
- [7] Gasser, B. *et al.* Protein folding and conformational stress in microbial cells producing recombinant proteins: a host comparative overview. *Microbial cell factories* **7**, 1–18 (2008).
- [8] Ignatova, Z. Monitoring protein stability in vivo. *Microbial Cell Factories* **4**, 1–6 (2005).
- [9] Ellis, R. J. Macromolecular crowding: obvious but underappreciated. *Trends in biochemical sciences* **26**, 597–604 (2001).
- [10] Minton, A. P. Effect of a concentrated “inert” macromolecular cosolute on the stability of a globular protein with respect to denaturation by heat and by chaotropes: a statistical-thermodynamic model. *Biophysical Journal* **78**, 101–109 (2000).

- [11] Minton, A. P. Models for excluded volume interaction between an unfolded protein and rigid macromolecular cosolutes: macromolecular crowding and protein stability revisited. *Biophysical journal* **88**, 971–985 (2005).
- [12] Hatters, D. M., Minton, A. P. & Howlett, G. J. Macromolecular crowding accelerates amyloid formation by human apolipoprotein c-ii. *Journal of Biological Chemistry* **277**, 7824–7830 (2002).
- [13] Uversky, V. N., Cooper, E. M., Bower, K. S., Li, J. & Fink, A. L. Accelerated α -synuclein fibrillation in crowded milieu. *FEBS letters* **515**, 99–103 (2002).
- [14] Fung, J., Darabie, A. A. & McLaurin, J. Contribution of simple saccharides to the stabilization of amyloid structure. *Biochemical and biophysical research communications* **328**, 1067–1072 (2005).
- [15] Sukenik, S. *et al.* Crowding alone cannot account for cosolute effect on amyloid aggregation. *PLoS One* **6**, e15608 (2011).
- [16] Sukenik, S. & Harries, D. Insights into the disparate action of osmolytes and macromolecular crowders on amyloid formation. *Prion* **6**, 26–31 (2012).
- [17] Elcock, A. H. Models of macromolecular crowding effects and the need for quantitative comparisons with experiment. *Current opinion in structural biology* **20**, 196–206 (2010).
- [18] Zhou, H.-X., Rivas, G. & Minton, A. P. Macromolecular crowding and confinement: biochemical, biophysical, and potential physiological consequences. *Annu. Rev. Biophys.* **37**, 375–397 (2008).
- [19] Batra, J., Xu, K. & Zhou, H.-X. Nonadditive effects of mixed crowding on protein stability. *Proteins: Structure, Function, and Bioinformatics* **77**, 133–138 (2009).
- [20] Senske, M. *et al.* Protein stabilization by macromolecular crowding through enthalpy rather than entropy. *Journal of the American Chemical Society* **136**, 9036–9041 (2014).
- [21] Nasica-Labouze, J. *et al.* Amyloid β protein and alzheimer’s disease: When computer simulations complement experimental studies. *Chemical reviews* **115**, 3518–3563 (2015).

- [22] Nguyen, P. H. *et al.* Amyloid oligomers: A joint experimental/computational perspective on alzheimer’s disease, parkinson’s disease, type ii diabetes, and amyotrophic lateral sclerosis. *Chemical reviews* **121**, 2545–2647 (2021).
- [23] O’Brien, E. P., Straub, J. E., Brooks, B. R. & Thirumalai, D. Influence of nanoparticle size and shape on oligomer formation of an amyloidogenic peptide. *The journal of physical chemistry letters* **2**, 1171–1177 (2011).
- [24] Magno, A., Caffisch, A. & Pellarin, R. Crowding effects on amyloid aggregation kinetics. *The Journal of Physical Chemistry Letters* **1**, 3027–3032 (2010).
- [25] Co, N. T., Hu, C.-K. & Li, M. S. Dual effect of crowders on fibrillation kinetics of polypeptide chains revealed by lattice models. *The Journal of Chemical Physics* **138**, 05B610_1 (2013).
- [26] Latshaw, D. C., Cheon, M. & Hall, C. K. Effects of macromolecular crowding on amyloid beta (16–22) aggregation using coarse-grained simulations. *The Journal of Physical Chemistry B* **118**, 13513–13526 (2014).
- [27] Petkova, A. T., Yau, W.-M. & Tycko, R. Experimental constraints on quaternary structure in alzheimer’s β -amyloid fibrils. *Biochemistry* **45**, 498–512 (2006).
- [28] Tjernberg, L. O. *et al.* Arrest of amyloid fibril formation by a pentapeptide ligand (β 21–30). *Journal of Biological Chemistry* **271**, 8545–8548 (1996).
- [29] Balbach, J. J. *et al.* Amyloid fibril formation by a β 16–22, a seven-residue fragment of the alzheimer’s β -amyloid peptide, and structural characterization by solid state nmr. *Biochemistry* **39**, 13748–13759 (2000).
- [30] Munishkina, L. A., Ahmad, A., Fink, A. L. & Uversky, V. N. Guiding protein aggregation with macromolecular crowding. *Biochemistry* **47**, 8993–9006 (2008).
- [31] Abraham, M. J. *et al.* Gromacs: High performance molecular simulations through multi-level parallelism from laptops to supercomputers. *SoftwareX* **1**, 19–25 (2015).
- [32] Bonomi, M. *et al.* Plumed: A portable plugin for free-energy calculations with molecular dynamics. *Computer Physics Communications* **180**, 1961–1972 (2009).

- [33] Huang, J. & MacKerell Jr, A. D. Charmm36 all-atom additive protein force field: Validation based on comparison to nmr data. *Journal of computational chemistry* **34**, 2135–2145 (2013).
- [34] Huang, J. *et al.* Charmm36m: an improved force field for folded and intrinsically disordered proteins. *Nature methods* **14**, 71–73 (2017).
- [35] Bussi, G., Donadio, D. & Parrinello, M. Canonical sampling through velocity rescaling. *The Journal of chemical physics* **126**, 014101 (2007).
- [36] Berendsen, H. J., Postma, J. v., van Gunsteren, W. F., DiNola, A. & Haak, J. R. Molecular dynamics with coupling to an external bath. *The Journal of chemical physics* **81**, 3684–3690 (1984).

A.5 Publication V

Structural dissection of the first events following membrane binding of the islet amyloid polypeptide

Khemtemourian L., **Fatafta H.**, Davion B., Lecomte S., Castano S., Strodel B. *Front. Mol. Biosci.*, 2022 Mar 15; 9:849979. doi: 10.3389/fmolb.2022.849979



Structural Dissection of the First Events Following Membrane Binding of the Islet Amyloid Polypeptide

Lucie Khemtemourian^{1*}, Hebah Fatafta^{2,3}, Benoit Davion¹, Sophie Lecomte¹, Sabine Castano¹ and Birgit Strodel^{2,3,4*}

¹Université de Bordeaux, CNRS, Bordeaux IMP, CBMN, Pessac, France, ²Institute of Biological Information Processing, Structural Biochemistry, Jülich, Germany, ³JuStruct, Jülich Center for Structural Biology, Jülich, Germany, ⁴Institute of Theoretical and Computational Chemistry, Heinrich Heine University Düsseldorf, Düsseldorf, Germany

OPEN ACCESS

Edited by:

Javier Oroz,
Spanish National Research Council
(CSIC), Spain

Reviewed by:

Philippe Derreumaux,
UPR9080 Laboratoire de Biochimie
Théorique (LBT), France
Ling-Hsien Tu,
National Taiwan Normal University,
Taiwan

*Correspondence:

Lucie Khemtemourian
lucie.khemtemourian@u-bordeaux.fr
Birgit Strodel
b.strodel@fz-juelich.de

Specialty section:

This article was submitted to
Protein Folding, Misfolding and
Degradation,
a section of the journal
Frontiers in Molecular Biosciences

Received: 06 January 2022

Accepted: 18 February 2022

Published: 15 March 2022

Citation:

Khemtemourian L, Fatafta H, Davion B,
Lecomte S, Castano S and Strodel B
(2022) Structural Dissection of the First
Events Following Membrane Binding of
the Islet Amyloid Polypeptide.
Front. Mol. Biosci. 9:849979.
doi: 10.3389/fmolb.2022.849979

The islet amyloid polypeptide (IAPP) is the main constituent of the amyloid fibrils found in the pancreas of type 2 diabetes patients. The aggregation of IAPP is known to cause cell death, where the cell membrane plays a dual role: being a catalyst of IAPP aggregation and being the target of IAPP toxicity. Using ATR-FTIR spectroscopy, transmission electron microscopy, and molecular dynamics simulations we investigate the very first molecular steps following IAPP binding to a lipid membrane. In particular, we assess the combined effects of the charge state of amino-acid residue 18 and the IAPP-membrane interactions on the structures of monomeric and aggregated IAPP. Distinct IAPP-membrane interaction modes for the various IAPP variants are revealed. Membrane binding causes IAPP to fold into an amphipathic α -helix, which in the case of H18K-, and H18R-IAPP readily moves beyond the headgroup region. For all IAPP variants but H18E-IAPP, the membrane-bound helix is an intermediate on the way to amyloid aggregation, while H18E-IAPP remains in a stable helical conformation. The fibrillar aggregates of wild-type IAPP and H18K-IAPP are dominated by an antiparallel β -sheet conformation, while H18R- and H18A-IAPP exhibit both antiparallel and parallel β -sheets as well as amorphous aggregates. Our results emphasize the decisive role of residue 18 for the structure and membrane interaction of IAPP. This residue is thus a good therapeutic target for destabilizing membrane-bound IAPP fibrils to inhibit their toxic actions.

Keywords: islet amyloid polypeptide, type 2 diabetes mellitus, amylin, amyloid aggregation, peptide-membrane interactions

1 INTRODUCTION

The formation of amyloid fibrils is involved in various human diseases, such as Alzheimer's disease, Parkinson's disease, or type 2 diabetes mellitus (T2DM). Amyloid forming proteins are often intrinsically disordered proteins (IDPs) or are proteins that contain one or more intrinsically disordered regions. The structure of those amyloid fibrils are very heterogeneous but they are all composed of arrays of cross β -sheets (Selkoe, 2004; Knowles et al., 2014; Willbold et al., 2021).

The human islet amyloid polypeptide (hIAPP), also known as amylin, is a 37-amino acid peptide hormone that is the main constituent of the islet amyloid mainly found in the pancreatic islets of T2DM patients, but also in many organs including the brain, the heart, and the kidney (Westermarck et al., 1987; Cooper et al., 1988; de Koning et al., 1995; Despa et al., 2012; Srodulski et al., 2014).

hIAPP is produced and secreted together with insulin by the pancreatic β -cells, and it plays a role in the control of glucose homeostasis and satiety by acting on the liver, gut, brain and pancreas (Lutz, 2010; Westermark et al., 2011). Under normal conditions, monomeric hIAPP lacks a well-defined structure as typical for an IDP, and mainly adopts a random coil conformation. However, in T2DM patients, hIAPP starts to aggregate into amyloid fibrils and the formation of these amyloid aggregates has been associated with the dysfunction and death of β -cells (Opie, 1901; Höppener et al., 2000).

While the toxic activity of hIAPP is still not completely understood, a link between hIAPP fibril formation at the membrane interface and hIAPP-induced cell death was observed, highlighting the relevance of the membrane (Gao and Winter 2015). A few putative mechanisms of cell membrane-disruption by hIAPP have been described and have been the subject of several studies (Mirzabekov et al., 1996; Janson et al., 1999; Engel et al., 2008; Hebda and Miranker, 2009; Martel et al., 2016). It has been suggested that the amyloid fibrils are not the primary toxic species, but oligomers formed by hIAPP are thought to be cytotoxic, either by forming membrane channels or by inducing bilayer disorder (Mirzabekov et al., 1996; Kaye et al., 2004; Quist et al., 2005). In agreement with these studies, molecular dynamics (MD) simulations demonstrated that membrane permeability was induced by oligomeric hIAPP (Poojari et al., 2013). Further experimental studies have indicated that the formation of hIAPP fibrils at the membrane causes membrane disruption by forcing the curvature of the bilayer to unfavorable angles or by the uptake of lipids by the fibrils (Sparr et al., 2004; Engel et al., 2008). Moreover, the composition of the membrane plays a role in the amount of membrane damage that can be caused by hIAPP (Zhang et al., 2017), and that by blocking hIAPP-membrane interactions by small-molecule ligands such as resveratrol, the membrane-induced toxicity of hIAPP can be alleviated (Evers et al., 2009). Even if the mechanism is not yet fully understood, altogether these studies revealed the importance of the membrane in hIAPP-induced cell death.

Along with these results, it has been recognized that the various amino acids of hIAPP are crucial in hIAPP fibril formation and in hIAPP-membrane disruption. The N-terminal residues are mainly responsible for membrane binding, the middle core drives amyloid fibril formation, while the C-terminal residues are also involved in amyloid fibril formation, yet to a lesser extent (Skeby et al., 2016; Engel et al., 2006; Brender et al., 2008a,b). The sequence of IAPP is highly conserved across different species (Cao et al., 2013; Caillon et al., 2016), however key differences, that play important roles in modulating the propensity of the peptide to aggregate, have been identified. The non-amyloidogenic, and non-toxic mouse IAPP differs from hIAPP by six residues out of 37; interestingly, five of the six residues are located in the amyloid-prone region 20–29 and mice do not develop T2DM. For that reason, it is essential to explore the sequence-structure relationship. While the region 20–29 is of relevance (Choi et al., 2021), it is not the sole region governing IAPP fibril formation, since proline mutations at positions 14, 15, 16, and or 17 can also induce a loss of fibril

formation (Abedini and Raleigh, 2006; Fox et al., 2010; Tu and Raleigh, 2012). Recent studies on residue 18, that is highly variable among species (Caillon et al., 2016), indicate that this residue is important in modulating 1) IAPP fibril formation in solution and in the presence of membranes (Khemtemourian et al., 2017; Hoffmann et al., 2018a), 2) membrane interaction and damage (Hoffmann et al., 2018a), 3) cell toxicity (Khemtemourian et al., 2017), and 4) hIAPP-zinc, and hIAPP-insulin affinity (Wineman-Fisher and Miller, 2016; Khemtemourian et al., 2021; Miller, 2022). The main findings from these studies are summarized in **Table 1**.

The characterization of the aggregation pathways and of the structure at a molecular and an atomic level at the membrane is thus a key step to understanding hIAPP cellular toxicity and its role in disease states. While the structure of hIAPP in solution was extensively studied (Goldsbury et al., 2000; Williamson and Miranker, 2007; Wiltzius et al., 2009; Camargo et al., 2017), only a few studies were performed in a membrane environment. These studies mainly used spectroscopic techniques such as circular dichroism (CD) or nuclear magnetic resonance (NMR) spectroscopy (Jayasinghe and Langen, 2005; Patil et al., 2009; Nanga et al., 2011; Caillon et al., 2013; Camargo et al., 2017; Milardi et al., 2021), which yield information on structural averages of the conformational ensemble, yet are not time-resolved enough to provide information on individual structures. A complicating aspect for NMR spectroscopy of hIAPP in the presence of lipid bilayers is the fast aggregation speed of hIAPP. To overcome this challenge, approaches have been adopted to reduce the fibrillation process, such as the use of low temperatures and/or detergent micelles that stabilize the monomeric form of hIAPP (Jayasinghe and Langen, 2005; Patil et al., 2009; Nanga et al., 2011; Caillon et al., 2013; Camargo et al., 2017). Here, we address this problem by employing a combination of two techniques that offer the possibility of obtaining time-resolved structural information of hIAPP in a membrane environment, namely attenuated total reflection Fourier-transform infrared (FTIR) spectroscopy and MD simulations. This allows us to provide structural information for both monomeric hIAPP as well as the first aggregation steps of hIAPP at the membrane. Previous simulation studies examined the membrane interactions of monomeric and oligomeric hIAPP (Martel et al., 2016; Dignon et al., 2017a; Dong et al., 2018; Press-Sandler and Miller, 2018; Qian et al., 2018; Qiao et al., 2019). The results from these simulations indicate that wild-type hIAPP interacts with the membrane by forming interactions between the anionic lipids of the membrane and the N-terminal part of hIAPP, which is in agreement with experimental data (Engel et al., 2006; Skeby et al., 2016). Stabilization of the α -helical state following the binding to a membrane was also observed in both experimental and simulation studies (Caillon et al., 2013; Dignon et al., 2017a; Christensen et al., 2021). FTIR spectroscopy has been previously used to provide insights into the membrane-bound monomeric and fibril structures of hIAPP (Mishra et al., 2008; Mishra and Winter 2008; Radovan et al., 2008). The studies indicated that a transition from unordered structures to β -sheet structures occurs on a time scale characteristic for amyloid fibril formation. Possible structures for membrane-bound hIAPP

TABLE 1 | Biophysical and biological characteristics of wild-type and mutated hIAPP as determined in previous studies.

	hIAPP	H18R-IAPP	H18K-IAPP	H18E-IAPP	H18A-IAPP
Fibril formation in solution	+++	++	+	+	+
Fibril formation at membranes	+++	+++	++	+	+
Membrane leakage	+++	+++	+++	+++	+++
Cell toxicity	+++	+	+	+	+

aggregates were suggested by MD simulations (Liu et al., 2020; Nguyen et al., 2021; Sepehri et al., 2021).

The purpose of this study is to reveal the structures of hIAPP directly after its binding to a lipid-membrane interface and to determine how these structures are influenced by histidine 18. To this end, both experiments and simulations were performed as they provide information on the structural evolution for different length and time scales and with different resolutions, thereby complementing each other. To study the effects of residue 18 on the hIAPP-membrane interactions and the emerging peptide structures, all the experiments and simulations were performed with wild-type hIAPP and four mutated peptides where histidine 18 has been replaced by arginine (H18R-IAPP), lysine (H18K-IAPP), glutamic acid (H18E-IAPP), and alanine (H18A-IAPP) to achieve variations in charge, shape, volume, and hydrophobicity. To evaluate the interaction of hIAPP and the mutated peptides with the membrane, we worked with a 1, 2-dioleoyl-sn-glycero-3-phosphocholine/1,2-dioleoyl-sn-glycero-3-phospho-L-serine (DOPC/DOPS) lipid mixture (ratio 7:3) to mimic eukaryotic β -cell membranes. These cells contain typically between 1 and 10% of negatively charged lipids; however in the case of T2DM, the high concentration of glucose increases the amount of negatively charged lipids up to 30% (Rustenbeck et al., 1994). We performed attenuated total reflection (ATR) FTIR spectroscopy at different incubation times to apprehend the initial structure of the peptides at the membrane and the evolution of structural changes. The putative perturbation of the lipid membranes after addition of the peptides was also investigated. We observed differences for the wild-type and the mutated peptides not only in the initial structures but also in the variation of secondary structure in time, highlighting the role of the residue histidine 18 in the membrane interactions of hIAPP and in the process of fibril formation. The ATR-FTIR results are complemented on either side of the length and time scales, by MD simulations to provide mechanistic insight into the structural transitions and peptide-membrane interactions and by transmission electron microscopy (TEM) to obtain images of the final fibrils.

2 MATERIALS AND METHODS

2.1 Sample Preparation

Peptide solutions were prepared as described previously (Khemtemourian et al., 2017; Hoffmann et al., 2018a). Briefly, stock solutions were obtained by dissolving the peptide powder at a concentration of 1 mM in hexafluoroisopropanol (HFIP) and by letting them incubate for an hour. HFIP was then evaporated under a stream of dry N_2 and further dried by vacuum in a

desiccator for at least 30 min. The resulting peptide film was then rehydrated with 100 μ l of buffer containing 10 mM tris(hydroxymethyl)aminomethane and 100 mM NaCl (pH 7.4) and 2 μ L of a 20 μ M $CaCl_2$ solution.

2.2 Preparation of Phospholipid Vesicles

DOPC and DOPS lipids were purchased from Avanti Polar Lipids. Lipid powders were dissolved in chloroform and mixed at the desired ratio. The solvent was evaporated under a stream of dry nitrogen and further dried under high vacuum in a desiccator for at least 30 min. Lipid films were then rehydrated for 1 h with a buffer of 10 mM Tris, 100 mM NaCl, pH 7.4 in 100% D_2O , obtaining large, and multilamellar vesicles (LMVs). Small, unilamellar vesicles (SUVs) were then prepared from the LMVs by tip sonication. The SUVs were burst onto a germanium ATR crystal to form a single bilayer which is controlled by the measurement of the absolute IR intensity. For the subsequent measurements, we added hIAPP (or its mutants) at 50 μ M concentration to the membrane and then rinsed the non-binding peptides off.

Large, unilamellar vesicles (LUVs) for the TEM were prepared using the same buffer conditions as for the LMVs, but containing 100% H_2O , which was subjected to 10 freeze-thaw cycles with alternating temperatures of about $-190^\circ C$ and $50^\circ C$. The lipid suspension was subsequently extruded 19 times through a mini-extruder (Avanti Polar Lipids) equipped with a 200 nm polycarbonate membrane. The phospholipid content of both lipid stock solutions and vesicles was determined as inorganic phosphate according to Rouser et al. (Rouser et al., 1970).

2.3 ATR-FTIR Spectroscopy

ATR-FTIR spectra were recorded on a Nicolet 6,700 spectrometer Thermo Scientific equipped with an MCT detector cooled at 77 K. A Ge-crystal was used as internal reflection unit. Since ATR-FTIR spectroscopy is sensitive to the orientation of the structures (Goormaghtigh et al., 1990; Goormaghtigh et al., 1994; Goormaghtigh et al., 1999), spectra were recorded with parallel (p) and perpendicular (s) polarizations of the incident light with respect to the ATR plate. 200 scans were recorded at a resolution of 8 cm^{-1} . All the orientation information is then contained in the dichroic ratio $R_{ATR} = A_p/A_s$, where A_p and A_s represent the absorbance underlying the band at p and s, respectively, polarization of the incident light. After subtraction of a spectrum of the lipid membrane with the buffer and subtraction of noise from water, the spectra were baseline-corrected between 1700 and $1,600\text{ cm}^{-1}$ corresponding to the amide I band area. Finally, a smoothing has been applied. To derive the secondary structure from the bands, the spectra were

analyzed with an algorithm based on a second-derivative function and a self-deconvolution procedure (GRAMS and OMNIC software, Thermo Fisher Scientific) to determine the number and wavenumber of the individual bands within the spectral range of the amide I band.

2.4 Transmission Electron Microscopy

TEM was performed at the “Institut de Biologie Paris Seine” (IBPS, Sorbonne Université, Paris, France). Peptides and LUVs were incubated for 2 days at room temperature. Aliquots (20 μ l) were adsorbed onto a glow-discharged carbon coated 200 mesh copper grid for 2 min and then negatively stained with saturated uranyl acetate for 45 s. Grids were examined using a ZEISS 912 Ω electron microscope operating at 80 kV.

2.5 Computational Methods

2.5.1 Setup of the Simulated Systems

The modeled systems are composed of the full-length (37 residues) hIAPP monomer (either wild-type or mutated at residue 18) and a DOPC/DOPS lipid bilayer in a 7:3 ratio mimicking the lipid composition of the experiments. As initial peptide structure, the most populated conformation from a preceding 1 μ s simulation of wild-type hIAPP as a monomer and with a disulfide bond between C2 and C7 in the aqueous phase was used. The mutated peptides were generated from this structure by replacing the neutral H18 residue (protonated only at N ϵ) by its positively charged counterpart (denoted by H18+), the neutral residue alanine, the negatively charged glutamate, or the positively charged lysine or arginine using the CHARMM-GUI interface (Lee et al., 2016). These peptides will be referred to as hIAPP, hIAPP(H18+), H18A-IAPP, H18E-IAPP, H18K-IAPP, and H18R-IAPP, respectively. CHARMM-GUI was also used to set up and equilibrate the DOPC/DOPS lipid bilayer as a symmetric membrane composed of 88 DOPC and 40 DOPS lipid molecules. The peptides were placed above the lipid bilayer (one peptide per simulation) at a distance of \approx 3 nm from the bilayer surface. Each system was then solvated with water using the TIP3P model (Jorgensen et al., 1983) and NaCl was added at physiological concentration of 150 mM, while also neutralizing the system. The total number of atoms N in each system was \approx 54,000 atoms and the simulation box size was about $6.5 \times 6.5 \times 12.0$ nm³.

2.5.2 MD Simulation Conditions

The MD simulations were carried out using the GROMACS 2018.2 simulation package (Abraham et al., 2015), along with CHARMM36 (Klauda et al., 2010) as force field for the lipids and CHARMM36m (Huang et al., 2017) for the IAPP peptides. Each system was first energy minimized using the steepest descent algorithm to remove initial atom clashes that may have resulted during the setup. This was followed by an equilibration using MD simulations under NVT conditions, where the reference temperature T of 302 K (which was chosen to be close to the temperatures used in the experiments) was regulated with a velocity-rescale thermostat (Bussi et al., 2007). Then, the system was equilibrated under NpT conditions to obtain a pressure p of 1.0 bar, which was realized by regulating the

pressure using a semi-isotropic Parrinello-Rahman pressure coupling scheme (Berendsen et al., 1984). The particle mesh Ewald (PME) method was used to calculate the electrostatic interactions in combination with periodic boundary conditions set in all directions. The electrostatic interactions in real space as well as the van der Waals interactions were cut at 1.2 nm. All bonds were constrained using the LINCS algorithm (Hess et al., 1997). For each of the six systems the MD simulations were run in triplicate and for 1 μ s per simulation (i.e., 3×1 μ s per system).

2.5.3 Analysis of the MD Simulations

All analysis programs mentioned are available via the GROMACS 2018.2 program package (Abraham et al., 2015). Only the MD snapshots where IAPP is within 0.5 nm of the bilayer were included in the analysis of the system in question. The peptide-lipid interactions were then determined by calculating the interaction energy between each IAPP residue and the DOPC and DOPS lipids, respectively, using “gmx energy”. The “gmx mindist” program was employed to determine the number of contacts between each IAPP residue and DOPC/DOPS. A contact was recorded when the distance between any two non-hydrogen atoms from a residue and a lipid was within 0.5 nm. The hydrogen bond propensity was determined as the ratio of the number of MD snapshots where one or more hydrogen bonds were formed between peptide and lipid and the total number of MD snapshots per system. The secondary structure of the peptides was determined using the ‘define secondary structure program’ (DSSP) (Kabsch and Sander, 1983) invoked via the GROMACS tool “do dssp”. To facilitate a clear representation, the data of similar secondary structures are grouped together: β -strand and β -bridge are combined as β -sheet, β -turn and bend as turn, and helix includes α -, π -, and 3_{10} -helices.

3 RESULTS

3.1 hIAPP and the Mutated Peptides Adopt a Mixture of Structures Upon Initial Binding to the Membrane

We first investigated, using ATR-FTIR spectroscopy, the structural behavior of wild-type and mutant hIAPP when interacting with a (supported) lipid bilayer composed of DOPC/DOPS (7:3). These phospholipids represent the most abundant zwitterionic phospholipid species (PC) and the dominant negatively charged phospholipid species (PS) in eukaryotic cells, and the 7:3 ratio is similar to the one of zwitterionic lipids to negatively charged lipids of the membrane of pancreatic islet cells (Rustenbeck et al., 1994). We performed polarized ATR-FTIR experiments in order to analyze the initial structures of the peptides at the membrane and to determine if the mutation at residue 18 could induce some structural changes. **Figure 1** shows the ATR-FTIR spectra in the amide I region of hIAPP and the mutated peptides interacting with DOPC/DOPS bilayers. Based on the amide I band analysis, hIAPP and H18K-IAPP exhibit two peaks at around $1643 \pm$

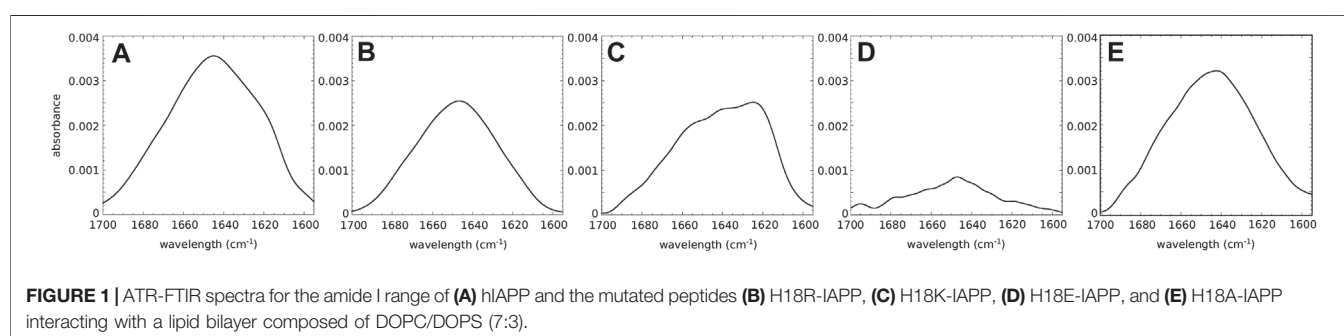


FIGURE 1 | ATR-FTIR spectra for the amide I range of (A) hIAPP and the mutated peptides (B) H18R-IAPP, (C) H18K-IAPP, (D) H18E-IAPP, and (E) H18A-IAPP interacting with a lipid bilayer composed of DOPC/DOPS (7:3).

TABLE 2 | Secondary structure content derived from ATR-FTIR spectra of hIAPP and its mutants interacting with a DOPC/DOPS membranes.

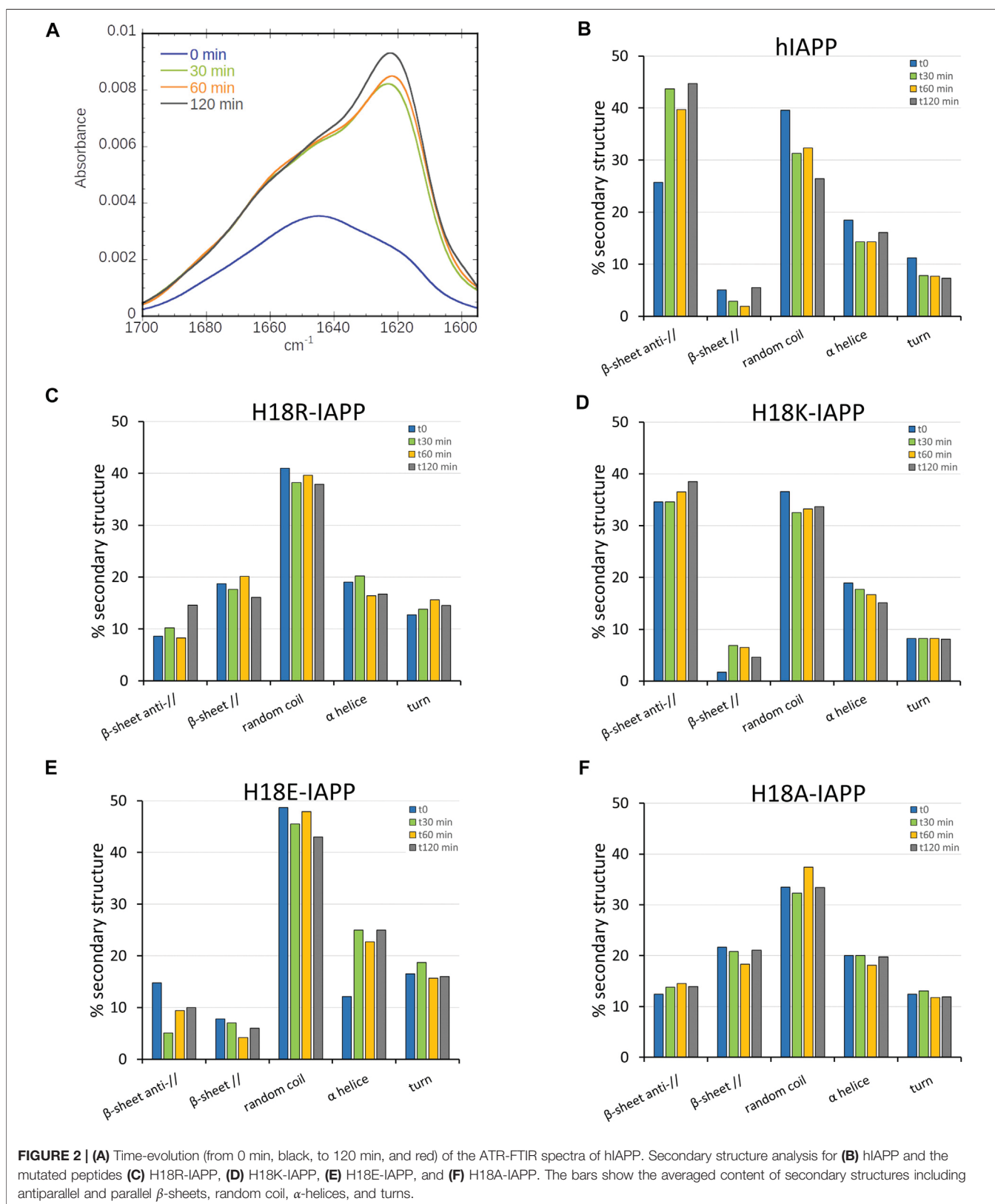
Secondary structure element	Wavenumber (cm ⁻¹)	Percentage of structural element				
		hIAPP	H18R-IAPP	H18K-IAPP	H18E-IAPP	H18A-IAPP
β -sheet (and anti-)	1615, 1624, 1632, 1686	31	27	36	23	34
Random coil	1643	40	41	37	49	34
α -helix	1654	18	19	19	12	20
Turn	1674	11	13	8	16	12

1 cm⁻¹ and 1623 ± 1 cm⁻¹ assigned to random coil and β -sheet structure, respectively. The mutated peptides H18R-IAPP, H18E-IAPP, and H18A-IAPP display predominantly an amide I band at around 1643 ± 1 cm⁻¹ that can be attributed to unordered secondary structures. The secondary structure content of the peptides bound to the DOPC/DOPS bilayers has then been evaluated from the analysis of the amide I band shape and curve fitting (Table 2). The bands at 1686 ± 1 cm⁻¹, 1632 ± 1 cm⁻¹, 1624 ± 1 cm⁻¹, and 1615 ± 1 cm⁻¹ were assigned to β -sheets (parallel and antiparallel), the band at 1654 ± 1 cm⁻¹ to α -helices, the band at 1643 ± 1 cm⁻¹ to random structures, and the one at 1674 ± 1 cm⁻¹ to β -turns. The results show that hIAPP is mainly unstructured (40%) with a contribution of β -sheets (31%), which is in agreement with previous studies (Khemtemourian et al., 2010; Seeliger et al., 2012). The peptides H18R-IAPP and H18K-IAPP adopt unstructured conformations with about the same probability as hIAPP (41 and 37%, respectively) but have different amounts of β -sheets (27 and 36%). The initial structure of H18E-IAPP differs substantially from the wild-type peptide with less β -sheet content and more random coil conformation. The peptide H18A-IAPP has the highest content of α -helical structure and the lowest amount of random coil, which is likely due to the inherent preference of alanine to adopt a helical conformation; in fact, alanine is regarded as the most stabilizing residue in helices. Such change in the initial structure may modify the kinetics of fibril formation as shown previously (Hoffmann et al., 2018a). Overall, the data indicate that at the membrane interface, hIAPP is initially largely unstructured, but depending on the kind of mutation at residue position 18, the peptides also adopt β -sheet, and α -helical structures to different extents. In order to determine if these mutations do also influence the kinetics of structural changes, the ATR-FTIR experiments were carried out during the course of a few hours.

3.2 Residue 18 is Decisive for the Conformational Rearrangements of Membrane-Bound IAPP

To evaluate the changes in secondary structure of the IAPP peptides at the DOPC/DOPS membrane interface, we collected ATR-FTIR spectra for 2 h in intervals of 30 min. Figure 2A shows that the maximum of the amide I band of hIAPP undergoes a pronounced shift from 1643 cm⁻¹ to 1624 cm⁻¹. This shift corresponds to a structural transition from an unstructured conformation to a structured one with antiparallel β -sheets, indicating the start of the peptide aggregation process. The maximum at 1624 cm⁻¹ is reached at 120 min. However, a shoulder at around 1650 cm⁻¹ remains, for which there are two possible explanations: 1) not all of the amino acids are involved in the intermolecular β -sheet formation, or 2) monomers and/or oligomers are still present after 2 h of incubation. In two previous studies, we observed that the monomeric hIAPP is fully consumed within 2 h and that low-molecular weight hIAPP oligomers were not detected Hoffmann et al. (2018a,b). doi: 10.1039/c7cp07516b.) The first explanation is thus the more probable. The secondary structure content of the membrane-bound hIAPP at different incubation times (from 0 to 120 min) resulting from the analysis of the amide I band shape and curve fitting is given in Figure 2B. The bar chart clearly indicates that the β -sheet content increased from 31 to 50%, while the random coil content decreased from 37 to 26%, meaning that hIAPP started to aggregate, in agreement with previous studies (Mishra et al., 2008). Nonetheless, some of the residues remained in an α -helical conformation, as this contribution dropped to only about 15%, starting from 18% at time zero.

The same kind of experiments were performed for the mutated peptides. While they all undergo structural rearrangements, different behaviors are observed. As for hIAPP, the antiparallel



β -sheet content of H18K-IAPP increases over time, thereby reducing the amount of random coil conformations, which suggests a self-assembly of the peptide (Figure 2D). It should

be noted that already the structure of H18K-IAPP at the beginning of the experiment contains considerable amounts of antiparallel β -sheet, indicating that the aggregation of this peptide

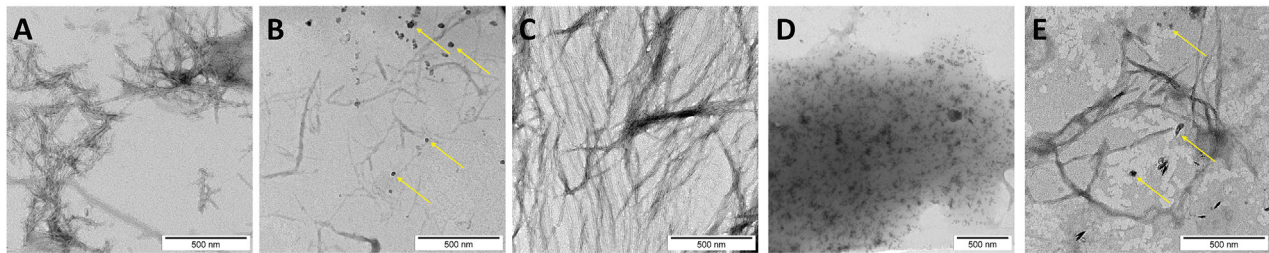


FIGURE 3 | TEM image of (A) native hIAPP and the mutated peptides: (B) H18R-IAPP, (C) H18K-IAPP, (D) H18E-IAPP, and (E) H18A-IAPP incubated with DOPC/DOPS liposomes. The yellow arrows indicate the amorphous aggregates found for H18R-IAPP and H18A-IAPP. Scale bars represent 500 nm.

is immediate. Also in the cases of H18R-IAPP and H18A-IAPP there are β -sheets present at $t = 0$, yet they include both parallel and antiparallel arrangements, suggesting the presence of two structural populations (Figures 2C,F). These two populations are largely stable over time; only for H18R-IAPP some increase in antiparallel β -sheet content is observed at $t = 120$ min. In the case of H18E-IAPP, on the other hand, the amount of both parallel and antiparallel β -sheet decreases, whereas α -helical structures are increasingly formed (Figure 2E), reaching helical contents of more than 20%. This suggests that the DOPC/DOPS membrane promotes an α -helical conformation in membrane-bound H18E-IAPP. It should be mentioned that also in the case of H18A-IAPP the initial α -helix that formed remained stable, with population values of about 20%, whereas in H18K-IAPP and H18R-IAPP the helical content decreased somewhat to about 15%, which is similar as for hIAPP. In order to corroborate these results and validate the presence of one or two β -sheet populations, we then performed TEM in the presence of DOPC/DOPS membranes.

3.3 Electron Microscopy Images Validate the Structural Differences Between the Peptides

TEM was applied to assess the presence of amyloid fibrils and/or amorphous aggregates interacting with the membrane. In the case of hIAPP, fibrils were obtained that exhibit a classical and mature amyloid-fibril morphology with widths of 6–10 nm (Figure 3A). It seems reasonable to assign these fibrils to the antiparallel β -sheets structure observed in the ATR-FTIR experiments. The same result is found for H18K-IAPP, where long and twisted fibrils are observed by TEM (Figure 3C), and which mainly harbor antiparallel β -sheets as revealed by the ATR-FTIR spectrum. For H18R-IAPP and H18A-IAPP, two aggregate morphologies are present in the TEM images, one corresponding to short fibrils, and the other one being small amorphous aggregates (indicated by yellow arrows in Figures 3B,E). These results correlate with the ATR-FTIR experiments of both peptide variants that display two β -sheet populations: parallel and antiparallel β -sheets. Based on the observation that in the cases of hIAPP and H18K-IAPP the fibrils are correlated with the appearance of antiparallel β -sheets, we assume that also for H18R-IAPP and H18A-IAPP the antiparallel β -sheets give rise to fibrils, and while the parallel

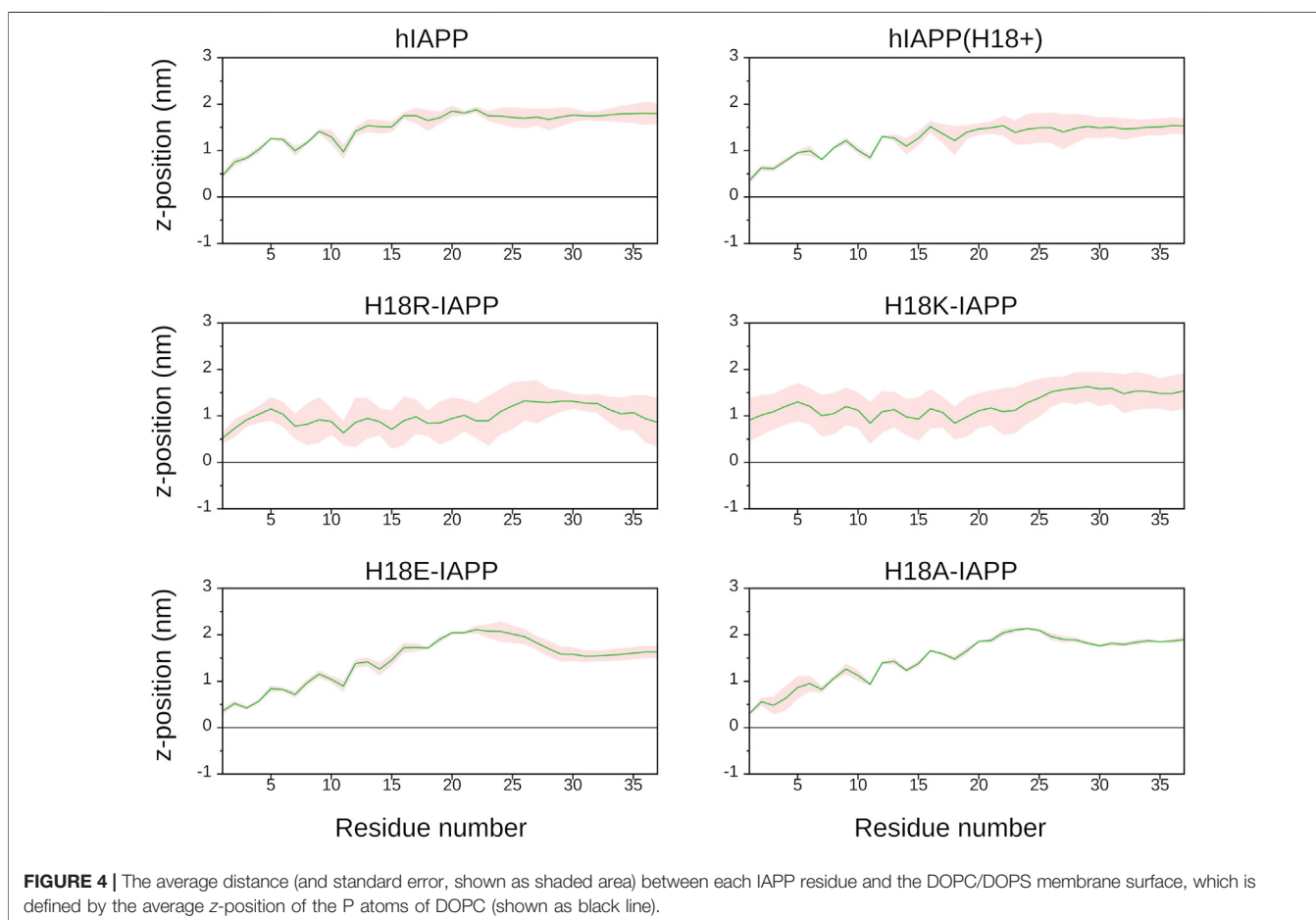
β -sheets are most likely present in the amorphous aggregates. This suggests that amorphous aggregates and fibrils can not only be distinguished from each other, but they also arise from different secondary and tertiary structures. For H18E-IAPP, no fibrils were detected in the TEM images, only small aggregates occurred (Figure 3D). The β -sheet content (both parallel and antiparallel) was also low; instead, the amount of random coil is rather high, suggesting that the amorphous H18E-IAPP aggregates are mainly unstructured while involving some helices. The current findings correlate with previous results that the substitution of the histidine 18 by an arginine, an alanine, or a glutamate stabilizes the oligomeric species and slows down the fibril formation (Hoffmann et al., 2018a). To gain more insights into the impact of residue 18 on the initial structure of the peptides and on the membrane interactions of IAPP and resulting structural changes, we performed all-atom MD simulations.

3.4 MD Simulations Provide Atomic Insight Into the Different Behaviors of the Membrane-Bound IAPP Peptides

In order to elucidate the structure of membrane-bound hIAPP in its monomeric form, which cannot be captured by experimental means as it is in equilibrium with aggregated peptide species at the temporal resolutions of the experimental techniques, we performed MD simulations. Moreover, to unravel the effects of residue 18 on the peptide-membrane interactions and their joint consequences on the peptide structure, we simulated hIAPP (with neutral H18 and positively charged H18, denoted as H18+) and its mutants H18A, H18E, H18R, and H18K. For each peptide variant, we performed $3 \times 1 \mu\text{s}$ MD simulations studying the binding of the peptides to a DOPC/DOPS (7:3) lipid bilayer.

3.4.1 Membrane Adsorption

To follow the association of the peptide with the membrane, we calculated the average distance between the center of mass of each residue and the average position along the bilayer normal of the phosphorus atoms of DOPC, which was used as a reference, and therefore set to zero (Figure 4). It can be seen that the peptides interact differently with the membrane. Similar distance profiles are observed for hIAPP, hIAPP(H18+), H18R-IAPP, and H18K-IAPP, while those of H18E-IAPP and H18A-IAPP are similar with



each other yet differ from the other four. The smallest distances are witnessed for H18R-IAPP and H18K-IAPP, followed by hIAPP(H18+), which indicates that a positive charge at position 18 is key for its interaction with the membrane. The peptides generally approach the membrane with their N-terminus, with close contacts being formed between region K1–R19 and the lipids, while residues S20–Y37 are further away from the membrane. However, this does not apply to H18K-IAPP and H18R-IAPP, where almost all residues are within ≈ 1.0 nm of the membrane surface. In particular in the latter case, also the C-terminus is close to the membrane, indicating a parallel alignment of the peptide to the membrane surface, and which is not as strongly visible for the other peptides. The profiles of the distance plots are characterized by a zigzag pattern, which suggests that the peptides adopt a helical structure on the membrane, and that especially involves the first half of the peptides.

Figure 5 shows representative snapshots for the membrane association of IAPP, which confirms that the peptides tend to adopt a helical conformation in the N-terminal half. However, the wild-type peptides hIAPP and hIAPP(H18+) also involve a β -sheet in the C-terminal region (S20–G33), which was not adopted by the other peptides. In agreement to the distance plot one can see that hIAPP(H18+) inserts more deeply into the membrane than hIAPP, while hIAPP is only on, but not in the membrane.

Nonetheless, in both cases the β -sheet interacts with the membrane, suggesting it to play a role in the subsequent aggregation when several peptides are membrane-adsorbed. These structures could even represent the α -to- β intermediate that was suggested to exist along the amyloid aggregation pathway of hIAPP, especially when this aggregation is assisted by the presence of lipid membranes (Abedini and Raleigh, 2009; Ling et al., 2009). Peptides H18R- and H18K-IAPP are seen to be immersed in the membrane. The helix, which reaches from T6 to G24 in both cases, lies below the lipid headgroup, and is parallel to the membrane surface. In the case of H18R-IAPP, also the C-terminal residues are close to the headgroups, whereas the C-terminus of H18K-IAPP points away from the membrane surface, which explains the slight difference in their distance profiles shown in **Figure 4**. In the case of H18E-IAPP, the helix is least developed and all residues that are not part of the helix point away from the membrane. With the H18A mutation, on the other hand, a helix is formed, and which however is not membrane-adsorbed. Only a few residues from the N- and C-terminal region make contact with the membrane, whereas the helix is several Angstrom above the membrane surface. The observation of a well-developed helix for H18A-IAPP is in line with the experimental findings and derives from the helix-promoting alanine introduced into the sequence. There are further findings from the simulations that agree with the experimental

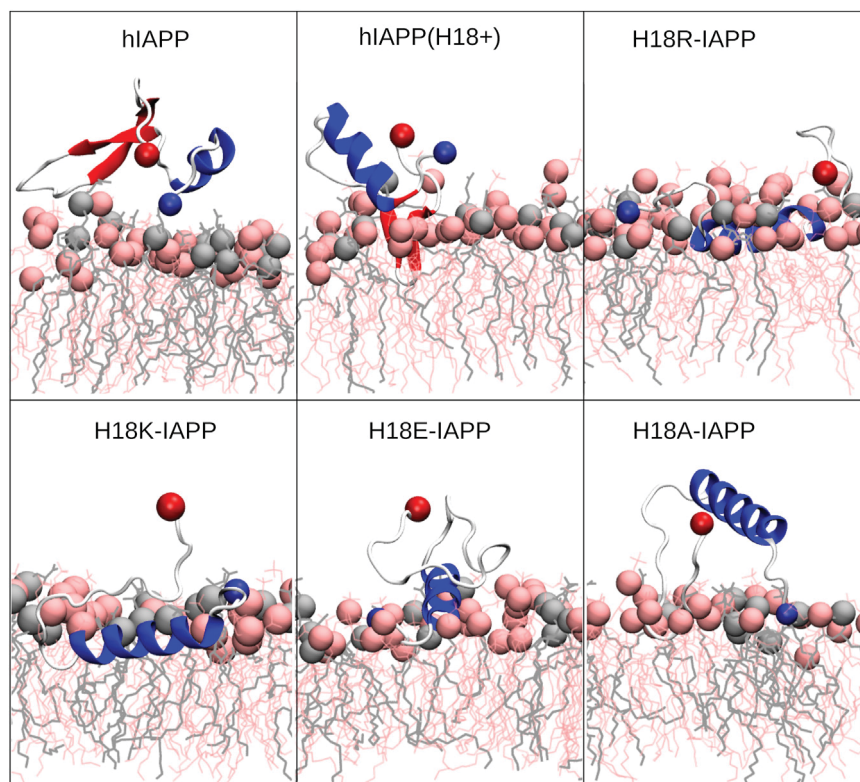


FIGURE 5 | Representative IAPP structures interacting with the DOPC/DOPS membrane. The peptide is shown as cartoon (with helix, β -sheet and coil being shown in blue, red and white, respectively), with their N- and C-termini being indicated as blue and red spheres, respectively. DOPC and DOPS lipids are shown as pink and gray sticks, respectively, with their P atoms indicated by spheres of the corresponding color.

results in **Table 2**. For instance, both simulations and experiments found that the α -helical content is smallest and that of random coil is largest for H18E-IAPP.

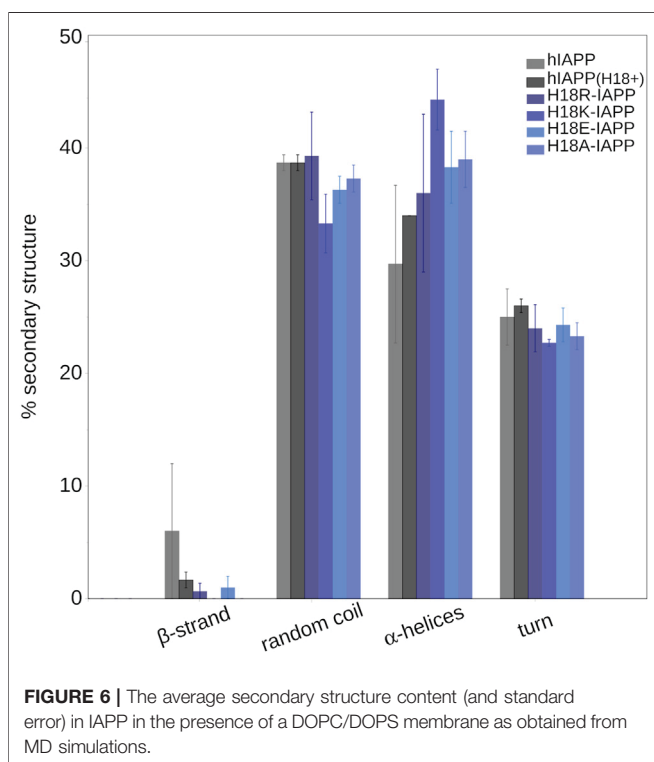
3.4.2 Secondary Structure

To quantify the effect of the peptide mutation and membrane adsorption on the peptide secondary structure, we determined the propensity of each peptide to adopt a helical conformation, to be part of a β -sheet (β -strand or β -bridge), or be in a turn or bend conformation. **Figure 6** shows that random coil and α -helices are the dominating structures, with probabilities between 30 and 40%, or even above. Turn conformations are populated with a probability of 20–25%, while the β -sheet content is $<1\%$, apart for hiIAPP where it is $\approx 5\%$. All of the mutants have a higher amount of helix than hiIAPP. For H18K-IAPP it even reaches 45%, which correlates with its close interaction with the membrane. However, while for H18R-IAPP the interaction with the membrane is similar, the increase in helix is not as pronounced (35%). The second highest amount in helix is observed for H18A-IAPP (38%), which agrees to the increase in helical propensity seen for this mutant in experiment (**Table 2**). Nonetheless, there are also certain differences between the secondary structures determined by the ATR-FTIR experiments and by the simulations, which can be explained with the different length,

and time scales that are probed by these techniques. In the MD simulations, we model the very first peptide–membrane interaction of the IAPP monomer, whereas with the ATR-FTIR experiments the structural evolution occurring at later times can be assessed. However, at the time when the first ATR-FTIR spectrum is recorded, there are already small IAPP oligomers present in addition to monomers. The application of simulations besides ATR-FTIR spectroscopy therefore allows to extract the characteristics of the IAPP monomers which are hidden in spectroscopic signals of the monomer-oligomer mixtures. The presence of monomers only in the simulations explains the generally low amount of β -sheet that is present in the simulated systems, as this is expected to increase upon IAPP aggregation. Only for hiIAPP, an average β -sheet content of 5% is observed that results from an intrapeptide β -hairpin that formed towards the end of the simulation. For hiIAPP(H18+) it formed even later, therefore the average β -sheet content is lower, even though for this system a β -hairpin is clearly visible in **Figure 5**.

3.4.3 Peptide–membrane Interactions

To rationalize the driving force for IAPP to interact with the DOPC/DOPS lipid bilayer, the interaction energy of each peptide residue with each component of the lipid bilayer was calculated and partitioned into its electrostatic (E_{Coul}) and Lennard-Jones



(E_{LJ}) contributions (**Supplementary Figure S1**). The results show that the major driving force for the peptide–membrane association are electrostatic attractions, especially between the negatively charged DOPS lipids, and the positively charged residues K1 and R11. These interactions occur in all cases and explain why IAPP approaches the membrane always via its N-terminus. This observation agrees with those from previous MD studies that highlighted the importance of anionic lipids like POPG (1-palmitoyl-2-oleoyl-sn-glycero-3-phosphoglycerol), POPE (1-palmitoyl-2-oleoyl-sn-glycero-3-phosphoethanolamine), and or DOPS in driving hIAPP–membrane interactions (Zhang et al., 2012; Dignon et al., 2017b; Mei et al., 2020). **Supplementary Figure S2** reveals that a positive charge at position 18 generally increases the tendency of the peptide to interact with the membrane. Almost all residues of the three peptides hIAPP(H18+), H18R- and H18K-IAPP form contacts with the membrane, whereas these contacts are mainly limited to K1–R11 in the other three cases. In the cases of H18R- and H18K-IAPP, the interaction between the positive charge of residue 18 and DOPS particularly enhances the association of the peptide with the membrane, which explains their deeper insertion into the membrane. This suggests that the size and/or flexibility of the side chain is important too. The electrostatic interactions partly involve H-bond formation in the region K1–R11, which extends to the C-terminal residues for hIAPP(H18+), and H18R- and H18K-IAPP (**Supplementary Figure S3**). Again, the positively charged residues are most involved in H-bond formation. The propensity of residue 18 to form an H-bond with DOPS or DOPC is particularly pronounced for H18R-IAPP, which is accompanied by further H-bonds between C-terminal residues and especially DOPC. Interestingly, in

the experiments this peptide appeared to form fewer fibrils and more amorphous aggregates compared to hIAPP and H18K-IAPP. Its tendency to form H-bonds with the lipids may explain why H18R-IAPP has a reduced propensity to form fibrils, which requires H-bonds to be formed between the peptides in order to enable β -sheet formation.

3.4.4 Membrane Insertion Pathways

All-atom MD simulations allow to unravel the steps leading to the different peptide–membrane interactions in detail. An important aspect here is the high amount of hydrophobic residues present in IAPP, which give rise to an amphipathic helix when residues Q10 to L27 adopt an α -helix (**Figure 7A**). When such a helix binds to a membrane, it orients itself parallel to the membrane surface, with the hydrophobic side of this helix inserting into the hydrophobic core of the membrane, and the hydrophilic residues of the other side interacting with the lipid headgroups or the aqueous solvent (Christensen et al., 2021). This situation is visible for H18R-IAPP (**Figure 7B**). However, as the helix formed in this peptide only extends to S19, residues F23, I26 and L27 are not inserted into the membrane. **Figure 7B** further shows that the initial binding to the membrane is clearly driven by electrostatic interactions between the N-terminus and K1, which is followed by membrane insertion of the hydrophobic side of the amphipathic helix. This binding pattern is stabilized by interactions between R18 and the lipid headgroups, which is facilitated due to the length and flexibility of this side chain. For H18K-IAPP, the situation is similar, whereas in the case of hIAPP(H18+) the side chain is too short to enable strong interactions with the lipid headgroups. **Figure 7C** shows that this residue tends to be oriented toward the solvent. The interaction of hIAPP(H18+) with the membrane is dominated by K1, but the hydrophobic residues of the C-terminal side (F23, I26, and L27) can also insert into the membrane, yet without forming a helix. Alternatively, these three residues can form a hydrophobic cluster, which can give rise to a β -hairpin as seen for both hIAPP and hIAPP(H18+) (**Figure Figure 5**).

3.5 The Peptides Have No Noteworthy Effects on the Membrane Properties

With polarized ATR-FTIR spectroscopy, not only the secondary structure of the peptides can be probed, also the effect of the peptides on the organization of the lipidic membrane can be determined. This is possible by measuring the position of the bands corresponding to antisymmetric and symmetric stretching modes of the methylene groups of the lipid tails, ν_{as} (CH_2) and ν_s (CH_2) in the absence and in the presence of the peptides as well as the dichroic ratio (R_{ATR}) of the ν_s (CH_2) bands (**Table 3**) (Goormaghtigh et al., 1999). The wavenumbers of these bands are known to be sensitive to changes in the configuration of the acyl chains, in chain mobility, and packing. For the bilayer alone, ν_s (CH_2) and ν_{as} (CH_2) are 2854 and 2945 cm^{-1} , respectively, and the value of R_{ATR} is 1.28, which is characteristic for fluid and packed acyl chains. The addition of hIAPP to the bilayer does not significantly change the wavenumbers, while there is a slight

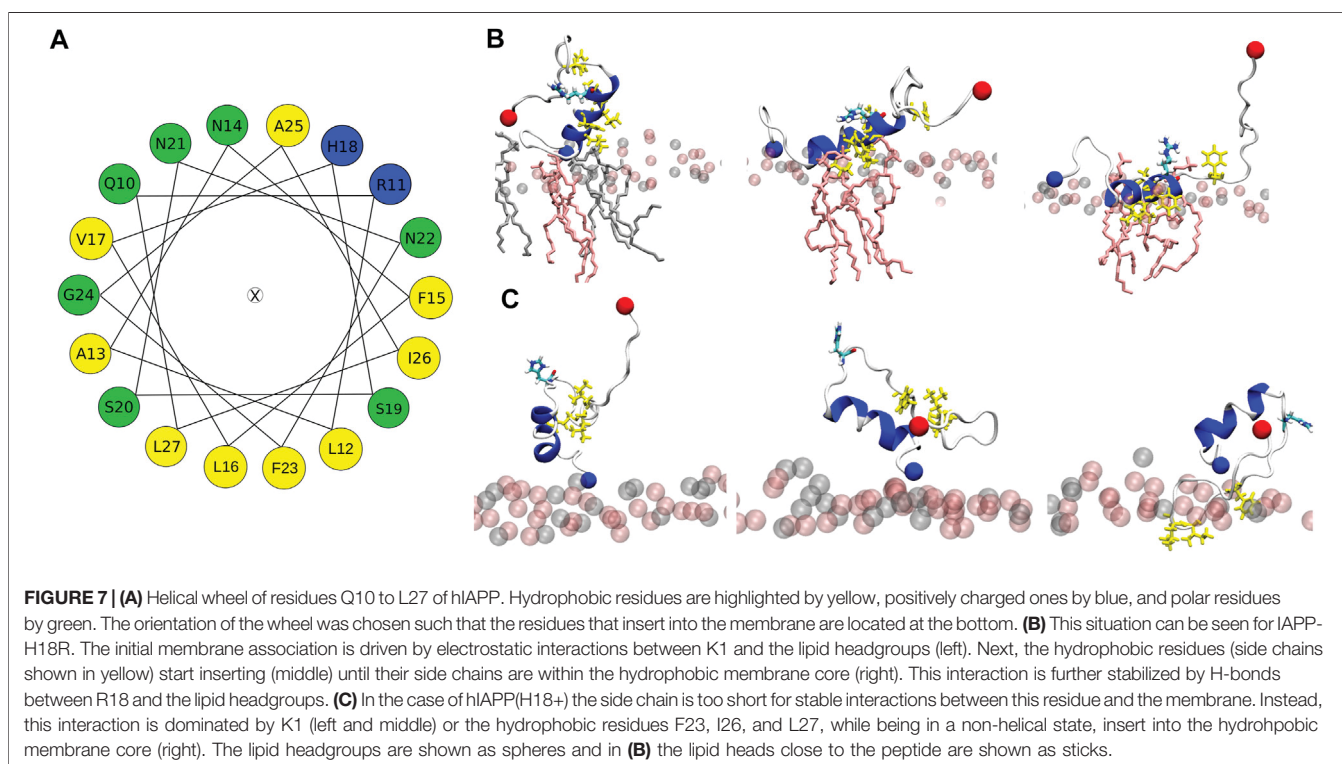


TABLE 3 | Wavenumbers and dichroic ratio for the methylene groups of the lipid chains in the absence and presence of IAPP peptides.

	$\nu_{as}(\text{CH}_2)$ (cm^{-1})	$\nu_s(\text{CH}_2)$ (cm^{-1})	$R_{ATR}(\nu_s(\text{CH}_2))$
Supported lipid bilayer	2924	2854	1.28 ± 0.07
+ hIAPP	2919	2851	1.34 ± 0.07
+ H18R-IAPP	2927	2855	1.29 ± 0.07
+ H18K-IAPP	2927	2855	1.27 ± 0.07
+ H18E-IAPP	2925	2854	1.26 ± 0.07
+ H18A-IAPP	2926	2855	1.20 ± 0.07

increase in R_{ATR} for the $\nu_s(\text{CH}_2)$ bands, which indicates a minor increase in disorder in the lipid chains. In contrast, in the presence of the mutated peptides, the wavenumbers are not modified, suggesting that these peptides do not or hardly affect the organization of the lipid bilayers. Thus, our results show that the mutated peptides do not alter the membrane properties during the first peptide-membrane interaction events, while hIAPP slightly increases the disorder in the membrane resulting from initial peptide insertions into the membrane.

This conclusion is supported by the analysis of the membrane bilayer properties from the MD simulations. From the mass density profiles of the DOPC and DOPS headgroups along the membrane z -axis we determined the average bilayer thickness as ≈ 4 nm. In order to assess whether the peptides affect the membrane properties, we analyzed the bilayer thickness around the membrane-associated peptides (**Supplementary Figure S4**). In these areas, reductions in the bilayer thickness of up to ≈ 0.1 nm are detected. However, hIAPP and H18A-IAPP

have only small to no effects on the bilayer thickness, suggesting that a charged amino acid at position 18 plays a role in causing membrane perturbations, especially when it enables membrane insertion. This is best seen for H18R- and H18K-IAPP that triggered the largest changes in membrane thickness, which are the same two peptides that inserted into the membrane during the simulations. For further characterization of the membrane properties, we calculated the order parameter of the C-H bonds in the lipid acyl chains (denoted as S_{CH}) for both DOPC and DOPS lipids. Here, we distinguished between lipids that are in the vicinity of the peptides (i.e., within 0.5 nm) and all other lipids, to observe whether the peptides can cause lipid disorder (**Supplementary Figure S5**). Similar S_{CH} profiles along the acyl chains (characterized by carbon number) are observed for DOPC and DOPS, with the order parameters of the latter being slightly higher. A strong drop in order is present at the double bonds positioned at carbon atom 10 of both palmitoyl and oleoyl chains of either lipid type. Most importantly, no notable change in lipid order due to the presence of any of the peptides is observed. This suggests that changes to the lipid thickness resulted only from the interactions between the peptides and the lipid headgroups, while the acyl chains are not affected as none of the peptides did insert deeply into the membrane core, maximally just below the headgroup region in the cases of H18R- and H18K-IAPP. Apart from hIAPP this agrees to the observations from the experiments, as also there the lipid tail packing was not affected by the peptides, suggesting that also in the experiments the peptides did not penetrate into the

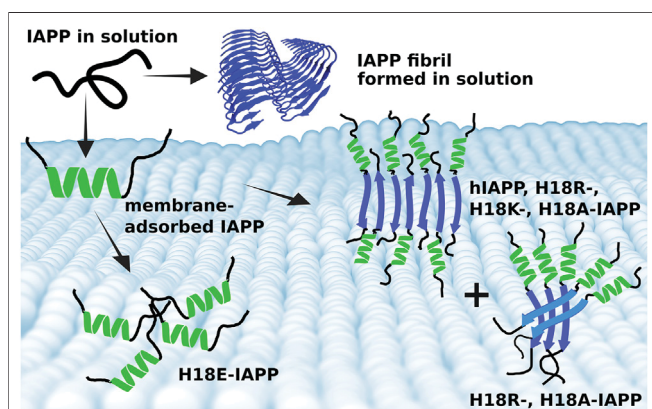


FIGURE 8 | Summary of the different IAPP-membrane interaction modes. (Top) In solution, IAPP is mainly intrinsically disordered and can aggregate into amyloid fibrils, which are characterized by parallel β -sheets (blue cartoon, produced from PDB entry 6Y1A (Röder et al., 2020)). (Bottom) On the membrane, IAPP adopts initially a helix (green), which is of amphipathic nature and hence tethers the peptide to the membrane. Following membrane binding, the peptides start aggregating where the structure, and size of the aggregates depend on the nature of residue 18. Wild-type hIAPP as well as H18R-, H18K-, and H18A-IAPP form fibrils with antiparallel β -sheets. However, there is also some helix and random coil present in these fibrillar structures, suggesting that the N-terminal and membrane-bound helix remains, while residues from S20 onward form an antiparallel β -sheet. This arrangement allows the fibrils to grow. In the case of a parallel β -sheet, on the other hand, the helices are too close to each other for fibril formation to take place. Instead, oligomers which appear as amorphous aggregates are formed, as observed for H18R- and H18A-IAPP. In the case of H18E-IAPP, no β -sheet formation takes place. Instead, random coil and helix are the prevailing secondary structures.

membrane core. Only in the case of hIAPP some minor changes in the acyl packing were recorded, indicating that in the experiments this peptide was able to notably reach beyond the headgroup region. Interestingly, this is the same peptide that formed the largest amounts of (antiparallel) β -sheets, suggesting that β -sheet formation and membrane insertion take place concurrently.

4 CONCLUSION

In the present study, ATR-FTIR and TEM experiments as well as all-atom MD simulations on the microsecond time scale have been performed to unravel the first structural changes of the islet amyloid polypeptide following its interaction with a lipid membrane. Moreover, the influence of residue 18 in this process was assessed by studying wild-type hIAPP and variants of it with mutations H18A, H18E, H18K, and H18R.

The secondary structure profiles from simulations suggest that initially the membrane-bound IAPP is mostly in a random coil conformation (≈ 30 – 40%) with some α -helices. All mutants show higher amounts of helix than hIAPP, especially H18K-IAPP ($\approx 45\%$) and H18A-IAPP ($\approx 38\%$). While alanine is commonly known to be a helix-promoting amino acid, also lysine has a high helix-forming propensity. The notably lower amounts in β -sheet in the simulations compared to what is observed experimentally is due to the different length and time scales that are assessed. The

simulations are limited to one peptide and one microsecond and, hence, focus on exploring the structural preferences of the IAPP monomers following membrane binding. On the time scale and with the temporal resolution of the experiments, on the other hand, peptide aggregation takes place to a certain extent; they therefore provide information on a changing mixture of monomers, oligomers and fibrils. The analysis of the ATR-FTIR spectra demonstrates that at the beginning of the experiments, the peptides are predominantly unstructured (35–50%) with contributions from α -helical structures (12% for H18E-IAPP and $\approx 20\%$ for the other peptides) and β -sheets (12–35%). During the course of 2 h of incubation, the ATR-FTIR spectra of hIAPP revealed an increase in the antiparallel β -sheet content and a reduction in the α -helical and random coil contents, and which is in agreement with the TEM images that revealed fibrils with typical amyloid morphology. Similar data as for hIAPP were obtained for H18K-IAPP that also experienced an increase in anti-parallel β -sheet content and exhibited typical amyloid fibrils. For H18R-IAPP and H18A-IAPP, both the ATR-FTIR spectra and TEM images indicate the presence of two species, one of them being structured in antiparallel β -sheets, and the other one involving parallel β -sheets. The TEM images further revealed two different supramolecular structures, thin and short fibrils as well as amorphous aggregates. We propose that the fibrils are composed of the antiparallel β -sheets, as seen for hIAPP and H18K-IAPP, while the amorphous aggregates contain parallel β -sheets. In all four peptides, the formation of β -sheets was accompanied by reductions in random coil, which was especially the case for hIAPP. The reductions in α -helix content were minor, with the helical amount remaining at 15–20%. H18E-IAPP is the only peptide for which no transitions into β -sheets were observed, neither in the ATR-FTIR spectra nor did fibrils occur in the TEM images. Instead, the amount of helix increased with time.

Based on these observations we suggest an aggregation scheme of membrane-adsorbed IAPP peptides as summarized in **Figure 8**. Considering that the amount of helix remains almost constant, or even increases in the case of H18E-IAPP, we assume that the initial membrane-anchoring helix in the N-terminal half of the peptide is very stable and resists the transformation into β -sheets. The simulations revealed that for all peptide variants this helix is located between residues Q10 and S19, but it generally does not involve all of these ten residues as this would amount to a helical content of more than 27%. The β -sheet formation is thus expected to take place in the C-terminal peptide region from residue S20 onwards. For several fragments of that region it has been shown that amyloid-fibril formation is possible. This especially applies to the region S20–S29, which is also considered the amyloid-core region of hIAPP. Solid-state NMR spectroscopy (Griffiths et al., 1995) and X-ray crystallography of microcrystals formed by hexa- or heptapeptides from that region (PDB entries 3DG1, 3DGJ, 5E61, and 5E5V) (Wiltzius et al., 2008, 2009; Soriaga et al., 2016) showed that these segments can form both antiparallel and parallel β -sheets, while for the fibrils formed in solution by full-length IAPP (**Figure 8**), only parallel β -sheets have been

reported (Röder et al., 2020; Gallardo et al., 2020; Cao et al., 2020). We thus conclude that for membrane-bound IAPP, the decision whether parallel β -sheets are formed in addition to antiparallel ones depends on the characteristics of the membrane-bound helix involving residue 18. In the case of antiparallel β -sheets, the helices are far enough away from each other (see **Figure 8**) that the nature of residue 18 does almost not matter, as this structure is adopted for all peptides but H18E-IAPP. In the latter case, the electrostatic repulsion arising from the interplay of E18 and the negative membrane-surface charges prevents an alignment of the helices for β -sheet formation to take place. For the occurrence of parallel β -sheets, the helices need to get even closer, as **Figure 8** shows. Such an arrangement seems only be possible for A18 and R18. While the former is not surprising given its small volume and neutral charge, the latter is more remarkable, especially when considering its similarity with K18 that did not yield parallel β -sheets. However, Lys and Arg are known to interact differently with lipid membranes: Arg attracts more phosphate and water in the membrane, and can form extensive hydrogen bonding with its five H-bond donors that stabilize Arg-phosphate clusters (Li et al., 2013). This should lead to an effective charge screening between the neighbored helices of H18R-IAPP. Nonetheless, it should be noted that, at the current stage, this is a hypothesis, which will be tested by our future studies.

Previous reports revealed that hIAPP and H18K-IAPP are toxic to β -cell lines (Khemtemourian et al., 2017). Based on our current observations, we suggest that the toxic hIAPP and H18K-IAPP species are those that are structured with antiparallel β -sheets, as different behaviors are observed for the other peptides. In the case of hIAPP, the joint analysis of the experimental and simulation data suggests that the β -sheet aggregates even started to insert into the lipid bilayers, causing membrane disorder, and which would explain their toxicity. The absence of pronounced β -sheet formation in the case of H18E-IAPP concurs with the previous finding that this peptide is the least toxic H18 mutant (Khemtemourian et al., 2017) and reinforces our hypothesis that cytotoxicity and the presence of antiparallel β -sheet structures are correlated in IAPP. For other amyloid proteins such correlation has already been demonstrated. Using a yeast amyloid from the HET-s prion domain of *Podospora anserina*, Cullin and coworkers showed that mutations within the HET-s prion domain give rise to antiparallel β -sheet structures and, at the same time, enhance the cytotoxicity (Berthelot et al., 2011). Other toxic amyloid-forming proteins also adopt an antiparallel β -sheet conformation, such as the amyloid- β peptide involved in Alzheimer's disease, and α -synuclein related to Parkinson's disease (Cerf et al., 2009; Celej et al., 2012), suggesting that the antiparallel β -sheet is a signature of amyloid toxicity.

Earlier studies indicated that hIAPP and the mutated peptides are able to induce membrane permeability (Hoffmann et al., 2018a). Here, we tested for possible membrane disorder induced by the peptide using both ATR-FTIR and MD simulations.

Consistent with previous MD studies, the peptides approach the membrane via their N-terminal residues (K1–R19) (Engel et al., 2006; Skeby et al., 2016). This interaction between peptide and membrane is mainly driven by electrostatic attractions between the positively charged residues K1 and R11 and the negatively charged lipid DOPS, which is strengthened when there is a third positive charge at position 18, as seen for H18K- and H18R-IAPP. However, hIAPP(H18+) did not interact more strongly with the membrane, suggesting that, in addition to the charge at residue 18, and also the size and/or flexibility of the side chain plays a role in affecting peptide–membrane interactions. In the simulations, the helical regions of H18K- and H18R-IAPP were able to insert into the membrane, adopting a parallel orientation with respect to the membrane surface where the hydrophobic side chains entered the hydrophobic membrane core and the hydrophilic side chains point in the opposite direction towards the aqueous phase. This orientation is stabilized by the long and flexible side chains of K1, R11, and K18 or R18. The ATR-FTIR results reflect that the mutated peptides H18R-, H18K-, H18E-, and H18A-IAPP do not alter the membrane properties during the initial peptide–membrane interactions, while hIAPP was able to slightly change the membrane properties. Since this is the peptide with the largest amount of β -sheets being formed, this suggests that β -sheets are needed for membrane disturbances. This conjecture is further supported by our MD data which revealed that the initial insertion of IAPP as a helix is only just below the headgroup region, which, apart from small effects on the membrane thickness around the peptide, does not change the lipid tail order. This agrees to the findings from the ATR-FTIR spectra. Hence, we conclude that apart from hIAPP, no deep insertions of the peptides into the membrane occurred in the current experiments. Various membrane damage mechanisms caused by hIAPP have been proposed and described in detail, which implicate the presence of large oligomers or fibrils and involve pore formation or lipid uptake (Engel, 2009). Our experimental and simulation results indicate that the initial IAPP aggregate species are not able to inflict such membrane destabilization.

In summary, the results of this study provide valuable molecular level insight into understanding of the initial IAPP–membrane interactions and demonstrate how mutations at residue 18 can affect this interaction and fibril formation of IAPP (**Figure 8**). We demonstrated that a single mutation of histidine 18 can yield vastly different results in terms aggregate morphology, membrane damage, and resulting toxicity, highlighting once again the importance of this residue in amyloid formation by hIAPP.

DATA AVAILABILITY STATEMENT

The original contributions presented in the study are included in the article/**Supplementary Material**, further inquiries can be directed to the corresponding authors.

AUTHOR CONTRIBUTIONS

LK designed the study. LK performed the TEM and analyzed the images. LK and BD performed the ATR-FTIR experiments; LK, SL, and SC analyzed the ATR-FTIR spectra. HF and BS designed the computer simulations. HF performed the simulations and analyzed them together with BS. LK, HF, and BS wrote the manuscript. All authors contributed to discussing the results and reviewing the manuscript.

FUNDING

HF and BS acknowledge funding for this project from the Palestinian-German Science Bridge financed by the German Federal Ministry of Education and Research.

REFERENCES

- Abedini, A., and Raleigh, D. P. (2009). A Critical Assessment of the Role of Helical Intermediates in Amyloid Formation by Natively Unfolded Proteins and Polypeptides. *Protein Eng. Des. Selection* 22, 453–459. doi:10.1093/protein/gzp036
- Abedini, A., and Raleigh, D. P. (2006). Destabilization of Human IAPP Amyloid Fibrils by Proline Mutations outside of the Putative Amyloidogenic Domain: Is There a Critical Amyloidogenic Domain in Human IAPP? *J. Mol. Biol.* 355, 274–281. doi:10.1016/j.jmb.2005.10.052
- Abraham, M. J., Murtola, T., Schulz, R., Páll, S., Smith, J. C., Hess, B., et al. (2015). GROMACS: High Performance Molecular Simulations through Multi-Level Parallelism from Laptops to Supercomputers. *SoftwareX* 1–2, 19–25. doi:10.1016/j.softx.2015.06.001
- Berendsen, H. J. C., Postma, J. P. M., van Gunsteren, W. F., DiNola, A., and Haak, J. R. (1984). Molecular Dynamics with Coupling to an External Bath. *J. Chem. Phys.* 81, 3684–3690. doi:10.1063/1.448118
- Berthelot, K., Ta, H. P., Géan, J., Lecomte, S., and Cullin, C. (2011). *In Vivo* and *In Vitro* Analyses of Toxic Mutants of Het-S: Ftir Antiparallel Signature Correlates with Amyloid Toxicity. *J. Mol. Biol.* 412, 137–152. doi:10.1016/j.jmb.2011.07.009
- Brender, J. R., Hartman, K., Reid, K. R., Kennedy, R. T., and Ramamoorthy, A. (2008a). A Single Mutation in the Nonamyloidogenic Region of Islet Amyloid Polypeptide Greatly Reduces Toxicity. *Biochemistry* 47, 12680–12688. doi:10.1021/bi801427c
- Brender, J. R., Lee, E. L., Cavitt, M. A., Gafni, A., Steel, D. G., and Ramamoorthy, A. (2008b). Amyloid Fiber Formation and Membrane Disruption Are Separate Processes Localized in Two Distinct Regions of IAPP, the Type-2-Diabetes-Related Peptide. *J. Am. Chem. Soc.* 130, 6424–6429. doi:10.1021/ja710484d
- Bussi, G., Donadio, D., and Parrinello, M. (2007). Canonical Sampling through Velocity Rescaling. *J. Chem. Phys.* 126, 014101. doi:10.1063/1.2408420
- Caillon, L., Hoffmann, A. R. F., Botz, A., and Khemtemourian, L. (2016/2016). Molecular Structure, Membrane Interactions, and Toxicity of the Islet Amyloid Polypeptide in Type 2 Diabetes Mellitus. *J. Diabetes Res.* 2016, 1–13. doi:10.1155/2016/5639875
- Caillon, L., Lequin, O., and Khemtemourian, L. (2013). Evaluation of Membrane Models and Their Composition for Islet Amyloid Polypeptide-Membrane Aggregation. *Biochim. Biophys. Acta (Bba) - Biomembranes* 1828, 2091–2098. doi:10.1016/j.bbame.2013.05.014
- Cao, P., Marek, P., Noor, H., Patsalo, V., Tu, L.-H., Wang, H., et al. (2013). Islet Amyloid: From Fundamental Biophysics to Mechanisms of Cytotoxicity. *FEBS Lett.* 587, 1106–1118. doi:10.1016/j.febslet.2013.01.046
- Cao, Q., Boyer, D. R., Sawaya, M. R., Ge, P., and Eisenberg, D. S. (2020). Cryo-em Structure and Inhibitor Design of Human IAPP (Amylin) Fibrils. *Nat. Struct. Mol. Biol.* 27, 653–659. doi:10.1038/s41594-020-0435-3
- Ceje, M. S., Sarrroukh, R., Goormaghtigh, E., Fidelio, G. D., Ruyschaert, J.-M., and Raussens, V. (2012). Toxic Prefibrillar α -synuclein Amyloid Oligomers Adopt a Distinctive Antiparallel β -sheet Structure. *Biochem. J.* 443, 719–726. doi:10.1042/bj20111924
- Cerf, E., Sarrroukh, R., Tamamizu-Kato, S., Breydo, L., Derclaye, S., Dufrêne, Y. F., et al. (2009). Antiparallel β -sheet: a Signature Structure of the Oligomeric Amyloid β -peptide. *Biochem. J.* 421, 415–423. doi:10.1042/bj20090379
- Choi, B., Kim, N. H., Jin, G. Y., Kim, Y. S., Kim, Y. H., and Eom, K. (2021). Sequence-dependent Aggregation-Prone Conformations of Islet Amyloid Polypeptide. *Phys. Chem. Chem. Phys.* 23, 22532–22542. doi:10.1039/D1CP01061A
- Christensen, M., Berglund, N. A., and Schiøtt, B. (2021). The Effect of Cholesterol on Membrane-Bound Islet Amyloid Polypeptide. *Front. Mol. Biosci.* 8, 657946. doi:10.3389/fmolb.2021.657946
- Cooper, G. J., Willis, A. C., Clark, A., Turner, R. C., Sim, R. B., and Reid, K. B. (1987). Purification and Characterization of a Peptide from Amyloid-Rich Pancreases of Type 2 Diabetic Patients. *Proc. Natl. Acad. Sci.* 84, 8628–8632. doi:10.1073/pnas.84.23.8628
- de Koning, E. J. P., Fleming, K. A., Gray, D. W. R., and Clark, A. (1995). High Prevalence of Pancreatic Islet Amyloid in Patients with End-Stage Renal Failure on Dialysis Treatment. *J. Pathol.* 175, 253–258. doi:10.1002/path.1711750214
- Despa, S., Margulies, K. B., Chen, L., Knowlton, A. A., Havel, P. J., Taegtmeier, H., et al. (2012). Hyperamylinemia Contributes to Cardiac Dysfunction in Obesity and Diabetes. *Circ. Res.* 110, 598–608. doi:10.1161/circresaha.111.258285
- Dignon, G. L., Zerbe, G. H., and Mittal, J. (2017a). Interplay between Membrane Composition and Structural Stability of Membrane-Bound HIAPP. *J. Phys. Chem. B* 121, 8661–8668. doi:10.1021/acs.jpcc.7b05689
- Dignon, G. L., Zerbe, G. H., and Mittal, J. (2017b). Interplay between Membrane Composition and Structural Stability of Membrane-Bound hIAPP. *J. Phys. Chem. B* 121, 8661–8668. doi:10.1021/acs.jpcc.7b05689
- Dong, X., Qiao, Q., Qian, Z., and Wei, G. (2018). Recent Computational Studies of Membrane Interaction and Disruption of Human Islet Amyloid Polypeptide: Monomers, Oligomers and Protofibrils. *Biochim. Biophys. Acta (Bba) - Biomembranes* 1860, 1826–1839. doi:10.1016/j.bbame.2018.03.006
- Engel, M. F. M., Khemtemourian, L., Kleijer, C. C., Meeldijk, H. J. D., Jacobs, J., Verkleij, A. J., et al. (2008). Membrane Damage by Human Islet Amyloid Polypeptide through Fibril Growth at the Membrane. *Proc. Natl. Acad. Sci.* 105, 6033–6038. doi:10.1073/pnas.0708354105
- Engel, M. F. M. (2009). Membrane Permeabilization by Islet Amyloid Polypeptide. *Chem. Phys. Lipids* 160, 1–10. doi:10.1016/j.chemphyslip.2009.03.008
- Engel, M. F. M., Yigittop, H., Elgersma, R. C., Rijkers, D. T. S., Liskamp, R. M. J., de Kruijff, B., et al. (2006). Islet Amyloid Polypeptide Inserts into Phospholipid Monolayers as Monomer. *J. Mol. Biol.* 356, 783–789. doi:10.1016/j.jmb.2005.12.020
- Evers, F., Jeworrek, C., Tiemeyer, S., Weise, K., Sellin, D., Paulus, M., et al. (2009). Elucidating the Mechanism of Lipid Membrane-Induced IAPP Fibrillogenesis and its Inhibition by the Red Wine Compound Resveratrol: A Synchrotron

ACKNOWLEDGMENTS

Christophe Piesse (Institut de Biologie Paris Seine, Université Pierre et Marie Curie, France) is acknowledged for the peptides synthesis. HF and BS gratefully acknowledge the computing time granted through JARA on the supercomputer JURECA at Forschungszentrum Jülich (project number JICS6C).

SUPPLEMENTARY MATERIAL

The Supplementary Material for this article can be found online at: <https://www.frontiersin.org/articles/10.3389/fmolb.2022.849979/full#supplementary-material>

- X-ray Reflectivity Study. *J. Am. Chem. Soc.* 131, 9516–9521. doi:10.1021/ja8097417
- Fox, A., Snollaerts, T., Errecart Casanova, C., Calciano, A., Nogaj, L. A., and Moffet, D. A. (2010). Selection for Nonamyloidogenic Mutants of Islet Amyloid Polypeptide (IAPP) Identifies an Extended Region for Amyloidogenicity. *Biochemistry* 49, 7783–7789. doi:10.1021/bi100337p
- Gallardo, R., Iadanza, M. G., Xu, Y., Heath, G. R., Foster, R., Radford, S. E., et al. (2020). Fibril Structures of Diabetes-Related Amylin Variants Reveal a Basis for Surface-Templated Assembly. *Nat. Struct. Mol. Biol.* 27, 1048–1056. doi:10.1038/s41594-020-0496-3
- Gao, M., and Winter, R. (2015). The Effects of Lipid Membranes, Crowding and Osmolytes on the Aggregation, and Fibrillation Propensity of Human Iapp. *J. Diabetes Res.* 2015, 1–21. doi:10.1155/2015/849017
- Goldsbury, C., Goldie, K., Pellaud, J., Seelig, J., Frey, P., Müller, S. A., et al. (2000). Amyloid Fibril Formation from Full-Length and Fragments of Amylin. *J. Struct. Biol.* 130, 352–362. doi:10.1006/jsbi.2000.4268
- Goormaghtigh, E., Cabiaux, V., and Ruyschaert, J.-M. (1994). Determination of Soluble and Membrane Protein Structure by Fourier Transform Infrared Spectroscopy. *Physicochemical methods in the study of biomembranes*, 405–450. doi:10.1007/978-1-4615-1863-1_10
- Goormaghtigh, E., Cabiaux, V., and Ruyschaert, J.-M. (1990). Secondary Structure and Dosage of Soluble and Membrane Proteins by Attenuated Total Reflection Fourier-Transform Infrared Spectroscopy on Hydrated Films. *Eur. J. Biochem.* 193, 409–420. doi:10.1111/j.1432-1033.1990.tb19354.x
- Goormaghtigh, E., Raussens, V., and Ruyschaert, J.-M. (1999). Attenuated Total Reflection Infrared Spectroscopy of Proteins and Lipids in Biological Membranes. *Biochim. Biophys. Acta (Bba) - Rev. Biomembranes* 1422, 105–185. doi:10.1016/s0304-4157(99)00004-0
- Griffiths, J. M., Ashburn, T. T., Auger, M., Costa, P. R., Griffin, R. G., and Lansbury, P. T., Jr (1995). Rotational Resonance Solid-State Nmr Elucidates a Structural Model of Pancreatic Amyloid. *J. Am. Chem. Soc.* 117, 3539–3546. doi:10.1021/ja00117a023
- Hebda, J. A., and Miranker, A. D. (2009). The Interplay of Catalysis and Toxicity by Amyloid Intermediates on Lipid Bilayers: Insights from Type II Diabetes. *Annu. Rev. Biophys.* 38, 125–152. doi:10.1146/annurev.biophys.050708.133622
- Hess, B., Bekker, H., Berendsen, H. J. C., and Fraaije, J. G. E. M. (1997). Lincs: a Linear Constraint Solver for Molecular Simulations. *J. Comput. Chem.* 18, 1463–1472. doi:10.1002/(sici)1096-987x(199709)18:12<1463:aid-jcc4>3.0.co;2-h
- Hoffmann, A. R. F., Caillon, L., Salazar Vazquez, L. S., Spath, P.-A., Carlier, L., Khemtemourian, L., et al. (2018b). Time Dependence of NMR Observables Reveals Salient Differences in the Accumulation of Early Aggregated Species between Human Islet Amyloid Polypeptide and Amyloid- β . *Phys. Chem. Chem. Phys.* 20, 9561–9573. doi:10.1039/C7CP07516B
- Hoffmann, A. R. F., Saravanan, M. S., Lequin, O., Killian, J. A., and Khemtemourian, L. (2018a). A Single Mutation on the Human Amyloid Polypeptide Modulates Fibril Growth and Affects the Mechanism of Amyloid-Induced Membrane Damage. *Biochim. Biophys. Acta (Bba) - Biomembranes* 1860, 1783–1792. doi:10.1016/j.bbame.2018.02.018
- Höppener, J. W. M., Ahrén, B., and Lips, C. J. M. (2000). Islet Amyloid and Type 2 Diabetes Mellitus. *N. Engl. J. Med.* 343, 411–419. doi:10.1056/NEJM200008103430607
- Huang, J., Rauscher, S., Nawrocki, G., Ran, T., Feig, M., de Groot, B. L., et al. (2017). CHARMM36m: an Improved Force Field for Folded and Intrinsically Disordered Proteins. *Nat. Methods* 14, 71–73. doi:10.1038/nmeth.4067
- Janson, J., Ashley, R. H., Harrison, D., McIntyre, S., and Butler, P. C. (1999). The Mechanism of Islet Amyloid Polypeptide Toxicity Is Membrane Disruption by Intermediate-Sized Toxic Amyloid Particles. *Diabetes* 48, 491–498. doi:10.2337/diabetes.48.3.491
- Jayasinghe, S. A., and Langen, R. (2005). Lipid Membranes Modulate the Structure of Islet Amyloid Polypeptide. *Biochemistry* 44, 12113–12119. doi:10.1021/bi050840w
- Jorgensen, W. L., Chandrasekhar, J., Madura, J. D., Impey, R. W., and Klein, M. L. (1983). Comparison of Simple Potential Functions for Simulating Liquid Water. *J. Chem. Phys.* 79, 926–935. doi:10.1063/1.445869
- Kabsch, W., and Sander, C. (1983). Dictionary of Protein Secondary Structure: Pattern Recognition of Hydrogen-Bonded and Geometrical Features. *Biopolymers* 22, 2577–2637. doi:10.1002/bip.360221211
- Kayed, R., Sokolov, Y., Edmonds, B., McIntire, T. M., Milton, S. C., Hall, J. E., et al. (2004). Permeabilization of Lipid Bilayers Is a Common Conformation-Dependent Activity of Soluble Amyloid Oligomers in Protein Misfolding Diseases. *J. Biol. Chem.* 279, 46363–46366. doi:10.1074/jbc.C400260200
- Khemtemourian, L., Antoniciello, F., Sahoo, B. R., Decossas, M., Lecomte, S., and Ramamoorthy, A. (2021). Investigation of the Effects of Two Major Secretory Granules Components, Insulin and Zinc, on Human-Iapp Amyloid Aggregation and Membrane Damage. *Chem. Phys. Lipids* 237, 105083. doi:10.1016/j.chemphyslip.2021.105083
- Khemtemourian, L., Engel, M. F. M., Liskamp, R. M. J., Höppener, J. W. M., and Killian, J. A. (2010). The N-Terminal Fragment of Human Islet Amyloid Polypeptide Is Non-fibrillogenic in the Presence of Membranes and Does Not Cause Leakage of Bilayers of Physiologically Relevant Lipid Composition. *Biochim. Biophys. Acta (Bba) - Biomembranes* 1798, 1805–1811. doi:10.1016/j.bbame.2010.05.022
- Khemtemourian, L., Guillemin, G., Foufelle, F., and Killian, J. A. (2017). Residue Specific Effects of Human Islet Polypeptide Amyloid on Self-Assembly and on Cell Toxicity. *Biochimie* 142, 22–30. doi:10.1016/j.biochi.2017.07.015
- Klauda, J. B., Venable, R. M., Freites, J. A., O'Connor, J. W., Tobias, D. J., Mondragon-Ramirez, C., et al. (2010). Update of the CHARMM All-Atom Additive Force Field for Lipids: Validation on Six Lipid Types. *J. Phys. Chem. B* 114, 7830–7843. doi:10.1021/jp101759q
- Knowles, T. P. J., Vendruscolo, M., and Dobson, C. M. (2014). The Amyloid State and its Association with Protein Misfolding Diseases. *Nat. Rev. Mol. Cell Biol.* 15, 384–396. doi:10.1038/nrm3810
- Lee, J., Cheng, X., Swails, J. M., Yeom, M. S., Eastman, P. K., Lemkul, J. A., et al. (2016). CHARMM-GUI Input Generator for NAMD, GROMACS, AMBER, OpenMM, and CHARMM/OpenMM Simulations Using the CHARMM36 Additive Force Field. *J. Chem. Theor. Comput.* 12, 405–413. doi:10.1021/acs.jctc.5b00935
- Li, L., Vorobyov, I., and Allen, T. W. (2013). The Different Interactions of Lysine and Arginine Side Chains with Lipid Membranes. *J. Phys. Chem. B* 117, 11906–11920. doi:10.1021/jp405418y
- Ling, Y. L., Strasfeld, D. B., Shim, S.-H., Raleigh, D. P., and Zanni, M. T. (2009). Two-dimensional Infrared Spectroscopy Provides Evidence of an Intermediate in the Membrane-Catalyzed Assembly of Diabetic Amyloid. *J. Phys. Chem. B* 113, 2498–2505. doi:10.1021/jp810261x
- Liu, Y., Zhang, D., Zhang, Y., Tang, Y., Xu, L., He, H., et al. (2020). Molecular Dynamics Simulations of Cholesterol Effects on the Interaction of Hiapp with Lipid Bilayer. *J. Phys. Chem. B* 124, 7830–7841. doi:10.1021/acs.jpcc.0c05742
- Lutz, T. A. (2010). The Role of Amylin in the Control of Energy Homeostasis. *Am. J. Physiology-Regulatory, Integr. Comp. Physiol.* 298, R1475–R1484. doi:10.1152/ajpregu.00703.2009
- Martel, A., Antony, L., Gerelli, Y., Porcar, L., Fluit, A., Hoffmann, K., et al. (2016). Membrane Permeation versus Amyloidogenicity: A Multitechnique Study of Islet Amyloid Polypeptide Interaction with Model Membranes. *J. Am. Chem. Soc.* 139, 137–148. doi:10.1021/jacs.6b06985
- Mei, L., Shen, W., Wu, X., Liu, J., Li, D., and Ji, B. (2020). Interactions of Human Islet Amyloid Polypeptide with Lipid Structure of Different Curvatures. *Theor. Appl. Mech. Lett.* 10, 412–418. doi:10.1016/j.taml.2020.01.053
- Milardi, D., Gazit, E., Radford, S. E., Xu, Y., Gallardo, R. U., Caffisch, A., et al. (2021). Proteostasis of Islet Amyloid Polypeptide: a Molecular Perspective of Risk Factors and Protective Strategies for Type II Diabetes. *Chem. Rev.* 121, 1845–1893. doi:10.1021/acs.chemrev.0c00981
- Miller, Y. (2022). Advancements and Future Directions in Research of the Roles of Insulin in Amyloid Diseases. *Biophysical Chem.* 281, 106720. doi:10.1016/j.bpc.2021.106720
- Mirzabekov, T. A., Lin, M.-C., and Kagan, B. L. (1996). Pore Formation by the Cytotoxic Islet Amyloid Peptide Amylin. *J. Biol. Chem.* 271, 1988–1992. doi:10.1074/jbc.271.4.1988
- Mishra, R., Bulic, B., Sellin, D., Jha, S., Waldmann, H., and Winter, R. (2008). Small-molecule Inhibitors of Islet Amyloid Polypeptide Fibril Formation. *Angew. Chem.* 120, 4757–4760. doi:10.1002/ange.200705372
- Mishra, R., and Winter, R. (2008). Cold- and Pressure-Induced Dissociation of Protein Aggregates and Amyloid Fibrils. *Angew. Chem. Int. Ed.* 47, 6518–6521. doi:10.1002/anie.200802027
- Nanga, R. P. R., Brender, J. R., Vivekanandan, S., and Ramamoorthy, A. (2011). Structure and Membrane Orientation of Iapp in its Natively Amidated Form at

- Physiological Ph in a Membrane Environment. *Biochim. Biophys. Acta (Bba) - Biomembranes* 1808, 2337–2342. doi:10.1016/j.bbmem.2011.06.012
- Nguyen, P. H., Ramamoorthy, A., Sahoo, B. R., Zheng, J., Fallor, P., Straub, J. E., et al. (2021). Amyloid Oligomers: A Joint Experimental/Computational Perspective on Alzheimer's Disease, Parkinson's Disease, Type II Diabetes, and Amyotrophic Lateral Sclerosis. *Chem. Rev.* 121, 2545–2647. doi:10.1021/acs.chemrev.0c01122
- Opie, E. L. (1901). The Relation Of Diabetes Mellitus to Lesions of the Pancreas. Hyaline Degeneration of the Islands Of Langerhans. *J. Exp. Med.* 5, 527–540. doi:10.1084/jem.5.5.527
- Patil, S. M., Xu, S., Sheftic, S. R., and Alexandrescu, A. T. (2009). Dynamic α -Helix Structure of Micelle-Bound Human Amylin. *J. Biol. Chem.* 284, 11982–11991. doi:10.1074/jbc.m809085200
- Poojari, C., Xiao, D., Batista, V. S., and Strodel, B. (2013). Membrane Permeation Induced by Aggregates of Human Islet Amyloid Polypeptides. *Biophysical J.* 105, 2323–2332. doi:10.1016/j.bpj.2013.09.045
- Press-Sandler, O., and Miller, Y. (2018). Molecular Mechanisms of Membrane-Associated Amyloid Aggregation: Computational Perspective and Challenges. *Biochim. Biophys. Acta (Bba) - Biomembranes* 1860, 1889–1905. doi:10.1016/j.bbmem.2018.03.014
- Qian, Z., Zou, Y., Zhang, Q., Chen, P., Ma, B., Wei, G., et al. (2018). Atomistic-level Study of the Interactions between Hiapp Protofibrils and Membranes: Influence of Ph and Lipid Composition. *Biochim. Biophys. Acta (Bba) - Biomembranes* 1860, 1818–1825. doi:10.1016/j.bbmem.2018.02.005
- Qiao, Q., Wei, G., Yao, D., and Song, Z. (2019). Formation of α -helical and β -sheet Structures in Membrane-Bound Human IAPP Monomer and the Resulting Membrane Deformation. *Phys. Chem. Chem. Phys.* 21, 20239–20251. doi:10.1039/c9cp03151k
- Quist, A., Doudevski, I., Lin, H., Azimova, R., Ng, D., Frangione, B., et al. (2005). Amyloid Ion Channels: A Common Structural Link for Protein-Misfolding Disease. *Proc. Natl. Acad. Sci.* 102, 10427–10432. doi:10.1073/pnas.0502066102
- Radovan, D., Smirnovas, V., and Winter, R. (2008). Effect of Pressure on Islet Amyloid Polypeptide Aggregation: Revealing the Polymorphic Nature of the Fibrillation Process. *Biochemistry* 47, 6352–6360. doi:10.1021/bi800503j
- Röder, C., Kupreichyk, T., Gremer, L., Schäfer, L. U., Pothula, K. R., Ravelli, R. B. G., et al. (2020). Cryo-EM Structure of Islet Amyloid Polypeptide Fibrils Reveals Similarities with Amyloid- β Fibrils. *Nat. Struct. Mol. Biol.* 27, 660–667. doi:10.1038/s41594-020-0442-4
- Rodriguez Camargo, D. C., Tripsianes, K., Buday, K., Franko, A., Göbl, C., Hartlmüller, C., et al. (2017). The Redox Environment Triggers Conformational Changes and Aggregation of hIAPP in Type II Diabetes. *Sci. Rep.* 7, 44041. doi:10.1038/srep44041
- Rouser, G., Fleischer, S., and Yamamoto, A. (1970). Two Dimensional Thin Layer Chromatographic Separation of Polar Lipids and Determination of Phospholipids by Phosphorus Analysis of Spots. *Lipids* 5, 494–496. doi:10.1007/bf02531316
- Rustenbeck, I., Matthies, A., and Lenzen, S. (1994). Lipid Composition of Glucose-Stimulated Pancreatic Islets and Insulin-Secreting Tumor Cells. *Lipids* 29, 685–692. doi:10.1007/bf02538912
- Seeliger, J., Weise, K., Opitz, N., and Winter, R. (2012). The Effect of A β on IAPP Aggregation in the Presence of an Isolated β -Cell Membrane. *J. Mol. Biol.* 421, 348–363. doi:10.1016/j.jmb.2012.01.048
- Selkoe, D. J. (2004). Erratum: Folding Proteins in Fatal Ways. *Nature* 428, 445. doi:10.1038/nature02477
- Sepehri, A., Nepal, B., and Lazaridis, T. (2021). Distinct Modes of Action of Iapp Oligomers on Membranes. *J. Chem. Inf. Model.* 61, 4645–4655. doi:10.1021/acs.jcim.1c00767
- Skeby, K. K., Andersen, O. J., Pogorelov, T. V., Tajkhorshid, E., and Schiøtt, B. (2016). Conformational Dynamics of the Human Islet Amyloid Polypeptide in a Membrane Environment: Toward the Aggregation Prone Form. *Biochemistry* 55, 2031–2042. doi:10.1021/acs.biochem.5b00507
- Soriaga, A. B., Sangwan, S., Macdonald, R., Sawaya, M. R., and Eisenberg, D. (2016). Crystal Structures of Iapp Amyloidogenic Segments Reveal a Novel Packing Motif of Out-Of-Register Beta Sheets. *J. Phys. Chem. B* 120, 5810–5816. doi:10.1021/acs.jpcc.5b09981
- Sparr, E., Engel, M. F. M., Sakharov, D. V., Sprong, M., Jacobs, J., de Kruijff, B., et al. (2004). Islet Amyloid Polypeptide-Induced Membrane Leakage Involves Uptake of Lipids by Forming Amyloid Fibers. *FEBS Lett.* 577, 117–120. doi:10.1016/j.febslet.2004.09.075
- Srodulski, S., Sharma, S., Bachstetter, A. B., Brelsfoard, J. M., Pascual, C., Xie, X. S., et al. (2014). Neuroinflammation and Neurologic Deficits in Diabetes Linked to Brain Accumulation of Amylin. *Mol. Neurodegeneration* 9, 30. doi:10.1186/1750-1326-9-30
- Tu, L.-H., and Raleigh, D. P. (2013). Role of Aromatic Interactions in Amyloid Formation by Islet Amyloid Polypeptide. *Biochemistry* 52, 333–342. doi:10.1021/bi3014278
- Westermarck, P., Andersson, A., and Westermarck, G. T. (2011). Islet Amyloid Polypeptide, Islet Amyloid, and Diabetes Mellitus. *Physiol. Rev.* 91, 795–826. doi:10.1152/physrev.00042.2009
- Westermarck, P., Wernstedt, C., Wilander, E., Hayden, D. W., O'Brien, T. D., and Johnson, K. H. (1987). Amyloid Fibrils in Human Insulinoma and Islets of Langerhans of the Diabetic Cat Are Derived from a Neuropeptide-like Protein Also Present in normal Islet Cells. *Proc. Natl. Acad. Sci.* 84, 3881–3885. doi:10.1073/pnas.84.11.3881
- Willbold, D., Strodel, B., Schröder, G. F., Hoyer, W., and Heise, H. (2021). Amyloid-type Protein Aggregation and Prion-like Properties of Amyloids. *Chem. Rev.* 121, 8285–8307. doi:10.1021/acs.chemrev.1c00196
- Williamson, J. A., and Miranker, A. D. (2007). Direct Detection of Transient α -helical States in Islet Amyloid Polypeptide. *Protein Sci.* 16, 110–117. doi:10.1110/ps.062486907
- Wiltzius, J. J. W., Sievers, S. A., Sawaya, M. R., Cascio, D., Popov, D., Riek, C., et al. (2008). Atomic Structure of the Cross- β Spine of Islet Amyloid Polypeptide (Amylin). *Protein Sci.* 17, 1467–1474. doi:10.1110/ps.036509.108
- Wiltzius, J. J. W., Sievers, S. A., Sawaya, M. R., and Eisenberg, D. (2009). Atomic Structures of Iapp (Amylin) Fusions Suggest a Mechanism for Fibrillation and the Role of Insulin in the Process. *Protein Sci.* 18, 1521–1530. doi:10.1002/pro.145
- Wineman-Fisher, V., and Miller, Y. (2016). Effect of Zn²⁺ Ions on the Assembly of Amylin Oligomers: Insight into the Molecular Mechanisms. *Phys. Chem. Chem. Phys.* 18, 21590–21599. doi:10.1039/C6CP04105A
- Zhang, X., St. Clair, J. R. J., London, E., and Raleigh, D. P. (2017). Islet Amyloid Polypeptide Membrane Interactions: Effects of Membrane Composition. *Biochemistry* 56, 376–390. doi:10.1021/acs.biochem.6b01016
- Zhang, Y., Luo, Y., Deng, Y., Mu, Y., and Wei, G. (2012). Lipid Interaction and Membrane Perturbation of Human Islet Amyloid Polypeptide Monomer and Dimer by Molecular Dynamics Simulations. *PLOS ONE* 7, e38191. doi:10.1371/journal.pone.0038191

Conflict of Interest: The authors declare that the research was conducted in the absence of any commercial or financial relationships that could be construed as a potential conflict of interest.

Publisher's Note: All claims expressed in this article are solely those of the authors and do not necessarily represent those of their affiliated organizations, or those of the publisher, the editors and the reviewers. Any product that may be evaluated in this article, or claim that may be made by its manufacturer, is not guaranteed or endorsed by the publisher.

Copyright © 2022 Khemtemourian, Fatafta, Davion, Lecomte, Castano and Strodel. This is an open-access article distributed under the terms of the Creative Commons Attribution License (CC BY). The use, distribution or reproduction in other forums is permitted, provided the original author(s) and the copyright owner(s) are credited and that the original publication in this journal is cited, in accordance with accepted academic practice. No use, distribution or reproduction is permitted which does not comply with these terms.

Supplementary Material

Structural dissection of the first events following membrane binding of the islet amyloid polypeptide

Lucie Khemtemourian^{1,*}, Hebah Fatafta^{2,3}, Benoit Davion¹, Sophie Lecomte¹, Sabine Castano¹ and Birgit Strodel^{2,3,4,*}

¹ Université de Bordeaux, CNRS, Bordeaux INP, CBMN, UMR 5248, F-33600 Pessac, France.

² Institute of Biological Information Processing: Structural Biochemistry, Forschungszentrum Jülich, 52428 Jülich, Germany.

³ JuStruct, Jülich Center for Structural Biology, Forschungszentrum Jülich, 52428 Jülich, Germany

⁴ Institute of Theoretical and Computational Chemistry, Heinrich Heine University Düsseldorf, 40225 Düsseldorf, Germany.

* Corresponding Authors: lucie.khemtemourian@u-bordeaux.fr, b.strodel@fz-juelich.de

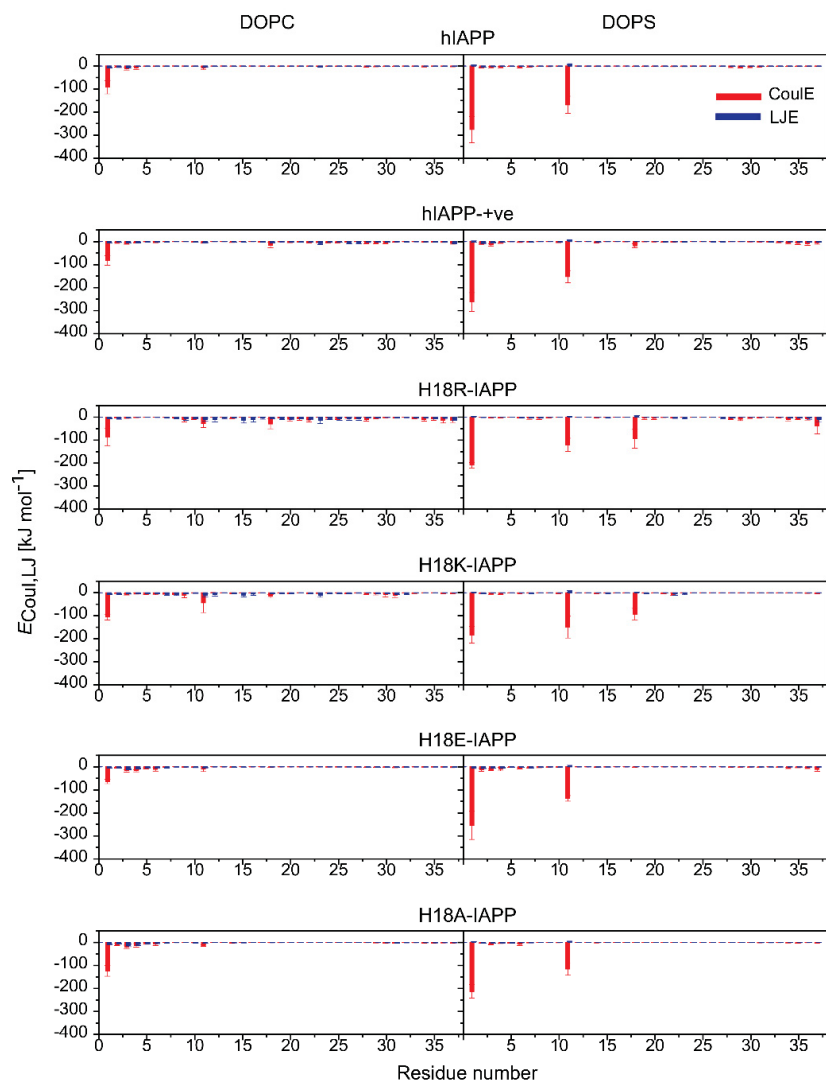


Figure S1: The average interaction energies (and standard error) of IAPP interacting with DOPC (left) and DOPS (right) lipids. Electrostatic and Lennard-Jones energies are shown in red and blue, respectively. Negative energies indicate attractive forces, positive energies correspond to repulsion.

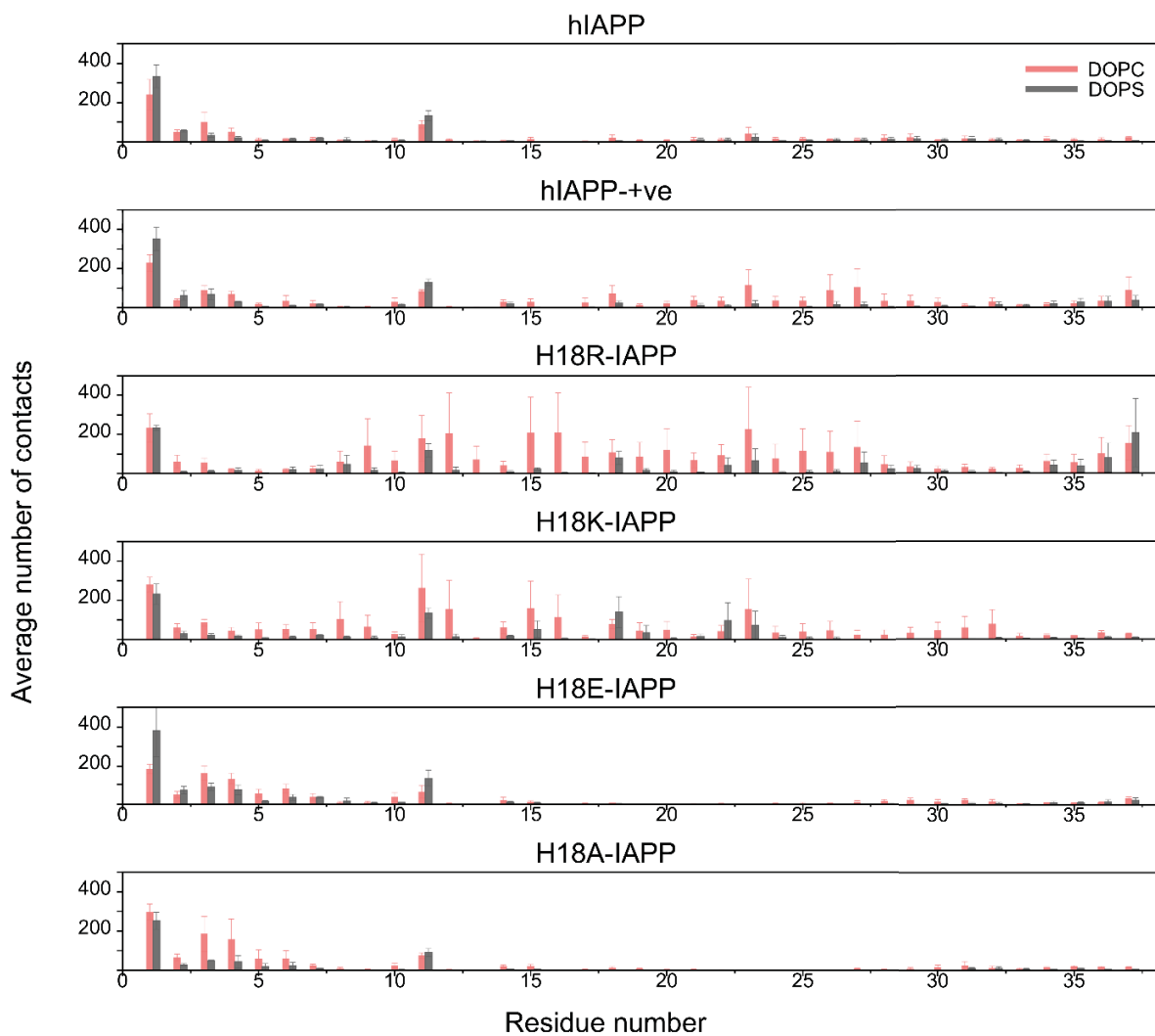


Figure S2: The average number of IAPP-lipid contacts (and standard error) for DOPC (pink) and DOPS (gray) lipids.

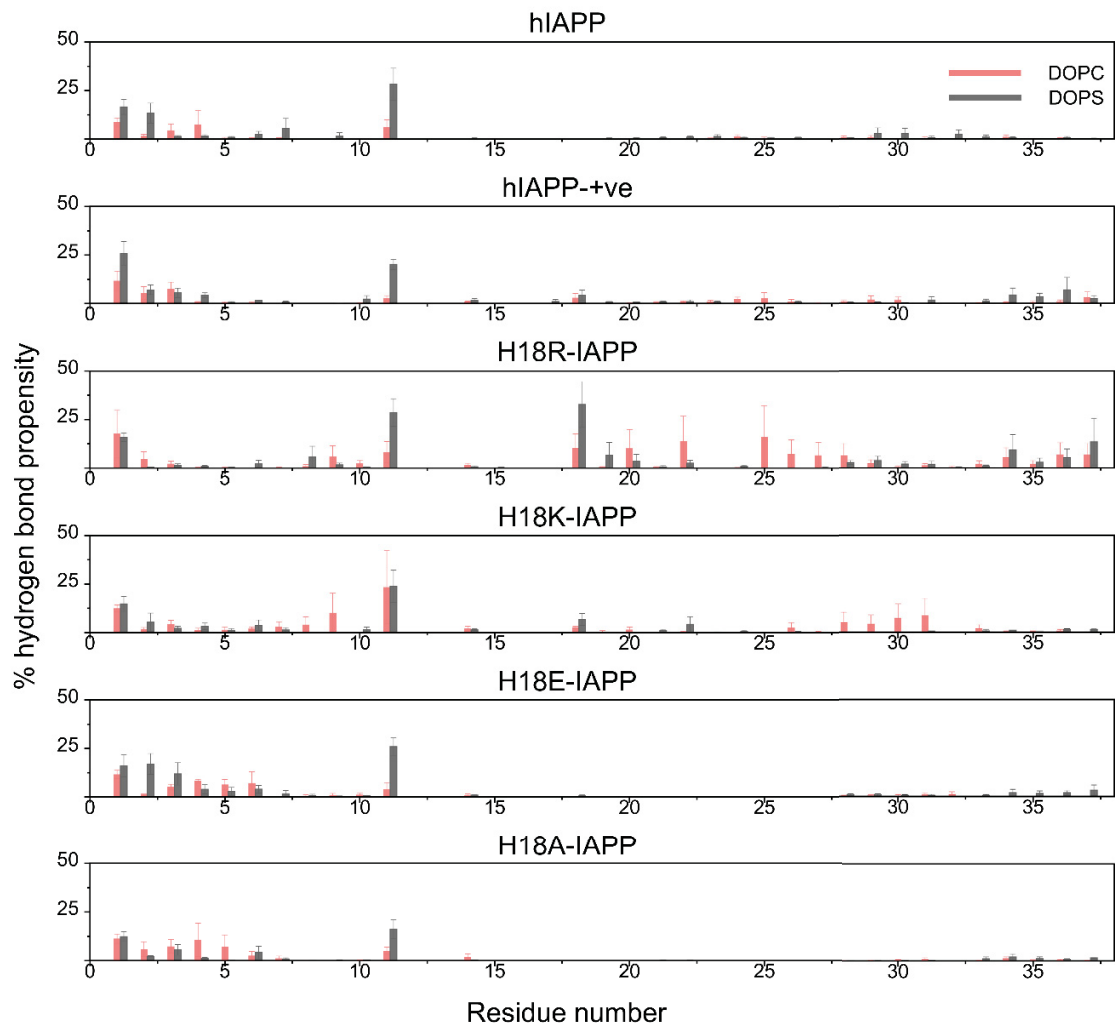


Figure S3: The average hydrogen bond propensity (and standard error) between IAPP and DOPC (pink) and DOPS (gray) lipids.

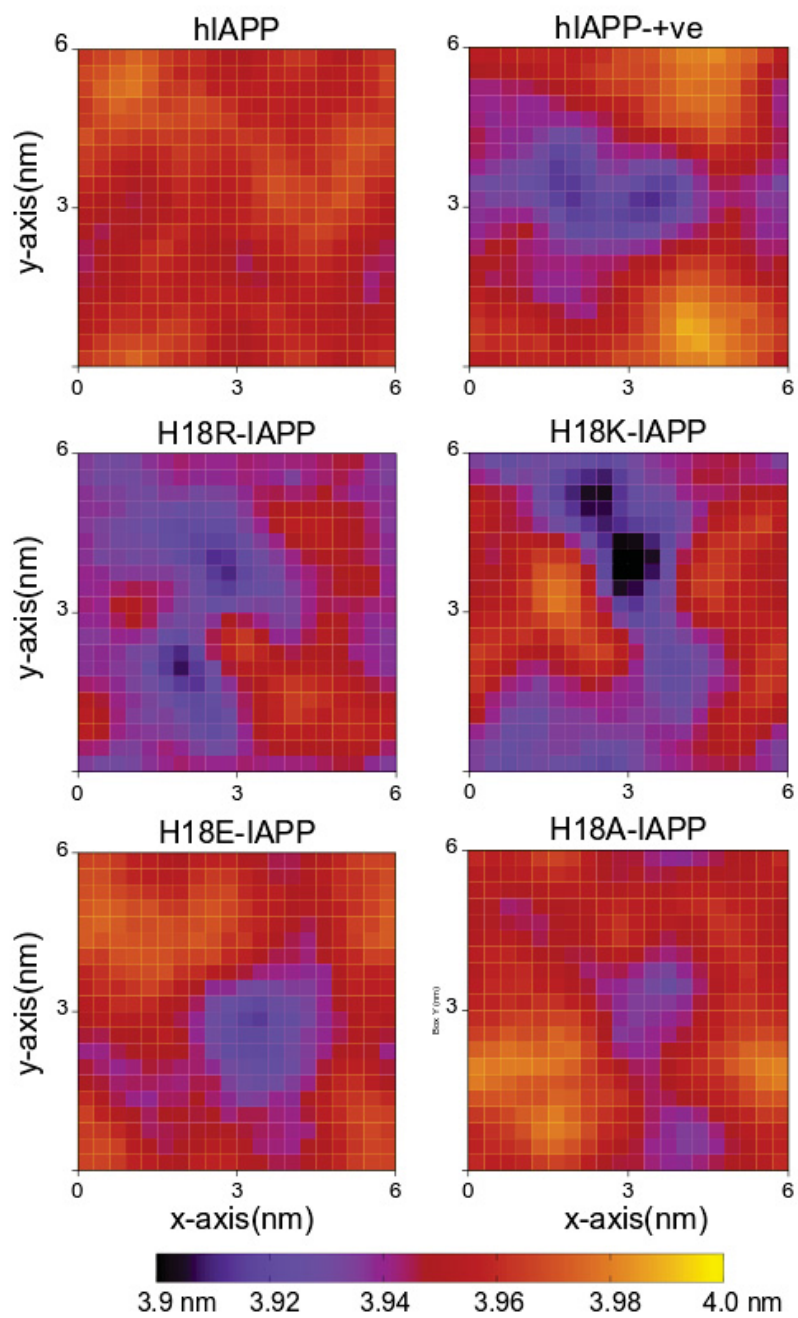


Figure S4: Average bilayer thickness calculated for the MD frames where the peptide is within 0.5 nm of the membrane. The x- and the y-axes represent the unit cell dimension in nm. The color bar shows the thickness range in nm.

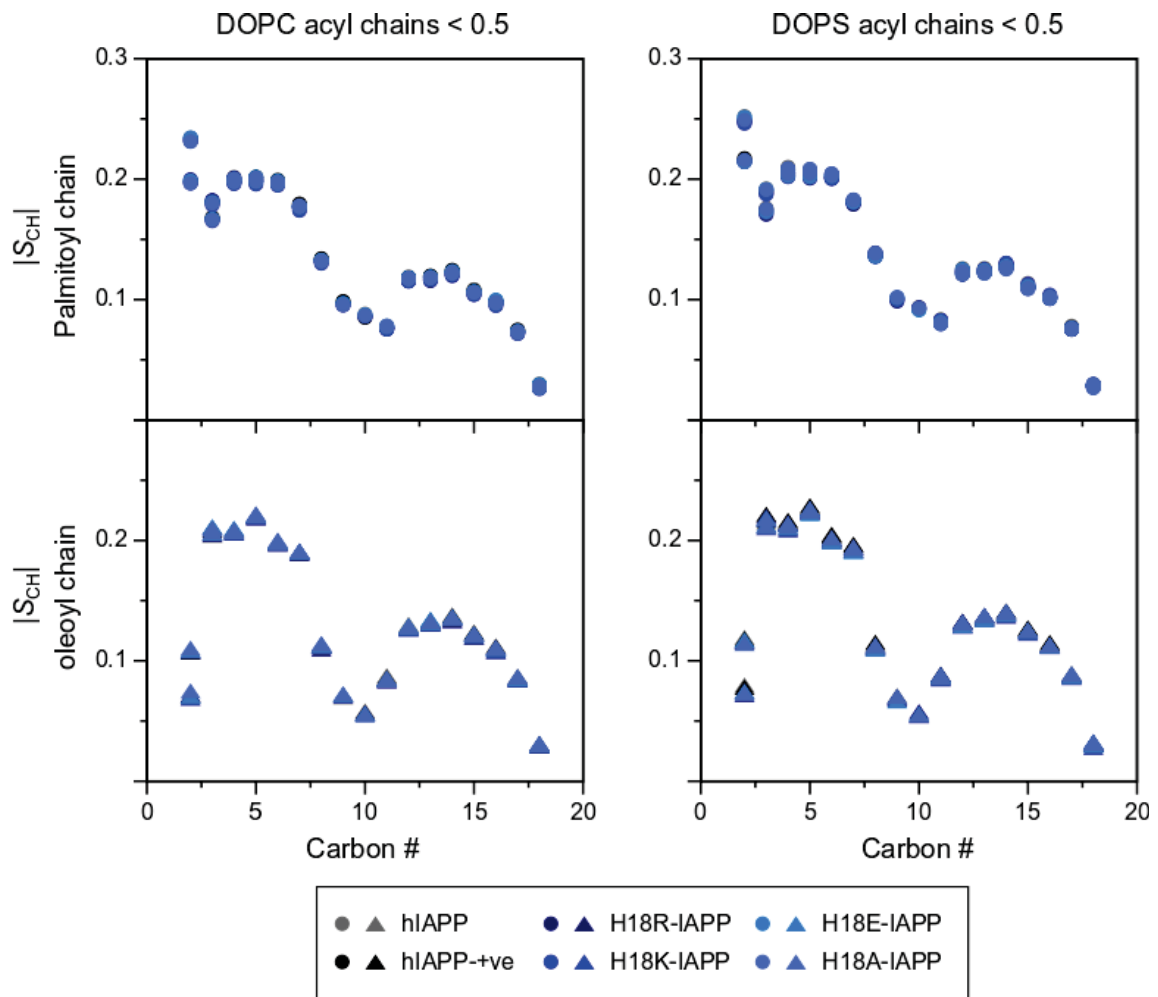


Figure S5: Average order parameters of the acyl chains (top: palmitoyl chains; bottom: oleyl chains) of DOPC (left) and DOPS (right) lipids.

Bibliography

- [1] Ken A Dill, S Banu Ozkan, M Scott Shell, and Thomas R Weikl. The protein folding problem. *Annu. Rev. Biophys.*, 37:289–316, 2008.
- [2] Eszter Herczenik and Martijn FBG Gebbink. Molecular and cellular aspects of protein misfolding and disease. *The FASEB Journal*, 22(7):2115–2133, 2008.
- [3] Niels Gregersen, Peter Bross, Søren Vang, and Jane H Christensen. Protein misfolding and human disease. *Annu. Rev. Genomics Hum. Genet.*, 7:103–124, 2006.
- [4] Claudio Soto and Lisbell D Estrada. Protein misfolding and neurodegeneration. *Archives of neurology*, 65(2):184–189, 2008.
- [5] F Ulrich Hartl. Protein misfolding diseases. *Annual review of biochemistry*, 86: 21–26, 2017.
- [6] Jennifer J McManus, Patrick Charbonneau, Emanuela Zaccarelli, and Neer Asherie. The physics of protein self-assembly. *Current opinion in colloid & interface science*, 22:73–79, 2016.
- [7] Dan Li and Cong Liu. Structural diversity of amyloid fibrils and advances in their structure determination. *Biochemistry*, 59(5):639–646, 2020.
- [8] Anthony WP Fitzpatrick and Helen R Saibil. Cryo-em of amyloid fibrils and cellular aggregates. *Current opinion in structural biology*, 58:34–42, 2019.
- [9] Katie J Wolfe and Douglas M Cyr. Amyloid in neurodegenerative diseases: friend or foe? In *Seminars in cell & developmental biology*, volume 22, pages 476–481. Elsevier, 2011.

- [10] Matthew G Iadanza, Matthew P Jackson, Eric W Hewitt, Neil A Ranson, and Sheena E Radford. A new era for understanding amyloid structures and disease. *Nature Reviews Molecular Cell Biology*, 19(12):755–773, 2018.
- [11] Ghulam M Ashraf, Nigel H Greig, Taqi A Khan, Iftekhar Hassan, Shams Tabrez, Shazi Shakil, Ishfaq A Sheikh, Syed K Zaidi, Mohammad Akram, Nasimudeen R Jabir, et al. Protein misfolding and aggregation in alzheimer’s disease and type 2 diabetes mellitus. *CNS & Neurological Disorders-Drug Targets (Formerly Current Drug Targets-CNS & Neurological Disorders)*, 13(7):1280–1293, 2014.
- [12] Nadeeja Wijesekara, Rosemary Ahrens, Miheer Sabale, Ling Wu, Kathy Ha, Giuseppe Verdile, and Paul E Fraser. Amyloid- β and islet amyloid pathologies link alzheimer’s disease and type 2 diabetes in a transgenic model. *The FASEB Journal*, 31(12):5409–5418, 2017.
- [13] Vladimir N Uversky. Introduction to intrinsically disordered proteins (idps). *Chemical reviews*, 114(13):6557–6560, 2014.
- [14] Jianhan Chen and Richard W Kriwacki. Intrinsically disordered proteins: structure, function and therapeutics. *Journal of molecular biology*, 430(16):2275, 2018.
- [15] Vladimir N Uversky. Intrinsically disordered proteins from a to z. *The international journal of biochemistry & cell biology*, 43(8):1090–1103, 2011.
- [16] Ursula Jakob, Richard Kriwacki, and Vladimir N Uversky. Conditionally and transiently disordered proteins: awakening cryptic disorder to regulate protein function. *Chemical reviews*, 114(13):6779–6805, 2014.
- [17] Monika Fuxreiter and Peter Tompa. Fuzzy complexes: a more stochastic view of protein function. *Fuzziness*, pages 1–14, 2012.
- [18] Prakash Kulkarni and Vladimir N Uversky. Intrinsically disordered proteins in chronic diseases, 2019.
- [19] Paola Mendoza-Espinosa, Victor García-González, Abel Moreno, Rolando Castillo, and Jaime Mas-Oliva. Disorder-to-order conformational transitions in protein structure and its relationship to disease. *Molecular and cellular biochemistry*, 330(1):105–120, 2009.

- [20] David Eisenberg and Mathias Jucker. The amyloid state of proteins in human diseases. *Cell*, 148(6):1188–1203, 2012.
- [21] Fabrizio Chiti and Christopher M Dobson. Protein misfolding, amyloid formation, and human disease: a summary of progress over the last decade. *Annual review of biochemistry*, 86:27–68, 2017.
- [22] Massimo Stefani. Protein aggregation diseases: toxicity of soluble prefibrillar aggregates and their clinical significance. *Protein Misfolding and Cellular Stress in Disease and Aging*, pages 25–41, 2010.
- [23] Massimo Stefani and Christopher M Dobson. Protein aggregation and aggregate toxicity: new insights into protein folding, misfolding diseases and biological evolution. *Journal of molecular medicine*, 81(11):678–699, 2003.
- [24] Tuomas PJ Knowles, Michele Vendruscolo, and Christopher M Dobson. The amyloid state and its association with protein misfolding diseases. *Nature reviews Molecular cell biology*, 15(6):384–396, 2014.
- [25] Dennis J Selkoe. Folding proteins in fatal ways. *Nature*, 426(6968):900–904, 2003.
- [26] Ronald Wetzel. Kinetics and thermodynamics of amyloid fibril assembly. *Accounts of chemical research*, 39(9):671–679, 2006.
- [27] Ravindra Kodali and Ronald Wetzel. Polymorphism in the intermediates and products of amyloid assembly. *Current opinion in structural biology*, 17(1):48–57, 2007.
- [28] Guo-fang Chen, Ting-hai Xu, Yan Yan, Yu-ren Zhou, Yi Jiang, Karsten Melcher, and H Eric Xu. Amyloid beta: structure, biology and structure-based therapeutic development. *Acta Pharmacologica Sinica*, 38(9):1205–1235, 2017.
- [29] Alistair Burns and Steve Iliffe. Alzheimer’s disease. *Bmj*, 338, 2009.
- [30] Verena H FINDER. Alzheimer’s disease: a general introduction and pathomechanism. *Journal of Alzheimer’s disease*, 22(s3):S5–S19, 2010.
- [31] Sagar H Barage and Kailas D Sonawane. Amyloid cascade hypothesis: Pathogenesis and therapeutic strategies in alzheimer’s disease. *Neuropeptides*, 52:1–18, 2015.

- [32] Gunnar K Gouras, Tomas T Olsson, and Oskar Hansson. β -amyloid peptides and amyloid plaques in alzheimer's disease. *Neurotherapeutics*, 12(1):3–11, 2015.
- [33] Reisuke H Takahashi, Toshitaka Nagao, and Gunnar K Gouras. Plaque formation and the intraneuronal accumulation of β -amyloid in alzheimer's disease. *Pathology international*, 67(4):185–193, 2017.
- [34] Ralf Dahm. Alzheimer's discovery. *Current Biology*, 16(21):R906–R910, 2006.
- [35] Pei-Pei Liu, Yi Xie, Xiao-Yan Meng, and Jian-Sheng Kang. History and progress of hypotheses and clinical trials for alzheimer's disease. *Signal transduction and targeted therapy*, 4(1):1–22, 2019.
- [36] John A Hardy and Gerald A Higgins. Alzheimer's disease: the amyloid cascade hypothesis. *Science*, 256(5054):184–186, 1992.
- [37] Richard P Cheng, Samuel H Gellman, and William F DeGrado. β -peptides: from structure to function. *Chemical reviews*, 101(10):3219–3232, 2001.
- [38] Thorsten Lührs, Christiane Ritter, Marc Adrian, Dominique Riek-Loher, Bernd Bohrmann, Heinz Döbeli, David Schubert, and Roland Riek. 3d structure of alzheimer's amyloid- β (1–42) fibrils. *Proceedings of the National Academy of Sciences*, 102(48):17342–17347, 2005.
- [39] Miriam A Kael, Daniel K Weber, Frances Separovic, and Marc-Antoine Sani. Aggregation kinetics in the presence of brain lipids of $a\beta$ (1–40) cleaved from a soluble fusion protein. *Biochimica et Biophysica Acta (BBA)-Biomembranes*, 1860(9):1681–1686, 2018.
- [40] Karen E Marshall, Devkee M Vadukul, Liza Dahal, Alina Theisen, Milena W Fowler, Youssra Al-Hilaly, Lenzie Ford, György Kemenes, Iain J Day, Kevin Staras, et al. A critical role for the self-assembly of amyloid- β 1-42 in neurodegeneration. *Scientific reports*, 6(1):1–13, 2016.
- [41] Kenjiro Ono, Margaret M Condrón, and David B Teplow. Structure–neurotoxicity relationships of amyloid β -protein oligomers. *Proceedings of the National Academy of Sciences*, 106(35):14745–14750, 2009.

- [42] Omar MA El-Agnaf, Devinder S Mahil, Bhroma P Patel, and Brian M Austen. Oligomerization and toxicity of β -amyloid-42 implicated in alzheimer's disease. *Biochemical and biophysical research communications*, 273(3):1003–1007, 2000.
- [43] Mark A Findeis. The role of amyloid β peptide 42 in alzheimer's disease. *Pharmacology & therapeutics*, 116(2):266–286, 2007.
- [44] Catriona A McLean, Robert A Cherny, Fiona W Fraser, Stephanie J Fuller, Margaret J Smith, Konrad Vbeyreuther, Ashley I Bush, and Colin L Masters. Soluble pool of $\alpha\beta$ amyloid as a determinant of severity of neurodegeneration in alzheimer's disease. *Annals of neurology*, 46(6):860–866, 1999.
- [45] Marina D Kirkitadze, Gal Bitan, and David B Teplow. Paradigm shifts in alzheimer's disease and other neurodegenerative disorders: the emerging role of oligomeric assemblies. *Journal of neuroscience research*, 69(5):567–577, 2002.
- [46] Kerensa Broersen, Frederic Rousseau, and Joost Schymkowitz. The culprit behind amyloid beta peptide related neurotoxicity in alzheimer's disease: oligomer size or conformation? *Alzheimer's research & therapy*, 2(4):1–14, 2010.
- [47] Andreas Müller-Schiffmann, Arne Herring, Laila Abdel-Hafiz, Aisa N Chepkova, Sandra Schäble, Diana Wedel, Anselm HC Horn, Heinrich Sticht, Maria A de Souza Silva, Kurt Gottmann, et al. Amyloid- β dimers in the absence of plaque pathology impair learning and synaptic plasticity. *Brain*, 139(2):509–525, 2016.
- [48] Gunnar Brinkmalm, Wei Hong, Zemin Wang, Wen Liu, Tiernan T O'Malley, Xin Sun, Matthew P Frosch, Dennis J Selkoe, Erik Portelius, Henrik Zetterberg, et al. Identification of neurotoxic cross-linked amyloid- β dimers in the alzheimer's brain. *Brain*, 142(5):1441–1457, 2019.
- [49] Per Westermark, Arne Andersson, and Gunilla T Westermark. Islet amyloid polypeptide, islet amyloid, and diabetes mellitus. *Physiological reviews*, 91(3):795–826, 2011.
- [50] Lucy Marzban, Kirily Park, and C Bruce Verchere. Islet amyloid polypeptide and type 2 diabetes. *Experimental gerontology*, 38(4):347–351, 2003.
- [51] Rehana Akter, Ping Cao, Harris Noor, Zachary Ridgway, Ling-Hsien Tu, Hui Wang, Amy G Wong, Xiaoxue Zhang, Andisheh Abedini, Ann Marie Schmidt,

- et al. Islet amyloid polypeptide: structure, function, and pathophysiology. *Journal of diabetes research*, 2016, 2016.
- [52] Ali Chaari and Moncef Ladjimi. Human islet amyloid polypeptide (hiapp) aggregation in type 2 diabetes: Correlation between intrinsic physicochemical properties of hiapp aggregates and their cytotoxicity. *International journal of biological macromolecules*, 136:57–65, 2019.
- [53] Leena Haataja, Tatyana Gurlo, Chang J Huang, and Peter C Butler. Islet amyloid in type 2 diabetes, and the toxic oligomer hypothesis. *Endocrine reviews*, 29(3):303–316, 2008.
- [54] Jeffrey R Brender, Samer Salamekh, and Ayyalusamy Ramamoorthy. Membrane disruption and early events in the aggregation of the diabetes related peptide iapp from a molecular perspective. *Accounts of chemical research*, 45(3):454–462, 2012.
- [55] Ping Cao, Peter Marek, Harris Noor, Vadim Patsalo, Ling-Hsien Tu, Hui Wang, Andisheh Abedini, and Daniel P Raleigh. Islet amyloid: from fundamental biophysics to mechanisms of cytotoxicity. *FEBS letters*, 587(8):1106–1118, 2013.
- [56] Maarten FM Engel. Membrane permeabilization by islet amyloid polypeptide. *Chemistry and physics of lipids*, 160(1):1–10, 2009.
- [57] Maarten FM Engel, Lucie Khemtémourian, Cécile C Kleijer, Hans JD Meeldijk, Jet Jacobs, Arie J Verkleij, Ben de Kruijff, J Antoinette Killian, and Jo WM Höppener. Membrane damage by human islet amyloid polypeptide through fibril growth at the membrane. *Proceedings of the National Academy of Sciences*, 105(16):6033–6038, 2008.
- [58] Helen Watson. Biological membranes. *Essays in biochemistry*, 59:43–69, 2015.
- [59] Doralicia Casares, Pablo V Escribá, and Catalina Ana Rosselló. Membrane lipid composition: Effect on membrane and organelle structure, function and compartmentalization and therapeutic avenues. *International journal of molecular sciences*, 20(9):2167, 2019.
- [60] Evert Gorter and FJEM Grendel. On bimolecular layers of lipoids on the chromocytes of the blood. *The Journal of experimental medicine*, 41(4):439, 1925.

- [61] KÜBRA TUĞÇE KALKAN and MUKADDES EŞREFOĞLU. The cell membrane: a historical narration. 2020.
- [62] S Jonathan Singer and Garth L Nicolson. The fluid mosaic model of the structure of cell membranes. *Science*, 175(4023):720–731, 1972.
- [63] Gerrit Van Meer, Dennis R Voelker, and Gerald W Feigenson. Membrane lipids: where they are and how they behave. *Nature reviews Molecular cell biology*, 9(2):112–124, 2008.
- [64] Robert Ernst, Christer S Ejsing, and Bruno Antonny. Homeoviscous adaptation and the regulation of membrane lipids. *Journal of molecular biology*, 428(24):4776–4791, 2016.
- [65] Richard M Epanand. Introduction to membrane lipids. In *Methods in membrane lipids*, pages 1–6. Springer, 2015.
- [66] Lawrence I Rothfield. *Structure and function of biological membranes*. Academic Press, 2014.
- [67] William Stillwell. *An introduction to biological membranes: composition, structure and function*. Elsevier, 2016.
- [68] Anthony G Lee. Biological membranes: the importance of molecular detail. *Trends in biochemical sciences*, 36(9):493–500, 2011.
- [69] Sajad Moradi, Amin Nowroozi, and Mohsen Shahlaei. Shedding light on the structural properties of lipid bilayers using molecular dynamics simulation: A review study. *RSC advances*, 9(8):4644–4658, 2019.
- [70] Heidi Koldsø, David Shorthouse, Jean Hélie, and Mark SP Sansom. Lipid clustering correlates with membrane curvature as revealed by molecular simulations of complex lipid bilayers. *PLoS computational biology*, 10(10):e1003911, 2014.
- [71] Helgi I Ingólfsson, Timothy S Carpenter, Harsh Bhatia, Peer-Timo Bremer, Siewert J Marrink, and Felice C Lightstone. Computational lipidomics of the neuronal plasma membrane. *Biophysical journal*, 113(10):2271–2280, 2017.
- [72] Michele FM Sciacca, Carmelo Tempa, Federica Scollo, Danilo Milardi, and Carmelo La Rosa. Amyloid growth and membrane damage: Current themes and

- emerging perspectives from theory and experiments on a β and hiapp. *Biochimica et Biophysica Acta (BBA)-Biomembranes*, 1860(9):1625–1638, 2018.
- [73] Adam El Saghir, Gianluca Farrugia, and Neville Vassallo. The human islet amyloid polypeptide in protein misfolding disorders: Mechanisms of aggregation and interaction with biomembranes. *Chemistry and Physics of Lipids*, 234:105010, 2021.
- [74] Eduardo J Fernandez-Perez, Christian Peters, and Luis G Aguayo. Membrane damage induced by amyloid beta and a potential link with neuroinflammation. *Current pharmaceutical design*, 22(10):1295–1304, 2016.
- [75] Krithika Rajagopalan, Ruoyi Qiu, Steven M Mooney, Shweta Rao, Takumi Shiraiishi, Elizabeth Sacho, Hongying Huang, Ellen Shapiro, Keith R Weninger, and Prakash Kulkarni. The stress-response protein prostate-associated gene 4, interacts with c-jun and potentiates its transactivation. *Biochimica et Biophysica Acta (BBA)-Molecular Basis of Disease*, 1842(2):154–163, 2014.
- [76] Prakash Kulkarni, Mohit Kumar Jolly, Dongya Jia, Steven M Mooney, Ajay Bhargava, Luciane T Kagohara, Yihong Chen, Pengyu Hao, Yanan He, Robert W Veltri, et al. Phosphorylation-induced conformational dynamics in an intrinsically disordered protein and potential role in phenotypic heterogeneity. *Proceedings of the National Academy of Sciences*, 114(13):E2644–E2653, 2017.
- [77] Xingcheng Lin, Prakash Kulkarni, Federico Bocci, Nicholas P Schafer, Susmita Roy, Min-Yeh Tsai, Yanan He, Yihong Chen, Krithika Rajagopalan, Steven M Mooney, et al. Structural and dynamical order of a disordered protein: Molecular insights into conformational switching of page4 at the systems level. *Biomolecules*, 9(2):77, 2019.
- [78] D Parker, K Ferreri, T Nakajima, VJ LaMorte, R Evans, SC Koerber, C Hoeger, and MR Montminy. Phosphorylation of creb at ser-133 induces complex formation with creb-binding protein via a direct mechanism. *Molecular and cellular biology*, 16(2):694–703, 1996.
- [79] David Parker, Morris Rivera, Tsaffir Zor, Alexandra Henrion-Caude, Ishwar Radhakrishnan, Alok Kumar, Linda H Shapiro, Peter E Wright, Marc Montminy, and

- Paul K Brindle. Role of secondary structure in discrimination between constitutive and inducible activators. *Molecular and cellular biology*, 19(8):5601–5607, 1999.
- [80] Hao Liu, Xiang Guo, Jingcheng Han, Ray Luo, and Hai-Feng Chen. Order-disorder transition of intrinsically disordered kinase inducible transactivation domain of creb. *The Journal of chemical physics*, 148(22):225101, 2018.
- [81] Amos D Korczyn. The amyloid cascade hypothesis. *Alzheimer's & dementia*, 4(3):176–178, 2008.
- [82] Christiane Reitz. Alzheimer's disease and the amyloid cascade hypothesis: a critical review. *International journal of Alzheimer's disease*, 2012, 2012.
- [83] Erika N Cline, Maíra Assunção Bicca, Kirsten L Viola, and William L Klein. The amyloid- β oligomer hypothesis: beginning of the third decade. *Journal of Alzheimer's Disease*, 64(s1):S567–S610, 2018.
- [84] Federica Scollo, Carmelo Tempra, Fabio Lolicato, Michele FM Sciacca, Antonio Raudino, Danilo Milardi, and Carmelo La Rosa. Phospholipids critical micellar concentrations trigger different mechanisms of intrinsically disordered proteins interaction with model membranes. *The journal of physical chemistry letters*, 9(17):5125–5129, 2018.
- [85] Federica Scollo and Carmelo La Rosa. Amyloidogenic intrinsically disordered proteins: new insights into their self-assembly and their interaction with membranes. *Life*, 10(8):144, 2020.
- [86] Michele F Sciacca, Fabio Lolicato, Carmelo Tempra, Federica Scollo, Bikash R Sahoo, Matthew D Watson, Sara García-Viñuales, Danilo Milardi, Antonio Raudino, Jennifer C Lee, et al. Lipid-chaperone hypothesis: A common molecular mechanism of membrane disruption by intrinsically disordered proteins. *ACS chemical neuroscience*, 11(24):4336–4350, 2020.
- [87] Carmelo La Rosa, Silvia Scalisi, Fabio Lolicato, Martina Pannuzzo, and Antonio Raudino. Lipid-assisted protein transport: A diffusion-reaction model supported by kinetic experiments and molecular dynamics simulations. *The Journal of chemical physics*, 144(18):184901, 2016.

- [88] Malena B Rone, Jinjiang Fan, and Vassilios Papadopoulos. Cholesterol transport in steroid biosynthesis: role of protein–protein interactions and implications in disease states. *Biochimica et Biophysica Acta (BBA)-Molecular and Cell Biology of Lipids*, 1791(7):646–658, 2009.
- [89] Jaspreet Sandhu, Shiqian Li, Louise Fairall, Simon G Pfisterer, Jennifer E Gurnett, Xu Xiao, Thomas A Weston, Dipti Vashi, Alessandra Ferrari, Jose L Orozco, et al. Aster proteins facilitate nonvesicular plasma membrane to er cholesterol transport in mammalian cells. *Cell*, 175(2):514–529, 2018.
- [90] Magda SC Abreu, Luís MBB Estronca, Maria João Moreno, and Winchil LC Vaz. Binding of a fluorescent lipid amphiphile to albumin and its transfer to lipid bilayer membranes. *Biophysical journal*, 84(1):386–399, 2003.
- [91] Gabriele Pizzino, Natasha Irrera, Mariapaola Cucinotta, Giovanni Pallio, Federica Mannino, Vincenzo Arcoraci, Francesco Squadrito, Domenica Altavilla, and Alessandra Bitto. Oxidative stress: harms and benefits for human health. *Oxidative medicine and cellular longevity*, 2017, 2017.
- [92] Graham J Burton and Eric Jauniaux. Oxidative stress. *Best practice & research Clinical obstetrics & gynaecology*, 25(3):287–299, 2011.
- [93] Katerina Krumova and Gonzalo Cosa. Overview of reactive oxygen species. 2016.
- [94] Carlo M Bergamini, Stefania Gambetti, Alessia Dondi, and Carlo Cervellati. Oxygen, reactive oxygen species and tissue damage. *Current pharmaceutical design*, 10(14):1611–1626, 2004.
- [95] TPA Devasagayam, JC Tilak, KK Bloor, Ketaki S Sane, Saroj S Ghaskadbi, and RD Lele. Free radicals and antioxidants in human health: current status and future prospects. *Japi*, 52(794804):4, 2004.
- [96] Mustafa Taha Mohammed, Sura Mohammed Kadhim, AM Noori Jassimand, and SI Abbas. Free radicals and human health. *International Journal of Innovation Sciences and Research*, 4(6):218–223, 2015.
- [97] Martin D Brand, Charles Affourtit, Telma C Esteves, Katherine Green, Adrian J Lambert, Satomi Miwa, Julian L Pakay, and Nadeene Parker. Mitochondrial superoxide: production, biological effects, and activation of uncoupling proteins.

- Free Radical Biology and Medicine*, 37(6):755–767, 2004. ISSN 0891-5849. doi: <https://doi.org/10.1016/j.freeradbiomed.2004.05.034>.
- [98] Julio F. Turrens. Mitochondrial formation of reactive oxygen species. *The Journal of Physiology*, 552(2):335–344, 2003. doi: <https://doi.org/10.1111/j.1469-7793.2003.00335.x>.
- [99] Julio F Turrens. Mitochondrial formation of reactive oxygen species. *The Journal of physiology*, 552(2):335–344, 2003.
- [100] Praveen Krishnamurthy and Ashish Wadhvani. Antioxidant enzymes and human health. *Antioxidant enzyme*, 3:1–17, 2012.
- [101] Saikat Sen and Raja Chakraborty. The role of antioxidants in human health. In *Oxidative stress: diagnostics, prevention, and therapy*, pages 1–37. ACS Publications, 2011.
- [102] Esra Birben, Umit Murat Sahiner, Cansin Sackesen, Serpil Erzurum, and Omer Kalayci. Oxidative stress and antioxidant defense. *World Allergy Organization Journal*, 5(1):9–19, 2012.
- [103] Hemant Kumar, Hyung-Woo Lim, Sandeep Vasant More, Byung-Wook Kim, Sushruta Koppula, In Su Kim, and Dong-Kug Choi. The role of free radicals in the aging brain and parkinson’s disease: Convergence and parallelism. *International Journal of Molecular Sciences*, 13(8):10478–10504, 2012. ISSN 1422-0067. doi: [10.3390/ijms130810478](https://doi.org/10.3390/ijms130810478).
- [104] C Cheignon, M Tomas, D Bonnefont-Rousselot, P Faller, Christelle Hureau, and F Collin. Oxidative stress and the amyloid beta peptide in alzheimer’s disease. *Redox Biol.*, 14:450–464, 2018.
- [105] M.Y. Aksenov, M.V. Aksenova, D.A. Butterfield, J.W. Geddes, and W.R. Markesbery. Protein oxidation in the brain in alzheimer’s disease. *Neuroscience*, 103(2): 373–383, 2001. ISSN 0306-4522. doi: [https://doi.org/10.1016/S0306-4522\(00\)00580-7](https://doi.org/10.1016/S0306-4522(00)00580-7).

- [106] Xinglong Wang, Wenzhang Wang, Li Li, George Perry, Hyoung-gon Lee, and Xiongwei Zhu. Oxidative stress and mitochondrial dysfunction in alzheimer's disease. *Biochimica et Biophysica Acta (BBA)-Molecular Basis of Disease*, 1842(8):1240–1247, 2014.
- [107] Xinglong Wang, Wenzhang Wang, Li Li, George Perry, Hyoung gon Lee, and Xiongwei Zhu. Oxidative stress and mitochondrial dysfunction in alzheimer's disease. *Biochimica et Biophysica Acta (BBA) - Molecular Basis of Disease*, 1842(8):1240–1247, 2014. ISSN 0925-4439. doi: <https://doi.org/10.1016/j.bbadis.2013.10.015>. Misfolded Proteins, Mitochondrial Dysfunction, and Neurodegenerative Diseases.
- [108] Rukhsana Sultana, Marzia Perluigi, and D Allan Butterfield. Protein oxidation and lipid peroxidation in brain of subjects with alzheimer's disease: insights into mechanism of neurodegeneration from redox proteomics. *Antioxidants & redox signaling*, 8(11-12):2021–2037, 2006.
- [109] D Allan Butterfield and Christopher M Lauderback. Lipid peroxidation and protein oxidation in alzheimer's disease brain: potential causes and consequences involving amyloid β -peptide-associated free radical oxidative stress. *Free Radical Biology and Medicine*, 32(11):1050–1060, 2002.
- [110] Danielle G. Smith, Roberto Cappai, and Kevin J. Barnham. The redox chemistry of the alzheimer's disease amyloid peptide. *Biochimica et Biophysica Acta (BBA) - Biomembranes*, 1768(8):1976–1990, 2007. ISSN 0005-2736. doi: <https://doi.org/10.1016/j.bbamem.2007.02.002>. Amyloidogenic Protein–Membrane Interaction.
- [111] Yan Zhao and Baolu Zhao. Oxidative stress and the pathogenesis of alzheimer's disease. *Oxid. Med. Cell. Longevity*, 2013:No. 316523, 2013.
- [112] Velia Minicozzi, Francesco Stellato, Massimiliano Comai, Mauro Dalla Serra, Cristina Potrich, Wolfram Meyer-Klaucke, and Silvia Morante. Identifying the minimal copper-and zinc-binding site sequence in amyloid- β peptides. *J. Biol. Chem.*, 283(16):10784–10792, 2008.
- [113] T Marino, N Russo, M Toscano, and M Pavelka. On the metal ion (zn^{2+} , cu^{2+}) coordination with beta-amyloid peptide: Dft computational study. *Interdiscip. Sci.: Comput. Life Sci.*, 2(1):57–69, 2010.

- [114] Marina V Aksenova, Michael Y Aksenov, Charles F Mactutus, and Rosemarie M Booze. Cell culture models of oxidative stress and injury in the central nervous system. *Current Neurovascular Research*, 2(1):73–89, 2005.
- [115] Michael C. Owen, David Gnutt, Mimi Gao, Sebastian K. T. S. Wärmländer, Jüri Jarvet, Astrid Gräslund, Roland Winter, Simon Ebbinghaus, and Birgit Strodel. Effects of in vivo conditions on amyloid aggregation. *Chem. Soc. Rev.*, 48:3946–3996, 2019. doi: 10.1039/C8CS00034D.
- [116] Steven B Zimmerman and Allen P Minton. Macromolecular crowding: biochemical, biophysical, and physiological consequences. *Annual review of biophysics and biomolecular structure*, 22(1):27–65, 1993.
- [117] Steven B Zimmerman and Stefan O Trach. Estimation of macromolecule concentrations and excluded volume effects for the cytoplasm of escherichia coli. *Journal of molecular biology*, 222(3):599–620, 1991.
- [118] Kenji Sasahara, Peter McPhie, and Allen P Minton. Effect of dextran on protein stability and conformation attributed to macromolecular crowding. *Journal of molecular biology*, 326(4):1227–1237, 2003.
- [119] Apratim Dhar, Antonios Samiotakis, Simon Ebbinghaus, Lea Nienhaus, Dirar Homouz, Martin Gruebele, and Margaret S Cheung. Structure, function, and folding of phosphoglycerate kinase are strongly perturbed by macromolecular crowding. *Proceedings of the National Academy of Sciences*, 107(41):17586–17591, 2010.
- [120] Elio A Cino, Mikko Karttunen, and Wing-Yiu Choy. Effects of molecular crowding on the dynamics of intrinsically disordered proteins. *PLoS One*, 7(11):e49876, 2012.
- [121] Sean R McGuffee and Adrian H Elcock. Diffusion, crowding & protein stability in a dynamic molecular model of the bacterial cytoplasm. *PLoS computational biology*, 6(3):e1000694, 2010.
- [122] Yaqiang Wang, Conggang Li, and Gary J Pielak. Effects of proteins on protein diffusion. *Journal of the American Chemical Society*, 132(27):9392–9397, 2010.
- [123] Cécile Leduc, Kathrin Padberg-Gehle, Vladimír Varga, Dirk Helbing, Stefan Diez, and Jonathon Howard. Molecular crowding creates traffic jams of kinesin motors

- on microtubules. *Proceedings of the National Academy of Sciences*, 109(16):6100–6105, 2012.
- [124] Kazuhiro Aoki, Masashi Yamada, Katsuyuki Kunida, Shuhei Yasuda, and Michiyuki Matsuda. Processive phosphorylation of erk map kinase in mammalian cells. *Proceedings of the National Academy of Sciences*, 108(31):12675–12680, 2011.
- [125] Jyotica Batra, Ke Xu, Sanbo Qin, and Huan-Xiang Zhou. Effect of macromolecular crowding on protein binding stability: modest stabilization and significant biological consequences. *Biophysical Journal*, 97(3):906–911, 2009.
- [126] Liqin Huang, Rui Jin, Jiarui Li, Kan Luo, Tao Huang, Di Wu, Wenxi Wang, Rui Chen, and Gengfu Xiao. Macromolecular crowding converts the human recombinant prpc to the soluble neurotoxic β -oligomers. *The FASEB Journal*, 24(9):3536–3543, 2010.
- [127] Zheng Zhou, Xu Yan, Kai Pan, Jie Chen, Zheng-Sheng Xie, Geng-Fu Xiao, Fu-Quan Yang, and Yi Liang. Fibril formation of the rabbit/human/bovine prion proteins. *Biophysical journal*, 101(6):1483–1492, 2011.
- [128] Qian Ma, Jun-Bao Fan, Zheng Zhou, Bing-Rui Zhou, Sheng-Rong Meng, Ji-Ying Hu, Jie Chen, and Yi Liang. The contrasting effect of macromolecular crowding on amyloid fibril formation. *PloS one*, 7(4):e36288, 2012.
- [129] Vladimir N Uversky, Elisa M Cooper, Kiowa S Bower, Jie Li, and Anthony L Fink. Accelerated α -synuclein fibrillation in crowded milieu. *FEBS letters*, 515(1-3):99–103, 2002.
- [130] Mark D Shtilerman, Tomas T Ding, and Peter T Lansbury. Molecular crowding accelerates fibrillization of α -synuclein: could an increase in the cytoplasmic protein concentration induce parkinson’s disease? *Biochemistry*, 41(12):3855–3860, 2002.
- [131] Larissa A Munishkina, Elisa M Cooper, Vladimir N Uversky, and Anthony L Fink. The effect of macromolecular crowding on protein aggregation and amyloid fibril formation. *Journal of Molecular Recognition*, 17(5):456–464, 2004.
- [132] Zheng Zhou, Jun-Bao Fan, Hai-Li Zhu, Frank Shewmaker, Xu Yan, Xi Chen, Jie Chen, Geng-Fu Xiao, Lin Guo, and Yi Liang. Crowded cell-like environment

- accelerates the nucleation step of amyloidogenic protein misfolding. *Journal of Biological Chemistry*, 284(44):30148–30158, 2009.
- [133] Andrea Magno, Amedeo Caffisch, and Riccardo Pellarin. Crowding effects on amyloid aggregation kinetics. *The Journal of Physical Chemistry Letters*, 1(20):3027–3032, 2010.
- [134] Marcus Bokvist and Gerhard Gröbner. Misfolding of amyloidogenic proteins at membrane surfaces: the impact of macromolecular crowding. *Journal of the American Chemical Society*, 129(48):14848–14849, 2007.
- [135] David C Latshaw, Mookyung Cheon, and Carol K Hall. Effects of macromolecular crowding on amyloid beta (16–22) aggregation using coarse-grained simulations. *The Journal of Physical Chemistry B*, 118(47):13513–13526, 2014.
- [136] Xianfeng Li and Ernest L Mehler. Simulation of molecular crowding effects on an alzheimer’s α -amyloid peptide. *Cell biochemistry and biophysics*, 46(2):123–141, 2006.
- [137] David C Latshaw II and Carol K Hall. Effects of hydrophobic macromolecular crowders on amyloid β (16–22) aggregation. *Biophysical journal*, 109(1):124–134, 2015.
- [138] Scott A Hollingsworth and Ron O Dror. Molecular dynamics simulation for all. *Neuron*, 99(6):1129–1143, 2018.
- [139] Michael P Allen et al. Introduction to molecular dynamics simulation. *Computational soft matter: from synthetic polymers to proteins*, 23(1):1–28, 2004.
- [140] Jan CA Boeyens and Peter Comba. Molecular mechanics: theoretical basis, rules, scope and limits. *Coordination Chemistry Reviews*, 212(1):3–10, 2001.
- [141] Norman L Allinger. *Molecular structure: understanding steric and electronic effects from molecular mechanics*. John Wiley & Sons, 2010.
- [142] David J Earl and Michael W Deem. Monte carlo simulations. In *Molecular modeling of proteins*, pages 25–36. Springer, 2008.
- [143] Sergio Filipe Sousa, Pedro Alexandrino Fernandes, and Maria Joao Ramos. Protein–ligand docking: current status and future challenges. *Proteins: Structure, Function, and Bioinformatics*, 65(1):15–26, 2006.

- [144] Tadashi Ando and Ichiro Yamato. Basics of molecular simulation and its application to biomolecules. In *Quantum Bio-Informatics II: From Quantum Information to Bio-Informatics*, pages 228–241. World Scientific, 2009.
- [145] Andrew R Leach and Andrew R Leach. *Molecular modelling: principles and applications*. Pearson education, 2001.
- [146] Berni Julian Alder and Thomas Everett Wainwright. Phase transition for a hard sphere system. *The Journal of chemical physics*, 27(5):1208–1209, 1957.
- [147] Aneesur Rahman. Correlations in the motion of atoms in liquid argon. *Physical review*, 136(2A):A405, 1964.
- [148] J Andrew McCammon, Bruce R Gelin, and Martin Karplus. Dynamics of folded proteins. *Nature*, 267(5612):585–590, 1977.
- [149] JA McCammon. Molecular dynamics study of the bovine pancreatic trypsin inhibitor. *Models for Protein Dynamics*, page 137, 1976.
- [150] Michael Levitt. Birth and future of multiscale modeling for macromolecular systems (nobel lecture). *Angewandte Chemie International Edition*, 53(38):10006–10018, 2014.
- [151] Themis Lazaridis and Martin Karplus. Effective energy function for proteins in solution. *Proteins: Structure, Function, and Bioinformatics*, 35(2):133–152, 1999.
- [152] Jens P Linge, Mark A Williams, Christian AEM Spronk, Alexandre MJJ Bonvin, and Michael Nilges. Refinement of protein structures in explicit solvent. *Proteins: Structure, Function, and Bioinformatics*, 50(3):496–506, 2003.
- [153] Bartosz Różycki and Evzen Boura. Large, dynamic, multi-protein complexes: a challenge for structural biology. *Journal of Physics: Condensed Matter*, 26(46):463103, 2014.
- [154] Kenneth Goossens and Hans De Winter. Molecular dynamics simulations of membrane proteins: An overview. *Journal of chemical information and modeling*, 58(11):2193–2202, 2018.
- [155] Ignacio Tinoco Jr and Jin-Der Wen. Simulation and analysis of single-ribosome translation. *Physical biology*, 6(2):025006, 2009.

- [156] Relly Brandman, Yigal Brandman, and Vijay S Pande. A-site residues move independently from p-site residues in all-atom molecular dynamics simulations of the 70s bacterial ribosome. *PloS one*, 7(1):e29377, 2012.
- [157] Jacob D Durrant and J Andrew McCammon. Molecular dynamics simulations and drug discovery. *BMC biology*, 9(1):1–9, 2011.
- [158] Marco De Vivo, Matteo Masetti, Giovanni Bottegoni, and Andrea Cavalli. Role of molecular dynamics and related methods in drug discovery. *Journal of medicinal chemistry*, 59(9):4035–4061, 2016.
- [159] Nalini Schaduangrat, Samuel Lampa, Saw Simeon, Matthew Paul Gleeson, Ola Spjuth, and Chanin Nantasenamat. Towards reproducible computational drug discovery. *Journal of cheminformatics*, 12(1):1–30, 2020.
- [160] Srinivas Aluru. *Handbook of computational molecular biology*. CRC Press, 2005.
- [161] Ron O Dror, Robert M Dirks, JP Grossman, Huafeng Xu, and David E Shaw. Biomolecular simulation: a computational microscope for molecular biology. *Annual review of biophysics*, 41:429–452, 2012.
- [162] Timothy Nugent and David T Jones. Membrane protein structural bioinformatics. *Journal of structural biology*, 179(3):327–337, 2012.
- [163] Mark E Tuckerman and Glenn J Martyna. Understanding modern molecular dynamics: Techniques and applications. *The Journal of Physical Chemistry B*, 104(2):159–178, 2000.
- [164] Alexander D MacKerell Jr. Empirical force fields for biological macromolecules: overview and issues. *Journal of computational chemistry*, 25(13):1584–1604, 2004.
- [165] Luca Monticelli and D Peter Tieleman. Force fields for classical molecular dynamics. *Biomolecular simulations*, pages 197–213, 2013.
- [166] Xiao Zhu, Pedro EM Lopes, and Alexander D MacKerell Jr. Recent developments and applications of the charmm force fields. *Wiley Interdisciplinary Reviews: Computational Molecular Science*, 2(1):167–185, 2012.
- [167] Bernard R Brooks, Robert E Bruccoleri, Barry D Olafson, David J States, S a Swaminathan, and Martin Karplus. Charmm: a program for macromolecular

- energy, minimization, and dynamics calculations. *Journal of computational chemistry*, 4(2):187–217, 1983.
- [168] Alexander D MacKerell Jr, Nilesh Banavali, and Nicolas Foloppe. Development and current status of the charmm force field for nucleic acids. *Biopolymers: Original Research on Biomolecules*, 56(4):257–265, 2000.
- [169] Jing Huang, Sarah Rauscher, Grzegorz Nawrocki, Ting Ran, Michael Feig, Bert L De Groot, Helmut Grubmüller, and Alexander D MacKerell. Charmm36m: an improved force field for folded and intrinsically disordered proteins. *Nature methods*, 14(1):71–73, 2017.
- [170] RW Pastor and AD MacKerell Jr. Development of the charmm force field for lipids. *The journal of physical chemistry letters*, 2(13):1526–1532, 2011.
- [171] Jeffery B Klauda, Viviana Monje, Taehoon Kim, and Wonpil Im. Improving the charmm force field for polyunsaturated fatty acid chains. *The journal of physical chemistry B*, 116(31):9424–9431, 2012.
- [172] Christopher I. Bayly, Kenneth M. Merz, David M. Ferguson, Wendy D. Cornell, Thomas Fox, James W. Caldwell, Peter A. Kollman, Piotr Cieplak, Ian R. Gould, and David C. Spellmeyer. A Second Generation Force Field for the Simulation of Proteins, Nucleic Acids, and Organic Molecules. *J. Am. Chem. Soc.*, 117(19):5179–5197, 1995. ISSN 15205126.
- [173] Bernard R. Brooks, Robert E. Bruccoleri, Barry D. Olafson, David J. States, S. Swaminathan, and Martin Karplus. CHARMM: A program for macromolecular energy, minimization, and dynamics calculations. *J. Comput. Chem.*, 4(2):187–217, 1983. ISSN 1096987X.
- [174] William L. Jorgensen and Julian Tirado-Rives. The OPLS Potential Functions for Proteins. Energy Minimizations for Crystals of Cyclic Peptides and Crambin. *J. Am. Chem. Soc.*, 110(6):1657–1666, 1988. ISSN 15205126.
- [175] Walter R.P. Scott, Philippe H. Hünenberger, Ilario G. Tironi, Alan E. Mark, Salomon R. Billeter, Jens Fennen, Andrew E. Torda, Thomas Huber, Peter Krüger, and Wilfred F. Van Gunsteren. The GROMOS biomolecular simulation program package. *J. Phys. Chem. A*, 103(19):3596–3607, 1999. ISSN 10895639.

- [176] Loup Verlet. Computer” experiments” on classical fluids. i. thermodynamical properties of lennard-jones molecules. *Physical review*, 159(1):98, 1967.
- [177] Helmut Grubmüller, Helmut Heller, Andreas Windemuth, and Klaus Schulten. Generalized verlet algorithm for efficient molecular dynamics simulations with long-range interactions. *Molecular Simulation*, 6(1-3):121–142, 1991.
- [178] Wilfred F Van Gunsteren and Herman JC Berendsen. A leap-frog algorithm for stochastic dynamics. *Molecular Simulation*, 1(3):173–185, 1988.
- [179] Søren Toxvaerd. Algorithms for canonical molecular dynamics simulations. *Molecular Physics*, 72(1):159–168, 1991.
- [180] Roger W Hockney. The potential calculation and some applications. *Methods Comput. Phys.*, 9:136, 1970.
- [181] Nicos S Martys and Raymond D Mountain. Velocity verlet algorithm for dissipative-particle-dynamics-based models of suspensions. *Physical Review E*, 59(3):3733, 1999.
- [182] William C Swope, Hans C Andersen, Peter H Berens, and Kent R Wilson. A computer simulation method for the calculation of equilibrium constants for the formation of physical clusters of molecules: Application to small water clusters. *The Journal of chemical physics*, 76(1):637–649, 1982.
- [183] David Beeman. Some multistep methods for use in molecular dynamics calculations. *Journal of computational physics*, 20(2):130–139, 1976.
- [184] WF Van Gunsteren and HJC Berendsen. Algorithms for brownian dynamics. *Molecular Physics*, 45(3):637–647, 1982.
- [185] Alexey V Akimov and Anatoly B Kolomeisky. Recursive taylor series expansion method for rigid-body molecular dynamics. *Journal of chemical theory and computation*, 7(10):3062–3071, 2011.
- [186] Ramzi Kutteh. New methods for incorporating nonholonomic constraints into molecular dynamics simulations. *The Journal of chemical physics*, 111(4):1394–1406, 1999.

- [187] WB Streett, DJ Tildesley, and G Saville. Multiple time-step methods in molecular dynamics. *Molecular Physics*, 35(3):639–648, 1978.
- [188] Anders MN Niklasson, CJ Tymczak, and Matt Challacombe. Time-reversible ab initio molecular dynamics. *The Journal of chemical physics*, 126(14):144103, 2007.
- [189] Sandra J Rosenthal, Ralph Jimenez, Graham R Fleming, PV Kumar, and M Maroncelli. Solvation dynamics in methanol: Experimental and molecular dynamics simulation studies. *Journal of Molecular Liquids*, 60(1-3):25–56, 1994.
- [190] Takaharu Mori, Naoyuki Miyashita, Wonpil Im, Michael Feig, and Yuji Sugita. Molecular dynamics simulations of biological membranes and membrane proteins using enhanced conformational sampling algorithms. *Biochimica et Biophysica Acta (BBA)-Biomembranes*, 1858(7):1635–1651, 2016.
- [191] Sachin Patodia, Ashima Bagaria, and Deepak Chopra. Molecular dynamics simulation of proteins: A brief overview. *Journal of Physical Chemistry & Biophysics*, 4(6):1, 2014.
- [192] Jessica Nasica-Labouze, Phuong H Nguyen, Fabio Sterpone, Olivia Berthoumieu, Nicolae-Viorel Buchete, Sebastien Cote, Alfonso De Simone, Andrew J Doig, Peter Faller, Angel Garcia, et al. Amyloid β protein and alzheimer’s disease: When computer simulations complement experimental studies. *Chemical reviews*, 115(9):3518–3563, 2015.
- [193] Denise E Kirschner and Jennifer J Linderman. Mathematical and computational approaches can complement experimental studies of host–pathogen interactions. *Cellular microbiology*, 11(4):531–539, 2009.
- [194] Hans C Andersen. Molecular dynamics simulations at constant pressure and/or temperature. *The Journal of chemical physics*, 72(4):2384–2393, 1980.
- [195] Shuichi Nose. Constant-temperature molecular dynamics. *Journal of Physics: Condensed Matter*, 2(S):SA115, 1990.
- [196] SH [Ubar] ICHI NOSE. A molecular dynamics method for simulations in the canonical ensemble. *Molecular Physics*, 100(1):191–198, 2002.
- [197] David S Corti. Isothermal-isobaric ensemble for small systems. *Physical Review E*, 64(1):016128, 2001.

- [198] Masataka Yamauchi, Yoshiharu Mori, and Hisashi Okumura. Molecular simulations by generalized-ensemble algorithms in isothermal–isobaric ensemble. *Biophysical reviews*, 11(3):457–469, 2019.
- [199] Philippe H Hünenberger. Thermostat algorithms for molecular dynamics simulations. *Advanced computer simulation*, pages 105–149, 2005.
- [200] AS Lemak and NK Balabaev. On the berendsen thermostat. *Molecular Simulation*, 13(3):177–187, 1994.
- [201] Victor Rühle. Berendsen and nose-hoover thermostats. *Am. J. Phys*, 2007.
- [202] Tetsuya Morishita. Fluctuation formulas in molecular-dynamics simulations with the weak coupling heat bath. *The Journal of Chemical Physics*, 113(8):2976–2982, 2000.
- [203] Giovanni Bussi, Davide Donadio, and Michele Parrinello. Canonical sampling through velocity rescaling. *The Journal of chemical physics*, 126(1):014101, 2007.
- [204] Giovanni Bussi, Tatyana Zykova-Timan, and Michele Parrinello. Isothermal-isobaric molecular dynamics using stochastic velocity rescaling. *The Journal of chemical physics*, 130(7):074101, 2009.
- [205] Carlos Braga and Karl P Travis. A configurational temperature nosé-hoover thermostat. *The Journal of chemical physics*, 123(13):134101, 2005.
- [206] AC Brańka, M Kowalik, and KW Wojciechowski. Generalization of the nosé–hoover approach. *The Journal of chemical physics*, 119(4):1929–1936, 2003.
- [207] Joseph E Basconi and Michael R Shirts. Effects of temperature control algorithms on transport properties and kinetics in molecular dynamics simulations. *Journal of chemical theory and computation*, 9(7):2887–2899, 2013.
- [208] Shuichi Nosé. A unified formulation of the constant temperature molecular dynamics methods. *The Journal of chemical physics*, 81(1):511–519, 1984.
- [209] William G Hoover. Canonical dynamics: Equilibrium phase-space distributions. *Physical review A*, 31(3):1695, 1985.
- [210] Victor Rühle. Pressure coupling/barostats. *Journal Club*, 2008.

- [211] Herman JC Berendsen, JPM van Postma, Wilfred F van Gunsteren, ARHJ DiNola, and Jan R Haak. Molecular dynamics with coupling to an external bath. *The Journal of chemical physics*, 81(8):3684–3690, 1984.
- [212] Michele Parrinello and Aneesur Rahman. Polymorphic transitions in single crystals: A new molecular dynamics method. *Journal of Applied physics*, 52(12):7182–7190, 1981.
- [213] Céline Anézo, Alex H de Vries, Hans-Dieter Höltje, D Peter Tieleman, and Siewert-Jan Marrink. Methodological issues in lipid bilayer simulations. *The Journal of Physical Chemistry B*, 107(35):9424–9433, 2003.
- [214] Tomas Hansson, Chris Oostenbrink, and WilfredF van Gunsteren. Molecular dynamics simulations. *Current opinion in structural biology*, 12(2):190–196, 2002.
- [215] Mounir Tarek, Glenn J Martyna, and Douglas J Tobias. Amplitudes and frequencies of protein dynamics: analysis of discrepancies between neutron scattering and molecular dynamics simulations. *Journal of the American Chemical Society*, 122(42):10450–10451, 2000.
- [216] Wolfgang Weber, Philippe H Hünenberger, and J Andrew McCammon. Molecular dynamics simulations of a polyalanine octapeptide under ewald boundary conditions: influence of artificial periodicity on peptide conformation. *The Journal of Physical Chemistry B*, 104(15):3668–3675, 2000.
- [217] Ulrich Welling and Guido Germano. Efficiency of linked cell algorithms. *Computer Physics Communications*, 182(3):611–615, 2011.
- [218] W Smith. The minimum image convention in non-cubic md cells. 1989.
- [219] Witold Dzwiniel, Jacek Kitowski, and Jacek Mościński. “checker board” periodic boundary conditions in molecular dynamics codes. *Molecular Simulation*, 7(3-4):171–179, 1991.
- [220] David Van Der Spoel, Erik Lindahl, Berk Hess, Gerrit Groenhof, Alan E Mark, and Herman JC Berendsen. Gromacs: fast, flexible, and free. *Journal of computational chemistry*, 26(16):1701–1718, 2005.

- [221] Mark James Abraham, Teemu Murtola, Roland Schulz, Szilárd Páll, Jeremy C Smith, Berk Hess, and Erik Lindahl. Gromacs: High performance molecular simulations through multi-level parallelism from laptops to supercomputers. *SoftwareX*, 1:19–25, 2015.
- [222] Sunhwan Jo, Xi Cheng, Jumin Lee, Seonghoon Kim, Sang-Jun Park, Dhilon S Patel, Andrew H Beaven, Kyu Il Lee, Huan Rui, Soohyung Park, et al. Charmm-gui 10 years for biomolecular modeling and simulation. *Journal of computational chemistry*, 38(15):1114–1124, 2017.
- [223] Xi Cheng, Yifei Qi, Jumin Lee, Sunhwan Jo, and Wonpil Im. Charmm gui membrane builder updates. *Biophysical Journal*, 108(2):159a, 2015.
- [224] Jumin Lee, Xi Cheng, Jason M Swails, Min Sun Yeom, Peter K Eastman, Justin A Lemkul, Shuai Wei, Joshua Buckner, Jong Cheol Jeong, Yifei Qi, et al. Charmm-gui input generator for namd, gromacs, amber, openmm, and charmm/openmm simulations using the charmm36 additive force field. *Journal of chemical theory and computation*, 12(1):405–413, 2016.
- [225] DHJ Mackay, AJ Cross, and AT Hagler. The role of energy minimization in simulation strategies of biomolecular systems. In *Prediction of protein structure and the principles of protein conformation*, pages 317–358. Springer, 1989.
- [226] BJ Jaidhan, P Srinivasa Rao, and Allam Apparao. Energy minimization and conformation analysis of molecules using steepest descent method. *Int. J. Comput. Sci. Inf. Technol.*, 5(3):3525–3528, 2014.
- [227] Emily B. Walton and Krystyn J. VanVliet. Equilibration of experimentally determined protein structures for molecular dynamics simulation. *Phys. Rev. E*, 74:061901, Dec 2006. doi: 10.1103/PhysRevE.74.061901.
- [228] William Dawson and François Gygi. Equilibration and analysis of first-principles molecular dynamics simulations of water. *The Journal of Chemical Physics*, 148(12):124501, 2018. doi: 10.1063/1.5018116.
- [229] Marco T. Gallo, Barry J. Grant, Miguel L. Teodoro, Julia Melton, Piotr Cieplak, George N. Phillips Jr., and Boguslaw Stec. Novel procedure for thermal equilibration in molecular dynamics simulation. *Molecular Simulation*, 35(5):349–357, 2009. doi: 10.1080/08927020802647272.

- [230] Scott A. Hollingsworth and Ron O. Dror. Molecular Dynamics Simulation for All. *Neuron*, 99(6):1129–1143, 2018. ISSN 0896-6273. doi: <https://doi.org/10.1016/j.neuron.2018.08.011>.
- [231] J. Schlitter, M. Engels, and P. Krüger. Targeted molecular dynamics: A new approach for searching pathways of conformational transitions. *Journal of Molecular Graphics*, 12(2):84–89, 1994. ISSN 0263-7855. doi: [https://doi.org/10.1016/0263-7855\(94\)80072-3](https://doi.org/10.1016/0263-7855(94)80072-3).
- [232] Donald Hamelberg, John Mongan, and J. Andrew McCammon. Accelerated molecular dynamics: A promising and efficient simulation method for biomolecules. *The Journal of Chemical Physics*, 120(24):11919–11929, 2004. doi: 10.1063/1.1755656.
- [233] Alessandro Laio and Francesco L. Gervasio. Metadynamics: a method to simulate rare events and reconstruct the free energy in biophysics, chemistry and material science. *Reports on Progress in Physics*, 71(12):126601, November 2008. doi: 10.1088/0034-4885/71/12/126601. Publisher: IOP Publishing.
- [234] Yuji Sugita and Yuko Okamoto. Replica-exchange molecular dynamics method for protein folding. *Chemical Physics Letters*, 314(1):141–151, 1999. ISSN 0009-2614. doi: [https://doi.org/10.1016/S0009-2614\(99\)01123-9](https://doi.org/10.1016/S0009-2614(99)01123-9).
- [235] Luca Maragliano and Eric Vanden-Eijnden. A temperature accelerated method for sampling free energy and determining reaction pathways in rare events simulations. *Chemical Physics Letters*, 426(1):168–175, 2006. ISSN 0009-2614. doi: <https://doi.org/10.1016/j.cplett.2006.05.062>.
- [236] Yi Isaac Yang, Qiang Shao, Jun Zhang, Lijiang Yang, and Yi Qin Gao. Enhanced sampling in molecular dynamics. *The Journal of Chemical Physics*, 151(7):070902, 2019. doi: 10.1063/1.5109531.
- [237] Rafael C. Bernardi, Marcelo C. R. Melo, and Klaus Schulten. Enhanced sampling techniques in molecular dynamics simulations of biological systems. *Biochimica et Biophysica Acta (BBA) - General Subjects*, 1850(5):872–877, 2015. ISSN 0304-4165. doi: <https://doi.org/10.1016/j.bbagen.2014.10.019>.
- [238] Anna S. Kamenik, Stephanie M. Linker, and Sereina Riniker. Enhanced sampling without borders: on global biasing functions and how to reweight them. *Phys.*

- Chem. Chem. Phys.*, pages –, 2022. doi: 10.1039/D1CP04809K. Publisher: The Royal Society of Chemistry.
- [239] Alessandro Laio and Michele Parrinello. Escaping free-energy minima. *Proc. Natl. Acad. Sci. U.S.A.*, 99(20):12562–12566, 2002.
- [240] Alessandro Barducci, Massimiliano Bonomi, and Michele Parrinello. Metadynamics. *Wiley Interdiscip. Rev. Comput. Mol. Sci.*, 1(5):826–843, 2011.
- [241] Alessandro Barducci, Giovanni Bussi, and Michele Parrinello. Well-tempered metadynamics: a smoothly converging and tunable free-energy method. *Phys. Rev. Lett.*, 100(2):020603, 2008.
- [242] Davide Branduardi, Giovanni Bussi, and Michele Parrinello. Metadynamics with adaptive gaussians. *J. Chem. Theory Comput.*, 8(7):2247–2254, 2012.
- [243] Giovanni Bussi, Francesco Luigi Gervasio, Alessandro Laio, and Michele Parrinello. Free-energy landscape for β hairpin folding from combined parallel tempering and metadynamics. *J. Am. Chem. Soc.*, 128(41):13435–13441, 2006.
- [244] Michael Deighan, Massimiliano Bonomi, and Jim Pfandtner. Efficient simulation of explicitly solvated proteins in the well-tempered ensemble. *J. Chem. Theory Comput.*, 8(7):2189–2192, 2012.
- [245] Paolo Raiteri, Alessandro Laio, Francesco Luigi Gervasio, Cristian Micheletti, and Michele Parrinello. Efficient reconstruction of complex free energy landscapes by multiple walkers metadynamics. *J. Phys. Chem. B*, 110(8):3533–3539, 2006.
- [246] Stefano Piana and Alessandro Laio. A bias-exchange approach to protein folding. *J. Phys. Chem. B*, 111(17):4553–4559, 2007.
- [247] Yinglong Miao and J Andrew McCammon. Unconstrained enhanced sampling for free energy calculations of biomolecules: a review. *Mol. Simul.*, 42(13):1046–1055, 2016.
- [248] Mengzhi Han, Ji Xu, Ying Ren, and Jinghai Li. Simulation of coupled folding and binding of an intrinsically disordered protein in explicit solvent with metadynamics. *J. Mol. Graph. Model.*, 68:114–127, 2016.

- [249] Daniele Granata, Fahimeh Baftizadeh, Johnny Habchi, Celine Galvagnion, Alfonso De Simone, Carlo Camilloni, Alessandro Laio, and Michele Vendruscolo. The inverted free energy landscape of an intrinsically disordered peptide by simulations and experiments. *Sci. Rep.*, 5(1):1–15, 2015.
- [250] Yuji Sugita and Yuko Okamoto. Replica-exchange molecular dynamics method for protein folding. *Chem. Phys. Lett.*, 314(1-2):141–151, 1999.
- [251] Nikolaos G Sgourakis, Yilin Yan, Scott A McCallum, Chunyu Wang, and Angel E Garcia. The alzheimer’s peptides a β 40 and 42 adopt distinct conformations in water: a combined md/nmr study. *J. Mol. Biol.*, 368(5):1448–1457, 2007.
- [252] Davit A Potoyan and Garegin A Papoian. Energy landscape analyses of disordered histone tails reveal special organization of their conformational dynamics. *J. Am. Chem. Soc.*, 133(19):7405–7415, 2011.
- [253] Weihong Zhang, Debabani Ganguly, and Jianhan Chen. Residual structures, conformational fluctuations, and electrostatic interactions in the synergistic folding of two intrinsically disordered proteins. *PLoS Comput Biol*, 8(1):e1002353, 2012.
- [254] Michael Knott and Robert B Best. A preformed binding interface in the unbound ensemble of an intrinsically disordered protein: evidence from molecular simulations. *PLoS Comput Biol*, 8(7):e1002605, 2012.
- [255] Cayla Miller, Gul H Zerze, and Jeetain Mittal. Molecular simulations indicate marked differences in the structure of amylin mutants, correlated with known aggregation propensity. *J. Phys. Chem. B*, 117(50):16066–16075, 2013.
- [256] Gul H Zerze and Jeetain Mittal. Effect of o-linked glycosylation on the equilibrium structural ensemble of intrinsically disordered polypeptides. *J. Phys. Chem. B*, 119(51):15583–15592, 2015.
- [257] Debabani Ganguly and Jianhan Chen. Atomistic details of the disordered states of kid and pkid. implications in coupled binding and folding. *J. Am. Chem. Soc.*, 131(14):5214–5223, 2009.
- [258] Giovanni Bussi. Hamiltonian replica exchange in gromacs: a flexible implementation. *Mol. Phys.*, 112(3-4):379–384, 2014.

- [259] Qinghua Liao, Michael C. Owen, Sofia Bali, Bogdan Barz, and Birgit Strodel. $A\beta$ under stress: the effects of acidosis, Cu^{2+} -binding, and oxidation on amyloid β -peptide dimers. *Chem. Commun.*, 54:7766–7769, 2018.
- [260] Hebah Fatafta, Chetan Poojari, Abdallah Sayyed-Ahmad, Birgit Strodel, and Michael C Owen. Role of oxidized gly25, gly29, and gly33 residues on the interactions of $a\beta_{1-42}$ with lipid membranes. *ACS Chem. Neurosci.*, 11(4):535–548, 2020.
- [261] Satoru G Itoh and Hisashi Okumura. Oligomer formation of amyloid- β (29–42) from its monomers using the hamiltonian replica-permutation molecular dynamics simulation. *J. Phys. Chem. B*, 120(27):6555–6561, 2016.
- [262] Utsab R Shrestha, Puneet Juneja, Qiu Zhang, Viswanathan Gurumoorthy, Jose M Borreguero, Volker Urban, Xiaolin Cheng, Sai Venkatesh Pingali, Jeremy C Smith, Hugh M O’Neill, et al. Generation of the configurational ensemble of an intrinsically disordered protein from unbiased molecular dynamics simulation. *Proc. Natl. Acad. Sci. U.S.A.*, 116(41):20446–20452, 2019.
- [263] Xiaorong Liu, Xiping Gong, and Jianhan Chen. Accelerating atomistic simulations of proteins using multiscale enhanced sampling with independent tempering. *J. Comput. Chem.*, 42(5):358–364, 2021.
- [264] James C Phillips, Rosemary Braun, Wei Wang, James Gumbart, Emad Tajkhorshid, Elizabeth Villa, Christophe Chipot, Robert D Skeel, Laxmikant Kale, and Klaus Schulten. Scalable molecular dynamics with namd. *J. Comput. Chem.*, 26(16):1781–1802, 2005.
- [265] Massimiliano Bonomi, Davide Branduardi, Giovanni Bussi, Carlo Camilloni, Davide Provasi, Paolo Raiteri, Davide Donadio, Fabrizio Marinelli, Fabio Pietrucci, Ricardo A Broglia, et al. Plumed: A portable plugin for free-energy calculations with molecular dynamics. *Comput. Phys. Commun.*, 180(10):1961–1972, 2009.
- [266] Louis Sokoloff. Energetics of functional activation in neural tissues. *Neurochemical research*, 24(2):321–329, 1999.
- [267] Alois Zauner, Wilson P Daugherty, M Ross Bullock, and David S Warner. Brain oxygenation and energy metabolism: part i—biological function and pathophysiology. *Neurosurgery*, 51(2):289–302, 2002.

- [268] G Tholey and M Ledig. Neuronal and astrocytic plasticity: metabolic aspects. In *Annales de medecine interne*, volume 141, pages 13–18, 1990.
- [269] Domenico Pratico. Oxidative stress hypothesis in alzheimer’s disease: a reappraisal. *Trends in pharmacological sciences*, 29(12):609–615, 2008.
- [270] Akihiko Nunomura, Rudy J Castellani, Xiongwei Zhu, Paula I Moreira, George Perry, and Mark A Smith. Involvement of oxidative stress in alzheimer disease. *Journal of neuropathology & experimental neurology*, 65(7):631–641, 2006.
- [271] Thijs Stuyver, David Danovich, and Sason Shaik. Captodative substitution enhances the diradical character of compounds, reduces aromaticity, and controls single-molecule conductivity patterns: A valence bond study. *The Journal of Physical Chemistry A*, 123(32):7133–7141, 2019.
- [272] Heinz G Viehe, Zdenek Janousek, Robert Merenyi, and Lucien Stella. The captodative effect. *Accounts of Chemical Research*, 18(5):148–154, 1985.
- [273] Arvi Rauk, David A Armstrong, and David P Fairlie. Is oxidative damage by β -amyloid and prion peptides mediated by hydrogen atom transfer from glycine α -carbon to methionine sulfur within β -sheets? *Journal of the American Chemical Society*, 122(40):9761–9767, 2000.
- [274] Mandy C Green, Sarah Stelzleni, and Joseph S Francisco. Spectral marker for α damage in beta peptides. *The Journal of Physical Chemistry A*, 117(3):550–565, 2013.
- [275] Michael J Davies. The oxidative environment and protein damage. *Biochimica et Biophysica Acta (BBA)-Proteins and Proteomics*, 1703(2):93–109, 2005.
- [276] Brigitte Gasser, Markku Saloheimo, Ursula Rinas, Martin Dragosits, Escarlata Rodríguez-Carmona, Kristin Baumann, Maria Giuliani, Ermenegilda Parrilli, Paola Branduardi, Christine Lang, et al. Protein folding and conformational stress in microbial cells producing recombinant proteins: a host comparative overview. *Microbial cell factories*, 7(1):1–18, 2008.
- [277] Zoya Ignatova. Monitoring protein stability in vivo. *Microbial Cell Factories*, 4(1):1–6, 2005.
- [278] Alice B Fulton. How crowded is the cytoplasm? *Cell*, 30(2):345–347, 1982.

- [279] R John Ellis. Macromolecular crowding: obvious but underappreciated. *Trends in biochemical sciences*, 26(10):597–604, 2001.
- [280] Phuong H Nguyen, Ayyalusamy Ramamoorthy, Bikash R Sahoo, Jie Zheng, Peter Faller, John E Straub, Laura Dominguez, Joan-Emma Shea, Nikolay V Dokholyan, Alfonso De Simone, et al. Amyloid oligomers: A joint experimental/computational perspective on alzheimer’s disease, parkinson’s disease, type ii diabetes, and amyotrophic lateral sclerosis. *Chemical reviews*, 121(4):2545–2647, 2021.
- [281] Eugene L Opie. The relation of diabetes mellitus to lesions of the pancreas. hyaline degeneration of the islands of langerhans. *The Journal of experimental medicine*, 5(5):527, 1901.
- [282] Katrine Kirkeby Skeby, Ole Juul Andersen, Taras V Pogorelov, Emad Tajkhorshid, and Birgit Schiøtt. Conformational dynamics of the human islet amyloid polypeptide in a membrane environment: toward the aggregation prone form. *Biochemistry*, 55(13):2031–2042, 2016.
- [283] Lucie Caillon, Anais RF Hoffmann, Alexandra Botz, and Lucie Khemtouriian. Molecular structure, membrane interactions, and toxicity of the islet amyloid polypeptide in type 2 diabetes mellitus. *Journal of diabetes research*, 2016, 2016.
- [284] Lucie Khemtouriian, Ghislaine Guillemain, Fabienne Foufelle, and J Antoinette Killian. Residue specific effects of human islet polypeptide amyloid on self-assembly and on cell toxicity. *Biochimie*, 142:22–30, 2017.
- [285] Anais RF Hoffmann, Manikam Sadasivam Saravanan, Olivier Lequin, J Antoinette Killian, and Lucie Khemtouriian. A single mutation on the human amyloid polypeptide modulates fibril growth and affects the mechanism of amyloid-induced membrane damage. *Biochimica et Biophysica Acta (BBA)-Biomembranes*, 1860(9):1783–1792, 2018.
- [286] Lucie Khemtouriian, Federico Antoniciello, Bikash R Sahoo, Marion Decossas, Sophie Lecomte, and Ayyalusamy Ramamoorthy. Investigation of the effects of two major secretory granules components, insulin and zinc, on human-iapp amyloid aggregation and membrane damage. *Chemistry and Physics of Lipids*, 237:105083, 2021.